ELSEVIER

Contents lists available at ScienceDirect

Progress in Materials Science

journal homepage: www.elsevier.com/locate/pmatsci



Radiation damage in nanostructured materials

Xinghang Zhang ^{a,*}, Khalid Hattar ^b, Youxing Chen ^c, Lin Shao ^d, Jin Li ^a, Cheng Sun ^e, Kaiyuan Yu ^f, Nan Li ^c, Mitra L. Taheri ^g, Haiyan Wang ^{a,h}, Jian Wang ⁱ, Michael Nastasi ^{i,j}

- ^a School of Materials Engineering, Purdue University, West Lafayette, IN 47907, USA
- ^b Department of Radiation-Solid Interactions, Sandia National Laboratories, Albuquerque, NM 87185, USA
- ^c MPA-CINT, Los Alamos National Laboratory, Los Alamos, NM 87545, USA
- ^d Department of Nuclear Engineering, Texas A&M University, College Station, TX 77843-3128, USA
- ^e Materials and Fuels Complex, Idaho National Laboratory, Idaho Falls, ID 83415, USA
- ^fDepartment of Materials Science and Engineering, China University of Petroleum-Beijing, Beijing 102246, China
- ^g Department of Materials Science and Engineering, Drexel University, Philadelphia, PA 19104, USA
- ^h School of Electrical and Computer Engineering, Purdue University, West Lafayette, IN 47907, USA
- ⁱDepartment of Mechanical and Materials Engineering, University of Nebraska-Lincoln, Lincoln, NE 68583-0857, USA
- ^jNebraska Center for Energy Sciences Research, University of Nebraska-Lincoln, Lincoln, NE 68583-0857, USA

ARTICLE INFO

Article history: Received 30 December 2016 Received in revised form 4 March 2018 Accepted 13 March 2018 Available online 15 March 2018

Keywords:
Radiation damage
Nanomaterials
Modeling
In situ radiation
Defect sinks
Materials design

ABSTRACT

Materials subjected to high dose irradiation by energetic particles often experience severe damage in the form of drastic increase of defect density, and significant degradation of their mechanical and physical properties. Extensive studies on radiation effects in materials in the past few decades show that, although nearly no materials are immune to radiation damage, the approaches of deliberate introduction of certain types of defects in materials before radiation are effective in mitigating radiation damage. Nanostructured materials with abundant internal defects have been extensively investigated for various applications. The field of radiation damage in nanostructured materials is an exciting and rapidly evolving arena, enriched with challenges and opportunities. In this review article, we summarize and analyze the current understandings on the influence of various types of internal defect sinks on reduction of radiation damage in primarily nanostructured metallic materials, and partially on nanoceramic materials. We also point out open questions and future directions that may significantly improve our fundamental understandings on radiation damage in nanomaterials. The integration of extensive research effort, resources and expertise in various fields may eventually lead to the design of advanced nanomaterials with unprecedented radiation tolerance.

© 2018 Elsevier Ltd. All rights reserved.

E-mail address: xzhang98@purdue.edu (X. Zhang).

Abbreviations: BCC, body-centered cubic; CG, coarse-grained; CTB, coherent twin boundary; DDZ, defect denuded zone; dpa, displacements-per-atom; ECAP, equal channel angular pressing; FCC, face-centered cubic; GB, grain boundary; HCP, hexagonal close-packed; HRTEM, high-resolution transmission electron microscopy; ITB, incoherent twin boundary; IVEM, intermediate voltage electron microscopy; KS, Kurdjumov-Sachs; MD, molecular dynamics; MDI, misfit dislocation intersection; NC, nanocrystalline; NP, nanoporous; NT, nanotwinned; NV-NT, nanovoid-nanotwinned; ODS, oxide dispersion strengthened; OKMC, object kinetic Monte Carlo; PED, precession electron diffraction; PKA, primary knock-on atom; PPM, parts per million; RT, room temperature; SAD, selected area diffraction; SFE, stacking fault energy; SFT, stacking fault tetrahedron; SIA, self-interstitial atom; SITB, symmetric incoherent twin boundary; SRIM, stopping and range of ions in matter; SS, stainless steel; STEM, scanning transmission electron microscopy; TB, twin boundary; TBAZ, twin boundary affected zone; TEM, transmission electron microscopy; TJ, triple junction; UFG, ultra-fine grained; VDZ, void denuded zone; XTEM, cross-sectional transmission electron microscopy; 0/1/2/3 D, zero/one/two/three dimensional.

^{*} Corresponding author.

Contents

1.		luction	
	1.1.	Motivation, scope and architecture	
		1.1.1. Motivation	
		1.1.2. Scope	219
		1.1.3. Architecture	220
	1.2.	Radiation induced defects in metals with various crystal structures.	
		1.2.1. Radiation induced defects in metals with face-centered-cubic (FCC) structures	
		1.2.2. Radiation induced defects in metals with body-centered-cubic (BCC) structures	
	1.3.	Radiation induced defects in metals with HCP structures	
	1.4.	Radiation induced cavities: Voids and gas bubbles	
		1.4.1. Voids and void swelling	
		1.4.2. Radiation induced He bubbles	230
	1.5.	Classical models of sink strength for various types of defects	. 230
	1.6.	Defect sinks and some general philosophies for alleviation of radiation damage	
2.	Radia	tion damage in nanocrystalline metals and ceramics	233
	2.1.	Sink strength of grain boundaries	. 233
	2.2.	Defect-GB interactions	
		2.2.1. Experimental observations of the defect-GB interactions in NC metals	
		2.2.2. MD simulations showing defect absorption/capture by GBs	
	2.3.	Effect of grain size on radiation tolerance – microstructure and mechanical properties	
	2.5.	2.3.1. Radiation damage in pure NC metals	
		2.3.2. Radiation damage in NC alloys	
		2.3.3. Radiation damage in non-metallic NC materials	
	2.4.	Need to refine the GB sink strength model	
		2.4.1. Complexity of GB nature on radiation damage in NC metals	
		2.4.2. Modified GB sink strength model	
		2.4.3. Application of the modified model for interpreting experimental findings	247
	2.5.	Stabilities of NC metals in radiation environments.	. 248
	2.6.	Challenges and future outlook	
3.		tion damage in metallic and ceramic nanolayers	
	3.1.	Sink strength of nanolayers	
	3.2.	Phenomena of defect-interface interactions	
	3.2.	3.2.1. <i>In situ</i> studies on absorption of radiation-induced defects by layer interfaces	
		3.2.2. Layer interface effect: distance dependent defect concentration profile	
		3.2.3. Layer-thickness-dependent defect concentration	
		3.2.4. He bubble denuded zones near layer interfaces.	
	3.3.	Size effect on mitigation of radiation damage in nanolayers	
	3.4.	Nature of interface on irradiation response of nanolayers	
	5.4.		
		3.4.1. Incoherent immiscible interfaces: The influence of misfit dislocation arrays	
		3.4.2. Immiscible coherent interfaces: The Influence of coherency stress	
		3.4.3. Miscible layer interfaces: radiation-induced intermixing	
	3.5.	Alternative mechanisms of reducing defect densities in nanolayers	. 263
	3.6.	Radiation damage in ceramic nanolayers: Amorphization and nanocrystallization	. 263
	3.7.	Size effect on hardening in irradiated nanolayers	. 267
	3.8.	Challenges and future outlook	. 273
4.	Radia	tion damage in nanotwinned metals	273
		Twin boundaries in FCC metals	
		4.1.1. Defective CTBs	
		4.1.2. Dislocation structures of ITBs	
	4.2.	Radiation effects of CTBs.	
	4.2.	4.2.1. Defect-CTB interactions	
	4.0		
	4.3.	Effects of ion irradiation on ITBs	
		4.3.1. Point defect–ITB interactions	
		4.3.2. Irradiation-induced ITB migration and dislocation–ITB interactions	
	4.4.	3D defect-TB interactions	
		4.4.1. SFT-TB interactions: mechanisms and experiments	282
		4.4.2. Helium bubbles in nanotwinned metals	286
	4.5.	Anomalous defect distribution in nanotwinned metals	. 287
	4.6.	Healing of nanovoids and alleviation of irradiation damage by nanovoid-nanotwinned architecture	. 288
	4.7.	Summary and future outlook	
5.		tion damage in nanoporous materials, nanowires and nanoparticles	
	5.1.	The sink strength of nanoporous materials	
	-	• • • • • • • • • • • • • • • • • • • •	

	5.2.	Free su	rface – defect interactions in nanoporous materials	291					
		5.2.1.	Capture of radiation-induced defect clusters by free surface	291					
		5.2.2.	Radiation induced void shrinkage	292					
	5.3.	Size eff	Size effect in irradiated nanoporous materials and nanowires						
		5.3.1.	Size effect in nanoporous materials	293					
		5.3.2.	Size effect in nanowires	297					
	5.4.	. Irradiation-induced structural change of nanoparticles							
	5.5.	5.5. The influence of free surfaces on the defect migration kinetics							
	5.6. Summary and future work								
6.	Sumn	nmary and future outlook							
	Ackno	owledge	ments	306					
	Refer	ences		306					

1. Introduction

1.1. Motivation, scope and architecture

1.1.1. Motivation

Nuclear energy accounts for more than 13% of electricity generated worldwide [1]. The design of advanced (next generation) nuclear reactors calls for materials that can survive an exceptionally high radiation dose of 400–600 dpa (displacements-per-atom), equivalent to the service lifetime of more than 80 years in advanced nuclear reactors. However, most materials adopted in the current nuclear reactors have not been tested over a dose of 200 dpa. Fundamental studies show that radiation by high-energy particles, including electrons, protons, neutrons, light and heavy ions, can introduce significant microstructural damage in a variety of metallic materials. Extensive research studies in the past few decades show that although the details of microstructural damage vary drastically for various materials, the nature of the damage in crystalline materials is mostly associated with the formation, distribution and interaction of point defects (vacancies and interstitials), and their clusters, such as Frenkel pairs (vacancy-interstitial pairs), vacancy clusters, interstitial loops, radiation induced dislocation segments and networks, inert gas bubbles and voids [1–3]. To a large extent, there are nearly no existing materials that are immune to radiation damage. Understanding the mechanisms of radiation damage clearly has a significant impact on the design of radiation tolerant materials for advanced nuclear energy applications.

1.1.2. Scope

Radiation involves extensive ion-solid interactions, which may have beneficial or deleterious impacts on the properties of materials [1,4]. For materials used in nuclear reactors, radiation damage can pose a serious challenge to the structural stability and reliability of these materials over a long period of time, which is relevant to the safe operation of nuclear reactors [5]. In this review article, we summarize recent progress in the investigation of radiation damage in nanostructured materials, focusing on metallic materials and/or metal-ceramic compounds. Radiation damage in nanostructured ferritic alloys and oxide dispersion strengthened (ODS) steels is another important subject that has been intensely studied but will not be covered here as there are several recent reviews and numerous highlights on this subject [6–16].

Radiation has also been used to achieve unique properties in various fields. For instance, ion implantation has been routinely adopted by semiconductor industry to tune electrical conductivity or to fabricate semiconductor devices [17–22]. Ion irradiation has also been applied to introduce various nanofeatures that may drastically change the chemical and physical

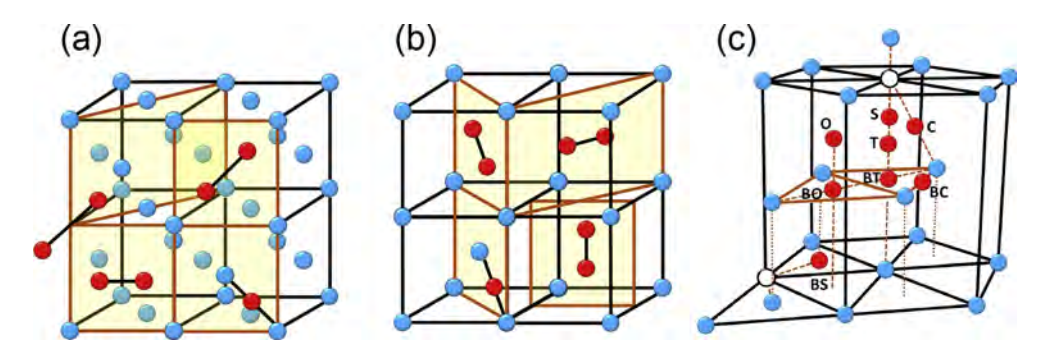


Fig. 1.1. Various types of interstitials in monolithic metals with FCC, BCC and HCP crystal structures. (a) FCC: $\langle 1\ 1\ 1\rangle$, $\langle 1\ 1\ 0\rangle$ and $\langle 1\ 0\ 0\rangle$ dumbbells, and crowdions; (b) BCC: $\langle 1\ 1\ 1\rangle$, $\langle 1\ 1\ 0\rangle$ and $\langle 1\ 0\ 0\rangle$ dumbbells and crowdions; (c) Eight available interstitial sites in HCP metals: octahedron (O), tetrahedron (T), BO and BT – on the basal plane below O and T sites, BC and C – crowdions halfway between two nearest neighbor atoms along $\langle 1\ 1\ 2\ 0\rangle$ (on the basal plane) and $1/6\langle 2\ 0\ 2\ 3\rangle$ direction (out of the basal plane), BS and S – split dumbbells within or orthogonal to the basal plane (replotted following [27]).

properties via surface engineering [23,24]. The subject on nanopatterning using ion irradiation technique is not the focus of the current review and is not included for further discussions.

1.1.3. Architecture

The architecture of the current review article is organized as follows. Section 1 briefly summarizes some basics on the nature and formation of defects and their interactions. Introducing these concepts is beneficial to understand radiation damage related to microstructure evolution at a fundamental level. The significance of various types of defect sinks is briefly introduced in this chapter. At the end of Section 1, an overview is provided to summarize various types of defect sinks that will be discussed separately in various nanostructured materials in succeeding chapters. Section 2 targets the impact of grain boundaries on the alleviation of radiation damage in fine grained materials. Section 3 focuses on the reduction of radiation damage by using various layer interfaces in metallic and metal/ceramics nanolayer composites. Section 4 eyes on the strategy of using twin boundaries in nano-twinned metals to transport and eliminate radiation induced defects. This chapter also describes the combination of nanotwins and nanovoids to design radiation tolerant materials. In Section 5, we discuss the influence of free surfaces in controlling the radiation tolerance of nanoporous, OD, and 1D materials.

Most of these sections will begin by discussing the sink strength of each type of defect sinks, present some *in situ* evidence for the absorption of radiation-induced defects by defect sinks, and discuss the size effect, that is the influence of defect sinks on mitigation of radiation damage. Certain sections will also address the concerns on the limitation of the current models for defect sink strength, and discuss modified sink strength formulas. Each section has its own outlook that is more specific for a

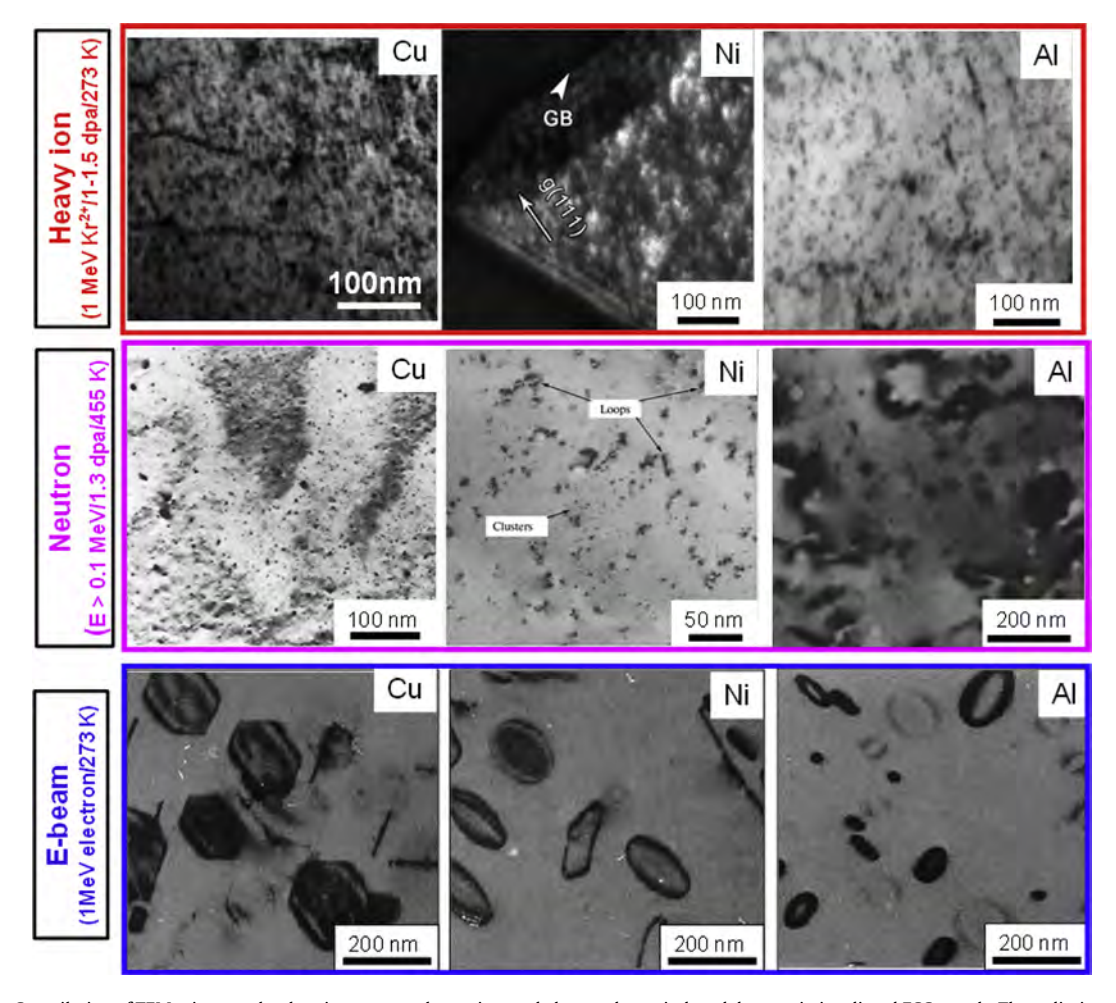


Fig. 1.2. Compilation of TEM micrographs showing neutron, heavy ion, and electron beam induced damage in irradiated FCC metals. The radiation condition in terms of dpa or fluence is also provided. Under heavy Kr ion irradiation at 273 K, a large number of small interstitial loops are generated in Cu, Ni and Al [29,30]. Neutron radiation at 455 K to a similar level of the dose generates defects with similar morphology (small loops) but with somewhat lower defect density [31–33]. Room temperature e-beam (1 MeV) irradiation introduces large interstitial loops, which are mostly faulted loops on {1 1 1} planes [34]. Reprinted with permission from Ref. [29,30–34].

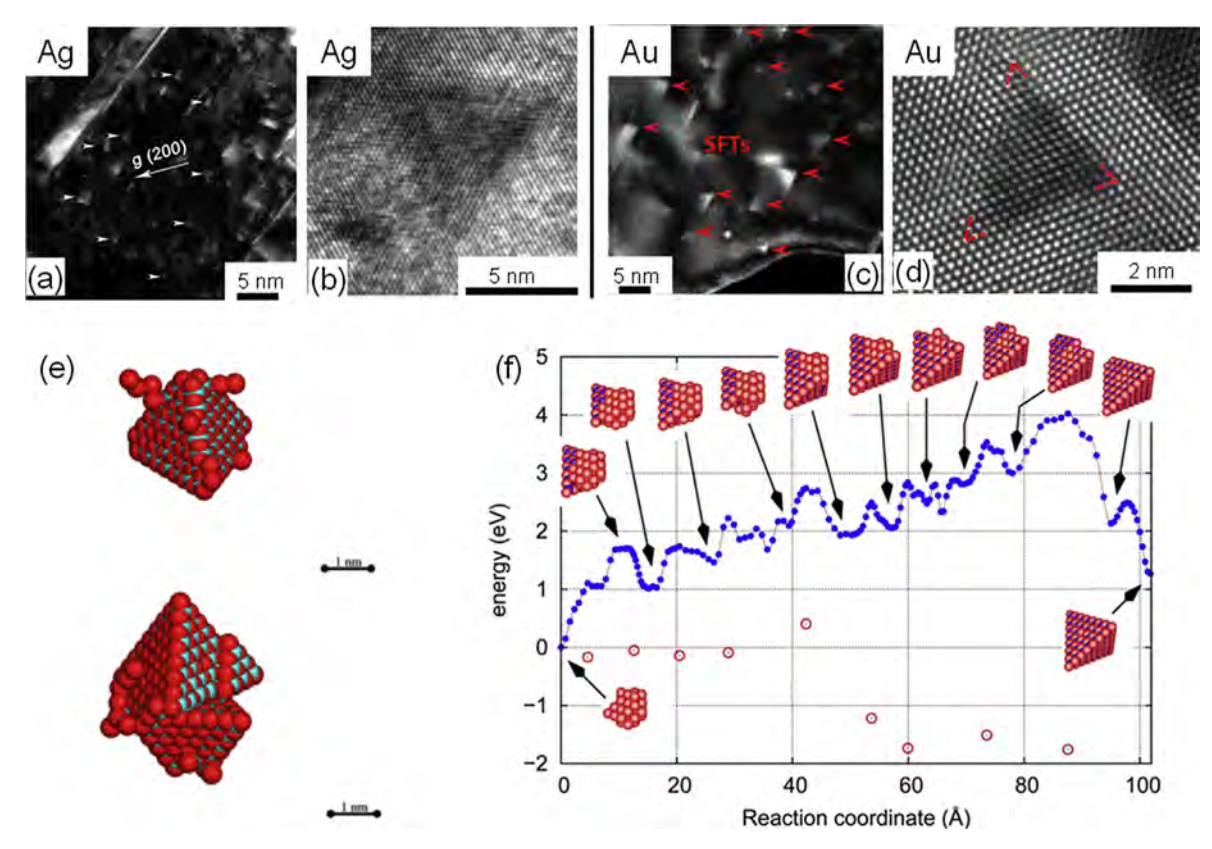


Fig. 1.3. SFTs in irradiated FCC metals. (a and b) Dark field TEM and HRTEM micrographs of SFTs in irradiated Ag films (1 MeV Kr ions/1 dpa/RT) [39]. (c and d) Dark field TEM and atomic resolution TEM micrographs of SFTs in irradiated Au films (1 MeV Kr ions/1 dpa/RT) [40]. (e) MD simulations on the formation and evolution of regular SFT and two adjunct SFTs in Cu [43]. (f) MD simulations showing the evolution of a void into an SFT [44]. Reprinted with permission from Ref. [39,40,43,44]

particular type of nanomaterials. At the end of the review, a broader view for the future work is presented to engage and stimulate collaborations among nuclear materials, nanomaterials, physics, chemistry, mechanics and modeling community. Intimate collaborations among scientists in these communities may be the key to push the forefront of science forward, and to accelerate the design of radiation tolerant and ultimately "radiation immune" materials for the future generations of nuclear reactors.

1.2. Radiation induced defects in metals with various crystal structures

1.2.1. Radiation induced defects in metals with face-centered-cubic (FCC) structures

Metallic materials with FCC structures are widely used as structural materials in nuclear reactors, including austenitic stainless steels, Ni alloys and certain Cu conducting cables [1–3,5,25]. Very often pure metals are irradiated as model systems, where the influence of chemistry from a second phase does not exist. Yet, the nature of defects induced in these pure metals is often similar to what has been identified in austenitic stainless steels. Also these FCC metals have drastically different stacking fault energy (SFE), which is critical to determine the type and morphology of radiation induced defects [26].

The vacancy migration energy for FCC metals typically varies from 0.7 to 1.7 eV, and it is typically 50–70% less than the vacancy formation energy. Several types of interstitials may exist, including 3 types of dumbbells, $\langle 1\ 1\ 1 \rangle$, $\langle 1\ 1\ 0 \rangle$, and $\langle 1\ 0\ 0 \rangle$ dumbbells, crowdions (shown in Fig. 1.1a), and the classical tetrahedral and octahedral interstitials (not shown here). As the interstitial formation energy is often the lowest for the $\langle 1\ 0\ 0 \rangle$ split dumbbells, the corresponding value is widely used to represent the general interstitial formation energy. The interstitial migration energy is typically 0.05–0.1 eV, significantly less than the vacancy migration energy. Hence it is widely accepted that interstitials (and interstitial loops) are highly mobile, even at room temperature, whereas vacancies mostly move at elevated temperatures. Such a drastic difference between vacancies and interstitials has a profound impact on the accumulation of radiation damage and void swelling in FCC metals and alloys. To some extent, the mobile interstitials (which evolve quickly into interstitial loops) leave vacancies behind, and the disparity in mobility of opposite types of point defects often accelerates the accumulation of vacancy and interstitial type clusters respectively.

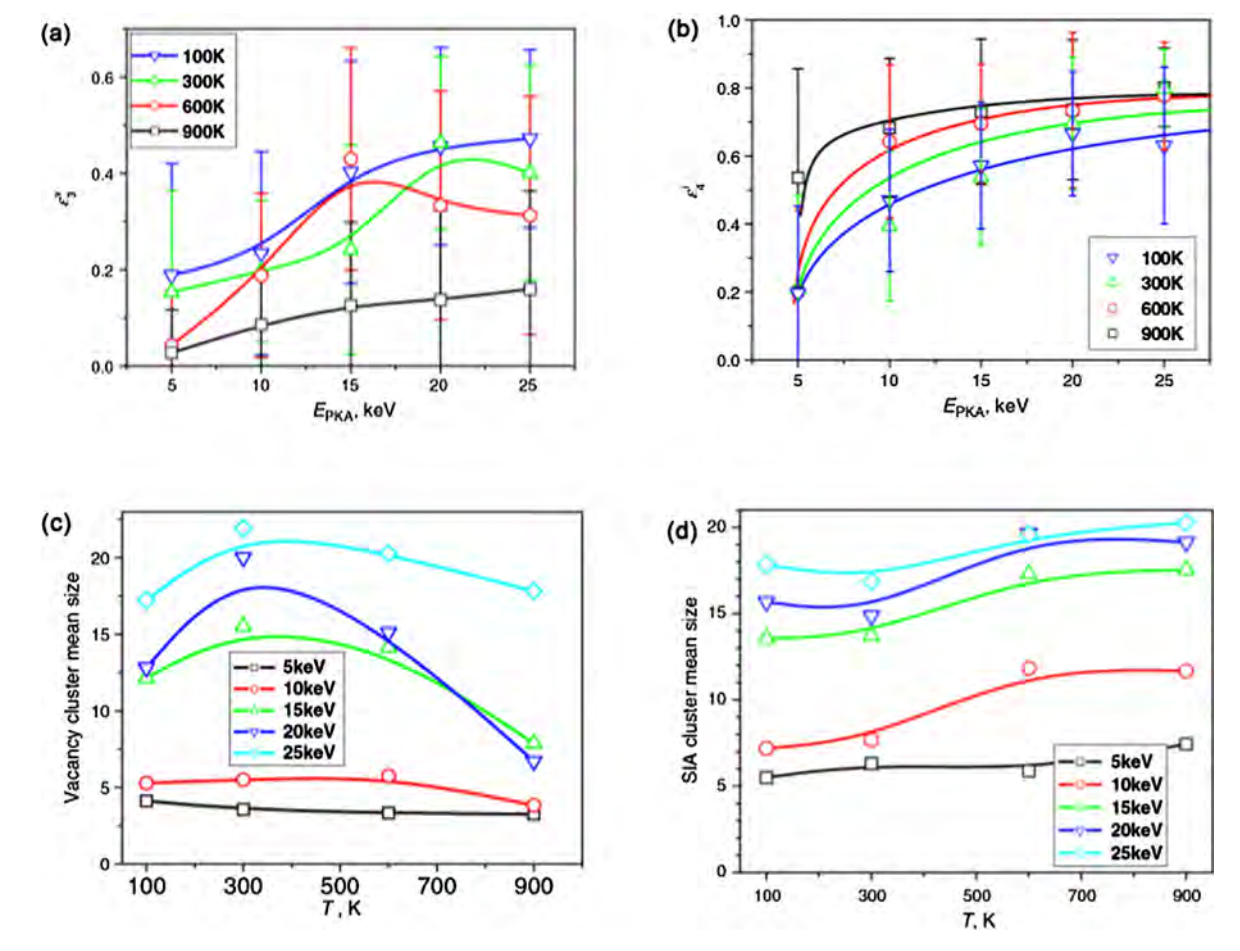


Fig. 1.4. MD simulation studies on self-ion irradiated Cu [43]. (a and b) Evolution of the fraction of vacancy and interstitial clusters at different temperatures in self-ion irradiated Cu. (c and d) Evolution of the mean size of vacancy and SIA clusters as a function of irradiation temperature. Reprinted with permission from Ref. [43].

The volume of a vacancy, V_V^F , is known to be less than the volume of one isolated atom, typically 0.75 Ω (Ω is the atomic volume). This is due to the relaxation of surrounding atoms. Such a relaxation volume, V_V^{rel} , can be written as:

$$V_V^{rel} = \Omega - V_V^F, \tag{1.1}$$

and is typically \sim 0.25 Ω for a suite of FCC metals [28]. The activation volume of self-diffusion (V_V^{SD}) in FCC metals is described as

$$V_V^{SD} = V_V^F + V_V^M, \tag{1.2}$$

where V_V^F, V_V^M are respective activation volume of vacancy formation and migration. Typically, the vacancy migration volume is 0.1Ω and the activation volume for self-diffusion in FCC metals is $\sim 0.85~\Omega$. The dilatational volume expansion associated with the insertion of a self interstitial atom (SIA) in an FCC lattice, V_{SIA}^F , is $\sim 1.1~\Omega$. Considering the volume expansion arising from non-linear elastic strain, δV , the relaxation volume for self-interstitials (V_{SIA}^{rel}), estimated by

$$V_{SIA}^{rel} = V_{SIA}^F + \delta V, \tag{1.3}$$

is typically $\sim 2 \Omega$. As will be shown later, the V_{SIA}^{rel} for SIA in BCC metals is much smaller. Such a difference has an important implication on different radiation tolerance (such as void swelling resistance) between BCC and FCC metals.

Isolated point defects tend to cluster together. Among the known defect clusters in FCC metals, interstitial loops and vacancy loops are widely observed. Furthermore, vacancy clusters can evolve into stacking fault tetrahedrons (SFTs), which are a type of 3D defect and difficult to be eliminated. In FCC metals with low-to-intermediate SFE, faulted dislocation (both vacancy and interstitial) loops are frequently observed. Many of these faulted loops are immobile. However, abundant Shockley partials (an inherent nature of FCC metals) can glide and interact with these faulted loops and consequently

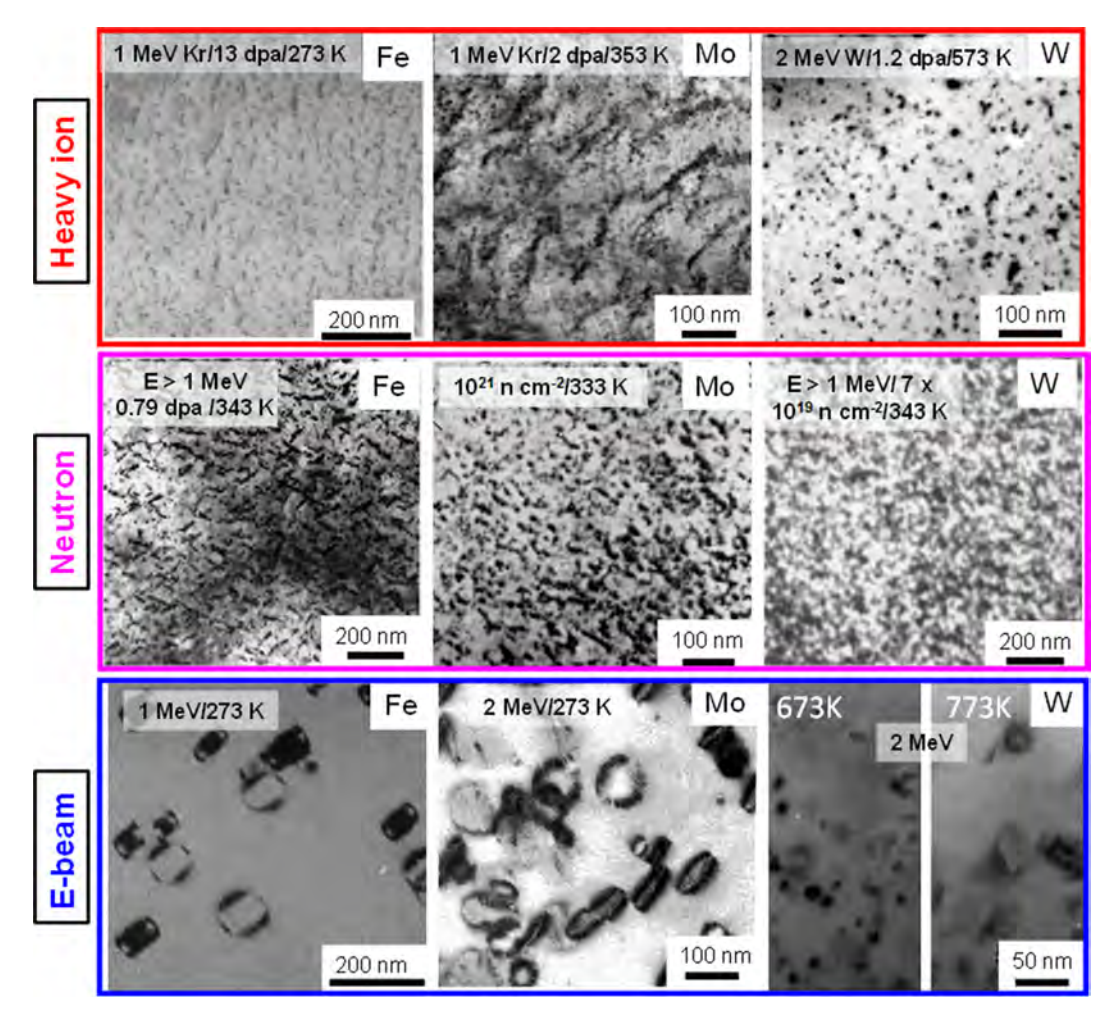


Fig. 1.5. Compilation of TEM micrographs showing radiation damage in Fe, Mo and W induced by heavy ions, neutrons and e-beam. The ion energy, dose/fluence and radiation temperature are also provided [25,34,51–53,55–58]. In general heavy ion and neutron radiation induce small dislocation loops, string or rafts of loops, whereas e-beam generates large isolated dislocation loops. Reprinted with permission from Refs. [25,34,51–53,55–58].

transform the sessile loops into mobile perfect loops, with Burgers vector of $\frac{1}{2}$ $\langle 1\ 1\ 0 \rangle$. The glide plane of these perfect loops is either $\{1\ 1\ 1\}$ or $\{1\ 1\ 0\}$ [2].

Fig. 1.2 collects selected examples of radiation damage in Cu, Ni and Al to a similar dose level by using heavy ions (such as Kr), neutrons and electron beam (e-beam). Under heavy Kr ion irradiation at 273 K to 1–1.5 dpa, a large number of small interstitial dislocation loops are observed in all 3 FCC metals [29,30]. Defect density appears to be greater in Cu than in Al. Neutron radiation at a higher temperature (455 K) to a similar fluence (1.3 dpa) generates defects with similar morphology (small loops) but with slightly lower defect density [31–33]. Meanwhile, e-beam (1 MeV) radiations at room temperature introduce rather large isolated interstitial loops in all FCC metals, which are mostly faulted loops on {1 1 1} planes [34]. The different defect morphologies between e-beam and neutron irradiation are mostly due to the fact that e-beam radiation typically gives rise to isolated low energy recoil atoms (0.1–1 kev), whereas neutron irradiations produce much more energetic recoil atoms (>10 kev). Consequently e-beam radiation induces isolated SIAs and vacancies that nucleate and coarsen via diffusion process [2]. In contrast, high-energy neutron radiation generates small defect clusters directly within the cascade. These small defect clusters act as defect sinks and curtail the coarsening of defect clusters [35–37]. Comparison of weighted average recoil spectra (a measure of fraction of defects with recoil energy) of neutrons, proton and heavy ions shows that Kr provides a much better approximation to neutron irradiation than light ions [38].

SFTs are another intriguing type of defects in irradiated FCC metals, and they often have triangular geometry under TEM. Some examples of SFTs are shown by dark field TEM and HRTEM in Fig. 1.3a and b for Ag [39] and in Fig. 1.3c and d for Au, irradiated by 1 MeV Kr ions to 1 dpa at room temperature [40]. The formation of SFTs has been investigated by MD simulations. In general, SFTs can evolve from vacancy clusters via the classical Silcox and Hirsch [41] mechanism as later visualized by MD simulations [42]. MD simulations of a large number of collision cascades show that a regular SFT or conjoint SFTs can form (Fig. 1.3e) [43]. SFT-like vacancy clusters are also frequently observed in irradiated FCC Cu. SIA loops can be either

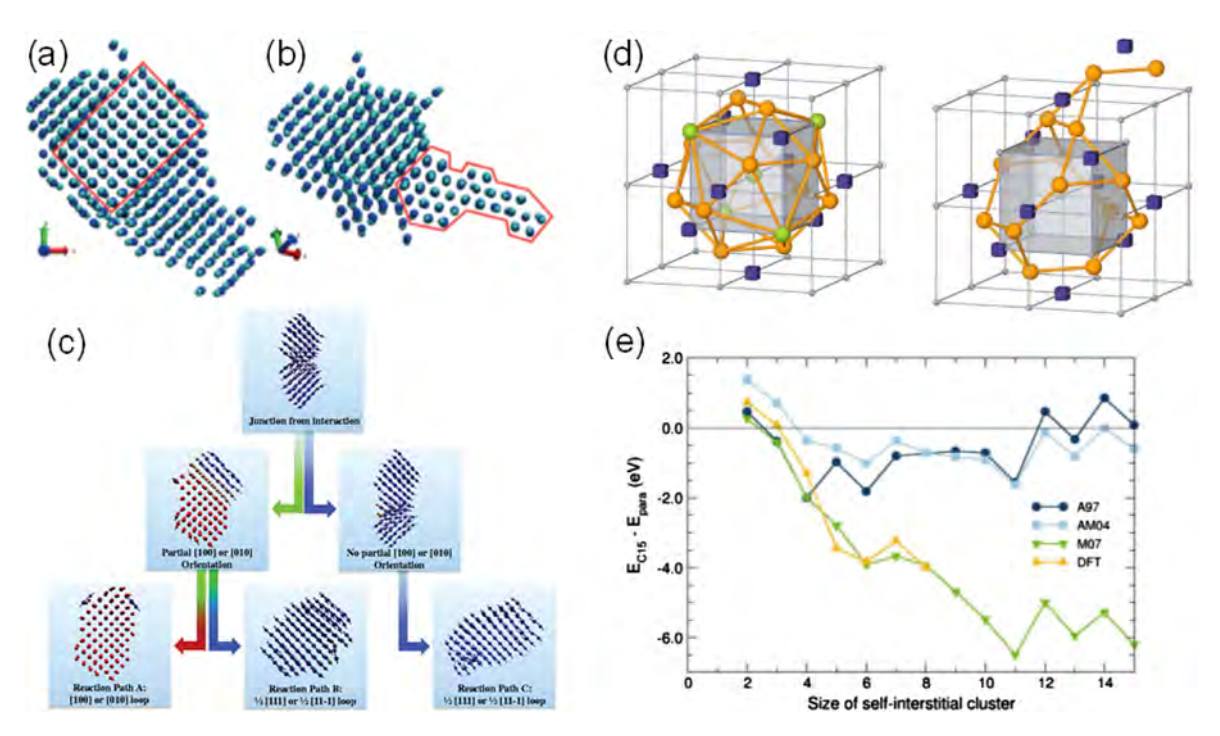


Fig. 1.6. (a-c) MD simulations showing the formation of $\langle 1\ 0\ 0 \rangle$ dislocation loops in BCC Fe [45,59]. (d and e) The formation of C15 clusters in irradiated Fe and the energy of the defect cluster [60]. Reprinted with permission from Refs. [45,59,60].

glissile, in the case of perfect interstitial loops with Burgers vector of $\frac{1}{2}$ $\langle 1\ 1\ 0 \rangle$, or sessile, in the case of faulted loops with Burgers vector of $\frac{1}{3}$ $\langle 1\ 1\ 1 \rangle$. Furthermore, the MD simulations also show that SFTs can even stem from a void, instead of Frank loops, as shown in Fig. 1.3f. The transformation is driven by a large increase in entropy, in spite of a high potential energy barrier. Such a mechanism may be applicable to a variety of FCC metals [44].

Large scale MD simulations (Fig. 1.4) also show that at ambient to intermediate (<600 K) temperatures, 40% of the vacancy clusters are composed of more than 3 vacancies; whereas 80% of the interstitial clusters have more than 4 interstitials [43]. The fraction of vacancy clusters decreases with increasing radiation temperature. In contrast, the fraction of interstitial clusters continues to increase at higher irradiation temperatures. The vacancy cluster size in irradiated Cu appears to reach a maximum at 300 K in certain cases, due to a transition from compact cascade below 300 K (yielding large vacancy clusters) to thermal spike promoted destabilization of large vacancy clusters (due to interstitial-vacancy recombination) at elevated temperature. In comparison, the SIA cluster size increases monotonically with increasing temperature due to their higher binding energy [43].

1.2.2. Radiation induced defects in metals with body-centered-cubic (BCC) structures

Radiation damage in BCC metals has also been extensively investigated [1,8,45,46]. Similar to FCC metals, a suite of point defects and their clusters are generated in irradiated BCC metals. The vacancy formation energy for BCC metals is typically 1.6–3 eV, and vacancy migration energy is 0.5–2 eV. Various types of interstitial can be generated in BCC metals, including crowdions, $\langle 1\ 1\ 1\rangle$, $\langle 1\ 1\ 0\rangle$ and $\langle 1\ 0\ 0\rangle$ dumbbells (as shown in Fig. 1.1b) and octahedral and tetrahedral SIAs. The activation volume for self-diffusion of interstitials in BCC metals is \sim 0.4–0.6 Ω [28,47,48], smaller than that in FCC metals, \sim 0.85 Ω [28,47,48]. In comparison to FCC metal, the volume expansion associated with the insertion of an interstitial atom in BCC metal is much smaller, \sim 0.64 Ω (versus 1.1 Ω for FCC) [28,47,48], presumably due to the lower packing density of BCC metals. The relaxation volume for self-interstitials in BCC metal is \sim 1.0–1.5 Ω [28,48], also much smaller than that in FCC metals, \sim 2 Ω [28,48]. These differences between FCC and BCC metals may explain the enhanced radiation tolerance of BCC metals vs. FCC metals to some extent.

The generally high SFE of BCC metals prohibits the formation of large faulted dislocation loops [49]. The perfect glissile loops in BCC metals have $\{1\ 1\ 0\}$ habit planes with $b = a/2\ (1\ 1\ 1)$, whereas the perfect sessile loops are often on $\{1\ 0\ 0\}$ habit planes with $b = a\ (1\ 0\ 0)\ [34,50]$. Fig. 1.5 shows various types of dislocation loops in BCC Fe, Mo and W irradiated by heavy ions, neutrons or e-beam [25,34,51–58]. In general, the defect clusters induced by heavy ions and neutrons are similar, in form of dislocation loops with dimensions of several to 10 nm, in these irradiated BCC metals. Heavy ion irradiation of Fe induces abundant dislocation loops (string of loops) [51], whereas neutron irradiation induces rafts in Fe [25]. In comparison, e-beam introduces much fewer loops with greater loop diameter. For instance, e-beam irradiation induces perfect $\{1\ 0\ 0\}$

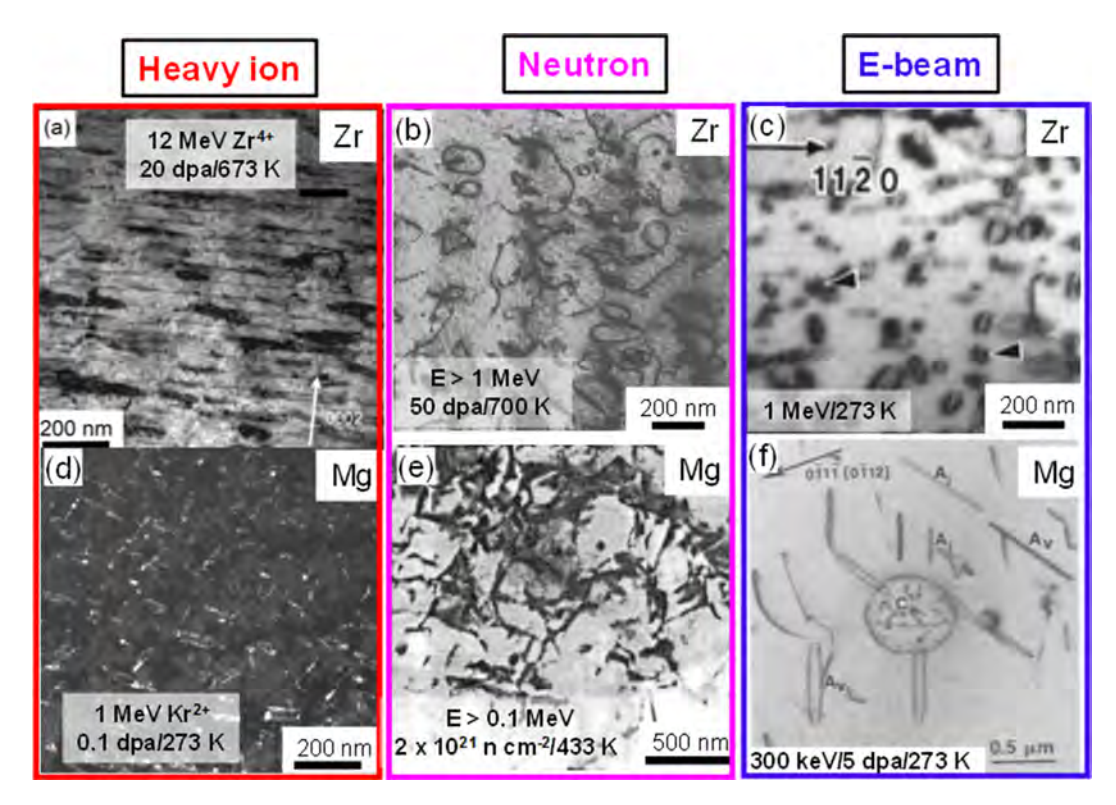


Fig. 1.7. Compilation of TEM micrographs showing radiation damage in HCP Zr and Mg irradiated by heavy ions, neutrons and e-beam. (a) Heavy self-ion irradiation of Zr showing c-component loops [64]. (b) Neutron irradiation of Zr introduces a loop and c-loops [65]. (c) E-beam irradiation of Zr induces a and c loops [65]. (d) 1 MeV Kr ion (273 K/0.1 dpa) irradiation of basal Mg foil showing abundant prism loops with Burgers vector of $1/3\langle 1\ 1\ 2\ 0\rangle$ [66]. (e) Neutron irradiation of Mg induces dislocation networks [67]. (f) E-beam irradiation of Mg (300 K/5 dpa) [63]. The a-type loops are vacancy (A_v.) and interstitial loops in character, and have Burgers vectors of $1/3\langle 1\ 1\ 2\ 0\rangle$; c-component interstitial loops (C₁) have Burgers vector of $1/6\langle 2\ 0\ 2\ 3\rangle$. Reprinted with permission from Ref. [63–67].

loops in Fe [34]. In comparison to e-beam irradiation of FCC metals, Kiritani reported that no vacancy clusters were observed in e-beam irradiated Fe [34].

Radiation damage in Fe has been extensively investigated by simulations. Recent MD simulation studies (Fig. 1.6a–c) show that the interaction between two $\frac{1}{2}$ (1 1 1) loops may have 3 scenarios (path A, B and C), one of which leads to the formation of $\frac{1}{2}$ 0 0 loops [45,59]. The mobility of $\frac{1}{2}$ (1 1 1) loops is important as such will ensure the probability of interaction among these loops [59]. Furthermore MD simulations have predicted the formation of nanoclusters with C15 structure in Fe (Fig. 1.6d). These C15 nanoclusters are of interstitial types but are immobile and have a low formation energy (Fig. 1.6e) [60].

1.3. Radiation induced defects in metals with HCP structures

The investigations on the nature of defects in HCP metals are largely driven by the application of HCP Zr based alloys as fuel cladding tubes in light water reactors. Vacancies and interstitials have much more complicated configurations in HCP metals than in cubic systems. Both monvacancies and divacancies have been investigated in HCP metals. The formation and migration energy for monovacancies are typically 0.6–2 eV and 0.3–1 eV respectively. The formation volume of monovacancies typically varies from 0.78 to 0.97 Ω [27,61,62]. Monovacancies can diffuse within or out of the basal planes. Calculations, though somewhat controversial in certain cases, suggest that the activation energy for self-diffusion (summation of vacancy formation and migration energy) is smaller for the non-basal plane for Zr with c/a less than ideal value [27,61,62], whereas the vacancy migration is more isotropic for Mg and Co with near ideal c/a ratios.

Two types of divacancies appear stable, including divacancies between the first nearest neighbors and second nearest neighbors. When c/a < 1.633, the first nearest divacancies are out of the basal plane, whereas the second nearest divacancies are within the basal plane [27]. The divacancies have formation energy of 1.1-3.5 eV, and formation volume of $1.5-1.9~\Omega$ [27]. Among numerous migration paths, two paths (within or out-of-basal planes) have the lowest energy of migration, 0.45-0.75 eV [27]. There are 8 different sites for SIAs in HCP metals, as shown in Fig. 1.1c, including octahedron (O), tetrahedron (T), BO and BT in the basal plane underneath the O and T sites. BC and C are crowdions located halfway between the two nearest neighbor atoms along (1.1.2.0) (on the basal plane) and 1/6 (2.0.2.3) direction (out of basal plane). BS and S are

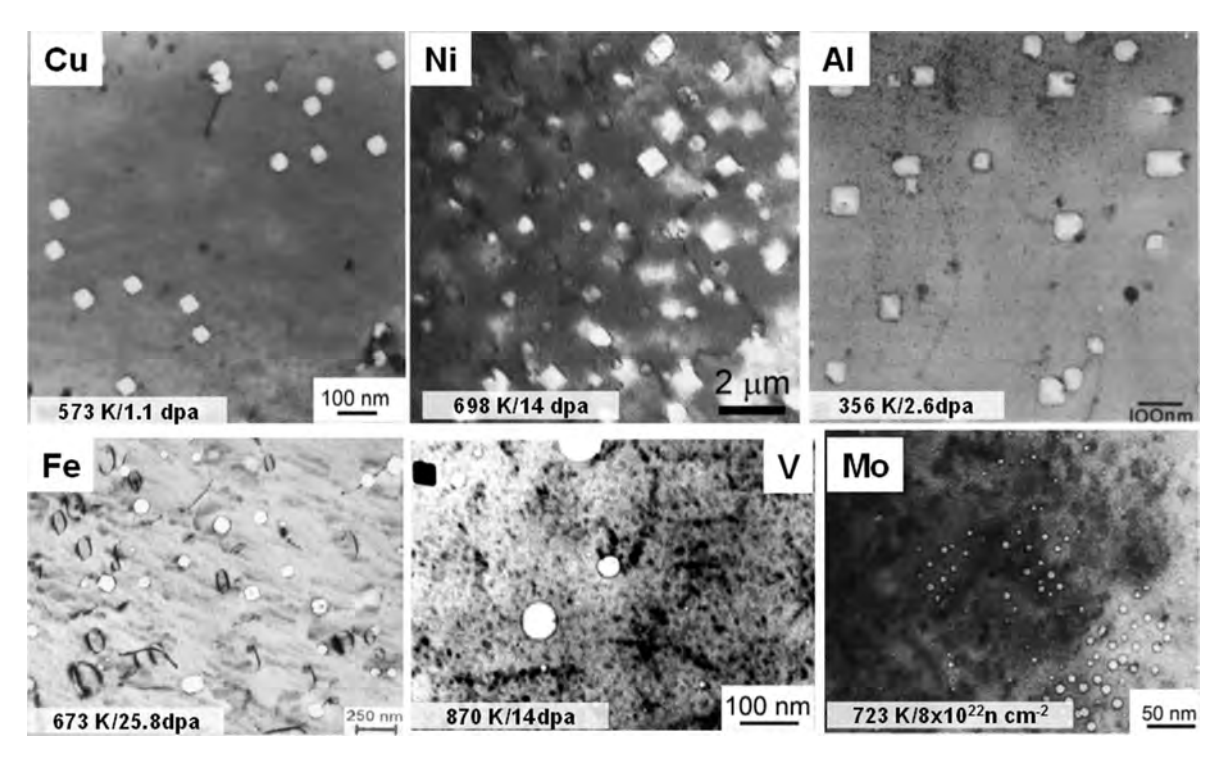


Fig. 1.8. Neutron irradiation induced voids in a variety of monolithic metals with FCC [3,80,81] and BCC [82–84] crystal structure. Voids with different geometry, spherical or rectangular, are observed. Reprinted with permission from Refs. [3,80–84].

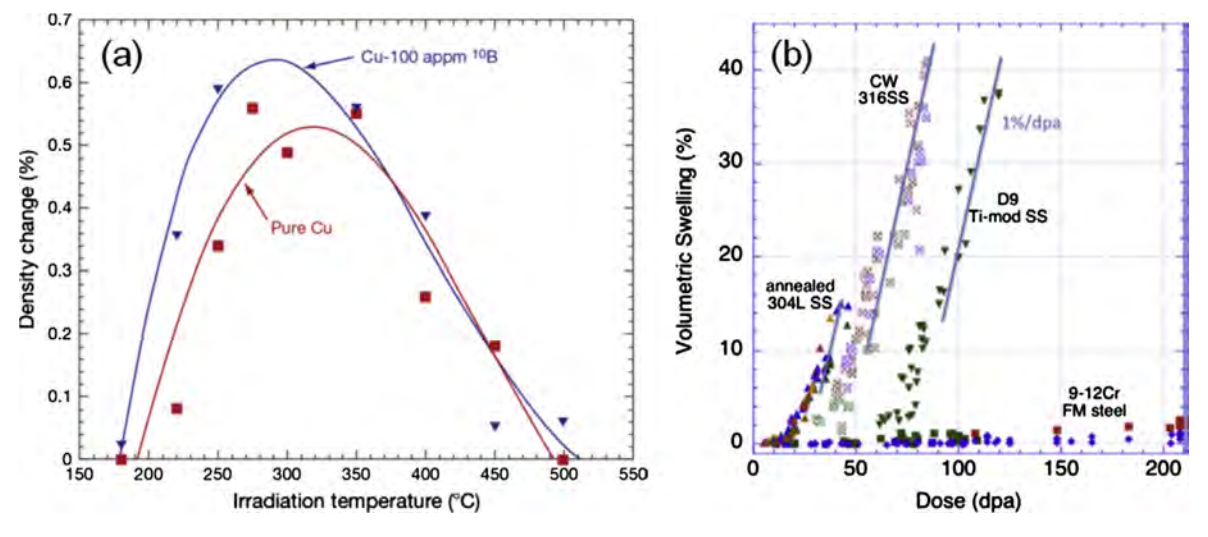


Fig. 1.9. (a) Density change in neutron irradiated Cu $(1-1.3 \text{ dpa}, 2 \times 10^{-7} \text{ dpa/s})$ as a function of irradiation temperature showing temperature dependent void swelling [2,3,87]. (b) Swelling curves for numerous neutron irradiated austenitic and ferritic/martensitic steels [1,2,78,88–90]. Reprinted with permission from Ref. [2].

respective split dumbbells within or orthogonal to the basal plane [27,61,62]. In general, the basal split or crowdion is the most stable configuration for HCP metals with a rather large deviation from the ideal c/a value, and the non-basal dumbbell (C or S) is the most stable configuration for metals with near ideal c/a ratios [27]. The interstitial formation energy in HCP metals is also high, typically 2–6 eV, whereas their migration energy is very low, 0.05–1 eV. The formation volume of interstitials is typically 0.6–1.2 Ω [27].

The major types of defect clusters generated by radiation in HCP metals include vacancy clusters and interstitial loops. A perfect vacancy loop resides on $\{1\ 0\ \bar{1}\ 0\}$ prismatic plane with Burgers vector of $1/3\ \langle 1\ 1\ \bar{2}\ 0\rangle$; and a faulted vacancy loop on $(0\ 0\ 0\ 1)$ basal plane has Burgers vector of $1/6\ \langle 2\ 0\ \bar{2}\ 3\rangle$. A perfect interstitial loop on $\{1\ 0\ \bar{1}\ 0\}$ plane also has the Burgers

Table 1.1 Peak void swelling temperature T_S^P in FCC metals.

FCC	T_V^M (K) [2]	T_S^P (K)	T _m (K)	T_S^P/T_{m}	Radiation source
Al	220	423	933	0.45 [91]	Al ⁺ ions
					1100 grade Al
Al	220	No void	933	[92]	Al ⁺ ions
					Pure Al (< 0.1 appm impurity)
Al	220	300	933	0.32 [92]	Al ⁺ ions
					pre-injected with 10 ppm He
Ag	240	-	1235	_	-
Au	290	=	1337	_	=
Cu	270	600	1358	0.44 [3,93]	Neutron
Ni	350	780	1728	0.45 [94]	Neutron
		873	1728	0.51 [95]	Ni ⁺ ions
Pd	350	_	1828	-	-
Pt	350	=	2041	-	=

Note: T_V^M - The temperature at which vacancies are mobile.

Table 1.2 Peak void swelling temperature (T_5^p) in BCC and HCP metals.

BCC	T_S^P (K)	$T_m(K)$	$T_S^P/\mathrm{T_m}$ ref	Source
Fe	630-780	1811	0.35-0.43 [74,94]	Neutron
Mo	740-870	2896	0.26-0.3 [84,96,97]	Neutron
Mo	1173	2896	0.41 [98]	Ni ⁺ ions
Nb	1073-1273	2750	0.4-0.46 [98,99]	Ni ⁺ ions
Ta	900	3290	0.27 [100]	Neutron
Ta	1400	3290	0.43 [101]	Cu ²⁺ ions
V	630	2183	0.41 [97]	Neutron
V	973	2183	0.45 [102]	Cu ⁺ ions
W	1000	3695	0.27 [103]	Neutron
Zr (HCP)	750	2128	0.35 [104]	Electron, pre-injected with 100 appm helium
Zr (HCP)	700-740	2128	0.33-0.35 [105,106]	Neutron

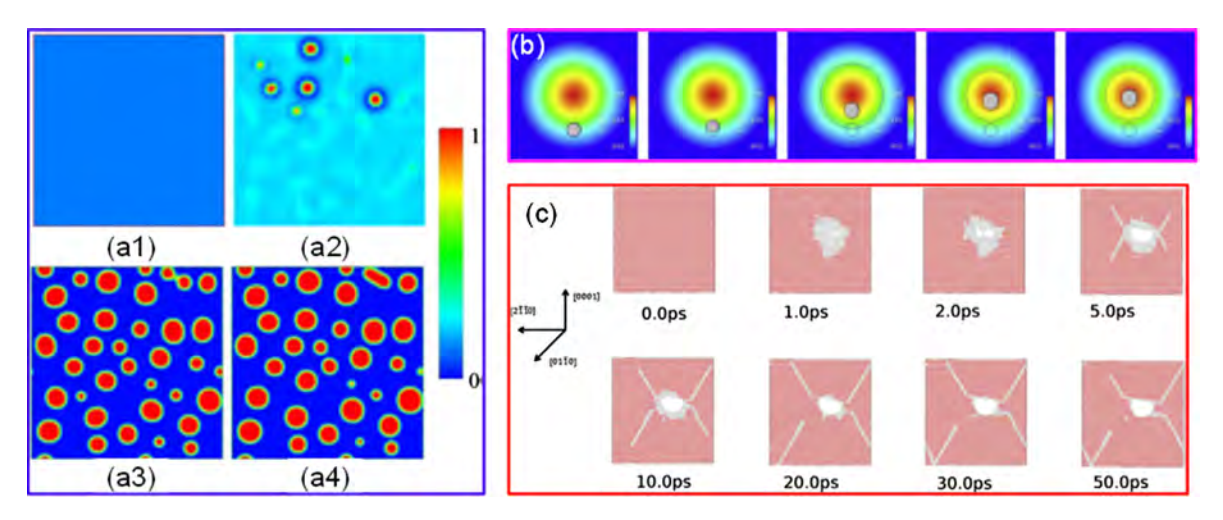


Fig. 1.10. (a) Phase field modeling of void swelling showing the concurrent nucleation and growth of voids with time in a system supersaturated with vacancies [108]. (b) Phase field modeling studies showing the migration and growth of a void to the interstitial enriched center region [109]. (c) MD simulations showing the formation of voids adjacent to dislocations in Zr subjected to radiation and tension [110]. Reprinted with permission from Refs. [108–110].

vector of $1/3 \langle 1 \ 1 \ \bar{2} \ 0 \rangle$; and faulted interstitial loops are typically observed on $(0 \ 0 \ 1)$ plane with Burgers vector of $1/6 \langle 2 \ 0 \ \bar{2} \ 3 \rangle$ or $1/2 [0 \ 0 \ 0 \ 1] [50,61,63]$.

Fig. 1.7 shows selected examples of heavy ion, neutron and e-beam irradiation induced damage in Zr and Mg. Heavy ion irradiation induced c-component loops in Zr have been observed (Fig. 1.7a) [64]. The density of c-loops in Zr decreases rapidly when T < 600 K. Neutron (Fig. 1.7b) and e-beam (Fig. 1.7c) irradiations induce both a-loops and c-loops in Zr [65].

In heavy ion (1 MeV Kr²⁺) irradiated Mg [66], nearly all basal loops have Burgers vector of $1/6 \langle 2\ 0\ \bar{2}\ 3\rangle$, and are interstitial loops in nature, whereas prism loops (interstitial and vacancy) have Burgers vector of $1/3 \langle 1\ 1\ \bar{2}\ 0\rangle$ (Fig. 1.7d). Meanwhile neutron irradiation of Mg induces dislocation networks (Fig. 1.7e) [67]. Griffiths [63] showed that e-beam irradiation of Mg (300 K/5 dpa) led to a-type vacancy (A_v,) and interstitial (A_i) loops with Burgers vectors $1/3 \langle 1\ 1\ \bar{2}\ 0\rangle$, and c-component interstitial loop (C_i) with Burgers vector of $1/6 \langle 2\ 0\ \bar{2}\ 3\rangle$ (Fig. 1.7f).

The relative stability of the dislocation loops in HCP metals generally depends on the c/a ratio and purity [68]. When c/a < 1.633, $\{1\ 0\ \bar{1}\ 0\}$ prismatic plane is the most closely packed plane, and dislocation loops (prism loops) typically have Burgers vector of $1/3\ \langle 1\ 1\ \bar{2}\ 0\rangle$. When c/a > 1.633, the basal planes are the most closely packed, and dislocation loops (Basal loops) have Burgers vector of $1/6\ \langle 2\ 0\ \bar{2}\ 3\rangle$ (or ½ [0 0 0 1]). In reality, however, the situation under irradiation is more complex than that dictated by this simple rule. Exceptions have been reported via both experiments and simulations. For instance, basal loops have been observed in Mg [69], Zr [70], Ti [71], in which the c/a ratio is less than the ideal value (1.633). In Zr and Ti, the situation is further complicated by the co-existence of prismatic loops with both vacancy and interstitial character [65]. When c/a < 1.633, the probability of basal loop nucleation increases with increasing impurity concentration. In Mg, for instance, prism loops with Burgers vector of $1/3\ \langle 1\ 1\ \bar{2}\ 0\rangle$ are dominant; whereas in Mg with low purity, basal loops with Burgers vector of $1/6\ \langle 2\ 0\ \bar{2}\ 3\rangle$ have been observed.

1.4. Radiation induced cavities: Voids and gas bubbles

1.4.1. Voids and void swelling

Void swelling, in the form of a prominent volume increase accompanied with the formation of voids, is a widely observed phenomenon in most neutron and heavy ion irradiated metallic materials [72–76]. In this review, we will briefly summarize several instances where void swelling can be significantly reduced or suppressed in nanocrystalline materials (Section 2). Furthermore there are numerous cases where voids are shown to shrink, instead of continuous growth, in irradiated nanotwinned (Section 4) or nanoporous (Section 5) materials.

High dose neutron irradiation can introduce volume expansion as large as several tens of percent [74,77,78]. Voids in irradiated materials can have various geometries, including faceted, rectangular, or spherical shapes. As voids are typical stress concentrators, and significantly degrade the fracture toughness of irradiated materials, void swelling can be a serious threat to the mechanical and structural integrity of reactor structural materials [72,74,79]. The battle against void swelling is manifested by an extensive investigation of void swelling in metals with FCC, BCC and HCP crystal structures and constantly

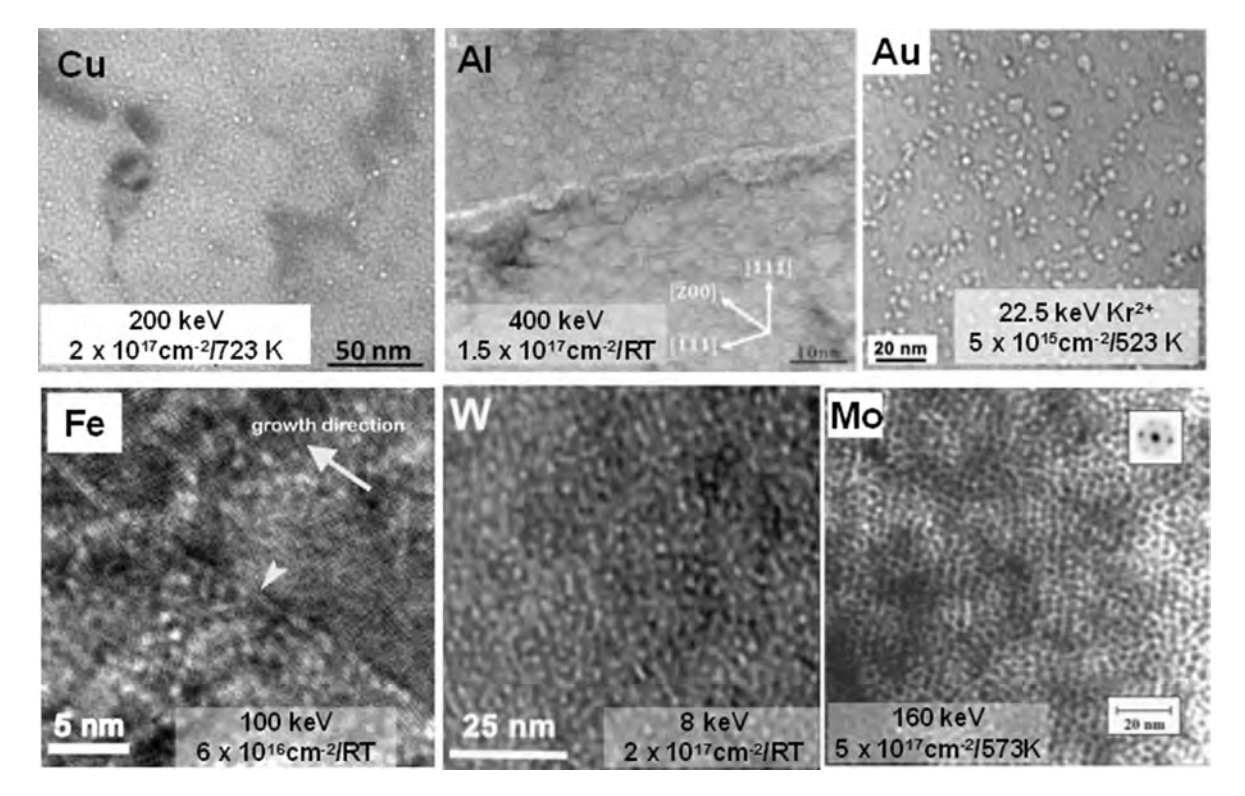
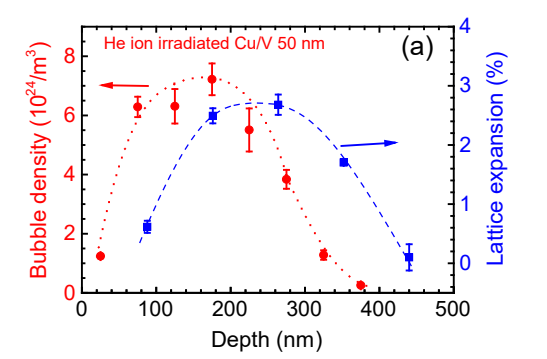


Fig. 1.11. The formation of He bubbles in He ion irradiated FCC [117–119] and BCC [120–122] metals. Note the formation of faceted He bubbles in Al [118], and superlattice of He bubbles in Mo [122]. Reprinted with permission from Refs. [117–122].



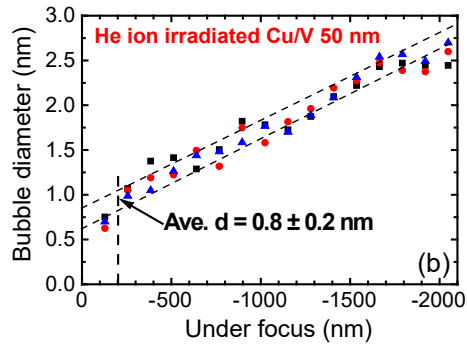


Fig. 1.12. (a) The density of He bubbles in He ion irradiated $(50 \text{ keV}/6 \times 10^{20}/\text{m}^2 \text{ at room temperature})$ Cu/V 50 nm multilayers evolves with depth and reaches a maximum at 180 nm from film surface. In parallel, the lattice expansion measured by using selected area diffraction (SAD) pattern from cross-section TEM studies shows a similar trend and reaches a maximum at ~280 nm [123]. (b) The determination of He bubble diameter by varying underfocus distance in TEM studies. The average diameter of He bubbles in He ion irradiated Cu/V 50 nm multilayers is ~0.8 nm, as determined from the underfocus distance of -200 nm [132]. Reprinted with permission from Ref. [132].

evolving designs of advanced void swelling resistant materials. Fig. 1.8 lists several examples of void swelling in neutron irradiated metals with FCC [3,80,81] and BCC [82–84] crystal structures. It should be noted that heavy ion irradiation typically generates a depth dependent variation of dose, and consequently the size and density of voids also vary as a function of radiation depth [85,86].

Void swelling is closely correlated to the radiation temperature. As shown in Fig. 1.9a where Cu specimens were irradiated at different temperatures, swelling percentage, represented by density change, can be divided into three temperature dominated phases [3,87]. Void growth is difficult at temperatures lower than 200 °C (phase 1) because of the poor mobility of point defects. When the temperature is higher than 500 °C (phase 3), defects of opposite types are effectively recombined or trapped by sinks rather than contributing to void growth. Therefore, swelling often occurs at intermediate temperature (phase 2) when the defects are mobile enough to agglomerate into voids, but less likely to be annihilated. Tables 1.1 and 1.2 summarize vacancy migration temperature (T_V^M) and peak void swelling temperature (T_S^P) for various metallic materials with FCC, BCC and HCP crystal structures. Void swelling is usually observed in metals and alloys at the temperatures of 0.3–0.5 T_m (where T_m is the melting temperature).

Swelling is also dose dependent. As radiation dose increases, swelling curve shows three regimes, which are transient swelling, steady state swelling and saturation swelling respectively. The steady state swelling undergoes the largest swelling rate. It has been reported that the eventual swelling rate of 316SS at all reactor-relevant temperatures is $\sim 1\%/\text{dpa}$ [107]. In comparison, the swelling rate of numerous ferritic/martensitic steels is merely 0.2%/dpa as shown in Fig. 1.9b [1,78,88–90]. A saturation regime may be applicable to only a few materials, and is often not observed in practice because it requires very high dose and most materials usually fail mechanically long before saturation dose.

The void swelling behavior has also been modeled extensively. Phase field modeling has been increasingly used to simulate the formation of voids. Fig. 1.10a1-a4 shows the simultaneous nucleation and growth of voids in irradiated system supersaturated with vacancies [108]. When the temperature gradient is superimposed in the cascade core, the interstitial concentration gradient is established. Consequently voids may grow and migrate towards the interstitial rich region (Fig. 1.10b) [109]. At a much smaller length scale, MD simulations have been applied to show the influence of dislocations on the formation of voids in irradiated Zr. The dislocations were formed as a consequence of tensile strain (applied concurrently with radiation) [110].

Helium (He) also plays an important role in void swelling. In general, He bubbles are preferential nucleation sites for voids. The evolution of void diameter with time, dr/dt, can be expressed by [111]:

$$\frac{dr}{dt} = -\frac{D_V X_V^e}{r} \exp\left(\frac{2\gamma\Omega}{(r-p)kT}\right),\tag{1.4}$$

where D_v is the diffusivity of vacancies, X_v^e is the vacancy concentration at equilibrium, γ is the surface energy. p is the He pressure inside cavities, and can be written as [111]:

$$p = \frac{3\kappa mkT}{4\pi r^3},\tag{1.5}$$

where κ is real gas compressibility factor, and m is the He atomic mass. The solution of dr/dt shows that He bubbles will grow (evolve) into voids when they reach a critical radius (typically several nm), or beyond a critical He concentration.

The influence of He on swelling is complicated. In general, there is an optimum He/dpa ratio for maximum void swelling in metallic materials, depending on the nature of nuclear reactors [112]. Meanwhile although He is attributed to the void swelling in many cases, a higher density of small He bubbles appear to suppress the magnitude of swelling [113]. To some

extent, pressurized small He bubbles act as defect sinks for vacancies and interstitials and alleviate void swelling [113]. However, the usage of He bubbles to suppress void swelling may not be a straightforward strategy as He bubbles are known to be nucleation sites for voids; and once He bubbles reach critical radius, they may grow continuously, and lead to significant void swelling.

Void formation has been observed in most HCP metals, such as neutron irradiated Mg [114], both neutron and electron irradiated Zr [104–106], neutron irradiated Ti [114] and Re [115]. Voids in HCP metals are normally faceted along $\{1\ 0\ \bar{1}\ 1\}$ and $(0\ 0\ 1)$ planes and often align in layers parallel to the basal plane, and in many cases, voids are reported to be faceted. For instance, voids formed in Marz-grade Zr during neutron irradiation in DFR at temperatures between 725 and 740 K were faceted along basal, prism, and pyramidal planes [68], and were mostly near grain boundaries.

1.4.2. Radiation induced He bubbles

Radiation damage induced by He ions has been widely investigated in a variety of metallic materials [116]. He is produced in neutron irradiated metallic materials due to the transmutation during neutron radiation. In numerous reactors, the concentration of He in irradiated metallic materials can achieve a few hundred to thousands of PPM level [111]. Fig. 1.11 compares the formation of He bubbles in a variety of irradiated monolithic metals with FCC [117–119] and BCC [120–122] crystal structures. He bubbles typically appear spherical in these metallic materials. However faceted (hexagonal) He bubbles emerge near grain boundaries in Al (in Al matrix composites). The faceted He bubbles may form to minimize surface energy of the cavities [118]. Furthermore, He bubbles form superlattices in He ion irradiated Mo [122].

When He/vacancy ratio is high, the pressured He bubbles may lead to lattice expansion as shown in Fig. 1.12a [123]. Interestingly, both lattice expansion (measured from selected area diffraction pattern in cross-sectional TEM studies) and He bubble density reach a peak value at \sim 200–300 nm. The equation of state for He has been described by multiple models [54,124–127]. Mills et al. provided a reliable empirical relation (MLB model) (based on experimental results) as follows [128]:

$$V = (22.575 + 0.00646557T - 7.26457T^{-1/2})P^{-1/3} + (-12.483 - 0.024549\,T)P^{-2/3} + (1.0596 + 0.10604T - 19.641\,T^{-1/2} + 189.84\,T^{-1})P^{-1}, \tag{1.6}$$

where the molar volume V has the unit of cm³, the pressure P is in kbar, T is absolute temperature.

The pressurized He bubbles could lead to lattice expansion based on the point source dilatation mechanism [129]. The pressure due to He bubbles is written as:

$$P = \frac{\mu \delta v}{\pi r_0^3},\tag{1.7}$$

where μ is the shear modulus of the metal matrix, and δv is the volume expansion induced by internal pressure, and r_0 is the radius of bubbles. Based on the measured peak lattice expansion in Cu/V 50 nm nanolayers, the pressure inside He bubbles is estimated to be \sim 3.8 GPa [123]. By using the equation of state of He, the molar volume of He is estimated to be 6.29 cm³/mol, or approximately 1.3 He/vacancy in V, and 1.1 He/vacancy in Cu are obtained, in agreement with literature values (1.4 He/vacancy in He bubbles of 4 GPa pressure in V, and 1.0 He/vacancy in He bubbles of 2.8 GPa pressure in Cu [116]). Wolfer has also described the mechanism of tensile stress induced lattice expansion arising from pressurized He bubbles [130]. He bubble induced lattice expansions have also been observed in numerous other systems, where the magnitude of lattice expansion is proportional to the He concentration [130,131]. It is well known that the diameter of measured He bubbles varies as a function of under-focus distance in TEM studies. An example of such study is shown in Fig. 1.12b for He bubbles observed in He ion irradiated Cu/V 50 nm multilayers [132].

There are numerous studies that show He can be managed by using a variety of defect sinks, such as phase boundaries (metal/oxide interfaces as shown in ODS alloys) and grain boundaries [6,9]. The discussion on the influence of defect sinks on He management is distributed in several succeeding sections in this review. Furthermore He tends to combine with vacancy and vacancy clusters to form pressurized He bubbles. Additionally He may segregate to the grain boundaries and lead to grain boundary embritlement, often referred to as He embritlement [133–135].

1.5. Classical models of sink strength for various types of defects

Forgoing sections describe the nature and types of defects that are generated by irradiations. Extensive studies have been carried out in the past few decades to improve the radiation tolerance of materials. An effective approach to mitigate radiation damage is to introduce various types of defect sinks, such as grain boundaries, phase boundaries and dislocations. These defect sinks interact with and eliminate, to a greater extent, the irradiation induced point defects and defect clusters.

The interaction of various types of defects with defect sinks has been described by using kinetic rate theory. In general the defect-sink reaction rate is estimated, followed by derivation of a sink strength formula.

For vacancy and interstitials, the following equations sustain [136,137]:

$$\frac{\partial C_V}{\partial t} = K_0 - K_{iV}C_iC_V - K_{VS}C_VC_S + \nabla \bullet D_V\nabla C_V \tag{1.8}$$

$$\frac{\partial C_i}{\partial t} = K_0 - K_{iV}C_iC_V - K_{iS}C_iC_S + \nabla \bullet D_i\nabla C_i \tag{1.9}$$

where C_v , C_i are vacancy and interstitial concentration; K_0 is defect production rate; K_{iV} is the vacancy-interstitial recombination rate coefficient; K_{VS} and K_{iS} are the vacancy-sink and interstitial-sink reaction rate coefficient. The reaction rate constants are estimated as follows:

$$K_{iV} = 4\pi r_{iv}(D_i + D_V) \approx 4\pi r_{iv}D_i \tag{1.10}$$

$$K_{iS} = 4\pi r_{iS} D_i \tag{1.11}$$

$$K_{VS} = 4\pi r_{VS} D_V \tag{1.12}$$

Note that the defect absorption rate can be rewritten with the concept of defect sink strength, k^2 :

$$K_{ix}C_iC_X = k^2C_iD_i, (1.13)$$

where K_{jx} the reaction rate between defect sink (X) and a mobile point defect (j). The sink strength k^2 has a unit of cm⁻². The inverse of k represents the average distance (or mean free path, λ) a mobile point defect can travel before being captured by a

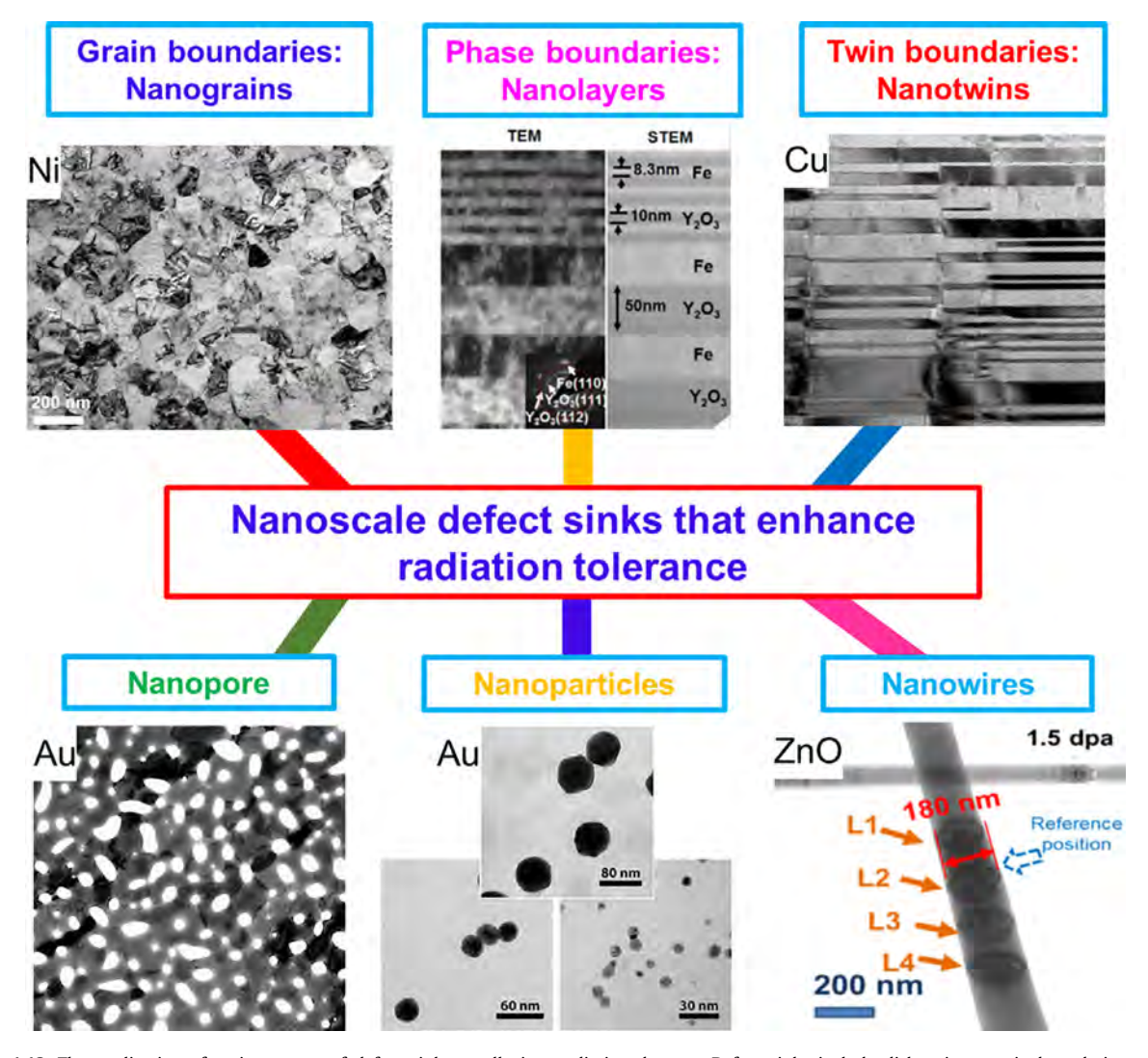


Fig. 1.13. The application of various types of defect sinks to alleviate radiation damage. Defect sinks include dislocations, grain boundaries, twin boundaries, layer interfaces, nanopores, nanoparticle, nanowires and amorphous materials. This review will cover radiation damage in various nanostructured materials, including nanocrystalline materials, nanotwinned metals, nanoporous metals, nanoparticles and nanowires.

defect sink. It follows that in nanostructured materials, λ is limited by the density of defect sinks, and its value would be similar to the value of grain size (d), twin spacing (t) or individual layer thickness (h) as illustrated in the following formula:

$$k^{-1} = \lambda = d$$
 or t or h (distance between defect sinks) (1.14)

Hence to enhance the defect sink strength, it is critical to scale down the dimension of nanofeatures or increase the density of defect sinks. When considering the defect-GB reaction rate, the steady-state atomic concentration of point defects is given by:

$$D\left[\frac{d^{2}c}{dr^{2}} + \frac{2}{r}\frac{dc}{dr}\right] + K - Dk_{sc}^{2}c = 0, \tag{1.15}$$

and the solution to the formula (assuming that GB is an ideal sink) is written as:

$$k_{gb}^{2} = \frac{k_{sc}^{2}[k_{sc}R \coth k_{sc}R - 1]}{\left[1 + \frac{k_{sc}^{2}R^{2}}{3} - k_{sc}R \coth k_{sc}R\right]},$$
(1.16)

where R is the radius of grains (half of grain size d). When the point defects are lost mostly to GB sinks, then it can be shown that [136,137]:

$$k_{\rm gb}^2 = 15/R^2 \tag{1.17}$$

Note the derivation is based on the cellular model using the average point defect concentration within a grain. When an embedding model is used, the GB sink strength becomes $14.4/R^2$, very close to the value derived from the cellular model. Clearly the smaller the grain size, the greater the sink strength.

Similarly using the cellular model, the sink strength for a void, k_V^2 , is described by:

$$k_V^2 = 4\pi a C_V^0 f_c,$$
 (1.18)

$$C_V^0 = \frac{3}{4\pi R_0^3},\tag{1.19}$$

$$f_c = \frac{5(R_c^3 - a^3)^2}{[5R_c^6 - 9aR_c^5 + 5a^3R_c^3 - a^6]}.$$
 (1.20)

where a is void radius, R_c is the radius at zero flow condition, that is dc/dr = 0, when $r = R_c$. To a first approximation, R_c may be estimated as the void-to-void separation distance. $R_0^3 = R_c^3 - a^3$; and C_V^0 is the initial volume distribution of voids. Note the sink strength formulas for twin boundaries or layer interfaces have not been derived to date.

1.6. Defect sinks and some general philosophies for alleviation of radiation damage

To date, there is literally no material known to be immune to radiation damage, especially beyond a dose level of several hundred dpa. As stated in the previous sections, all crystalline materials, regardless of their crystal structures (FCC, BCC or HCP), are vulnerable to radiation damage. Although a large number of point defects may recombine immediately after damage cascade, the residual defects can lead to the accumulation of radiation damage in terms of microstructural evolution. It remains a major challenge to design materials that have significantly enhanced radiation tolerance at extreme conditions.

Zinkle and Snead [138] reviewed several strategies to alleviate radiation damage in irradiated materials. First, metallic materials with BCC structures appear to be more resistant to radiation damage compared with those with FCC structures, presumably due to the higher number density, smaller defect clusters generated during cascade in irradiated BCC metals than in FCC metals [50,138–141]. Second, when either vacancies or interstitials are immobile at the operation temperature, the immobile point defects may facilitate recombination of opposite type of point defects [138]. Third, high sink strength or high sink density reduces radiation damage.

The adoption of predesigned defects (sinks) to eliminate radiation induced defects, though appears counterintuitive at the beginning, is in fact a very effective approach. Defects in crystalline materials can be characterized by their dimensions, including 0D – point defects, 1D – dislocations, 2D – grain boundaries, phase boundaries and surfaces, and 3D – voids, pores, precipitates and 2nd phase, etc. The applications of point defects to alleviate radiation have been mostly implemented through the design of solid solutions or alloys, where solid solution can assist the recombination of defects and reduce radiation damage [6,142–145]. Dislocation networks have also been used to reduce radiation damage, although dislocations are often considered as biased defect sinks, which may accelerate the formation of voids in certain cases [110]. There are numerous examples that show dislocations, including mobile dislocations, can interact with SFTs and sweep them away [146–149]. Other widely used defect sinks include grain boundaries, phase boundaries, voids and He bubbles. Literature data show that a sink strength of $10^{16}/m^2$ may be necessary to curtail void swelling in steels to less than 5% [138]. Such a high sink strength

is difficult to achieve in conventional materials. We will show in the succeeding chapters that various types of nanomaterials may reach such a high sink strength depending on the characteristic defect spacing.

The influence of point defects and dislocations on radiation induced damage will not be covered in this review. Instead we will focus on the following nanostructured materials: nanocrystalline materials with fine grains, nanotwinned metals with a high density of twin boundaries, nanolayer composites with layer interfaces, and nanoporous materials, nanoparticles and nanowires with abundant free surfaces. Fig. 1.13 illustrates the application of these defect sinks in various nanostructured materials to alleviate radiation damage.

The review article covers the emerging field (nanomaterials under extreme radiation environments) and emergent needs for the design of superior radiation tolerant nanomaterials. This article highlights what the community has learned to date on the radiation response of various nanomaterials, and points out future directions to move forward. We hope the article can stimulate broad interest in the field of "nano under radiation" with the ultimate goal to discover new strategies (including nanoengineering) and design novel materials with unprecedented radiation tolerance.

2. Radiation damage in nanocrystalline metals and ceramics

This section examines the methods, observations, and mechanisms associated with the radiation response of nanocrystalline (NC) systems. A majority of the work to date has focused on pure metal systems, but limited work in NC metallic alloys and ceramic systems will also be highlighted. This section does not cover NC metals or ceramics in which the internal structure is dominated by heterogeneous interfaces such as nanolayered films (to be covered in Section 3), nanotwinned metals dominated by twin boundaries (Section 4), or nanoporous metals with abundant free surfaces (Section 5). In addition, a few previous reviews on radiation tolerant materials have been written, which included, in part, the studies of the radiation tolerance of NC materials. These include a wide-sweeping review of irradiation effects on nanomaterials [150], the formation of nanostructures by irradiation techniques [151], the radiation tolerance of ODS steels [6], the radiation and creep responses of metals with embedded nanoscale second phases [152], the recent development of accelerator technologies for investigating such systems [153], and the potential for processing radiation tolerant nanomaterials [154].

2.1. Sink strength of grain boundaries

In Section 1.4, Eqs. (1.15)–(1.17) show that the sink strength of a GB can be described by k_{gb}^2 = $15/R^2$ [137]. Note the derivation is based on the cellular model by using the average point defect concentration within a grain. When an embedding model is used, the GB sink strength becomes $14.4/R^2$ [137], very close to the value derived using the cellular model. Clearly, the smaller the grain size, the greater the sink strength. We shall see such a prominent grain size effect through the review of a combination of experimental studies and MD simulations [26,150,154–180]. The following section will also show that *in situ* experiments and MD simulations permit direct characterizations of the interactions of radiation induced

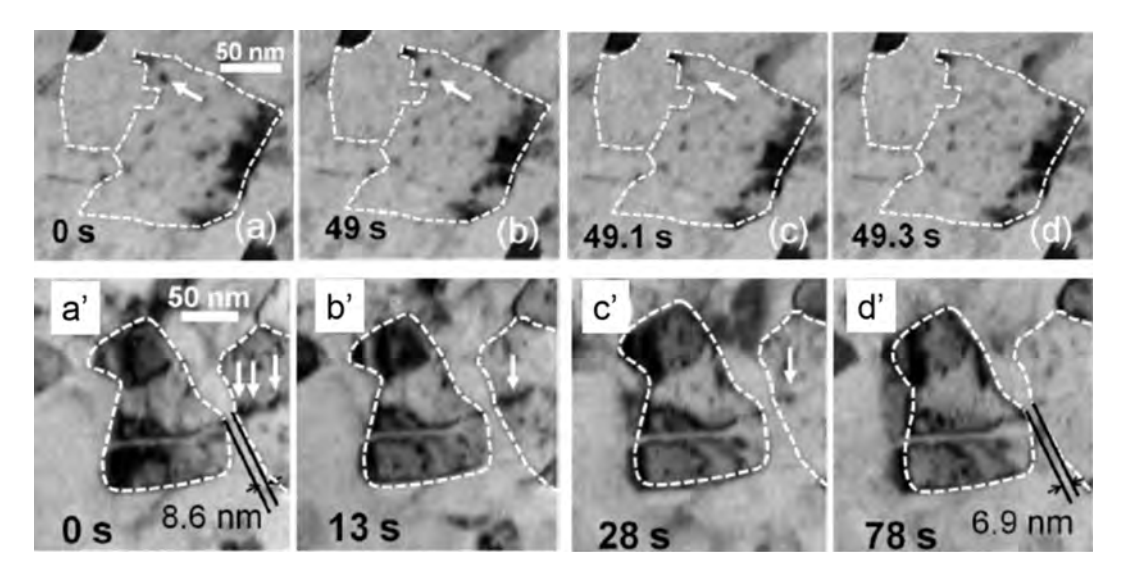


Fig. 2.1. (a–c) *In situ* evidence of the absorption of an individual loop by a grain boundary (GB) in NC Ni. The Kr ion radiation dose increased from 1.67 to 1.72 dpa within 49.3 s. (a–d) The abrupt absorption of an individual dislocation loop (identified by an arrow) by a nearby GB. After a dwelling time of 49 s, the loop migrated rapidly toward the GB within 0.1 s and was fully absorbed by the GB. (a′–d′) The gradual absorption of dislocation segment by GB. Three discernible dislocation loops formed one dislocation segment, which was absorbed continuously by the adjacent GB [30]. Reprinted with permission from Ref. [30].

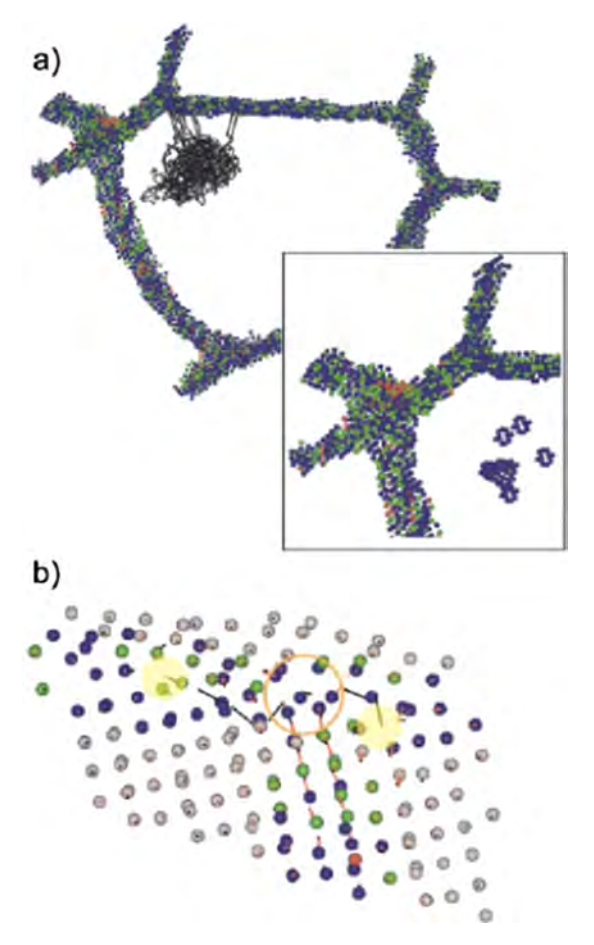


Fig. 2.2. (a) Selected area of the 12 nm NC Ni grain, the GB atoms and the displacement vector (>1.5 Å) between the atoms due to a 5 keV primary knock on (PKA). The insert shows a magnified view of the defect region after cooling down. (b) An example of the GB acting as an interstitial sink, by the annihilation of interstitials with free volume in the GB [182]. Reprinted with permission from Ref. [182].

defect clusters with GBs (i.e. point defect-sink interactions). However, there are some limitations in the current formula, which will be discussed later. The need to improve thermal and radiation stability of nanograins will also be discussed.

2.2. Defect-GB interactions

2.2.1. Experimental observations of the defect-GB interactions in NC metals

Recently, there have been an increasing number of experimental studies on radiation damage in pure NC metals, including Ni [30], Mo [180], W [181] and Fe [120,168]. Fig. 2.1 shows several examples of the absorption of defect clusters by GBs in NC Ni under *in situ* Kr ion irradiation at room temperature [30]. At least two types of absorption events have been identified in this study. First, a mobile dislocation loop in the vicinity of a high-angle GB in the NC Ni reduced its diameter gradually over 49 s, migrated abruptly over 10 nm towards the GB within 0.1 s (Fig. 2.1a-d), and was eliminated at the GB. In a second case, a dislocation segment consisting of a string of dislocation loops was gradually absorbed by a GB (Fig. 2.1a'-d') over 78 s.

2.2.2. MD simulations showing defect absorption/capture by GBs

The role of GBs in the alleviation of radiation damage becomes significant when the average grain size approaches the mean free paths of the SIAs and vacancies created during the cascade events. MD simulations can be utilized to examine the effects of GB character and structure on radiation tolerance at atomistic levels that are extremely difficult to accomplish if not impossible during irradiation experiments. An MD simulation study in Fig. 2.2 on self-ion irradiated NC Ni shows that GBs act as effective defect sinks for interstitials [182]. One major advantage of utilizing MD simulations is the determination of the underlying physical mechanisms at a resolution of ps or faster. Another mechanism showing the role of GBs in the absorption of defects is the interstitial emission model presented by Bai et al. in Figs. 2.3 and 2.4 [183]. Interstitials migrate towards GBs at a speed faster than vacancies do, leaving behind vacancies, which can subsequently form clusters and thus modify the formation and migration of other defects in their vicinity (Fig. 2.3). As shown in Fig. 2.4, point defects and their clusters tend to form in or near the GBs more so than in the grain interiors. Interestingly, this MD study predicted that point-

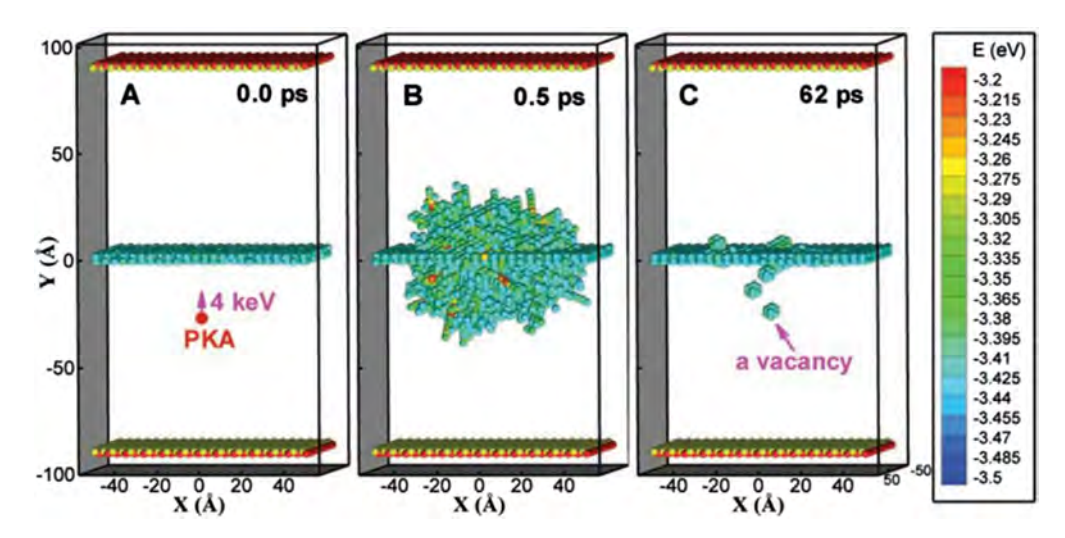


Fig. 2.3. Representative snapshots of a MD simulation of a collision cascade near a $\Sigma 11$ symmetric tilt GB at 300 K in Cu. The atoms are colored by their potential energy; atoms with energies less than 3.43 eV are treated as nondefective and are not shown. The top and bottom layers are fixed surfaces. (A) Initially, a 4-keV PKA is initiated at 25 Å below the GB with its velocity directed perpendicularly toward the GB. (B) After 0.5 ps, the cascade reaches its maximum size. (C) After 62 ps, the cascade cools down with some vacancies remaining below and above the GB. In this display scheme, a vacancy is characterized as a 12-atom cluster, as indicated in (C), because of the increase in energy of the 12 nearest neighboring atoms of the vacancy [183]. Reprinted with permission from Ref. [183].

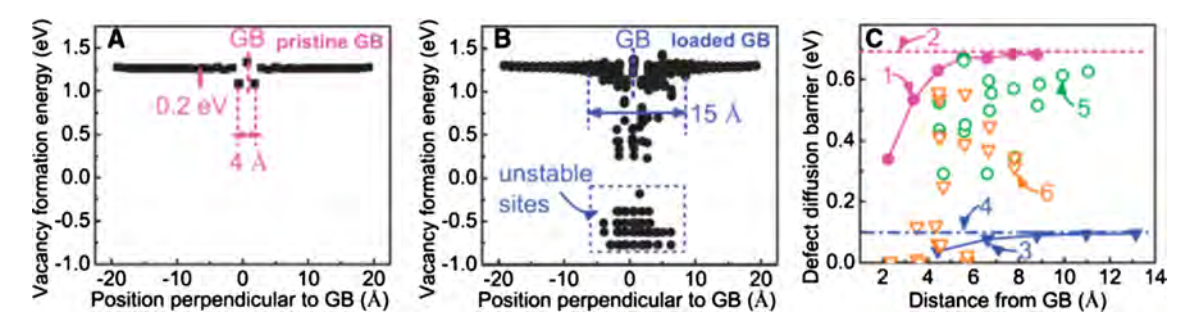


Fig. 2.4. Influence of interstitial loading on defect properties near the symmetric ∑11 GB in Cu. (A) Vacancy formation energy profile of a pristine GB. (B) Vacancy formation energy profile of a GB loaded with 10 interstitials, representing the situation occurring after a collision cascade. (C) Defect diffusion barriers as a function of distance from a pristine and an interstitial-loaded GB. Number 1−6 represents vacancy diffusion barriers near the pristine GB, interstitial diffusion barrier in the bulk, interstitial diffusion barriers near the pristine GB, interstitial diffusion barrier in the bulk, vacancy diffusion barriers near the interstitial-loaded GB, respectively [183]. Reprinted with permission from Ref. [183].

defect diffusion becomes easier in the interstitial-loaded GBs than in pristine boundaries [183]. Self-healing has also been observed by simulations near GBs in irradiated Cu [166].

Similarly, it was shown in the MD simulation of Fe by Chen et al., Fig. 2.5, that the mechanism by which the cascade damage is absorbed by the boundary depends on the local GB structure [184]. In this work, two mechanisms, bulk chain-like (BC) absorption and GB chain-like (GBC) absorption are shown to work independently or simultaneously to eliminate the radiation induced damage [184].

2.3. Effect of grain size on radiation tolerance – microstructure and mechanical properties

The concept of decreasing grain size to enhance radiation tolerance has been proposed in the early work by Singh, who examined the role of GBs in void formation [185]. There are subsequent studies on the irradiation tolerance of fine-grained materials [137,172,186–193]. In this section, we will begin by examination of the size effects on radiation damage in pure (elemental) NC metals, and then review studies on NC alloys and NC non-metallic materials.

2.3.1. Radiation damage in pure NC metals

The successful synthesis of a wide range of NC metals enabled the studies on radiation tolerance in some of these metals. Rose et al. evaluated the role of grain size on Kr ion irradiated NC Pd [194] and showed decreasing defect cluster densities at smaller grain sizes (Fig. 2.6a). Similarly, an *in situ* Kr ion irradiation study shows the irradiated NC Ni has less defect clusters

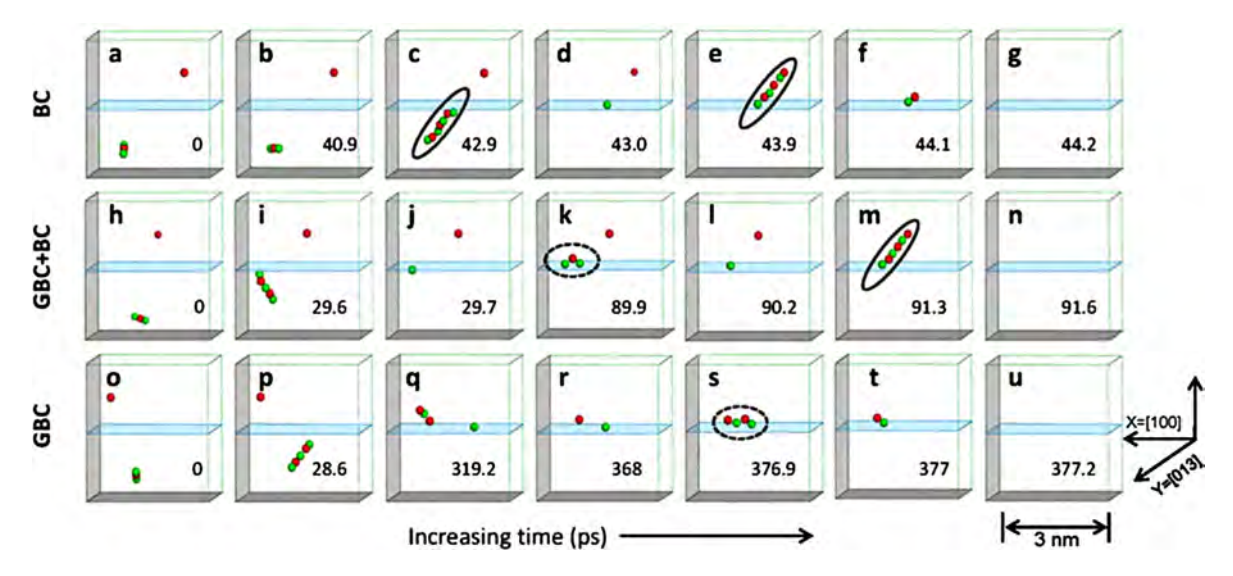


Fig. 2.5. Representative snapshots of an MD simulation of three different defect annihilation processes for (0 1 3) [100] \$\S\$5 symmetric title GB in BCC Fe. All simulations start with one bulk vacancy and one bulk dumbbell defect close to a GB. (a-g) The process involving a bulk chain-like (BC) defect for annihilation: A BC defect is created at time t = 542.9 ps to transport an interstitial to the boundary and then another BC defect is created t = 543.9 ps to annihilate a bulk vacancy. (h-n) The process involving a grain boundary chain-like (GBC) defect for boundary migration and BC defect for annihilation: A GBC defect is created at t = 589.9 ps to move a boundary trapped interstitial, and then a BC defect is created at t = 591.3 ps to annihilate a bulk vacancy. (o-u) The process involving GBC defect for annihilation on the boundary: A GBC defect is created at t = 5 376.9 ps to annihilate a defect pair separated and trapped on the boundary. The boundary is represented by a blue shadowed plane. The green balls refer to interstitial and red balls refer to vacancy. The solid circles refer to GBC defects and dash circles refer to GBC defects [184]. Reprinted with permission from Ref. [184].

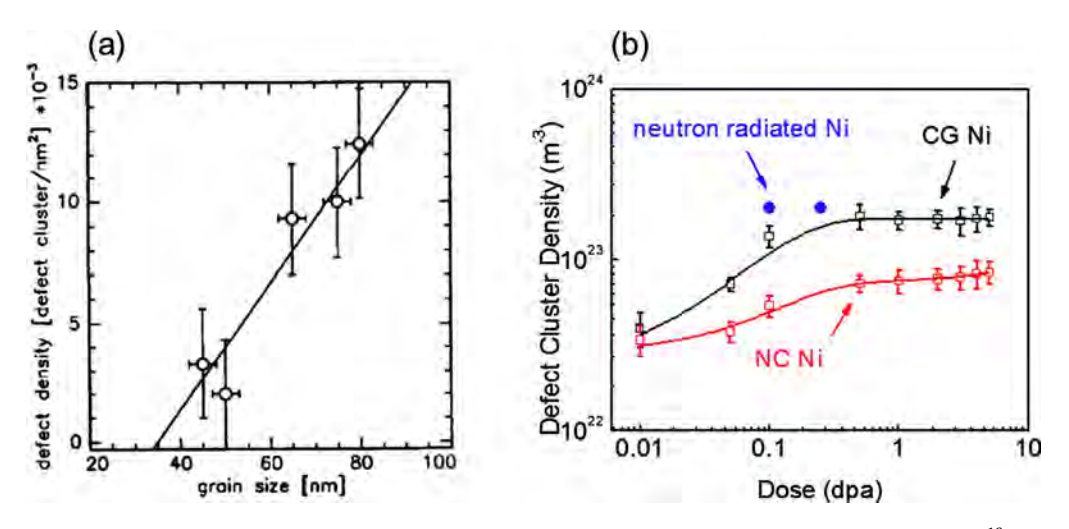


Fig. 2.6. (a) Defect densities vs. grain size on the irradiated NC Pd under Kr ion irradiation with energy of 240 keV to a fluence of 2×10^{16} ions/cm² [194]. (b) The density of dislocation loops of CG Ni increased rapidly within 0.1 dpa and appeared to reach saturation at \sim 0.5 dpa. Meanwhile the density of loops in NC Ni increased slowly and gradually throughout the radiation up to 5 dpa. At 5 dpa, the average loop density of CG Ni is 2 times greater than that of NC Ni [30]. Reprinted with permission from Refs. [30,194].

than that in the coarse-grained (CG) Ni (Fig. 2.6b) [30]. Fig. 2.7a–c shows another example where the density and size of the radiation induced defects, as well as the radiation induced hardening decrease with the reduction of average grain size in BCC Mo [180]. These studies suggest that nanograins can effectively alleviate radiation induced microstructural damage and radiation hardening.

The influence of radiation temperature on the radiation tolerance of NC metals remains less well understood, as there are rather limited studies on this subject. As shown in Fig. 2.7d and e, the He bubble density in He ion irradiated NC Fe is lower at 700 K than at 500 K. Further, grain size appears to have little influence on He bubble density in NC Fe irradiated at 500 K [168], whereas smaller grains lead to lower He bubble density at 700 K. The magnitude of swelling in NC Fe was estimated to be 0.63% (independent of grain size) at 500 K, vs. 0.0096 to 0.98% (grain size dependent) for NC Fe irradiated at 700 K. It is

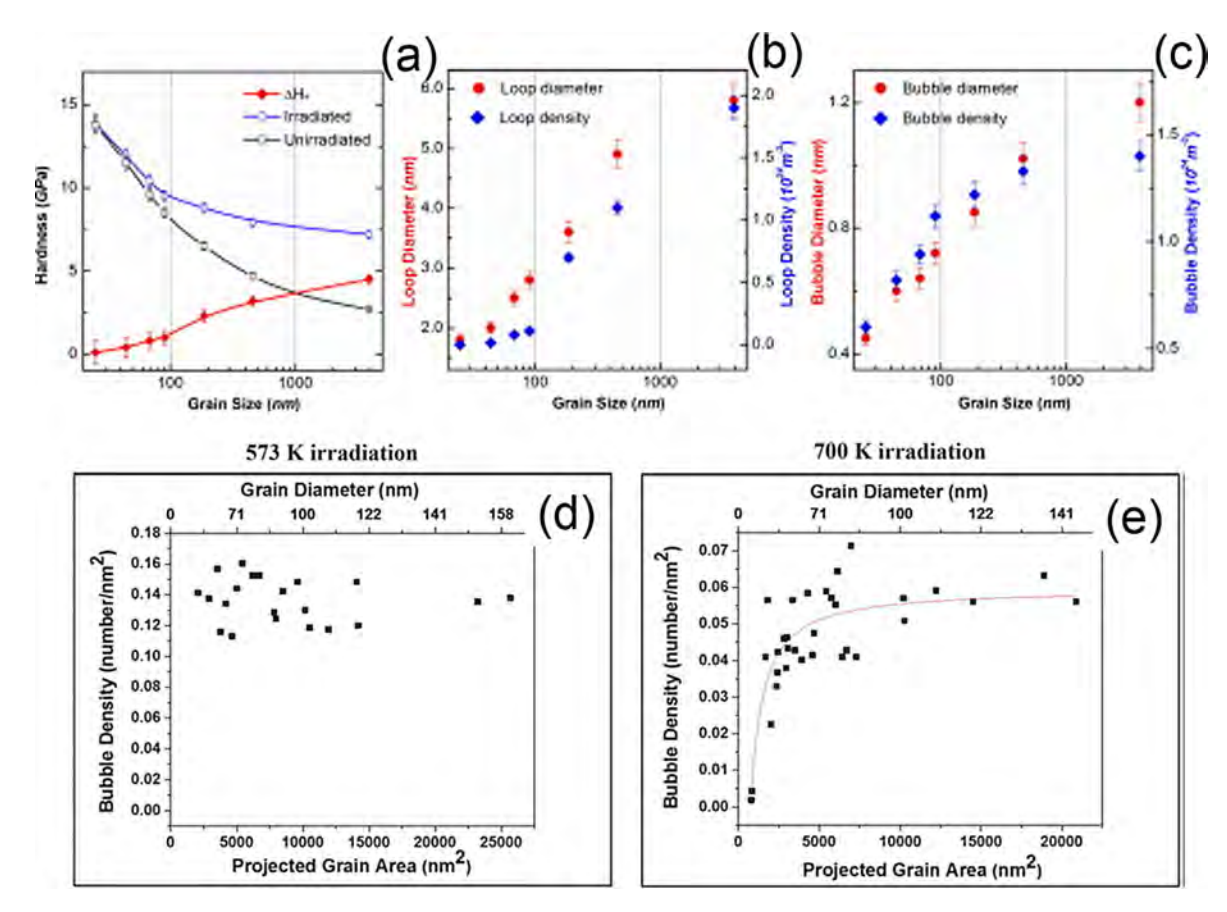


Fig. 2.7. (a–c) He ion irradiation of BCC Mo. (a) Grain size effect on the hardening behaviors of nonirradiated and He-ion-irradiated BCC Mo. (b and c) Distributions of size and density of irradiation-induced He bubbles and dislocation loops in the irradiated BCC Mo, respectively [180]. (d and e) Areal bubble density (number/nm²) vs. grain size (area) for 10 keV He ion irradiation of nanocrystalline Fe at (d) 573 and (e) 700 K. The red best-fit curve in (e) demonstrates the trend in the change in bubble density [168]. Reprinted with permission from Ref. [168,180].

likely that small He-vacancy clusters are mobile at 700 K, promoting their coalescence and the elimination of defect clusters at GBs [168]. It remains unclear why there is a lack of size effect on defect density in NC Fe irradiated at 500 K.

Little is known on the influence of ion types on radiation damage in the NC metals. Fig. 2.8 compares few existing studies on various types of ion irradiations induced microstructure evolution in NC Ni [30,169] and UFG W. [167,181]. In general the nature and density of various types of heavy ion radiation induced defects appear comparable for the same material. In comparison, He ion irradiation induces He bubbles.

2.3.2. Radiation damage in NC alloys

In addition to pure NC metals, the role of grain size has also been investigated in various alloys [86,192]. Sun et al. compared the evolution of microstructures in He ion irradiated ($100 \text{ keV/room temperature}/6 \times 10^{20} \text{ ions/m}^2$) CG austenitic Fe-14Cr-16Ni with that of UFG specimens processed by severe plastic deformation [195]. The CG Fe-Cr-Ni alloy has abundant He bubbles, some of which decorate the GBs, and dislocation loops (Fig. 2.9a1-a3). In comparison, the irradiated UFG Fe-14Cr-16Ni alloy has a reduced He bubble density with fewer dislocation loops (Fig. 2.9b and c). The magnitude of radiation hardening in the UFG alloy, probed by nanoindentation (Fig. 2.9d), is much less than that in CG Fe-14Cr-16Ni alloy indented at various depths.

Heavy ion irradiations have also been performed to investigate void swelling in several NC alloys. In the 304L SS study, GB engineering via equal channel angular pressing (ECAP) was used to refine the grains of the alloy without significant changes in the phase distribution. As shown in Fig. 2.10, after irradiation by 3.5 MeV Fe to tens of dpa, the CG 304L SS contains a significant number of voids, whereas the UFG microstructure has much less voids [86]. Fig. 2.11 shows that the magnitude of void swelling in heavy ion and neutron irradiated 304L SS is comparable. However the transient period of the swelling curve delayed in the UFG 304L SS, and the UFG grains significantly suppress the magnitude of void swelling [196]. In another study, Song et al. examined a ferritic/martensitic T91 (9Cr-1Mo) steel under Fe ion irradiation and found that the swelling rate was three times lower in an UFG microstructure (320-nm average grain size) produced by ECAP than in a CG microstructure (2-um average grain size) [85]. It is worth mentioning that the magnitude of void swelling and microstructure damage is

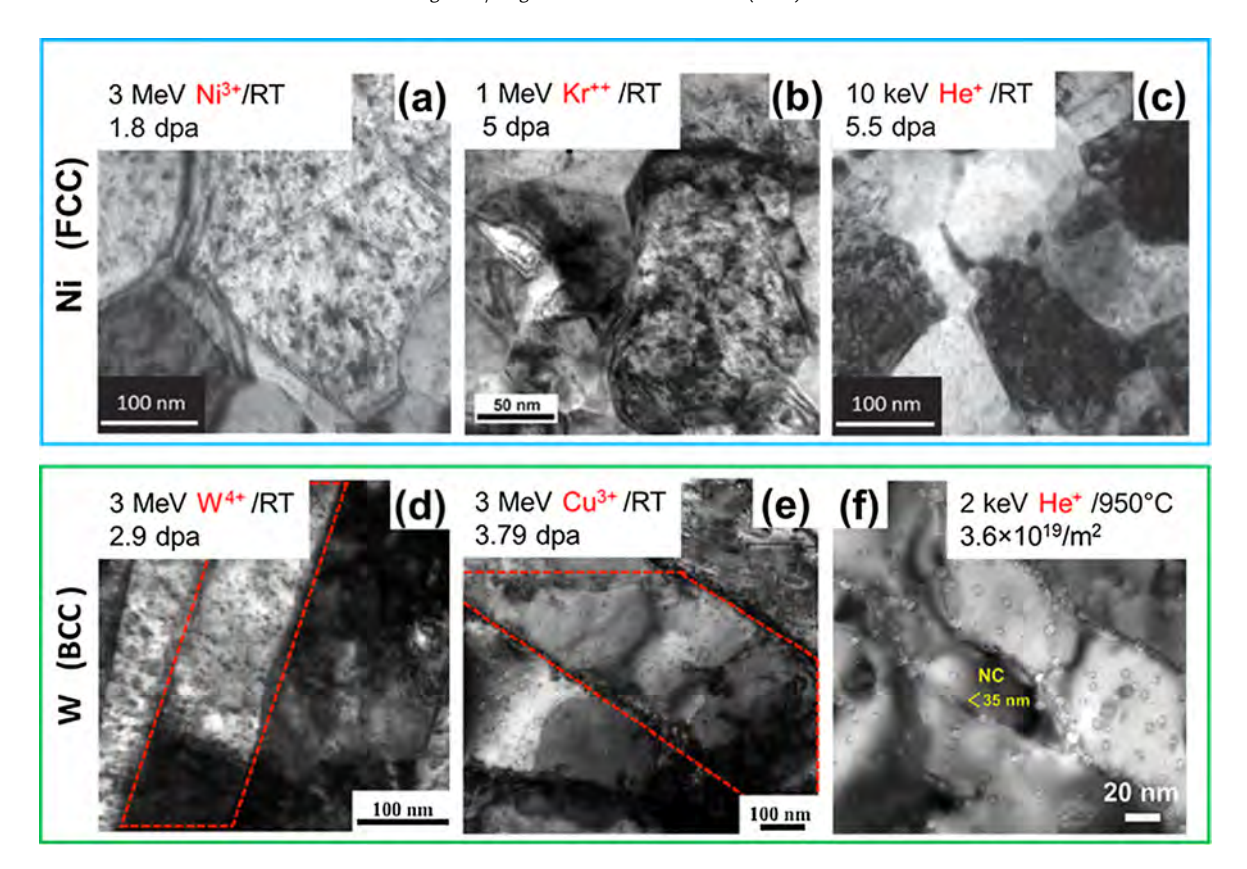


Fig. 2.8. The microstructure evolutions of NC Ni irradiated by (a) 1.8 dpa of Ni ions [169] and (b) 5 dpa of Kr ions [30] show similar defect sizes and densities even though the maximum irradiation doses are different. (c) He ion irradiation of NC Ni [169]. (d and e) NC W subjected to self-ion irradiation (2.9 dpa) and Cu ion irradiation (3.79 dpa). Cu ion irradiated W shows small dislocation loops with somewhat lower defect density as compared to W ion irradiated W [181]. (f) He ion irradiation led to the formation of He bubbles [167]. Reprinted with permission from Ref. [30,167,169,181].

similar in heavy ion and neutron irradiated austenitic 304L SS [86]. A full comparison of these radiation environments (neutrons, heavy ions and protons) induced microstructural evolution is beyond the scope of this review, further information on these important topics can be found elsewhere [197–199].

Radiation induced grain coarsening and segregation have been investigated in NC alloys. Annealing of NC 316 SS with an average grain size of 40 nm (processed by high pressure torsion experiments) at 350 °C for 24 h had no influence on the grain size, whereas the average grain size increased to 60 nm under 160-keV Fe ion irradiations at 350 °C, suggesting the radiation enhanced grain growth (discussed in detail in Section 2.5) [191]. Atom probe tomography shows that the GBs are enriched in Ni and Si and depleted in Cr. No intragranular extended defects or precipitates were observed in the irradiated NC 316 SS [191].

A summary of the radiation conditions (ion species, energy, fluence, and flux) for a majority of investigated NC/UFG metals and alloys is listed in Table 2.1. These studies have generally shown that the radiation induced defect size and density decreases with decreasing grain sizes to the UFG and NC regimes. These studies consider a range of radiation environments produced by linear accelerators ranging from He [168,181] to heavy ion irradiation [30,181]. Even in the heavy ion irradiation experiments, the choice of ion mass and energy was important to the kinetics of defect formation [181]. A majority of these studies have investigated the size, density, and types of radiation induced defects as a function of radiation conditions. Although these microstructural investigations permit a fundamental understanding of the irradiation response of NC materials and are important for accurate model development, more studies are necessary to explore the influence of radiations on the evolution of structural dimension (i.e., void swelling) and material properties (such as yield strength and corrosion rate), which are of interest to nuclear industry. Furthermore neutron radiation studies on NC metals and alloys remain limited.

2.3.3. Radiation damage in non-metallic NC materials

In comparison to radiation studies on NC metallic materials, there are limited number of investigations on the irradiation response of non-metallic NC systems. This can be seen in the visual comparison between Table 2.1 (review of NC metals) and Table 2.2 (review of NC ceramics). As shown in Table 2.2, various irradiation conditions and ceramic chemistries and crystallography have been investigated for a limited number of NC ceramics. Although it is difficult to draw conclusions on the

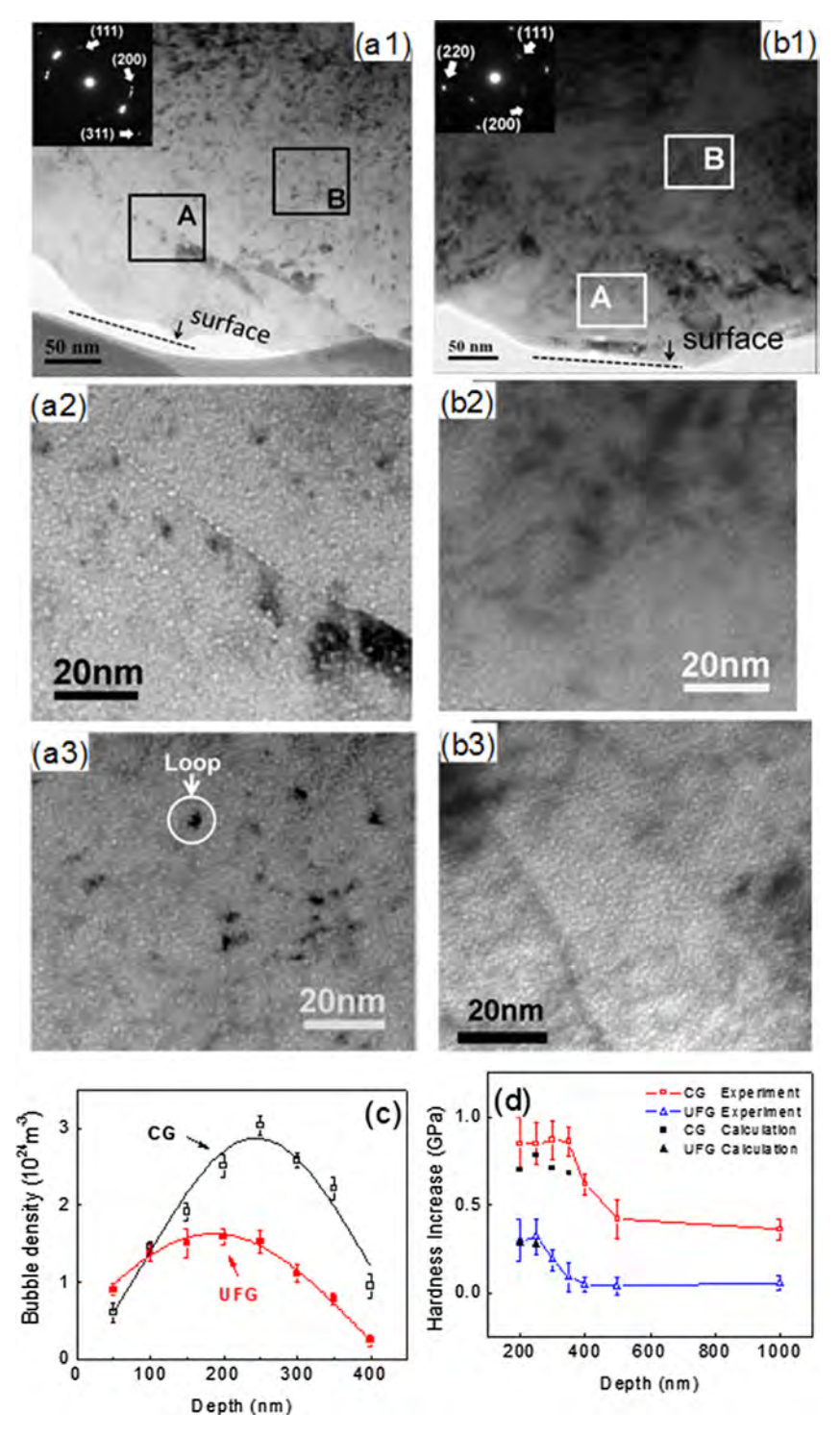


Fig. 2.9. Comparison of microstructures and radiation hardening of He ion irradiated UFG Fe-14Cr-16Ni alloys (100 keV He ions at RT to 6×10^{20} ions/m²)) [195]. (a1) Underfocused XTEM micrograph of He ion irradiated CG Fe-Cr-Ni alloy. (a2) The magnified image of region A shows bubbles aligned along grain boundaries. (a3) The magnified image of region B shows dislocation loops and high density of He bubbles. (b1-b3) Under focused XTEM micrograph of He ion irradiated UFG Fe-Cr-Ni alloy. Magnified image of region B shows bubbles, but not dislocation loops. (c) Depth dependent He bubble density of He irradiated CG and UFG Fe-Cr-Ni alloy. Both the peak and average He bubble density are reduced in the UFG alloy. (d) Hardness increase ($H_{after irradiation} - H_{before irradiation}$) of the He ion irradiated CG and UFG Fe-Cr-Ni alloy as a function of indentation depth. The measured radiation hardening of the CG and UFG Fe-Cr-Ni alloy is indicated by open squares and triangles, respectively. The calculated radiation hardening in the peak damage region is shown by solid squares and triangles. In the CG alloy, both He bubbles and dislocation loops result in hardening, whereas hardening in the UFG alloy arises mainly from He bubbles [195]. Reprinted with permission from Ref. [195].

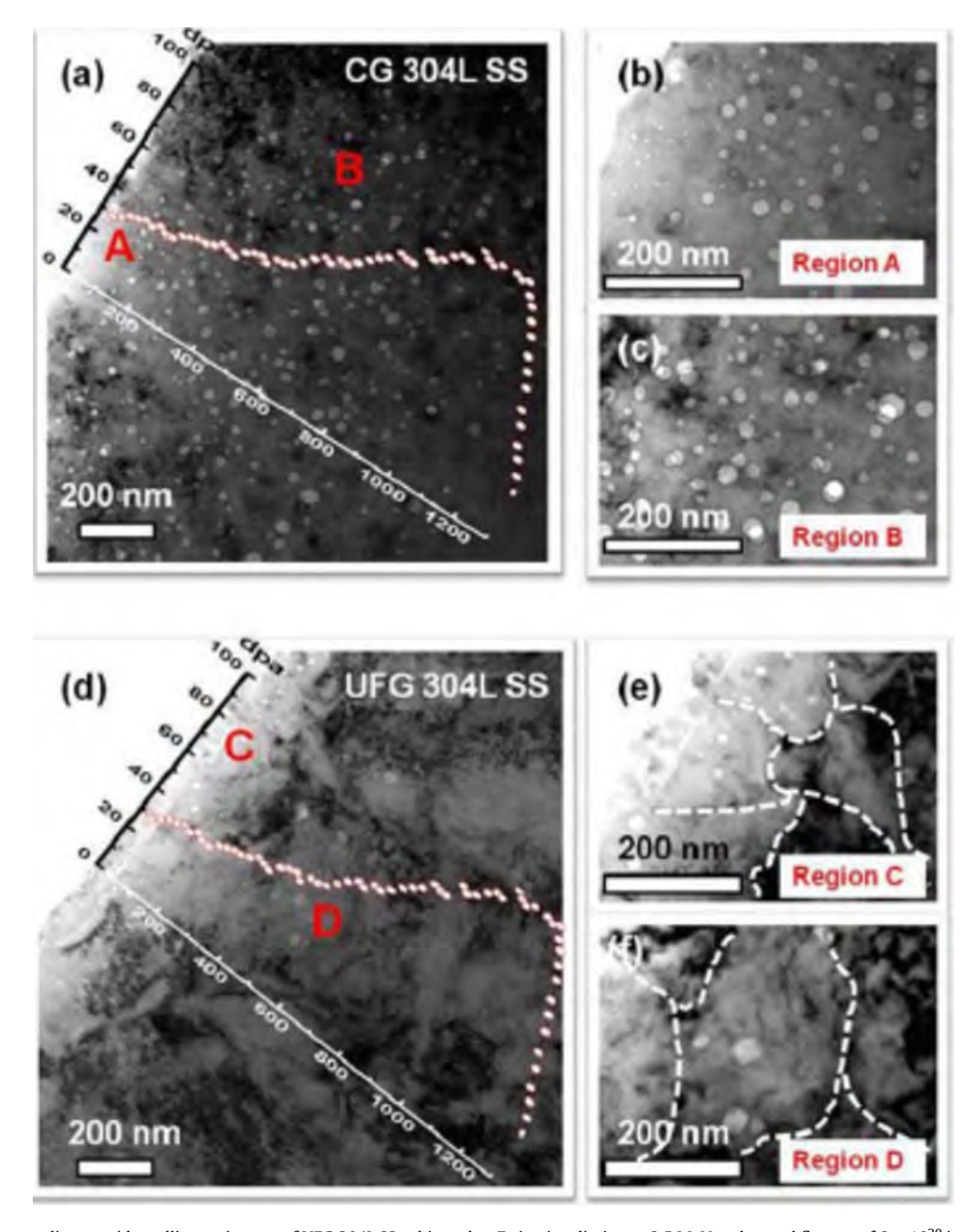


Fig. 2.10. Extraordinary void swelling resistance of UFG 304L SS subjected to Fe ion irradiation at 3.5 MeV and a total fluence of 6×10^{20} ions/m² at 500 °C by defocusing the ion beam. (a) Panoramic cross-section TEM micrograph of Fe ion irradiated CG 304L SS showing a large number of voids. (b) The magnified TEM image of region A in (a) shows high-density small voids near the surface of irradiated CG 304L SS. (c) In region B, 500 nm below the surface, high-density large voids were observed. (d) Cross-section TEM overview of irradiated UFG 304L SS showing far fewer voids. (e) The magnified TEM image of surface region C in irradiated UFG 304L SS shows numerous, faceted voids distributed primarily along GBs. (f) The magnified TEM micrograph of region D in (d), ~500 nm from surface, shows much lower void density than that at the same depth of the irradiated CG counterpart [86]. Reprinted with permission from Ref. [86].

roles of ceramic chemistry and crystallography on the irradiation tolerance of NC ceramics, many interesting observations have been made from these limited studies.

An earlier study by Wang et al. showed that NC TiN demonstrated enhanced irradiation tolerance [206]. Similar effects have also been reported in Ceria and Zirconia by Y.W. Zhang et al. [202–204]. Grain growth from 7 nm to approximately 30 nm, similar to those reported for NC metals, was clearly demonstrated in NC Zirconia after 35 dpa of irradiation by 2 MeV Au ions [202]. MD simulation in conjunction with experimental observations suggested disorder based mechanisms driving the grain growth in nanostructured ceramics [204]. Jiao et al. also reported a decrease in the density of the irradiation induced defects in ZrN as a function of grain size, as shown in TEM characterizations in Fig. 2.12 [205]. The enhanced

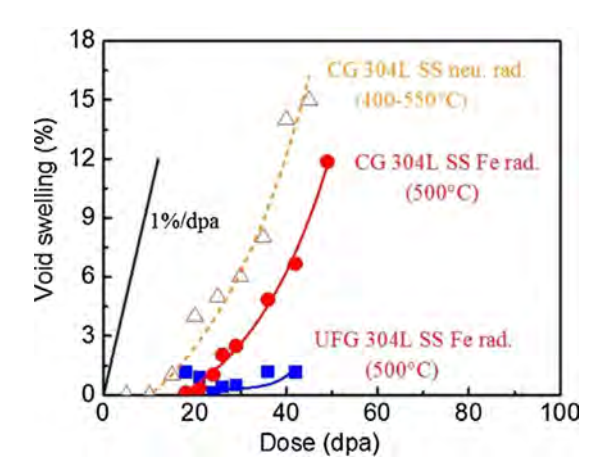


Fig. 2.11. A comparison of the void swelling of Fe ion irradiated CG and UFG 304L SS with data on neutron irradiated 304L SS [196]. Reprinted with permission from Ref. [196].

Table 2.1Selected published results of radiation damage in NC and UFG metals and alloys.

Material	Sample crystallography	Initial Grain Size (nm)	Radiated Particle	Particle Energy (MeV)	Fluence (ion/cm ² or dpa when noted)	Flux (ion/cm ² /s or dpa/s when noted)	Final grain size (nm)	Ref.
Au	FCC	10-15	Ar	0.5	5E14, 2E15	0.012 dpa/s	NA	[200]
Au	FCC	10-200	Si	10	2.70E+15	6.60E+11	10-275	[201]
Pt	FCC	10-15	Ar	0.5	5E14, 2E15	0.013 dpa/s	NA	[200]
Pt	FCC	10-15	Kr	1	5E14, 2E15	0.018 dpa/s	No change	[200]
Pd	FCC	10-300	Kr	4	NA	9.00E+12	40-80	[194
Pd	FCC	10	Kr ⁺	4	1E17 to 6E17	NR	NA	[194
Porous Pd (20%)	FCC	10-80	Kr	0.24	170–210 dpa	NR	NA	[150
Mo	BCC	25-455	He	0.2	1.40E+17	NR	NA	[180
Zr	HCP	10-15	Kr	0.5	5E14, 2E15	0.021 dpa/s	NA	[200
Cu	FCC	10-15	Kr	0.5	5E14, 2E15	0.023 dpa/s	NA	[200
Cu-0.5Al2O3	FCC	180	Н	0.59	0.91 dpa	NR	495	[150
Cu-0.5A2O3	FCC	178	H^{+}	590	0.91 dpa	1.5E-06 dpa/s	493	[190
Ti49.4Ni50.6	Metal alloy	23	Ar ⁺	1.5	5.6 dpa	6.40E+12	NA	[193
Fe	BCC	49	He	0.1	6E20	NR	96	[168
304L SS	FCC	100	Fe	3.5	6E20	0.003 dpa/s	200	[86]
Austenitic Steel (316 SS)	FCC	40	Fe	0.16	10 dpa	NR	NA	[150
Fe-14Cr-16Ni	Metal alloy	400	He	0.1	6E16	NR	400	[195
T91	Metal alloy	320	Fe	3.5	9E16	NR	NA	[85]
Ferritic Steels 14YWT	BCC	500, 1000	n	>0.1	1.2-1.6 dpa	NR	NA	[150
Low-C Steel	BCC	350	n	NA	1.15E-3 dpa	1.6E-9 dpa/s	360	[192
CrN Steel SUS316L + 1%TiC	FCC	100-50,000	n	>1	1.14E19-1.14E20	NR	NA	[150
Ni	FCC	55	Kr+	1	5	0.003 dpa/s	62	[30]
Ni	FCC	115	H ⁺	590	0.56 dpa	1.5E-06 dpa/s	38	[190
Ni	FCC	15-150	He ⁺	0.01	2E16, 8E16	10 ¹³	No change	[169
Ni	FCC	6-20,000	n	>1	1.14E19-1.14E20	NR	NA	[150
ED Ni	FCC	20-30	Ni	0.84	5 dpa	NR	no change	[150
SPD Ni	FCC	115	Н	0.59	0.56 dpa	NR	38	150
Ni	FCC	15-150	Ni ³⁺	3	5.4E14, 2.7E14	1.50E+11	No change	[169
PLD Ni	FCC and HCP	FCC: 13.9	Ni ⁶⁺	35	3.00E+14	NR	HCP: 14,	[158
	phases	(HCP: 8)					FCC: 17.4	
Ni-W	Metal alloy	6 to 20,000	n	>1	1.14E19-1.14E20	NR	NA	[150
W	BCC	60-400	Si ²⁺	3	6.20E+14	3.40E+11	NA	[181
W	BCC	60-400	W ⁴⁺	3	3.30E+14	1.80E+11	NA	[181
W	BCC	60-400	Cu ³⁺	3	5.80E+14	1.40E+11	NA	[181
W with (0.25–0.8)% TiC	BCC	50-200	He	3	2.00E+23	NR	NA	[150

irradiation tolerance is not just limited to NC nitrides. In NC MgGa₂O₄ irradiated by 300 keV Kr ions, Shen et al. showed a significant decrease in displacement damage relative to the single crystal counterpart [208]. Amorphization occurs in single crystal MgGa₂O₄, whereas NC specimens show little indication of amorphization as shown in Fig. 2.13. A similar phenomenon was observed in *in situ* Kr-ion irradiation studies of CePO₄ nanocrystals [213].

Table 2.2 A selected summary of studies on irradiation damage in nanocrystalline ceramics.

Material	Initial Grain Size (nm)	Radiated Particle	Particle Energy (MeV)	Fluence (ion/cm ² or dpa when noted)	Ref.
Zirconia	7.7	Au	2	1.00E+16	[202]
Ceria	6	Au	3	≤2E16	[203]
Ceria	NA	Au	3	0.3 dpa	[204]
ZrN	9, 31	Fe ²⁺	0.9	6.00E+15	[205]
TiN	8-100	Не	0.012, 0.035	4E8, 1E9	[206]
Porous VN _x	5–50	He	0.02	1.2E9	[207]
Porous CrN _x	5-50	Не	0.02	1.0E+13	[207]
MgGa ₂ O ₄	4-12	Kr	0.3	12-96 dpa	[208]
Porous ZrO ₂	10-300	Kr	4	3–8 dpa	[194,209]
ZrO_2	10-300	Kr	4	NA	[194,209]
Pyrochlore	17	Kr ⁺	1	1.875E14, 7.5E14, 2.5E15, 6.25E14	[210]
Porous α-SiC	36	Xe	95	8 dpa	[211]
ZrO ₂ in a-SiO ₂	3	Xe	1	0.3-0.9 dpa	[212]

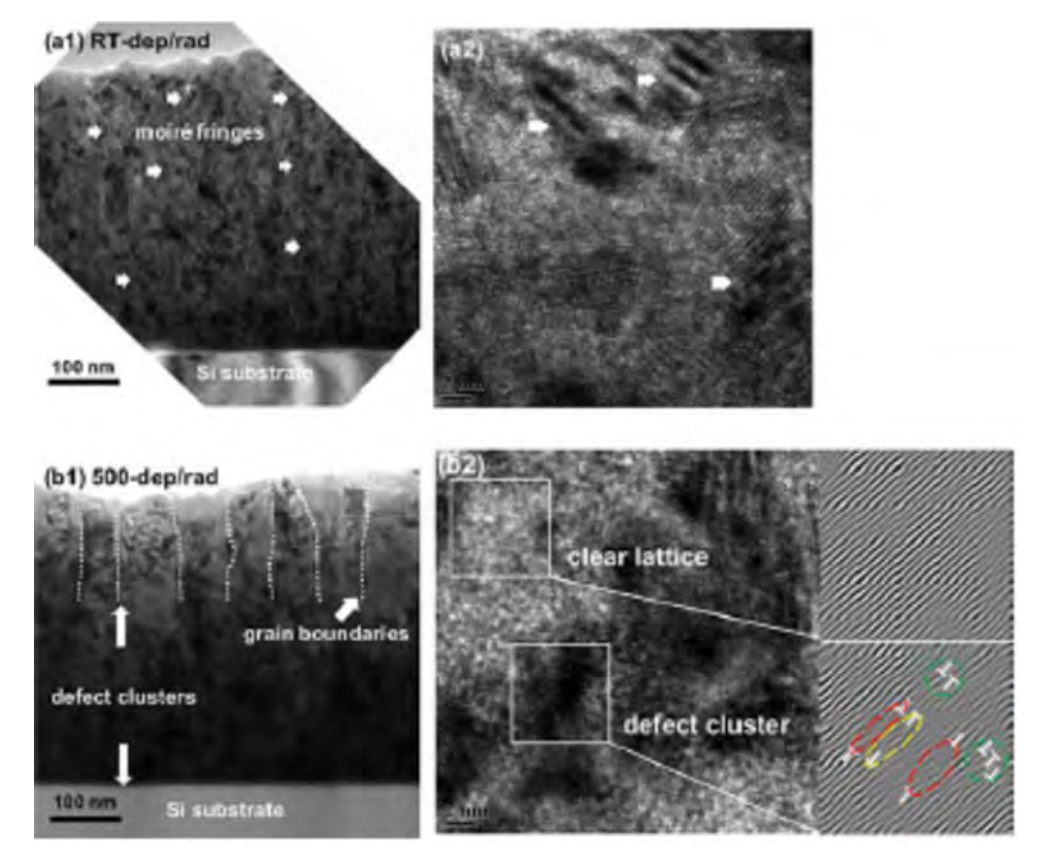


Fig. 2.12. (a1) A bright field TEM image of the irradiated NC ZrN film. (a2) An HRTEM image of the irradiated NC ZrN film shows a low density of defect clusters. (b1 and b2) TEM images of ZrN film with larger grain size. A high-density of defect clusters was formed inside the grains [205]. Reprinted with permission from Ref. [205].

Grain size effect on radiation damage in NC ceramics is a very complex subject. Amorphization and phase transformation may take place in addition to the benefit provided by defect sinks in these NC ceramics [214,215]. The chemistry and atomic arrangement of oxides can be complex, and annealing NC structures may alter the atomic structures to some extent, as exemplified in the work by Zhang et al. in pyrochlore $Gd_2(Ti_{0.65}Zr_{0.35})_2O_7$ [216]. The interplay between damage, grain size, and the annealing temperature needed for phase change is shown in Fig. 2.14. When the grain size is less than 100 nm, the critical dose for amorphization of $Gd_2(Ti_{0.65}Zr_{0.35})_2O_7$ increases rapidly to \sim 2 dpa. Whereas the same material with an average grain size of 100–400 nm shows little variation in the amorphization radiation dose, \sim 0.73 dpa. Furthermore, during grain coarsening at high annealing temperatures, the occupancy of Gd in 16c position changes from 0.57 to 0.8, further

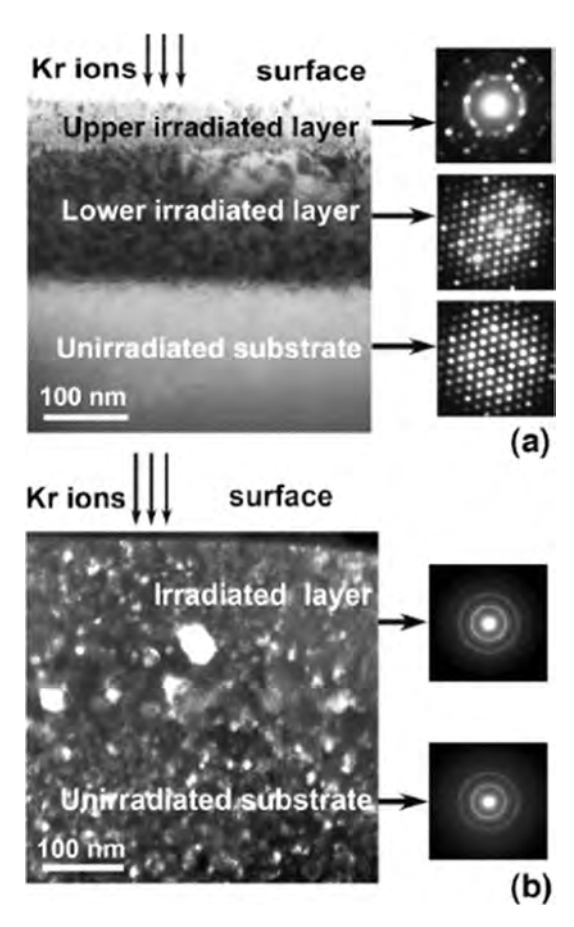


Fig. 2.13. Cross-sectional TEM images and corresponding selected-area diffraction patterns obtained from irradiated polycrystalline MgGa₂O₄ samples. (a) CG MgGa₂O₄ irradiated to a dose of 12 dpa. The selected-area diffraction pattern shows that amorphization occurs in the upper irradiated region of the specimen, whereas the lower and nonirradiated regions remained single crystal. (b) The NC MgGa₂O₄ specimen irradiated to a dose of 96 dpa retained its NC characteristics, with little indication of amorphization [208]. Reprinted with permission from Ref. [208].

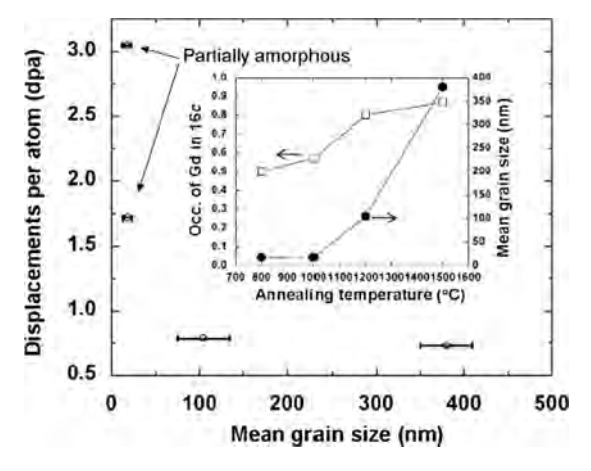


Fig. 2.14. Grain size dependent critical amorphization radiation doses of pyrochlore $Gd_2(Ti_{0.65}Zr_{0.35})_2O_7$ annealed at different temperatures. Inset shows the relationship between grain size and degree of disorder that occurs during annealing [216]. Reprinted with permission from Ref. [216].

complicating the interpretation of size effect on radiation damage. In general, due to the slow diffusion kinetics of ceramics, the GB density in ceramics needs to be greatly increased to demonstrate enhanced radiation tolerance at magnitudes comparable to NC metallic systems.

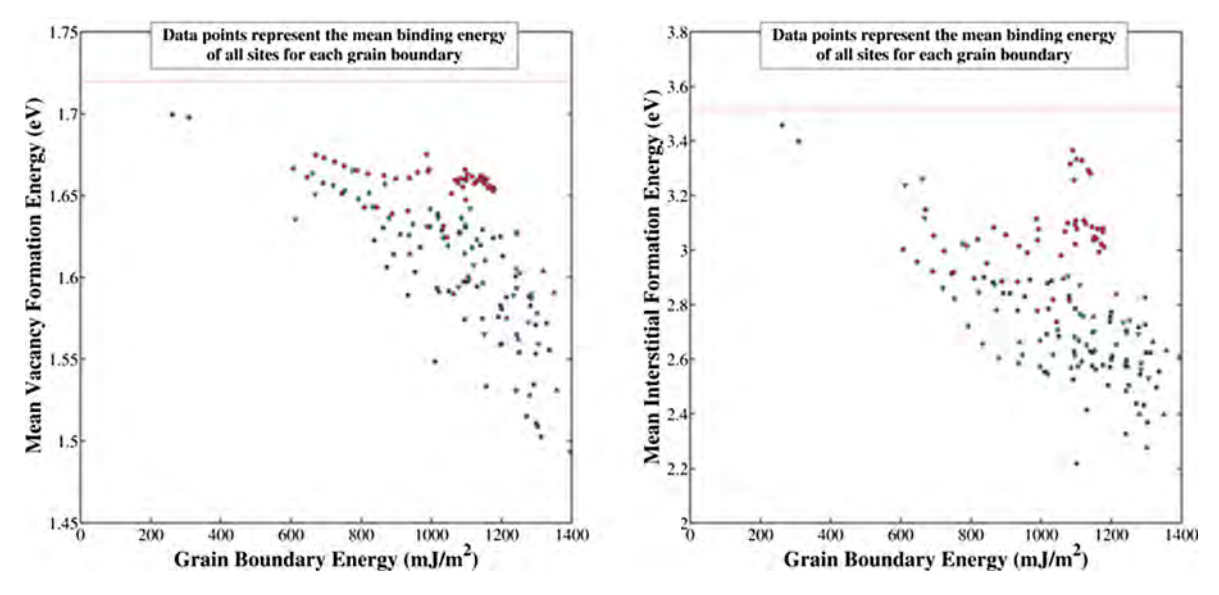


Fig. 2.15. The decreasing point defect formation energies for vacancies and interstitials with increasing GB energy for BCC Fe simulated for a variety of GBs [232]. Reprinted with permission from Ref. [232].

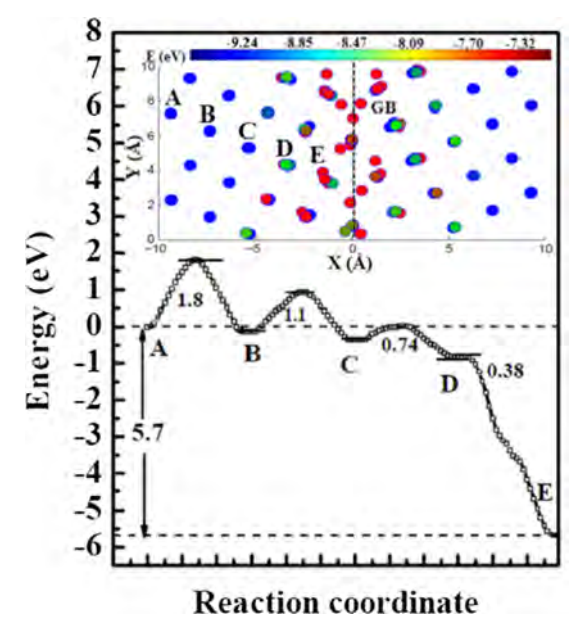


Fig. 2.16. An annihilation path for the vacancy near the GB in tungsten with interstitials trapped at the GB. The axes X and Y axes are oriented along [310] and $[\bar{1}30]$, respectively [235]. Reprinted with permission from Ref. [235].

Although numerous studies show that NC ceramics have enhanced radiation resistance, some studies show the opposite. For instance, bulk ZrO₂ is known to be one of the most radiation resistant ceramics [217–220], showing no evidence of irradiation-induced amorphization at high dose, such as 110 dpa [221]. However, Meldrum et al. showed that merely 1 dpa of Xe ion irradiation (1MeV) was sufficient to amorphize ZrO₂ nanoparticles (3 nm in diameter) embedded in an SiO₂ matrix [212]. It was argued that tetragonal nanograins raise the system free energy to facilitate amorphization. However, it is interesting to see that NC cubic ZrO₂ film is stable against amorphization [202]. The studies on amorphization resistance of NC SiC are mixed with opposite observations. It has been shown that stacking faults in NC SiC improve radiation resistance [222,223]. But NC SiC has been shown to reduce the amorphization resistance in some other cases [210,224–229]. The complexity arises from the internal microstructure (phases) of SiC, radiation temperature and even ion sources [230].

2.4. Need to refine the GB sink strength model

2.4.1. Complexity of GB nature on radiation damage in NC metals

The radiation tolerance of NC metallic materials is directly related to the nature of the GB structure and the radiation environment [179,231–234]. The potential complexity is nicely demonstrated in the work of Uberuaga et al. [231], as well as the work by Arjhangmehr and Feghhi [179]. Both of these studies examined the role of GB angles, GB characters, the distances of the cascades to the boundaries, and the damage states already present in the GBs. The resulting microstructure can also be dependent on the cascade type that occurs (semi-spheroid, semi-ellipsoid, or fragmented distribution) [179]. The large variation in the predicted defect density suggests that the GB characters, structures, and radiation histories play a significant role in the radiation damage from each cascade.

The sink strength was investigated in great detail as a function of the GB character by Tschopp et al. utilizing molecular statistics simulations [232]. This study surveyed a significant number of GBs and outlined some important findings:

- (1) In general, GB sites have much lower vacancy/interstitial formation energies than in the bulk. However, certain GB sites have higher vacancy/interstitial formation energy than bulk lattices, indicating that such sites will preferentially capture (annihilate) radiation induced point defects.
- (2) Although both low-angle GBs (LAGBs) and high-angle GBs (HAGBs) are effective sinks for point defects, the sink efficiency depends on the exact GB character with a general rule that HAGBs are more efficient defect sinks owing to their lower point defect formation energy.
- (3) Point defect (vacancy or interstitial) formation energies also decrease with increasing misorientation angles for LAGBs (less than 15°), but less so for HAGBs.
- (4) Point defect formation energies also decrease with increasing GB energy as shown in Fig. 2.15.
- (5) The simulations also show that there is a greater tendency for interstitials to segregate to GBs than vacancies. This observation suggests that GBs are in general biased defect sinks. Another implication of this finding is that the characteristics of GBs (GB energies and misorientation angles, etc.) may change during long-term radiation as the preferential absorption of interstitials will gradually change the atomic configurations of the GBs.

Clearly, such atomistic views on GB defect sinks have not been taken into account when developing the analytical GB sink strength formulas.

One detail that appears to be very important is the defect structure present in the boundary either from initial production, mechanical deformation, or previous radiation damage [172,179]. That being said, most MD simulations have also predicted that a single GB can accommodate multiple cascades without a substantial decrease in the sink efficiency and will outperform a single crystal of the same composition with regards to radiation tolerance [184]. The exact structural evolution associated with each new cascade event is not predicted to be the same. This can be seen in the data of damage profiles presented for a pristine and defect loaded boundaries. Different from the generally accepted theory that the GBs in NC metals serve as efficient sinks, an MD simulation predicted single crystal W outperforms NC W owing to the hindered motions of SIAs in this system [170]. Despite this one study, the prevailing view based on numerous studies remains that GBs in NC metals can incorporate the defects produced by multiple sequential cascades in a typical radiation environment. The modeling work by Li et al. shows the complexity of the annihilation pathway for a single vacancy near a GB that contains trapped interstitials, as can be seen in Fig. 2.16 [235]. A path with this many local minima suggests a range of complex and evolving defect and boundary structures are possible depending on the local kinetics.

A major concern in trying to understand defect evolution in NC models utilizing MD simulations is the time limitations associated with the models. To understand the defect evolutions near boundaries at relevant time scales, recent work by Dunn et al. has attempted to utilize a spatially resolved stochastic cluster dynamics model [156]. Another factor hindering the validation of MD simulations is the limited amount of experimental data due to the difficulties of characterizing GB character and structure during irradiation studies. Advanced microscopy tools, coupled with simulation, have recently been demonstrated to be successful pathways of exploring the interplay between GB characters and defect absorptions [236–238].

2.4.2. Modified GB sink strength model

The simple rate equation (Eq. (1.17)) correctly predicts the trend that GB sink strengths are grain size dependent; that is smaller grains have higher sink strength. However there are a couple of issues with this equation. First, the equation predicts that when R reduces to several nm, the sink strength approaches an unrealistically large value. Second, the equation does not differentiate between different types of GBs. For instance there is increasing evidence showing that HAGBs are stronger defect sinks than LAGBs. Third, the sink strengths of GBs decay because GBs cannot fully recover (self-heal) after absorbing a large number of point defects. NC grains may coarsen during long-term irradiation. Thus the assumption that GBs are ideal defect sinks is less likely to hold in continuous, long term, radiation environments.

Detailed derivation of a formula that considers all these factors is beyond the scope of this review, however a simple analytical formula can probably suffice for the current purpose. The absorption of point defects, such as interstitials will require GBs having excess free volume, and HAGBs have greater excess free volume than LAGBs. Hence a fundamental assumption is that not the entire GB can accommodate point defects, instead there are active sites on a GB that can preferentially capture point defects. Thus the following factor is introduced when estimating the sink strength of a GB:

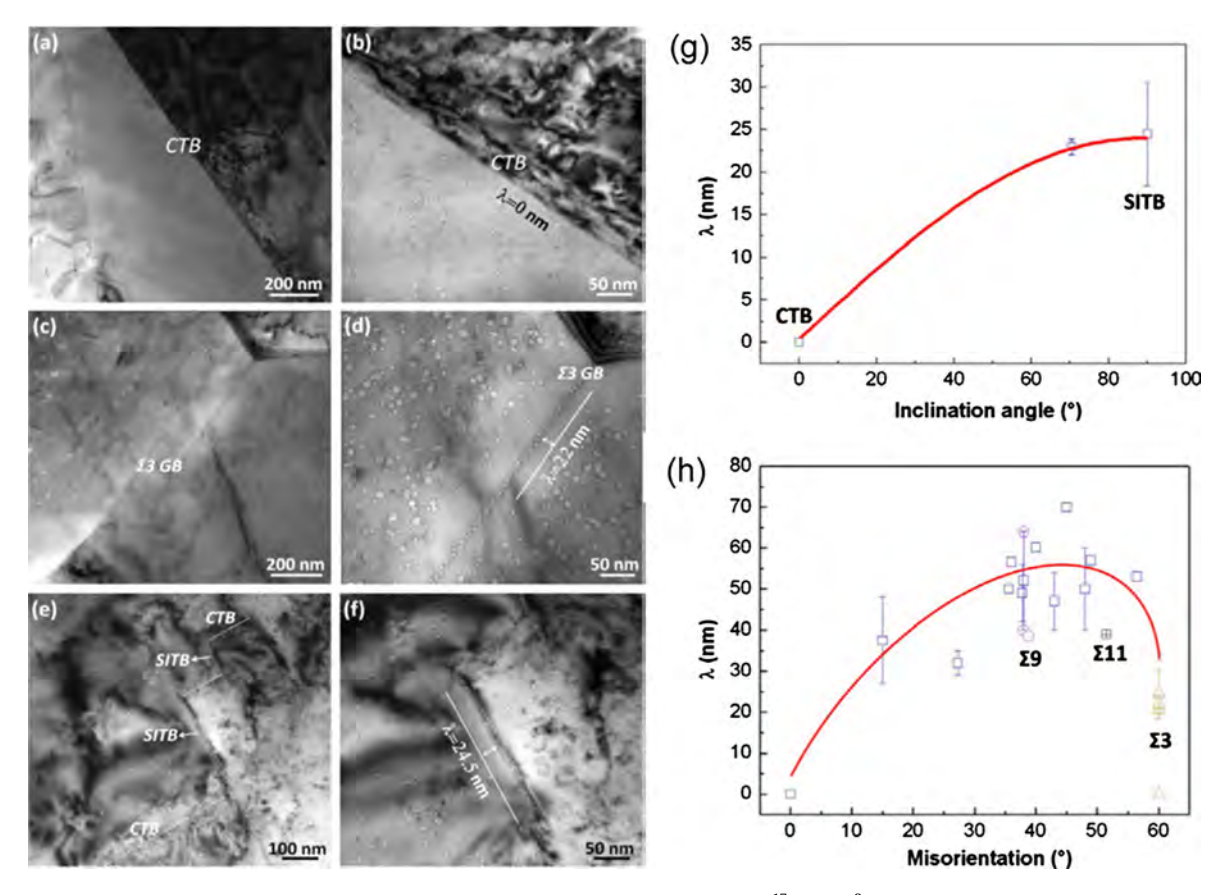


Fig. 2.17. $\sum 3 \langle 1 \ 1 \ 0 \rangle$ tilt GBs in Cu irradiated at 450 °C by 200-keV He ions at a fluence of 2×10^{17} ions cm²: (a) and (b) show radiation-induced voids but no void denuded zone (VDZ) near a coherent twin boundary (CTB); (c) and (d) show a VDZ near an asymmetric $\sum 3 \langle 1 \ 1 \ 0 \rangle$ tilt GB; (e) and (f) show a VDZ at a symmetric incoherent twin boundary (SITB). All images were taken under a defocus of $-5 \ \mu m$. (g and h) The width of the VDZ as functions of inclination angle and misorientation angle [236]. Reprinted with permission from Ref. [236].

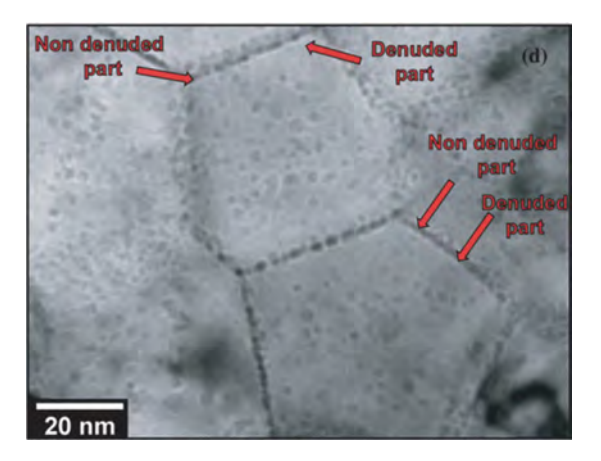


Fig. 2.18. Over-focused bright field TEM image showing partially denuded GBs (indicated by red arrows) in NC Fe irradiated with 10 keV He at 700 K [168]. Reprinted with permission from Ref. [168].

$$k_{gb}^2 = 15f(\theta, \gamma)/R^2 \tag{2.1}$$

where $f(\theta, \gamma)$ is a function of GB energy (γ) , and misorientation angle (θ) , and $f(\theta, \gamma) = 1$ for an ideal HAGBs, and $0 \le f(\theta) < 1$ for LAGBs. Such a formula has the advantage of integrating the characteristics of GBs (such as sink efficiency) with sink strength, and it may also be consistent with the experimental observations that:

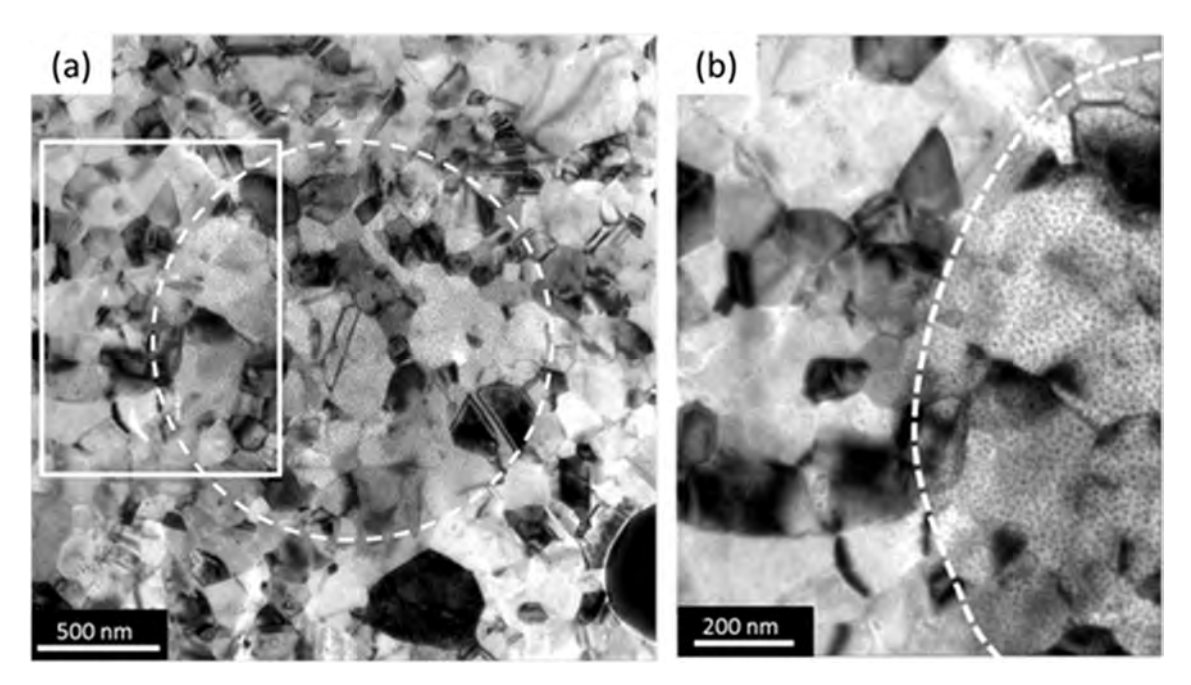


Fig. 2.19. The influence of an electron beam on the formation of cavities in self-ion irradiated NC Ni. (a) Defocused TEM image taken after annealing, demonstrating that the voids are only present in the area irradiated by the electron beam during annealing. (b) Higher magnification image of the box in (a) showing drastically different defect density in irradiated NC Ni [309]. Reprinted with permission from Ref. [309].

- (1) the capability of GBs to absorb defects decays or alters in some form after long term radiation and grain coarsening, and
- (2) the GB denuded zone width scales with GB misorientation angles, that is HAGBs typically have a broader GB denuded zone.

2.4.3. Application of the modified model for interpreting experimental findings

The aforementioned model can be used to explain the results of some recent studies, where the defect denuded zones appear to vary for different types of GBs. A recent study by Han et al. has investigated the sink strengths of various GBs in He ion irradiated Cu at elevated temperatures by measuring the resulting denuded zones around each individual boundary [236]. Based on the observation of He bubble denuded zones (Fig. 2.17), a simplistic yet elegant model was developed by associating the width of the denuded zone (λ) of an asymmetrical $\Sigma 3\langle 1\ 1\ 0\rangle$ GB with the misorientation angle (θ) and the width of denuded zones of the coherent twin boundary (CTB) and the symmetric incoherent twin boundary (SITB):

$$\lambda_A = \lambda_{CTB} \cos \theta + \lambda_{SITB} \sin \theta \tag{2.2}$$

This study indicates that the sink strengths of the GBs are strongly related to the GB character [236], as shown in Eq. (2.1). Significant work is needed to substantiate this model (described in Eq. (2.1)) at various temperatures, in different material systems, and under different radiation conditions. Progress has been made with respect to examining grain boundary character and structure in specific boundaries using coordinated experimental and theoretical approaches [237,238], but much work is needed to extend this type of approach to NC metals. A challenge remains in that NC metals often contain non-equilibrium GBs, which is discussed later in this chapter.

The finding on the influence of GB characteristics on its sink strength was further supported by a recent *in situ* He ion irradiation TEM study, which showed that, even for the same NC Fe grain, not all GBs responded the same way during irradiation (Fig. 2.18) [168]. It is likely that the GBs surrounding the same grain have different characteristics and thus, as predicted by Eq. (2.1), they have different sink capacity. Another interesting observation made during irradiation at elevated temperatures is that cavities in irradiated NC Cu form mainly along GBs, but less so in grain interiors [236]. The number density and average radius of cavities in NC Cu are smaller than those of cavities in the irradiated single crystal and CG Cu. Although these initial findings are intriguing, the details of governing mechanisms are unclear and require further investigation.

A large body of literature on radiation damage in nanostructured metals has used He ions for radiation studies as He bubble induced degradation of mechanical properties is one of the concerns in irradiated structural materials. There are abundant examples on He ion irradiation studies of bulk structural materials [239–248], as discussed briefly in Section 1.3. He bubbles may coalesce to form large voids, which lead to blistering and embrittlement after high dose irradiation

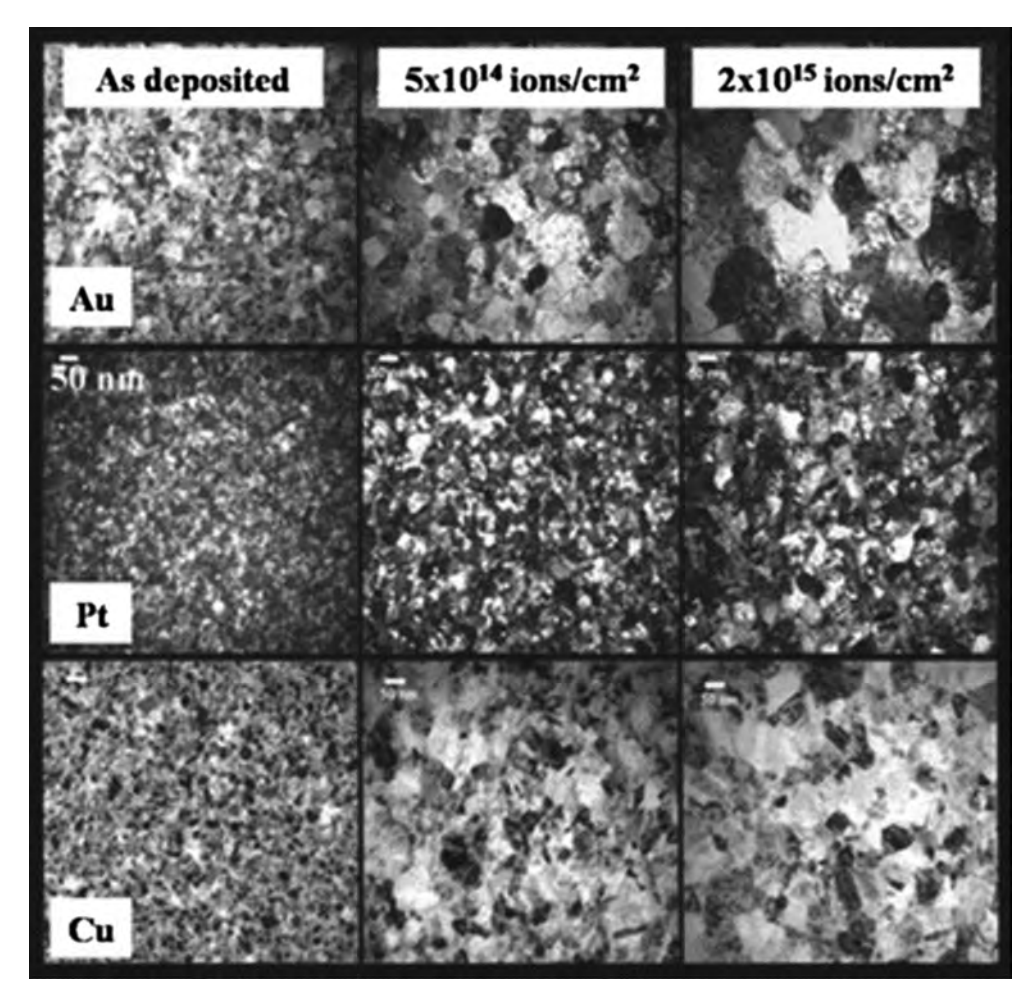


Fig. 2.20. Sequence of bright-field TEM images taken at different ion doses showing grain growth induced by ion irradiation at room temperature; from left to right: as deposited, 5×10^{14} ions/cm², 2×10^{15} ions/cm²; from top to bottom: pure Au thin-film irradiated with 500-keV Ar ions, Pt irradiated with 500-keV Ar ions, and Cu irradiated with 500-keV Kr ions [200]. Reprinted with permission from Ref. [200].

[249–308]. Hence GBs in NC metals and alloys provide an important method of managing He, e.g. by prohibiting the formation or growth of large He-filled cavities.

In situ TEM is a powerful tool in determining the underlying mechanism governing the evolution of defects and microstructure in irradiated NC metals in real time. However, one must understand the limitations associated with sample geometry, experimental conditions, and the effects of electron beam on the observed results during these in situ TEM studies. Recently, Muntifering et al. showed that during a sequential in situ 3 MeV self-ion irradiation and annealing of NC Ni, the defect evolution kinetics could be greatly influenced by the electron beam [309]. In Fig. 2.19, the region exposed to the electron beam developed cavities much sooner than those receiving much less electron beam exposure. This experiment was done in metal that should not undergo radiolysis and was well below the knock-on threshold for Ni, thus eliminating the two major forms of electron beam damage expected in TEM samples. The electron-beam facilitated formation of cavities in NC Ni can be attributed to the increasing growth of oxide known to occur in Ni and many other metals exposed to electron beams [309]. As a result, the identification of radiation sink rates and other effects from in situ studies should be approached with care.

2.5. Stabilities of NC metals in radiation environments

Understanding the absorption of cascades by GBs is only one part of the story. The other major aspect is understanding the mobilities of GBs and the associated networks present in NC materials as a result of the radiation damage and associated temperature rises. MD simulations have shown that GBs can move over a significant distance in ps after cascade events [173,182,190]. Such simulations suggest a fast GB migration mechanism resulting from either the absorption of the cascade damage or the associated thermal spike. Understanding the extent of grain growth in these types of samples is difficult from post irradiation examination, so *in situ* irradiation with TEM has been used to examine the structural evolution arising from

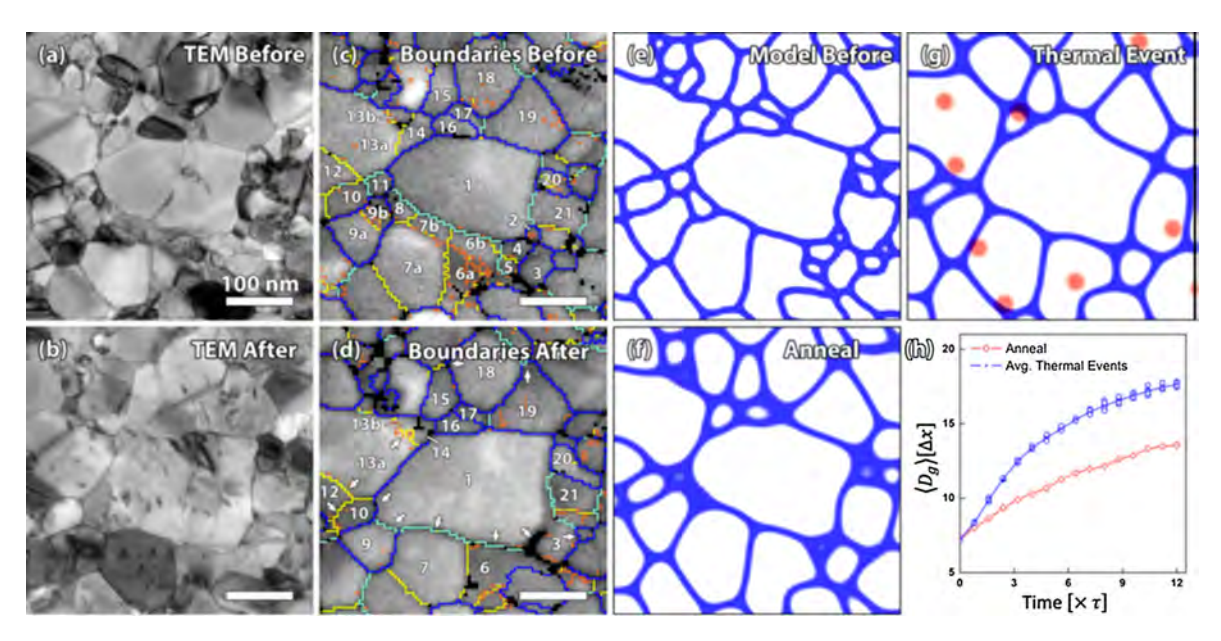


Fig. 2.21. Bright-field TEM micrographs of NC Au (a) and (b) and index maps (c) and (d) with GBs highlighted before and after irradiation. Orange, yellow, cyan, and blue indicate GBs with misorientation angles in the respective ranges of $\varphi < 3^\circ$, $3^\circ < \varphi < 15^\circ$, $15^\circ < \varphi < 30^\circ$, and $30^\circ < \varphi$. The grains are numbered clockwise from the bottom right. The arrows in (d) indicate the directions in which the boundaries moved. (e) The phase-field representation of the structure shown in (c). (f) The grain structure after homogenous annealing. (g) The snapshot taken during the simulated irradiation. The red spots indicate one set of thermal events. In panels (e)–(g), white (blue) regions represent grain (boundary) regions. (h) Average grain diameter as a function of characteristic time. The red diamonds represent the homogenously annealed grain structure, while the blue circles indicate 5 thermal event runs. The blue line shows the average of these 5 runs [201]. Reprinted with permission from Ref. [201].

displacement damage. A radiation induced grain growth model was put forward by Kaoumi et al. for a range of monolithic metal system based on a thermal spike assumption [200]. Their analytical model is expressed as follows:

$$D^{3} - D_{0}^{3} = K\Phi t = \left[36\gamma d_{spike} \chi \delta \frac{V_{at} v \sqrt{\frac{3}{5}} \Gamma(\frac{8}{3}) k_{B}^{5/3}}{10\pi C_{0}^{2/3} \kappa_{0}} \frac{Q^{5/3}}{E_{a}^{8/3}} \right] \Phi t$$
 (2.3)

In this equation, the final grain diameter (D) is dependent on the initial grain size (D_0), the average thermal spike size (d_{spike}), the number of thermal spikes per ion (χ), the thermal spike energy (Q), ion flux (Φ), thermal conductivity (κ_0), heat capacity (c_0), atomic volume (V_{at}), GB surface energy (γ), the activation energy required for atomic jumps in the thermal spike (E_a), the gamma function (Γ), and the Boltzmann's constant (E_a). This model is a derivation of the classical thermal grain growth model with the addition of an empirically derived term that incorporates the ion irradiation effect. This model assumes that during a cascade event, GBs migrate owing to atomic jumps and variations in local curvature resulting from the thermal spike. These atomic jumps promote the migration of GBs and the local curvature dictates the direction of boundary migration. The grain size distribution was obtained directly from TEM micrographs and videos captured during *in situ* ion irradiation, as shown in Fig. 2.20 [200].

Understanding the radiation effects on grain coarsening was furthered by Bufford et al. [201], who combined *in situ* self-ion irradiation of NC Au film with precession electron diffraction (PED) and mesoscale modeling of GB stability. They showed that both the global texture and overall GB network character could evolve during irradiation induced grain growth. In addition, they showed a single boundary associated with one of the larger grains had migrated until it hit a set of subgrains [201]. The overlaid GB character map and bright-field TEM images of the nonirradiated and irradiated NC Au films can be directly compared to the mesoscale model and the associated predictions for radiation-induced grain growth, as shown in Fig. 2.21. Additional post-irradiation examinations utilizing PED and other advanced characterization techniques have suggested that non-equilibrium phases may be prone to grain growth over thermodynamically preferred phases in systems ranging from pure metals to complex ceramics [158,209]. Very recently, this idea has been taken further by Yu et al., who reported *in situ* Kr ion irradiation induced grain rotations in NC Ag, Cu, and Ni and associated it with significant in-plane strain [26]. Understanding the complex interactions of GBs, grooves, and thin film effects during irradiation is still an area requiring significant research.

In addition to ion-irradiation induced grain coarsening, two recent and somewhat surprising observations were made regarding the potential for strikingly minimal interactions between GBs and voids in irradiated NC Ni. In this study Muntifering et al. showed, using *in situ* TEM irradiation and annealing in combination with PED, that defect sizes and shapes were not limited to the sizes of the underlying NC grains [169]. At this damage level, the grain structure was no longer discernable by

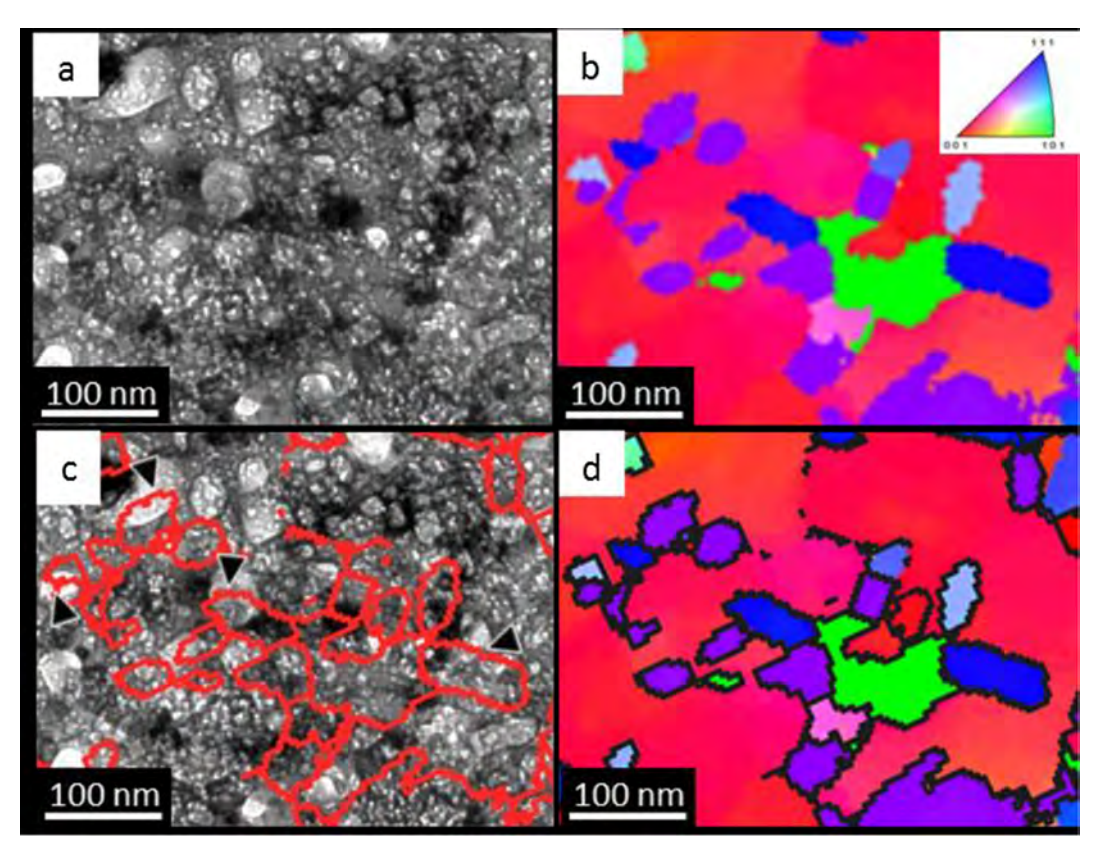


Fig. 2.22. (a) Under-focused bright-field TEM image of cavities in Helium then self-ion irradiated NC Ni film annealed to 400 °C. (b) Orientation map of (a) revealing the grain structure and strong texture. (c) GBs (red) overlaid on (a), demonstrating that many cavities cross GBs, several examples of which are highlighted with black arrows. (d) Orientation map with GBs delineated by black lines [169]. Reprinted with permission from Ref. [169].

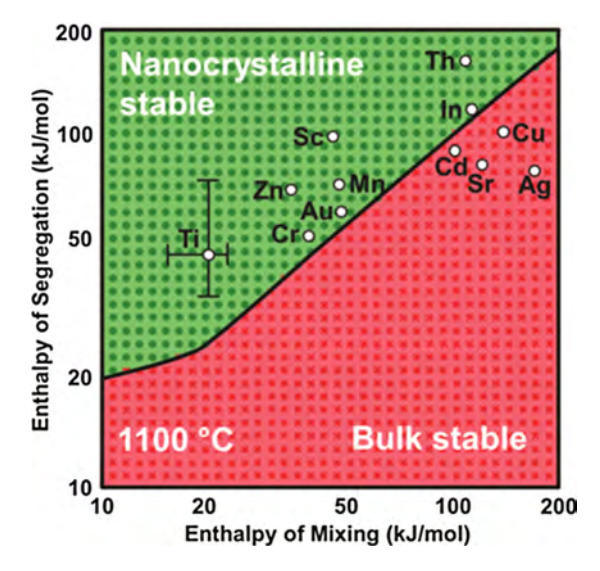


Fig. 2.23. The significance of solutes and segregation profiles on the stabilities of GBs in W calculated for various solutes calculated at 1100 °C [311]. Comparison of enthalpy of segregation vs. enthalpy of mixing predicts that solutes in the green colored region may stabilize nanograins in W. Reprinted with permission from Ref. [311].

traditional TEM imaging technique owing to the large number of defects. However, the PED orientation and grain-structure maps in Fig. 2.22 clearly show the underlying microstructure and the cavities seem to have no associated correlation to the underlying GB structure [169]. Similarly, Vetterick et al. showed that the presence of voids at a GB can decrease the mobility of a GB by four orders of magnitude via a Zener pinning like mechanism [164]. The combined observations of cavities growing straight through boundaries or pinning GBs demonstrate the large number of competing mechanisms that are active in NC samples exposed to radiation. It is our opinion that the dominant mechanism and subsequent radiation tolerance may be highly dependent on the composition, and the character of the GBs (not just on the average grain size), as well as on the radiation environments to which the sample will be exposed to during the operational lifetimes of the relevant components.

2.6. Challenges and future outlook

Although research on radiation responses of NC materials has been limited, it is rapidly increasing. There are plenty of research and engineering challenges ahead of us, such as: elucidating the role of GB character and GB stability in the radiation damage of NC materials, validating their roles in realistic radiation environments, and the commercial scale processing of the bulk nanostructured materials. Although the vast majority of studies investigating the radiation stabilities of NC materials only focus on the average grain size, a small subset of those has started to look at the role of grain size distribution [181]. However, it was not until very recently that GB character was being considered in the design and characterization of radiation-tolerant materials [168,236]. Due to experimental limitations, the GB character has typically been limited to the GB orientation, but only recently has GB plane and GB defect structure been taken into account in coordinated experimental and theoretical approaches [237,238]. Further experimental and modeling efforts are needed to determine how local GB character, composition, and defect distribution alter the radiation responses of GBs as defect sinks, and validate the model described by Eq. (2.1). Such studies will not only advance the basic understanding of the underlying physics of defect-GB interactions, but also facilitate the design of commercial NC alloys showing complex interplay between the chemistry and structural effects in various radiation environments.

As shown in Section 2.5, the stabilities of NC materials in various radiation environments and the unique abilities of GBs to absorb cascade damage can be significantly compromised by irradiation induced grain coarsening. Additionally, a recent study by one of the coauthors suggests that GBs in NC materials produced by methods such as severe plastic deformation and sputter deposition are not equilibrium structures, and therefore exhibit drastically different behavior under irradiations [238]. For any irradiated NC materials, the concern of grain stability must be addressed. Fortunately, it is currently being tackled through alloying [310,311], the tailored introduction of stable oxides in pure metal systems [312,313], the production of ODS alloys [314,315], and through various combinations thereof [152,154,169,311,316-381]. Although there is still much controversy over the balance played between the roles played by thermodynamic and kinetic driving forces in stabilizing NC systems, recent studies have predicted that solute atoms may significantly enhance the thermal stabilities of nanograins. For instance, the comparison of the enthalpy of mixing vs. the enthalpy of segregation for W alloys at 1100 °C (in Fig. 2.23) predicts that certain solutes, such as Ti, may improve the thermal stabilities of W nanograins at temperatures as high as 1100 °C, and the prediction was validated by ball milling of the W-Ti alloys [311]. This approach may also assist us in the identification of NC alloys with advanced thermal and radiation stabilities. It has also been shown that nanograins can be stabilized at high temperatures by the addition of oxides along GBs [382]. We suggest that utilizing such a strategy might also mitigate the radiation induced grain growth frequently observed in high-purity NC metals [201]. The addition of oxides can also significantly mitigate radiation damage, as observed in bulk ODS alloys [152]. In general, the next step towards the design of radiation-tolerant NC systems may be to employ multiphase NC alloys.

New developments of characterization tools are needed to thoroughly examine the radiation response of complex NC alloys, and greatly advance the fundamental understanding with increased spatial, chemical, and temporal resolution. Thorough interrogations of local microstructural details, including GB characters and defects and solute distributions are important for understanding the radiation responses of NC materials. The development of advanced characterization tools also calls for significant advancement in data processing and large-scale nondestructive characterization of nanostructured materials. Many of these capabilities are supported by national and global research infrastructures, such as those supported by the US Department of Energy (DOE) – Nuclear Energy, Nuclear Science User Facilities and DOE Basic Energy Sciences, Nanoscale Science Research Centers (NSRCs), and other similar international research infrastructures.

Two other aspects necessary for the regulatory-approved incorporation of NC materials systems into nuclear applications are validation of such materials in realistic radiation environments and the commercial scale processing of the nanostructured materials. These aspects are as important as, if not more important than, those mentioned previously, but they have been studied much less to date. A vast majority of the radiation studies on NC materials use ion beams. The differences in damage and damage rates between neutron and ion irradiations remain intensely debated topics in the nuclear energy field [156,199,383]. It has been suggested that altering the ion beam radiation temperature can compensate for the elevated damage rate during ion irradiation, and utilizing triple beam facilities can incorporate synergistic effects resulting from transmutation [136,384,385]. The development of triple beam facilities can be found in a review by Chao et al. [153]. There are a very limited number of studies on the different structural evolutions of NC systems as functions of sequential vs. concurrent exposures to heavy ion irradiations (e.g., displacement cascades), gas implantations (e.g., transmutated species), and various temperatures [169,309,386]. Most of these studies have shown a drastic change in internal microstructures as functions of the irradiation history.

In a similar manner, the industrial-scale processing of such nanostructured materials can utilize the advancements made in the past few decades, ranging from the work developed for electrochemical coating over areas as large as semi-truck bumpers [387] to severe plastic deformations for bulk structural materials [388–395]. A review of other possible routes of producing radiation-resistant bulk nanostructured metals was completed by Beyerlein et al. [154]. Synergistic and extensive research studies are necessary to design radiation tolerant NC materials, and such studies may pave the way for the application of NC materials to advanced nuclear energy systems.

3. Radiation damage in metallic and ceramic nanolayers

As mentioned in Section 1, it is a major challenge to design "radiation-immune" materials that resist radiation damage while maintaining their high strength and toughness. Recently, the strategy of incorporating high-density heterophase layer interfaces as defect sinks to enhance damage resistance has been investigated intensively. Among various defect sinks, layer interfaces are unique in many aspects. Physically coherent and incoherent interfaces can be constructed between materials with different lattice mismatches [396,397]. Chemically, various types of chemical bonds can be formed across interface planes [398]. Furthermore, the mechanical behaviors of multilayer nanocomposites, including ductility, yield strength, hardness, etc., can be tailored [399,400]. Geometrically, the layer thickness of each constituent can be precisely controlled down to 1 nm, providing ample opportunity to investigate the size effect on radiation damage in nanomaterials. Hence nanolayer composites have been increasingly used as model systems to explore the role of interfaces on radiation tolerance. The improved understanding on interactions between interfaces (defect sinks) and radiation-induced defects has provided significant insight into the design of advanced radiation-tolerant structural nanomaterials.

3.1. Sink strength of nanolayers

Rate theory has been widely used to describe the evolution of radiation-induced damage. In 1970, the concept of "sink strength" was proposed by Wiedersich to simplify the solution of steady state defect concentration [401]. Meanwhile, it has been used as a determinant reflecting the strength or affinity of certain sinks for radiation-induced defects. Later, the concept was broadened by Brailsford, Bullough, Hayns, Rauh, and Wood et al. to explore different types of defect sinks [137,402–406].

Although the sink strength of GBs has been described analytically in Eqs. (1.15)–(1.17), there has not been a similar formula for describing the sink strength of layer interfaces to date. To develop such an equation, we start with the idea of sink strength for thin foil surfaces [137]. Using Cartesian coordinates, the point defect concentration, c, within a thin foil can be described by:

$$D\frac{d^2c}{dx^2} + K - Dk_{sc}^2c = 0 ag{3.1}$$

where the *x*-axis is perpendicular to the foil surface, *D* is the point defect diffusion coefficient, *K* is the defect production rate, and k_{sc}^2 is the sink strength of all the microstructure within the foil. For a thin foil with a thickness of 2*l*, the solution to the formula, based on the boundary condition (c = 0 when x = 0, *i.e.* the free surface is an ideal defect sink) and the symmetry condition (dc/dx = 0 when x = l), is given by:

$$c(x) = \frac{K}{Dk_{sc}^2} \left[\frac{1 - \cosh k_{sc}(x-1)}{\cosh k_{sc}l} \right]$$

$$(3.2)$$

It can be shown that the sink strength of free surfaces can be written as:

$$k_s^2 = \frac{k_{sc}/l}{\coth(k_{sc}l) - \frac{1}{k_{sc}l}}$$
 (3.3)

In the extreme case, when $k_s d \to 0$, i.e. for thin foils where free surface defect sinks dominate, it can be shown that:

$$k_s^2 = \frac{3}{l^2} \tag{3.4}$$

Similarly for A/B nanolayers with equal individual layer thickness, h, if we assume that the layer interface is an ideal defect sink, then the sink strength of nanolayers can be written as:

$$k_h^2 = \frac{2k_{sc}/h}{\coth(k_{sc}h/2) - \frac{2}{k_{sc}h}},$$
(3.5)

When $k_{sc}h \rightarrow 0$, we arrive that:

$$k_h^2 = \frac{12}{h^2} \tag{3.6}$$

Note this formula also assumes that the columnar grain size of each layer is much greater than h. Thus the overall sink strength of nanolayers (without the consideration of GB sinks within the layers) may be underestimated.

With the ideal boundary conditions, the defect flux into two ideal interfaces (F^{ideal}) across the layer can be estimated as:

$$F^{ideal} = \frac{2D}{h} \frac{dc}{dx}\Big|_{x=0} = \frac{2K}{k_{sc}h} \tanh k_{sc}h/2 \tag{3.7}$$

The boundary condition for ideal sinks (c = 0 when x = 0) applies well to free surfaces. However, heterophase boundaries in nanolayers present limited defect concentrations at the interfaces and the values are closely correlated with sink efficiencies, η . Note that in the simplified version of Eq. (3.6), the intrinsic nature of layer interfaces, such as coherency strains, misfit dislocation densities (*i.e.*, interfacial energies) and heats of mixing, are not considered. Here we introduce the concept of sink efficiency (η) as the ratio of the defect flux into an interface (F^{real}) to the defect flux into a perfect sink interface (F^{ideal}) [407]:

$$\eta = \frac{F^{real}}{F^{ideal}} \tag{3.8}$$

Replacing the ideal sink boundary condition by:

$$F^{real} = \frac{2D}{dc} \frac{h}{dx}\Big|_{x=0} = \eta F^{ideal}$$
 (3.9)

we obtain the particular solution:

$$c(x) = c_1 e^{k_{sc}x} + c_2 e^{-k_{sc}x} + \frac{K}{Dk_{sc}^2}$$
(3.10)

where:

$$c_{1} = -\frac{K\eta}{k_{sc}^{2}D} \frac{e^{-k_{sc}h/2}}{e^{k_{sc}h/2} + e^{-k_{sc}h/2}}$$

$$c_{2} = -\frac{K\eta}{k_{sc}^{2}D} \frac{e^{k_{sc}h/2} + e^{-k_{sc}h/2}}{e^{k_{sc}h/2} + e^{-k_{sc}h/2}}$$
(3.11)

When $\eta = 1$, the solution is the same as Eq. (3.2). The correlated sink strength of layer interfaces changes to:

$$k_h^2 = \frac{k_{sc}^2}{\frac{k_{sc}h}{2n}\coth(k_{sc}h/2) - 1}$$
(3.12)

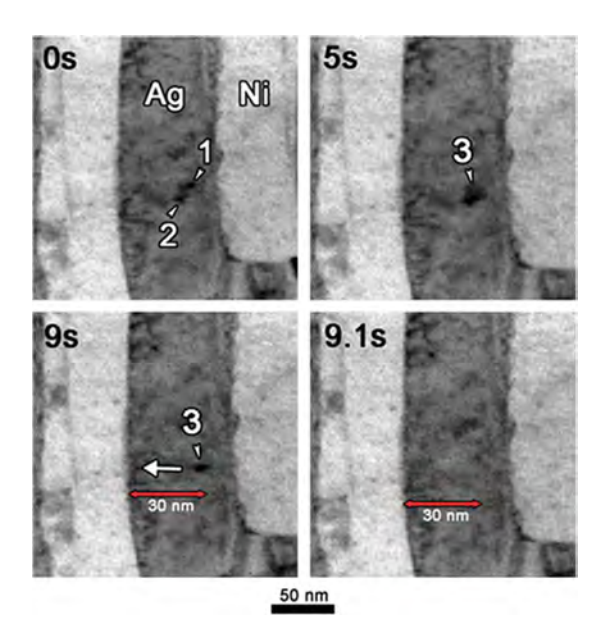


Fig. 3.1. In situ observation of dislocation loops absorption by layer interface over a dose range of 0.131-0.133 dpa $(0.262-0.266 \times 10^{14} \text{ ions/cm}^2)$. The loops are indicated by white arrows. Two loops nucleated at 0 s, then reached a quasi-steady state. They merged to form one larger dislocation loop, \sim 6 nm in diameter, by 5 s. The loop was stable until 9 s. Then within 0.1 s, the loop migrated left toward the layer interface and nearly disappeared. The big arrow indicates the migration trajectory [408]. Reprinted with permission from Ref. [408].

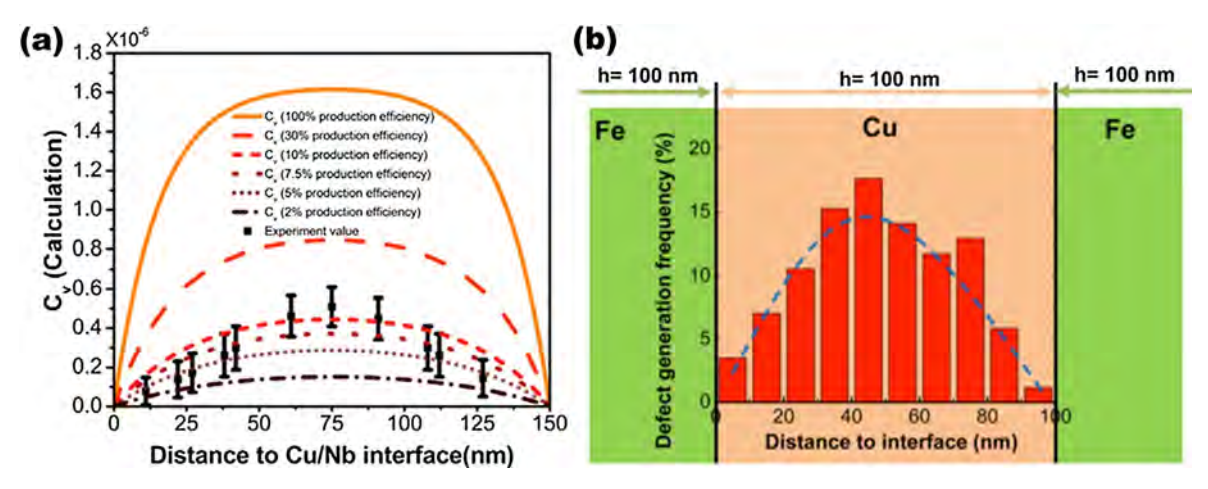


Fig. 3.2. (a) Sink strength of Cu/Nb nanolayers (from experiments): The local steady-state vacancy concentrations are plotted as functions of distance to the interface in the samples irradiated to 8×10^{14} ions/cm² at 300 °C along with the vacancy concentration profile calculated based on a steady-state rate equation and varying defect production efficiency [409]. (b) A statistical study on the accumulated frequency of defect clusters generated in Cu layers in 100 nm-thick Cu/Fe nanolayers acquired during *in situ* Cu ion irradiation (3MeV) in TEM (0.25–0.31 dpa in 160 s). Fewer defects are identified near the Cu/Fe interfaces during irradiation. The defect-generation frequency reaches a maximum in the center of the Cu layers. The dashed line is a visual guide delineating the defect cluster-concentration profile [410]. Reprinted with permission from Ref. [409,410].

When $k_{sc}h \rightarrow 0$, it evolves to:

$$k_h^2 = \frac{k_{\rm sc}^2}{\frac{1}{n} + \frac{k_{\rm sc}^2 h^2}{2n} - 1}$$
(3.13)

Note that when η is considered, although the formula for sink strength becomes much more complicated, the general trend remains the same; that is, sink strength increases with increasing η . When $\eta \to 1$, the equation reduces to a format similar to (Eq. (3.6)):

$$k_h^2 = \frac{12\eta}{h^2} \tag{3.14}$$

where η is large for incoherent, immiscible layer interfaces with high interfacial energies, and small (but > 0) for coherent, miscible layer interfaces with low-to-intermediate interfacial energies. In addition, η for layer interfaces may evolve with irradiation time/fluence as the characteristics of layer interfaces may continuously change during irradiation [231].

3.2. Phenomena of defect-interface interactions

Before examining the detailed mechanisms of how layer interfaces interact with radiation-induced defects, several experimental observations are presented first to show that such intimate interactions do exist in irradiated nanolayers.

3.2.1. In situ studies on absorption of radiation-induced defects by layer interfaces

In spite of extensive studies on radiation damage in metallic nanolayers, *in situ* evidence showing defect-interface interactions in real time remains scarce. Room temperature *in situ* Kr ion irradiation experiments were employed by Yu et al. to investigate the role of Ag/Ni interfaces in absorbing radiation-induced defects [408]. As shown in Fig. 3.1, a radiation-induced dislocation loop migrated towards the immiscible Ag/Ni layer interface during irradiation, followed by its absorption at the layer interface. Note the sputtered Ag/Ni has immiscible incoherent FCC/FCC layer interface in this study. Assuming that the absorption of the mobile interstitial loop is attracted and annihilated by a vacancy loop at the layer interface, the interactive energy between these two defect clusters is estimated to be \sim 0.4 eV [408].

3.2.2. Layer interface effect: distance dependent defect concentration profile

In principle, since layer interfaces can act as defect sinks, defect concentrations near interfaces are anticipated to be lower than that away from the interface. To validate this hypothesis, recently, Mao et al. proposed a method to estimate the local vacancy concentration in Cu layer near immiscible incoherent Cu/Nb interface [409]. Fig. 3.2a shows the parabolic profile of the local steady-state vacancy concentration plotted as a function of distance to the layer interfaces, implying that the Cu/Nb interface is an efficient defect sink. Similar effect is observed in an immiscible Cu/Fe nanolayers by *in situ* Cu ion irradiation experiment (Fig. 3.2b). The evolution of defect clusters under irradiation has been quantified in real time. An increase in

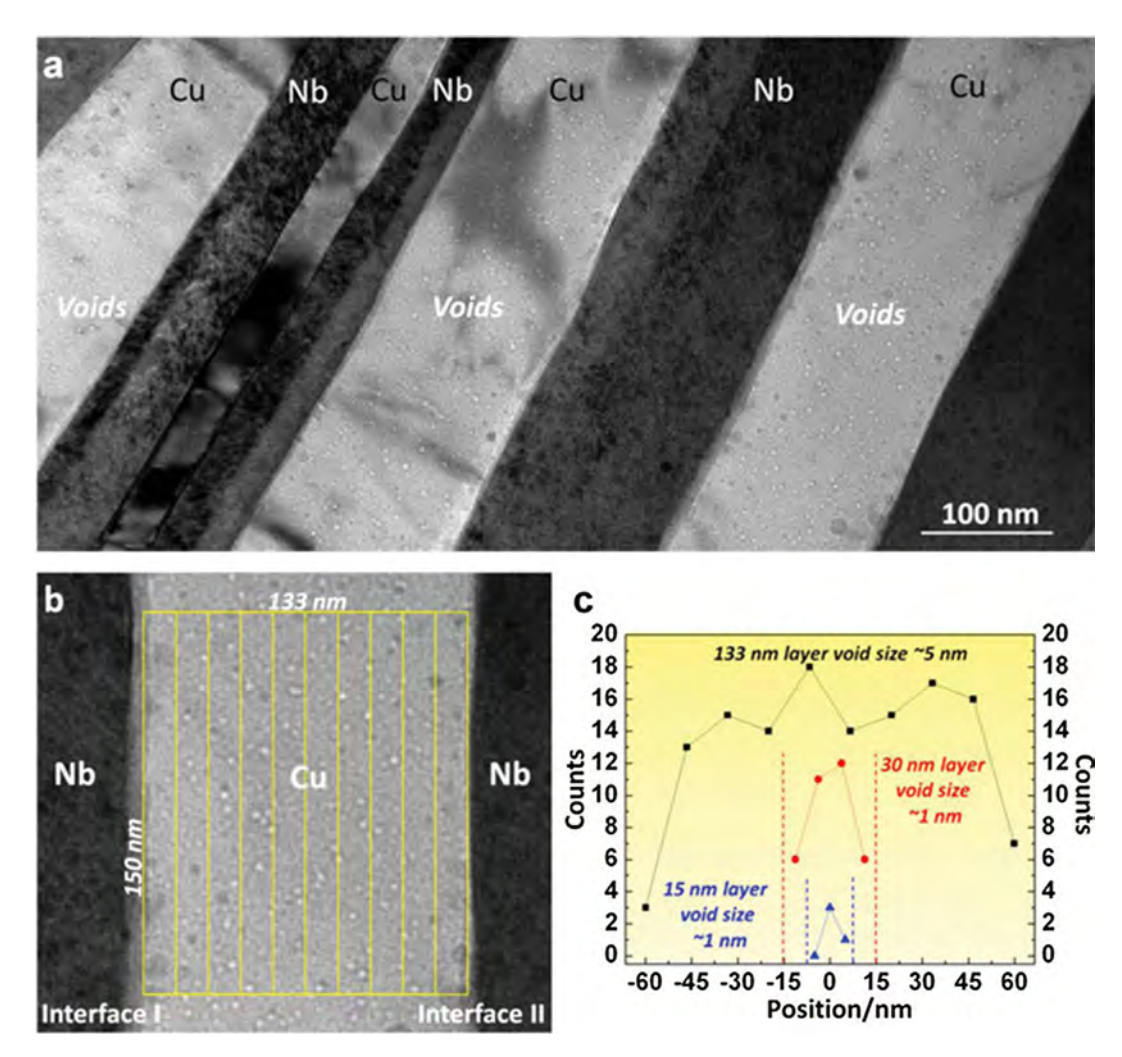


Fig. 3.3. Interface affected zone in He ion irradiated Cu/Nb nanolayers. (a) He ion irradiation-induced voids in Cu layers in irradiated Cu/Nb with 135 nm individual layer thickness. (b) Illustration of the method of determining the void number densities in the Cu layers. (c) Void number density plotted as functions of distance from the center of the layer in 133-nm-, 30-nm-, and 15-nm-thick Cu layers [411]. Reprinted with permission from Ref. [411].

defect-generation frequency is observed further away from the Cu/Fe layer interfaces and the defect-generation frequency reaches a maximum near the center of the Cu layers [410].

3.2.3. Layer-thickness-dependent defect concentration

According to Eq. (3.13), a smaller h leads to higher sink strength. The corresponding mean defect concentrations in layers are expected to be lower as well. The He ion irradiated Cu/Nb nanolayers (in Fig. 3.3) showed layer-thickness-dependent void distribution (i.e., He bubble) [411]. Meanwhile, a void depleted zone was identified at the interface. Similar scenarios have been studied by He ion and proton irradiation in immiscible Ag/Ni nanolayers [30].

3.2.4. He bubble denuded zones near layer interfaces

As shown in preceding section, defect concentrations near interfaces are reduced in comparison to the steady-state concentrations in the layer interiors. When the local vacancy concentration is less than the critical concentration needed for void nucleation, a defect denuded zone may form near the interface [412]. Fig. 3.4 shows a clear He bubble denuded zone in He ion irradiated SiOC/Fe multilayers [413].

3.3. Size effect on mitigation of radiation damage in nanolayers

The initial motivation for investigating on radiation damage in nanolayered composites hinges on the hypothesis that certain types of layer interfaces can absorb radiation-induced defects, and thus alleviate radiation damage [396,414]. The

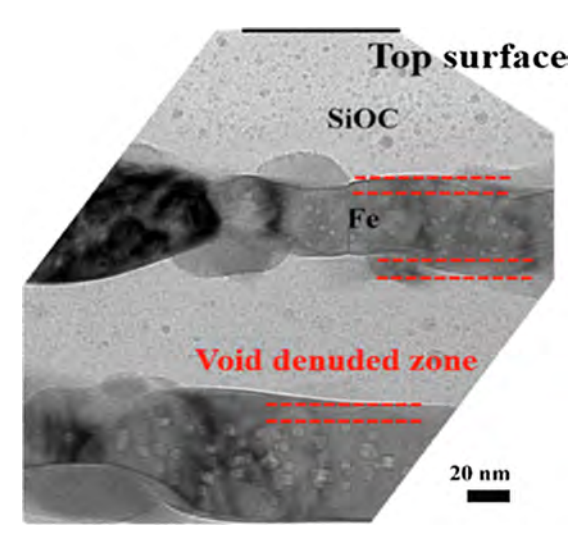


Fig. 3.4. He bubble denuded zone in a He ion irradiated SiOC/Fe multilayer. A typical cross-sectional TEM image showing the formation of nanovoids (He bubbles) in the SiOC/Fe multilayer irradiated to 10.7 dpa at 600 °C [413]. Reprinted with permission from Ref. [413].

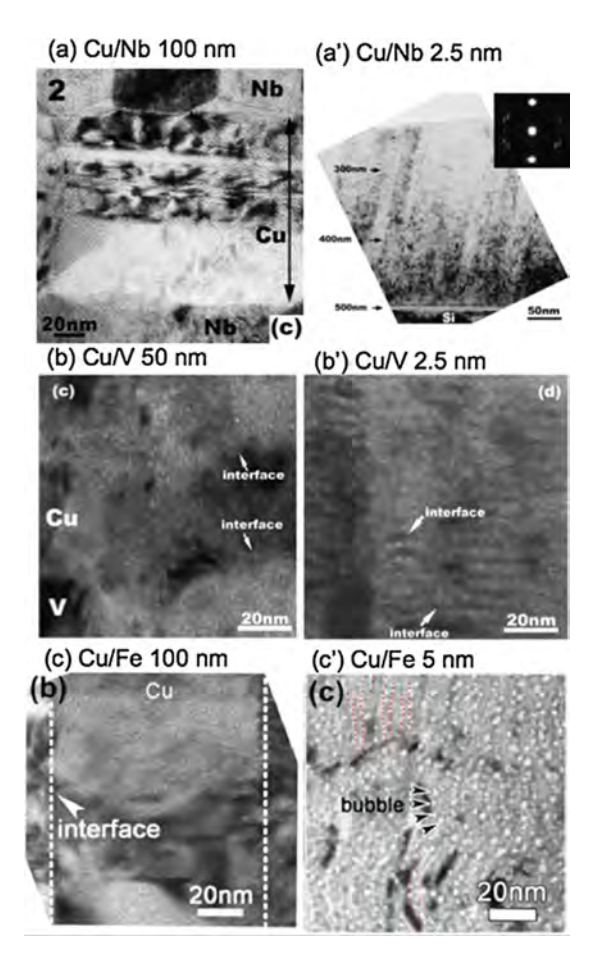


Fig. 3.5. Several FCC/BCC multilayer systems showing that layer interfaces can suppress He ion irradiation damage. Cross-section TEM micrographs of several FCC/BCC nanolayer systems showing clear size effect (layer-thickness-dependent evolution of He bubble density) (a, a') Cu/Nb [414], (b, b') Cu/V [123] and (c, c') Cu/Fe [451]. In general, He bubble density is much lower in nanolayers with smaller h. Reprinted with permission from Refs. [123,414,451].

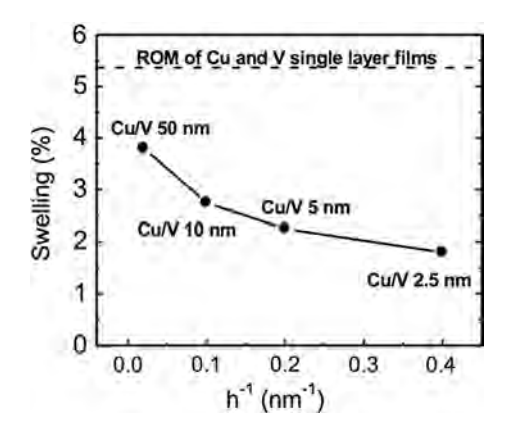


Fig. 3.6. Size effect of He bubble induced swelling (measured from step height) in Cu/V nanolayers [123]. Swelling in He ion-irradiated Cu/V nanolayers with various individual layer thicknesses (h) shows a continuous swelling reduction with decreasing h. The rule-of-mixture (ROM) swelling in irradiated Cu and V single layer films is also shown by the horizontal dashed line. Reprinted with permission from Ref. [123].

studies on radiation damage in nanolayer systems can be classified as either sink efficiency or sink strength based. As pointed out in [415], sink efficiency describes the ability of a single, specific interface to absorb defects from neighboring grains, which is related to interface features such as misfit dislocation patterns at the interface; while sink strength describes the net effect of defect traps (distributed throughout the material) on the average (radiation-induced) defect concentration [402]. Thus it is often accepted that sink strength may depend on the sink efficiency of the interface and the thickness of the layers (size dependence of the radiation damage) as described in Eqs. (3.13) and (3.14).

The influences of various types of interfaces on size-dependent radiation resistances have been studied in numerous nanolayer systems, including metallic nanolayers with FCC/BCC, FCC/FCC, BCC/BCC, BCC/HCP, and FCC/HCP interfaces, metal/amorphous, and metal/ceramics nanolayers. Among them, FCC/BCC systems have attracted significant attention both theoretically and experimentally. Thus, we will review more studies on the FCC/BCC systems, as such studies would also provide insights on radiation tolerance in other nanolayer systems.

The FCC/BCC systems reported in the literature include Cu/Nb (experiments [305,396,409,411,414,416–426] and modeling [407,427–442]), Cu/V [123,443,444], Cu/Mo [445,446], Cu/W [447–450], Cu/Fe [410,451], Ag/V [452], Ag/Ni [453], and Ni/Fe [454,455]. Different types of interfaces have various sink efficiencies. Most FCC/BCC systems explored experimentally show a clear trend that radiation damage is alleviated by decreasing *h*. Some examples in Cu/Nb [414], Cu/V [123] and Cu/Fe nanolayers [451] are shown in Fig. 3.5.

In general, layer interfaces promote the recombination of opposite point defects and hence reduce the accumulative radiation damage, such as defect (He bubble) densities and swelling. A systematic study on He bubble induced swelling in Cu/V nanolayers clearly shows continuous swelling reduction with decreasing h (Fig. 3.6) [123]. However, the derivation of the correlation between swelling and h from the simplified diffusion equation (Eq. (3.1)) is non-trivial. Other factors, such as the migration of other defects besides point defects (e.g. di-vacancies), and temperature-dependent vacancy-interstitial mutual recombination, must be considered to provide a better estimation of swelling. In addition, with increasing population of He bubbles generated inside layers, the bubble sink strength must be involved in the diffusion equation as well.

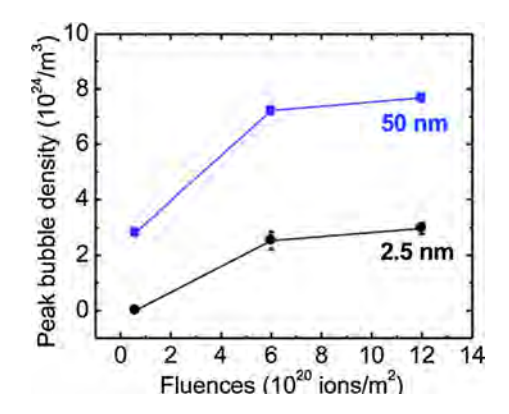


Fig. 3.7. The influence of fluence on the size-dependent radiation damage in Cu/V nanolayers. Peak He bubble densities, obtained from XTEM micrographs taken at the same under-focus distance of 400 nm, are plotted as functions of fluence for He ion-irradiated Cu/V 50- and 2.5-nm-thick nanolayers [444]. Reprinted with permission from Ref. [444].

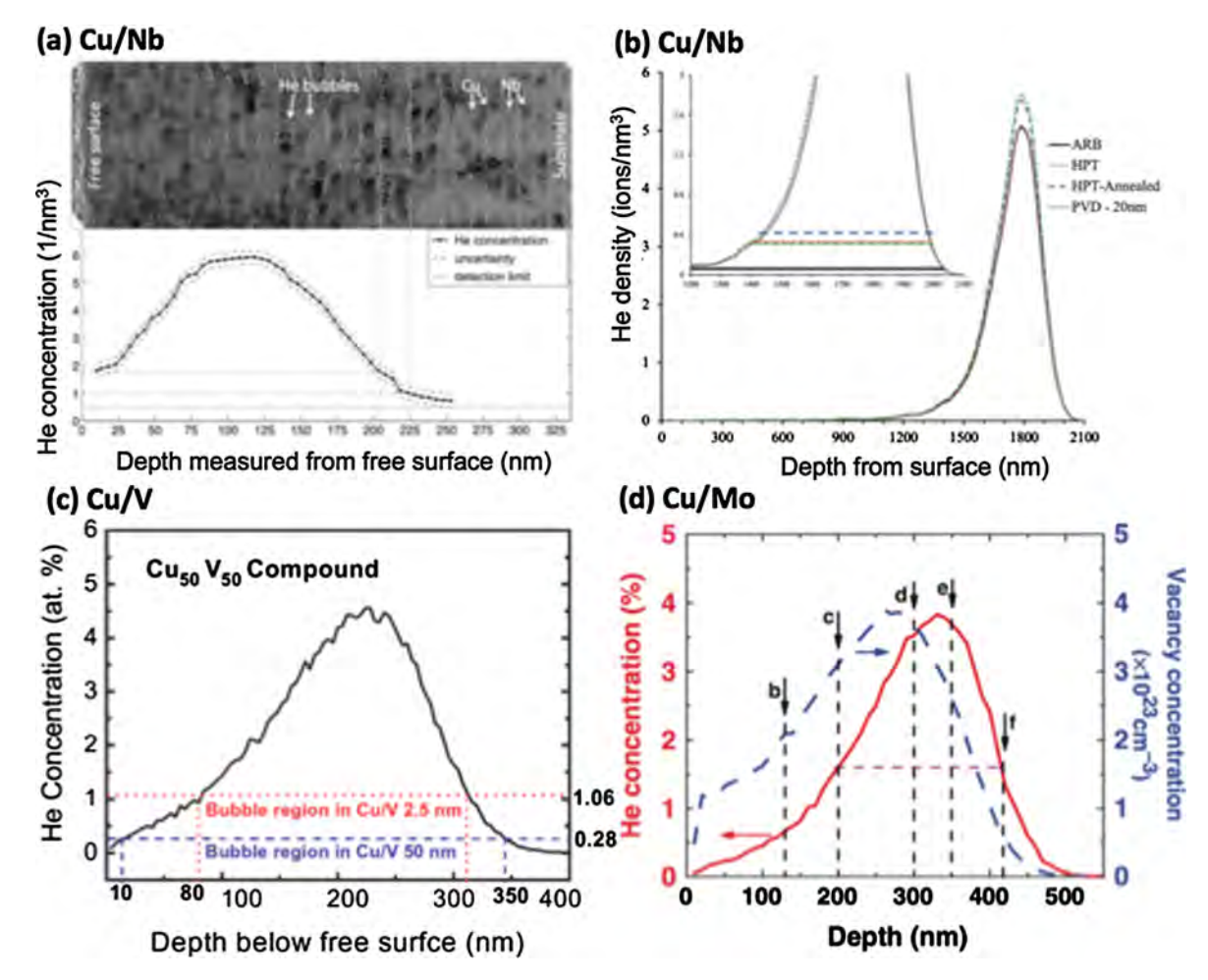


Fig. 3.8. Experimental evidence for the threshold He concentration forming He bubbles in several immiscible FCC/BCC nanolayers [123,424,430,445]: (a) Cross-sectional TEM image of He ion irradiated 5.6-nm-thick Cu/Nb nanolayer and the corresponding He concentration profile show that no He bubbles were detected in the surface region when the He concentration was <1.4/nm³ [430]. (b) The Cu/Nb nanolayers deformed by accumulative roll bonding or high-pressure torsion showed a similar phenomenon. The horizontal lines show the range where He bubbles were observed for each specimen [424]. (c) The minimum He concentration beyond which He bubbles were detectable in the 2.5-nm-thick Cu/V nanolayers was 1 at.%, ~4 times greater than that (0.26 at. %) in the 50-nm-thick Cu/V nanolayers [123]. (d) He (solid curve) and vacancy concentration (dashed curve) profiles of He ion irradiated 5-nm-thick Cu/Mo films. Note that although locations c and f have the same He concentration, but the vacancy concentration at c is much greater than at f [445]. Reprinted with permission from Ref. [123,424,430,445].

Although there are abundant studies on the size effect on radiation damage in nanolayers, research on the influence of fluence (dose) on the size-dependent radiation responses of nanolayers remains limited. Fu et al. demonstrated that the bubble density in He ion irradiated Cu/V nanolayers is strongly tied to the radiation fluence [444] (Fig. 3.7); that is, the magnitude of the peak bubble density increases with increasing (He ion) fluence before reaching saturation. Furthermore, the size effect on alleviation of radiation damage remains prominent in the fluence-dependent radiation studies.

3.4. Nature of interface on irradiation response of nanolayers

The roles of various interfaces in the alleviation of radiation damage have been studied in numerous nanolayer systems. Different interfaces exhibit various sink efficiencies. Three important interface characteristics (*i.e.*, misfit dislocation arrays, coherency stress, and miscibility) are highlighted here to uncover their respective influences on interface-defect interactions.

3.4.1. Incoherent immiscible interfaces: The influence of misfit dislocation arrays

As described in Section 1, radiation can induce the formation of various vacancy and interstitial clusters. When such clusters migrate to layer interfaces, they may dissociate into point defects and in turn modify interface structures simultaneously [428,456]. Layer interfaces promote the recombination of such vacancies and interstitials. However, He bubbles at interfaces are different as the inert gas atoms stabilize vacancy clusters at interfaces.

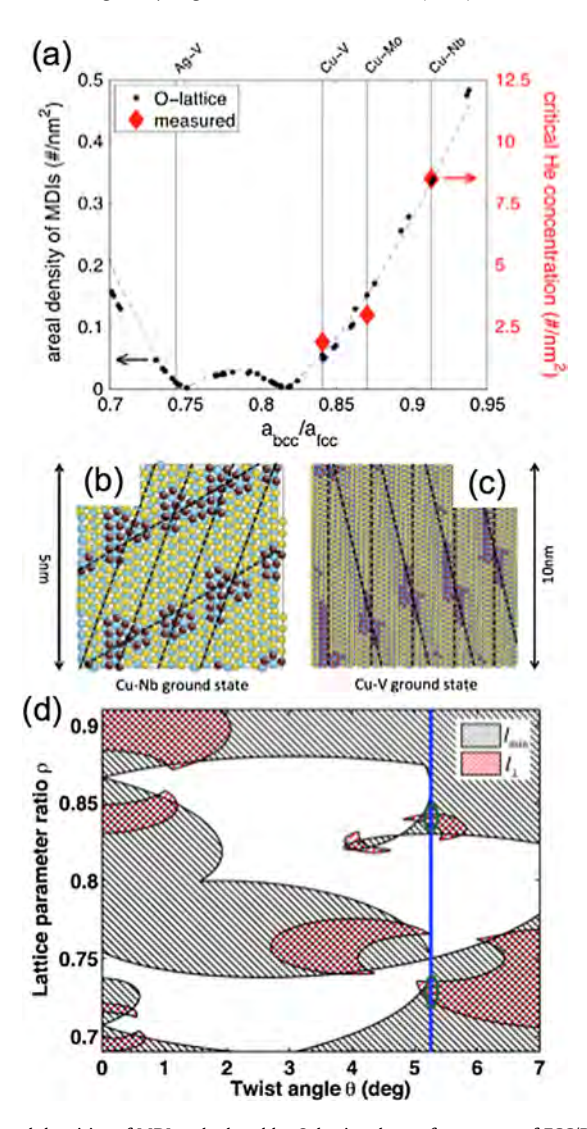


Fig. 3.9. (a) The black dots present the areal densities of MDIs calculated by O-lattice theory for a range of FCC/BCC pairs with different lattice parameter ratios, but identical interface crystallography (Kurdjumov–Sachs orientation relation and closest–packed interface planes). The red diamonds are critical He concentrations measured to detect He bubbles in TEM. The dashed line is a visual guide [302]. (b) and (c) show the MDIs in Cu/Nb and Cu/V interfaces. The dashed lines indicate interface misfit dislocations [302]; (d) To mitigate He ion irradiation damage (He bubbles), a new approach for designing interfaces is proposed to promote precipitation of He into continuous linear channels. The solution space for this new design is the intersection of envelopes. The vertical blue line at $\theta \approx 5.26^\circ$ denotes interfaces synthesized by PVD. The ovals highlight the intersection of the solution space with this line [440]. Reprinted with permission from Refs. [302,430,440].

He is a byproduct of neutron capture (n,α) reactions. As He solubility in most metals is extremely low [457–459], He tends to migrate and get trapped by defects. For instance, He can rapidly combine with vacancies and their clusters to reduce their formation energy, leading to the formation of He bubbles. Pressurized He bubbles may grow continuously to become voids and eventually embrittle irradiated materials [437]. At least two strategies have been applied to delay the transformation of He bubbles into voids and extend the lifetime of irradiated materials: (1) maximize the critical diameter beyond which He bubbles transform into voids, or (2) increase the number density of stable He bubbles by maximizing the number of He bubble nucleation sites [415]. The interests of introducing nanolayers with high-density interfaces to manage He bubbles arise from the assumption that certain layer interfaces can store He atoms and provide abundant nucleation sites for He bubbles, especially when h is only a few nm.

3.4.1.1. Threshold He concentration. The hypothesis of He storage at layer interface was proposed in 2005 [396]. It follows that there is a critical He concentration, below which, He atoms are distributed uniformly along layer interfaces without forming He bubbles. The hypothesis for the threshold He concentration forming He bubbles was later validated in He ion irradiated Cu/V [123], Cu/Nb (synthesized by sputtering [430] and accumulative roll bonding [424]), and Cu/Mo [445] nanolayers via nuclear reaction analysis and through-focus cross-sectional TEM studies (Fig. 3.8).

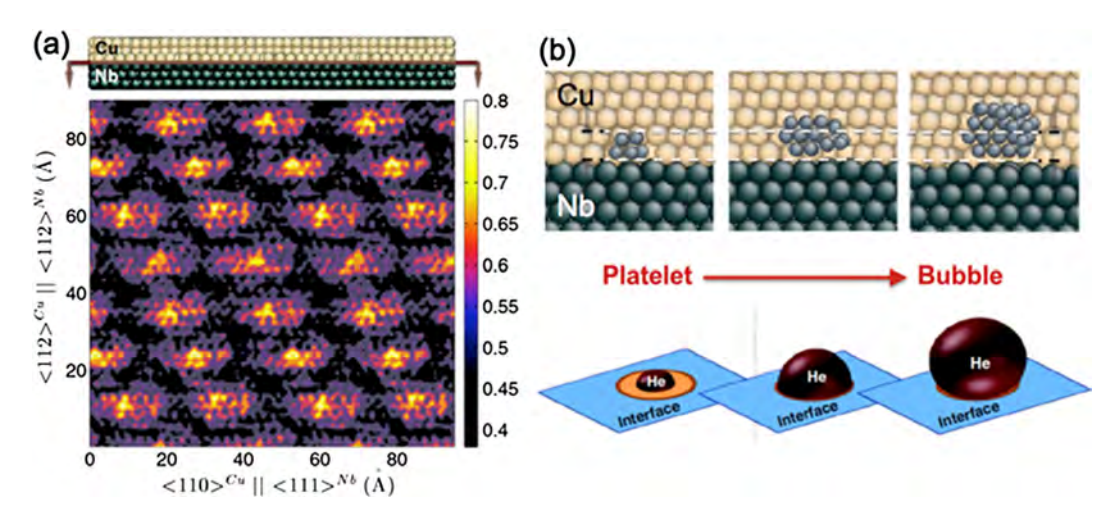


Fig. 3.10. He platelet-to-bubble transition at Cu/Nb interface: (a) Location dependence of γ_{CuNb} (J/m²), looking normal to the interface plane. Patches of the highest energy coincide with MDIs. (b) Atomistic modeling of the evolution of He-vacancy clusters at an MDI at a Cu/Nb interface. The clusters initially grow as flat platelets by wetting regions of high interface energy. Later, the He platelet transforms into a more equiaxed precipitate above approximately 20 He atoms [435]. Reprinted with permission from Ref. [435].

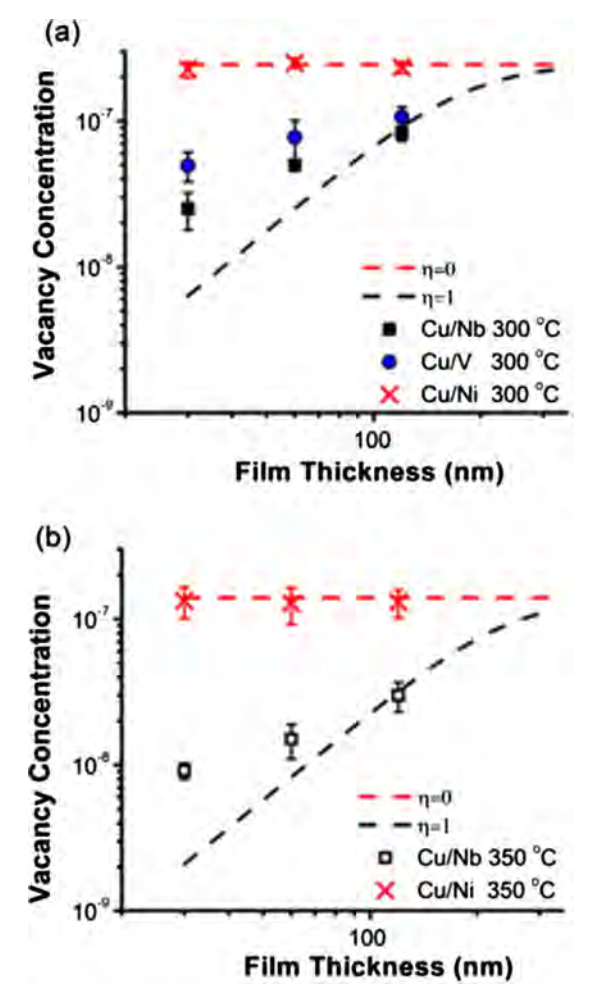


Fig. 3.11. Vacancy concentrations at the film center plotted as functions of film thickness measured at (a) 300 °C and (b) 350 °C. Trends calculated for the bounding sink efficiencies of η = 0 and η = 1 are plotted as guides, assuming a defect production efficiency of 1% [426]. Reprinted with permission from Ref. [426].

When converted into the number of He atoms per unit of interface area, the critical concentrations at which He bubbles are observed in the sputtered and roll-bonded Cu/Nb, Cu/V and Cu/Mo are \sim 8.5 [430], \sim 1.1–5.8 [424], \sim 1.9 [123] and \sim 3 [415,445] atoms/nm², respectively. The different interfacial He storage capacities are ascribed to different densities of misfit dislocation intersections (MDIs) at interfaces, which will be discussed later.

Besides the He storage capacities of different interfaces, He/vacancy ratios can also affect the formation of He bubbles. As shown in Fig. 3.8d, the stopping and range of ions in matter (SRIM) simulation predicts that the He concentration in Cu/Mo nanolayers is identical at locations c and f. However, He bubbles clearly align along the layer interfaces at location f, but not at location c. A major difference is that location f near the tail of the irradiation zone has a much lower vacancy concentration than that in region c [445]. More vacancies trap more He atoms and form tiny He-vacancy clusters undetectable by TEM. At the tail of the irradiated zone, where the vacancy concentration is low, He can migrate readily to the layer interfaces instead of being captured by vacancies. Hence, He can combine with vacancies at the interface to nucleate bubbles.

3.4.1.2. Bubble nucleation. The nature of interfaces determines their He storage capacities. Several studies have reported that the misfit dislocation intersection (MDI) density dominates the density of He atoms stored at interfaces. Interfaces with a higher density of MDIs can store more He atoms, as shown in Fig. 3.9a–c. Information about MDIs can be obtained from atomistic simulations [428] or O-lattice theory [427,440]. For the same interfacial crystallography, misfit dislocation densities increase in the following order: Cu/V < Cu/Mo < Cu/Nb. From the known He storage capability, it can be calculated that each MDI can store \sim 25 He atoms in both Cu/Nb and Cu/V without forming a He bubble [302]. The extraordinary He storage capacity of these interfaces is far beyond expectations from the equilibrium solubility of He in metals. Motivated by this observation, Kashnath et al. studied the state of He atoms at interfaces and proposed a new class of He precipitates at interfaces: nanoplatelets [435].

He atoms near interfaces prefer to migrate towards interfaces and stay thereafter [437]. Among dislocation lines, MDIs and coherent structures (separated by misfit dislocations) at interfaces, MDIs are the favorite sites for He trapping, where He platelets form by wetting high-energy interface regions. As shown in Fig. 3.10, He platelets remain stable under irradiation up to \sim 20 He atoms. The clusters are two atomic layers thick, and they expand as flat platelets by increasing the interface areas they occupy, which is consistent with the previous experimental observation of \sim 25 atoms [435]. When the cluster sizes increase beyond 20 He atoms, however, the clusters grow by increasing their thickness one layer at a time while maintaining a constant area along the interface, forming 3D bubbles. Thus, stable storage of He atoms at interfaces leads to less He-induced swelling prior to bubble/void formation as the volume of such platelets is nearly three times smaller than that of bubbles in FCC Cu.

He platelet-to-bubble transitions are driven by a competition among three pressures acting on interfacial He-filled cavities [154,421,435]: the mechanical pressure (P_{He}) of the trapped He gas, the osmotic pressure (P_V) due to the flux of radiation-induced vacancies to the cavity, and the capillary pressure (P_C) arising from the surface energy of the cavity. P_{He} and P_V tend to expand the cavity while P_C tends to shrink it. If the three pressures are balanced, *i.e.*:

$$P_{He} + P_V = P_C \tag{3.15}$$

then the cavity is in equilibrium; that is, it neither expands nor contracts [154]. Platelets have higher capillary pressures than spherical bubbles, which balances the mechanical and osmotic pressures. However, when a platelet grows beyond the "heliophilic" interface region and reaches the surrounding "heliophobic" interface region, the capillary pressure drops and the He platelet tends to transform into a spherical He bubble.

With the understanding of the role of MDIs, Yuryev and Demkowicz [440] developed a solution space (Fig. 3.9d) to search for an optimized interface design that allows the bubbles to connect in one direction, forming bubble channels sufficiently separated such that they do not interact with each other in the other direction. This approach can be achieved by tuning two parameters that influence MDI distributions: the ratios of cubic lattice parameters of the neighboring crystals, and the twist angle describing the relative rotations of crystals parallel to the interface plane. The essential idea of this study lies in the hypothesis that He atoms can migrate out of the material through such bubble channels instead of forming large bubbles/voids [460]. Therefore, the design of dislocation patterns at interfaces becomes an important topic [439,461].

Another interesting experimental study on the sink efficiencies of different interfaces is shown in Fig. 3.11. Significant variations in interfacial Cu vacancy sink efficiencies (η) were measured for interfaces including approximately ideal Cu/Nb sinks with Kurdjumov-Sachs (KS) (η > 0.9) interfaces, a moderate Cu/V sink with KS interfaces (η \approx 0.9), and an ineffective heteroepitaxial Cu/Ni sink (η < 0.5) [426]. The trend is qualitatively consistent with predictions from MD simulations, that is the average point defect absorption probability should be the highest for the Cu/Nb interfaces and the lowest for the Cu/Ni interfaces [433].

3.4.2. Immiscible coherent interfaces: The Influence of coherency stress

Prior studies on radiation damage in nanolayers suggest that incoherent interfaces with high-density misfit dislocations and MDIs are more efficient in alleviating radiation damage. One piece of supporting evidence is that coherent twin boundaries in NT Cu without misfit dislocations do not reduce the density of He bubbles compared to He ion irradiated single-crystal Cu [462]. However, as will be shown extensively in Section 4, NT metals have outstanding radiation tolerance as TBs are effective defect sinks. Furthermore several studies show that immiscible coherent interfaces may also play a positive role in mitigating radiation damage. He ion irradiated (1 0 0) Cu/Co with a coherent FCC/FCC interface [463] shows a clear

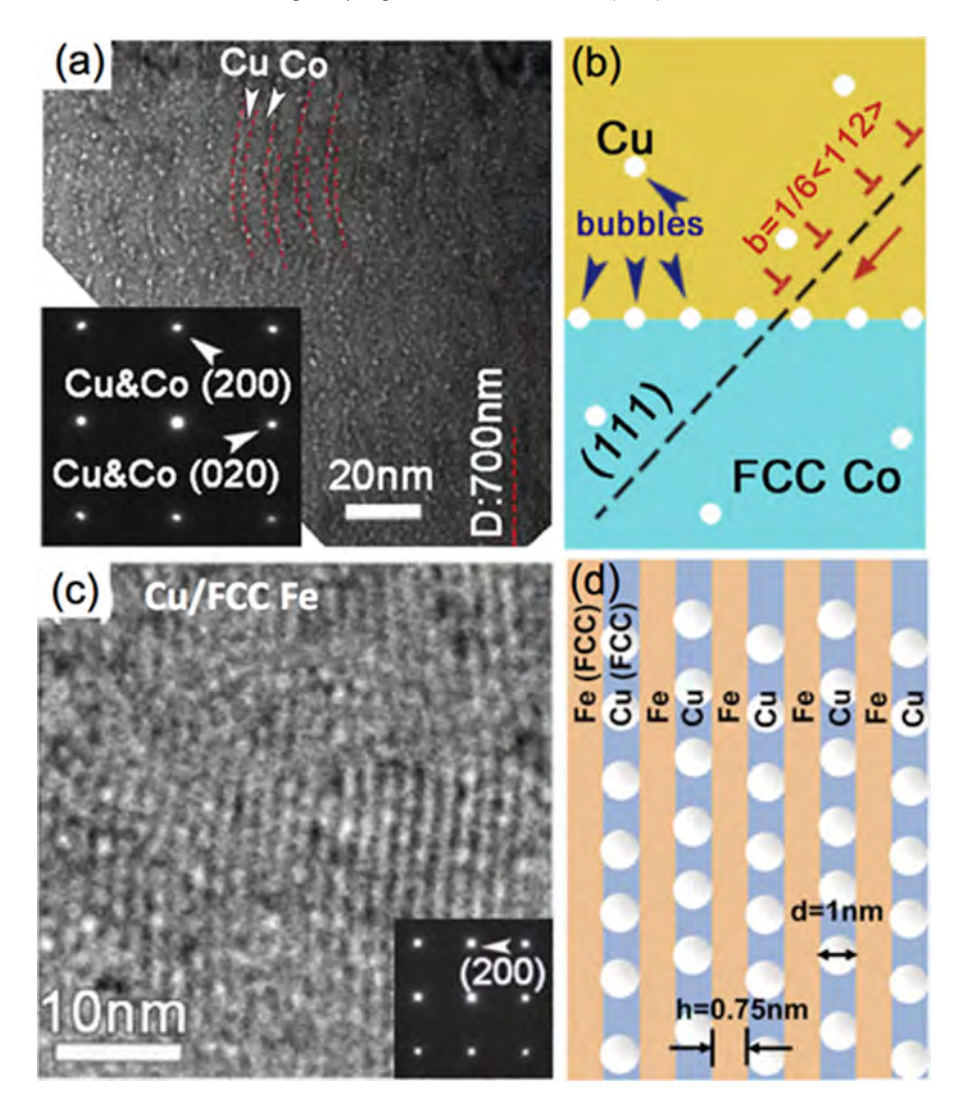


Fig. 3.12. (a and b) XTEM image and schematics showing clear alignment of He bubbles along layer interfaces in He ion irradiated immiscible coherent 5-nm-thick Cu/Co nanolayers. The embedded SAD pattern shows that the film retains epitaxial structure with a fully coherent FCC (1 0 0) Cu/ Co interface [463]. (c and d) The fully coherent FCC Cu/Fe interface in 0.75-nm-thick Cu/Fe nanolayers subjected to He ion irradiation to 2.5 dpa. He bubbles prefer to nucleate in Cu layers and are constricted to reside inside the Cu layers, resulting in smaller bubbles than those in other Cu/Fe nanolayers with larger h [451]. Reprinted with permission from Ref. [451,463].

size dependence. He bubbles nucleate and align along the coherent Cu/Co interfaces (Fig. 3.12a and b), presumably due to the following reasons. First, the interaction between radiation-induced defects and coherent interfaces may create disconnections at interfaces, which serve as defect sinks. Second, the coherency stress may promote defect migration towards layer interfaces [442]. Third, the coherent Cu/Co interface may inhibit bubble growth, similar to the radiation response of incoherent interfaces. In fully coherent immiscible 0.75-nm-thick FCC Cu/Fe nanolayers [451], He bubbles nucleate and align within the Cu layers (Fig. 3.12c and d). The alignment of abundant He bubbles inside the Cu layers consumes a large amount of He atoms and vacancies, and the interface confinement prohibits the coarsening of He bubbles, thus suppressing the formation of voids. The alignment of He bubbles in narrow nanolayers is, to some extent, similar to the construction of directional He storage/transportation channels for storing more He atoms by reducing the MDI spacing in one direction [440].

Recently, Vattre et al. proposed that the reduced defect migration energies/barriers near interface might be primarily responsible for the enhancement in sink strength, inducing a preferential drift of point defects toward interfaces [442]. As shown in Fig. 3.13a and b, the reduced defect migration barriers arise from the elastic stress field in the layered structure. The sink strength of interface for both vacancies and interstitials in elastic interaction (blue line in Fig. 3.13c and d) are significantly higher than those not in elastic interactions (orange line in Fig. 3.13c and d). Furthermore, the recombination of vacancies and interstitials could also be promoted by the emission of interstitials from the interface into layer interior [434], which is similar to another observation near GBs [183].

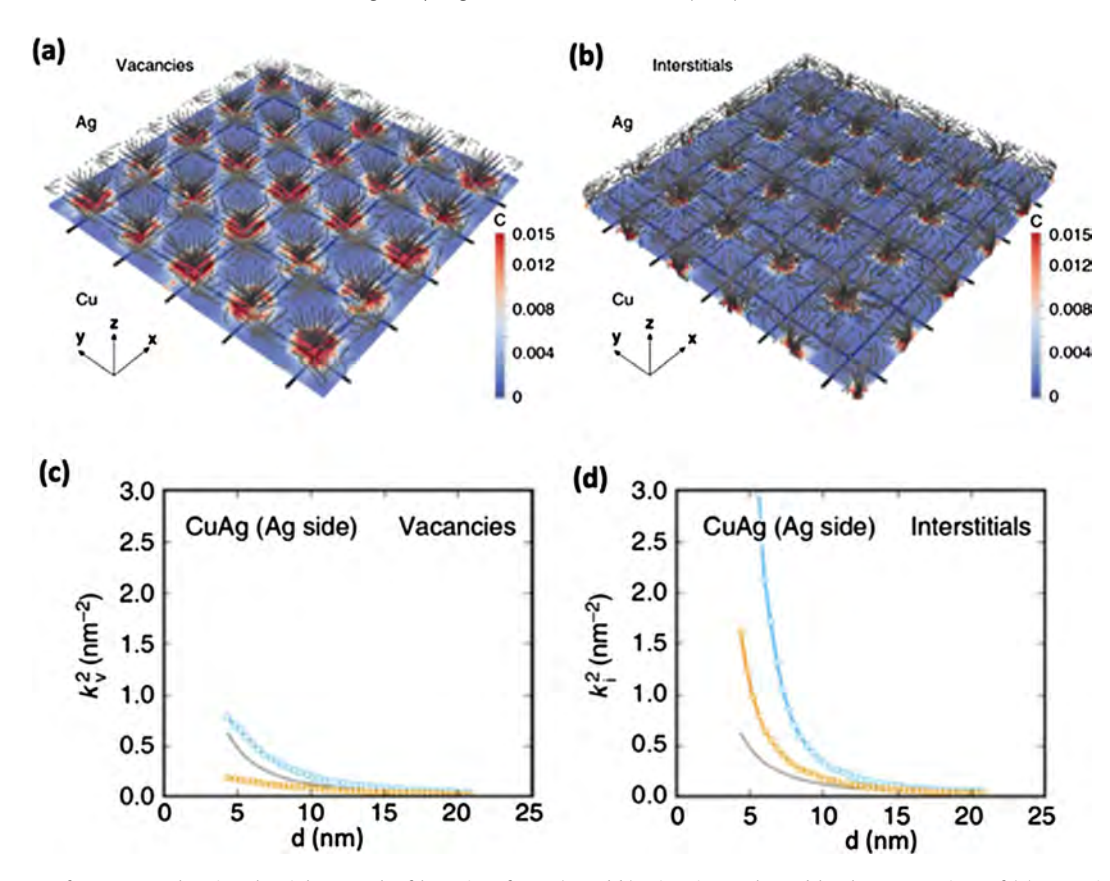


Fig. 3.13. Interface stress enhancing the sink strength of layer interfaces: (a and b) Migration paths and local concentrations of (a) vacancies and (b) interstitials on the Ag side of the semicoherent Ag–Cu interface. Migration paths, shown as grey lines, originated 1 nm away from the interface. The square grid of black lines represents interface dislocations. The normalized concentrations of point defects are plotted in a plane located two atomic distances away from the interface. Any normalized concentration values higher than 0.015 are shown equal to 0.015. (c and d) Enhanced sink strength of semicoherent interfaces. Sink behaviors of Ag–Cu interfaces for (c) vacancies and (d) interstitials in Ag are plotted as functions of layer thickness, d. Orange and blue lines correspond to the object kinetic Monte Carlo (OKMC) calculations without saddle point anisotropy and with the fully anisotropic interaction model, respectively [442]. Reprinted with permission from Ref. [442].

3.4.3. Miscible layer interfaces: radiation-induced intermixing

Immiscible nanolayer systems retain layer interfaces under radiation as the positive heat of mixing between the layer constituents thermodynamically drives demixing to maintain chemically distinct layer interfaces during irradiation or annealing. In contrast, irradiation of miscible nanolayer systems can induce significant interdiffusion (e.g. Cu/Ni [464]), resulting in the formation of intermetallics (e.g. Al/Nb [465], Al/Ti [466,467] and Fe/W [468]) or amorphous structures (e.g. Ni/Ti [469,470]). Taking the Al/Nb nanolayer as an example [465], Fig. 3.14 shows the chemistry of the layer interface in the surface, peak damage and nonirradiated regions of He ion irradiated Al/Nb nanolayers. The peak damage region clearly shows interdiffusion between Al and Nb, forming intermetallics at interfaces.

3.5. Alternative mechanisms of reducing defect densities in nanolayers

The role of interfaces is not just limited to the annihilation of defects at layer interfaces. The sandwiched layers can provide a sweeping channel for dislocations to annihilate opposite defects. *In situ* TEM snapshots have captured one such defect annihilation process in Fe/Fe₂Zr nanolayers [471]. Dislocation loop A (outlined in the circle in Fig. 3.15a) nucleated at 0.755 dpa migrated until it encountered and annihilated loop B within the same layer. The Fe₂Zr layers have become amorphous after only slight irradiation and the crystal/amorphous layer interface confines the migration of dislocation loops within the Fe layers. It remains unclear if such a mechanism may also operate in other multilayer systems. Further studies on radiation damage in multilayers with crystal/amorphous interfaces are necessary to substantiate such a mechanism.

3.6. Radiation damage in ceramic nanolayers: Amorphization and nanocrystallization

Radiation damage in ceramic nanolayers is a complex subject owing to the complicated structures of oxide compounds, the higher bonding energies of ceramics, electrostatic effects, and the preference for preserving stoichiometries in

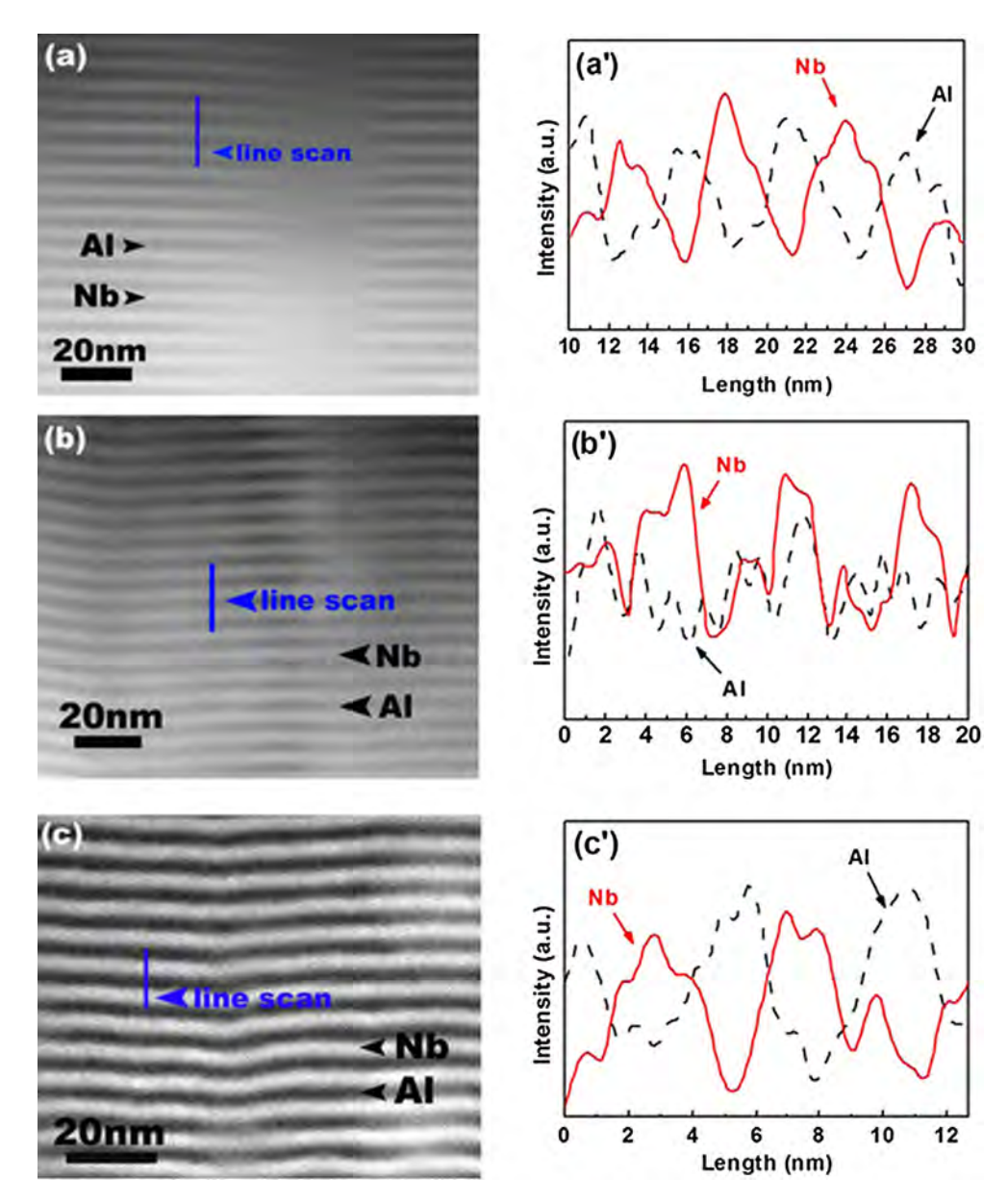


Fig. 3.14. STEM micrographs of He ion irradiated 2.5-nm-thick Al/Nb nanolayers at (a) surface, (b) peak damage, and (c) nonirradiated region. Distinctive layer interfaces are clearly resolved in all regions. Figures (a')–(c') show the corresponding composition analyses along line markers. Although modulated composition profiles are revealed in (a') and (c'), intermixing clearly occurs in region (b') [465]. Reprinted with permission from Ref. [465].

compounds [472]. Certain ceramic nanolayers, such as CrN/AlTiN [473,474] and TiN/MgO [475], can effectively remove radiation-induced defects, as layer interfaces can act as defect sinks, suppressing amorphization [476].

Amorphization is an important issue for the irradiated ceramics [477]. Some irradiated ceramics have a higher tendency toward amorphization than others [478]. For instance, the CeO₂/SrTiO₃ system [479] showed enhanced amorphization at interfaces because (1) layer interfaces act as biased sinks for different defects; that is, interface steps attract cation interstitials, leaving behind an excess of immobile vacancies, and (2) defects at interface steps induce significant structural and chemical distortions.

However, TiN/AlN nanolayers [476] showed suppressed amorphization in AlN layers and reduced irradiation-induced softening (Fig. 3.16). The nanolayers showed a clear size-dependent reduction in radiation damage. More specifically, when h = 10-20 nm, the TiN/AlN nanolayers showed the best He ion irradiation tolerance and a critical layer thickness of more than 5 nm, which is necessary to prevent severe intermixing. This study suggests that both the interface characteristics and the critical length scale (layer thickness) contribute to the reduction of the He ion irradiation-induced damage in nitride-based ceramic nanolayers. Note that prior studies have shown that polycrystalline AlN is resistant to radiation

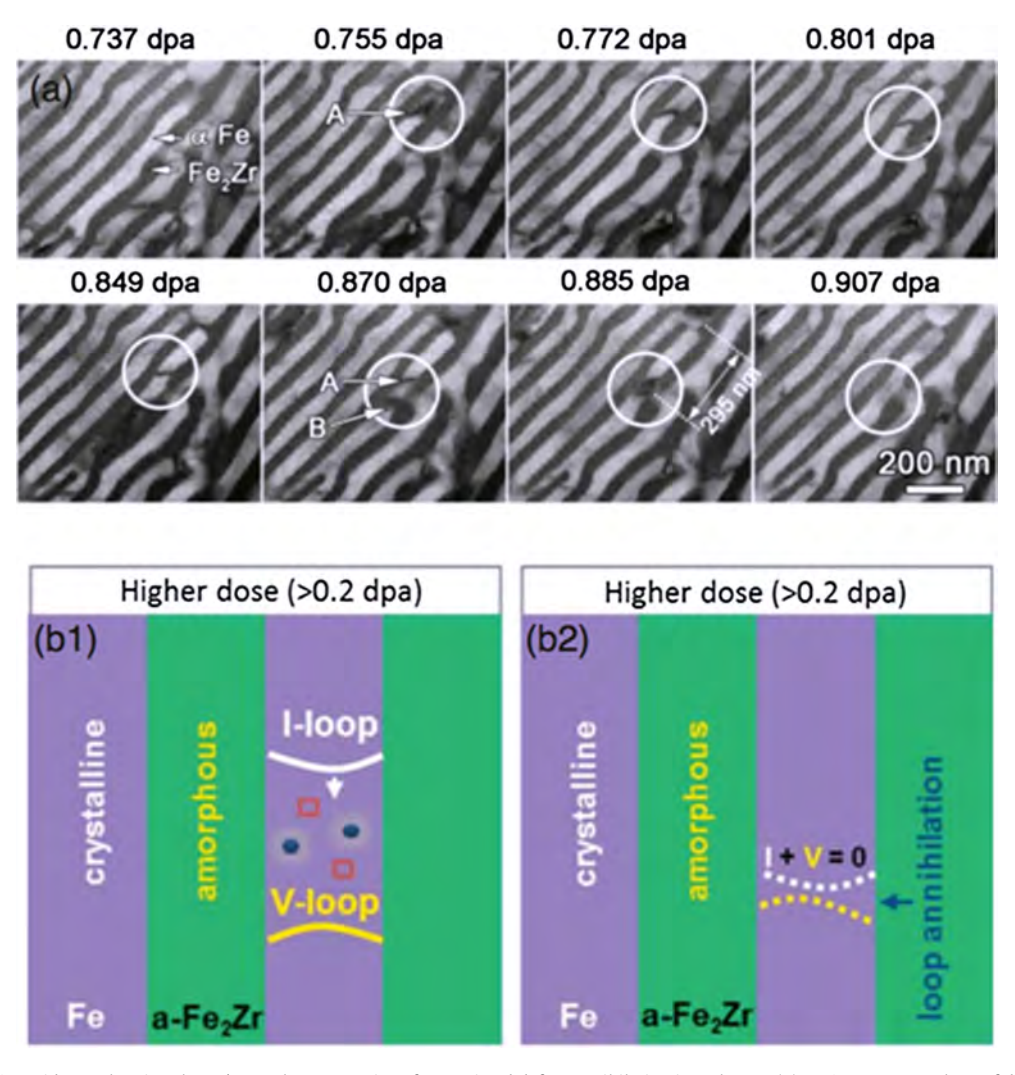


Fig. 3.15. In situ evidence showing the Fe/amorphous Fe₂Zr interface assisted defect annihilation in Fe layers. (a) In situ TEM snapshots of dislocation loop migration over a dose range of 0.737–0.907 dpa (over 70 s) in confined nanolaminates. At 0.755 dpa, dislocation loop A was generated and started to migrate within the α -Fe layer, as outlined by the circle. Loop A migrated over a distance of 295 nm by 0.885 dpa before it encountered loop B. The two loops then interacted and combined with each other. (b) Schematics of the defect removal mechanism illustrating the migration of dislocation loops in α -Fe channels confined by the crystal/amorphous layer interface and the recombination of opposite dislocation loops [471]. Reprinted with permission from Ref. [471].

induced amorphization under 700 MeV Bi ion irradiation [476]. Hence it is likely the amorphization resistance of AlN also depends on the types of ion source for radiation studies [480]. In addition, TiN/AlN nanolayers also have good radiation resistance against Ar [481,482] and Xe [483] ion irradiation to 92–127 dpa. Although the interfaces remain intact, radiation may lead to lateral grain growth in individual layers.

Uberuaga et al. [484] pointed out that the phases of layer constituents may influence the defect evolution during irradiation. They compared the radiation damage of SrTiO₃ (STO) coupled with three different oxides [478,485,486], forming nearly perfect coherent interfaces and discovered that, under similar irradiation conditions, the STO showed very different behaviors in the three systems (Fig. 3.17). BaTiO₃/STO did not show any amorphization, the STO side of STO/LaAlO₃ showed significant amorphization, and the TiO₂ side of TiO₂/STO showed the formation of a defect denuded zone at the interface. The drastic differences in the radiation response of the materials with same chemistry but different interfaces are surprising as atomistic modeling reveals that there are no thermodynamic trap states for defects at these interfaces (Fig. 3.17d). From these interesting observations, Uberuaga et al. hypothesized that the controlling parameters (which dictate the radiation responses of the materials) are the defect properties within the bulk phase and that the interfaces simply act as transition points between the two materials. Using a reaction-diffusion model, they demonstrated that the formation and migration energies of defects within each phase determine the eventual responses at the interface. The formation energies dictate the directions of the defect flows, while the migration energies determine the rates of the defect flows.

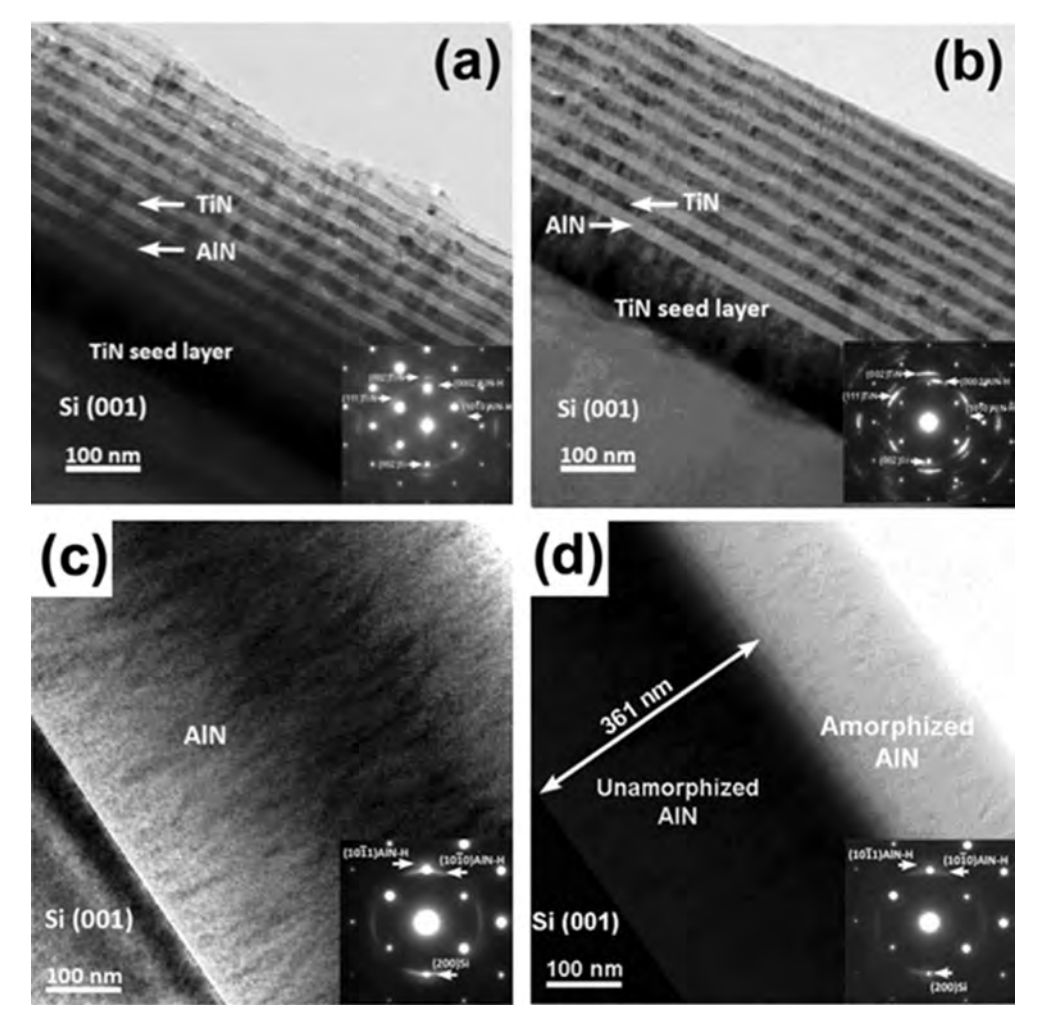


Fig. 3.16. Suppression of AlN amorphization in irradiated TiN/AlN layered structure. TEM micrographs and SAD patterns of (a) as-deposited and (b) He ion irradiated 20-nm-thick TiN/AlN nanolayers. No amorphization was detected in AlN layers. (c and d) In contrast, the He ion irradiated AlN single layer experienced obvious amorphization [476]. Reprinted with permission from Ref. [476].

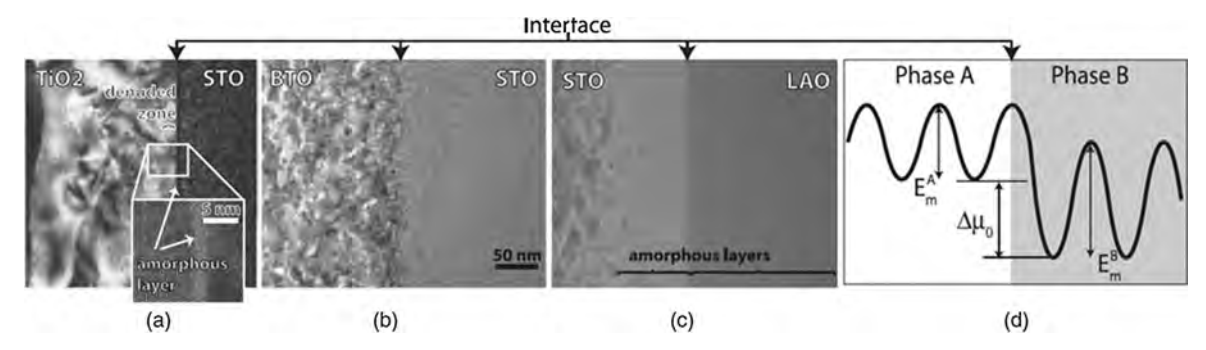


Fig. 3.17. Examples of irradiation responses of different oxide heterointerfaces [484]: (a) $TiO_2/SrTiO_3$, (b) $BaTiO_3/SrTiO_3$, and (c) $SrTiO_3/LaAlO_3$. In each case, the film thickness was between 250 and 300 nm and the irradiation conditions were chosen such that about 3-4 dpa occurred just below the interface. The energy of the implanted Ne and the total fluence were (left) 250 keV and 1.11×10^{16} ions/cm², (middle) 300 keV and 1.55×10^{16} ions/cm², and (right) 260 keV and 8.23×10^{16} ions/cm². The positions of the denuded zone and amorphous layers are labeled. The scale bar for all three images is the same. (d) A schematic of the typical energetic landscape for point defects, as determined from atomistic calculations. Details about these experiments and the corresponding atomistic calculations can be found in [484]. Reprinted with permission from Ref. [484].

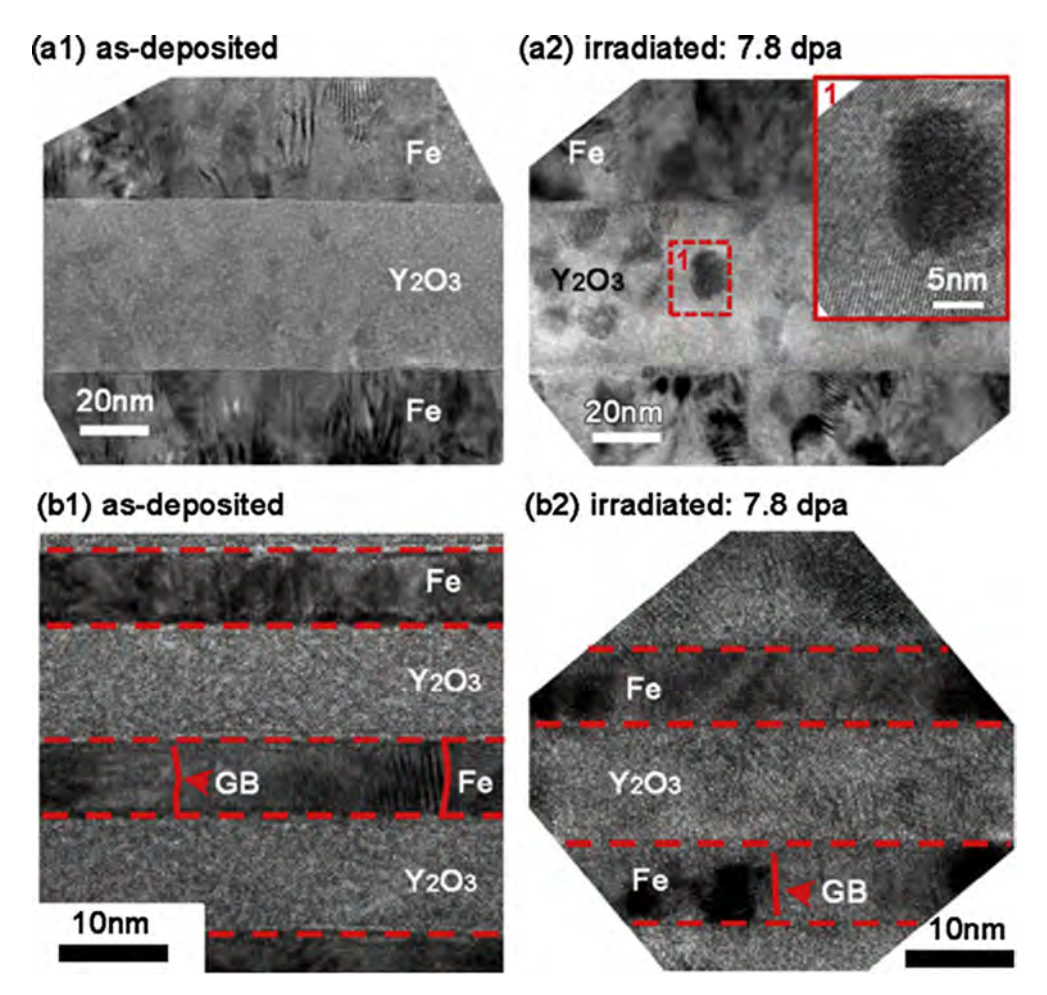


Fig. 3.18. Suppression of nanocrystallization in amorphous Y_2O_3 in Fe/ Y_2O_3 nanolayers [488]. *In situ* Kr ion irradiation studies (at room temperature) showing evidence of the suppression of crystallization in oxide layers by interfaces in Fe/ Y_2O_3 multilayers. Comparison of the microstructures of 50-nm-thick Fe/ Y_2O_3 and 10-nm-thick Fe/ Y_2O_3 nanolayers before (a1) and (b1) and after (a2) and (b2) Kr ion irradiation (up to 7.8 dpa). (a1) The as-deposited Y_2O_3 in the 50-nm-thick Fe/ Y_2O_3 nanolayer shows primarily an amorphous phase with some embedded nanograins. (a2) The subsequent irradiation of the 50-nm-thick Fe/ Y_2O_3 leaves to extensive crystallization in the 50-nm-thick Y_2O_3 layers. A typical nanograin is shown in the embedded HRTEM image. For 10-nm-thick Fe/ Y_2O_3 , the micrographs taken before (b1) and after (b2) the irradiation shows negligible variation in the microstructures of the Fe and Y_2O_3 layers. The Y_2O_3 in the irradiated 10-nm-thick Fe/ Y_2O_3 multilayer remains predominantly amorphous. Reprinted with permission from Ref. [488].

Meanwhile, in situ radiation experiments reveal the suppression of nanocrystallization in amorphous Y_2O_3 layers by the Fe/Y_2O_3 layer interface [487,488]. As shown in Fig. 3.18, after Kr ion irradiation to 7.8 dpa, the as-deposited amorphous Y_2O_3 in the 50-nm-thick Fe/Y_2O_3 nanolayer crystallizes, in contrast to very little crystallization in the 10-nm-thick Y_2O_3 layers, implying size-dependent enhancement of radiation tolerance [488]. Within the interface affected zones (\sim 10 nm), interfaces absorb radiation-induced defects and produce interfacial stress to mitigate radiation-induced crystallization.

3.7. Size effect on hardening in irradiated nanolayers

Radiation introduces significant microstructural damage in the form of drastic increases in defect density and in turn, prominent irradiation hardening. Irradiation hardening is manifested by increases in yield strength, hardness, and flow stress and is often accompanied by losses of toughness and ductility [489,490]. Hence, measuring irradiation hardening may be used as an indirect method of evaluating the influence of radiation damage on the deformabilities of irradiated materials. Most radiation experiments pertaining to this section were conducted by He or heavy ion irradiation, and thus the radiation damage resided in shallow surfaces (a few hundreds of nanometers to a couple of micrometers). Consequently, irradiation hardening in nanolayers is typically measured by nano/micro mechanical testing techniques, such as nanoindentation [491,492], and micropillar compression in SEM [418,425,491] and TEM [423]. Nanoindentation remains the most widely used method of probing irradiation hardening. Earlier systematic irradiation hardening measurements of the metallic

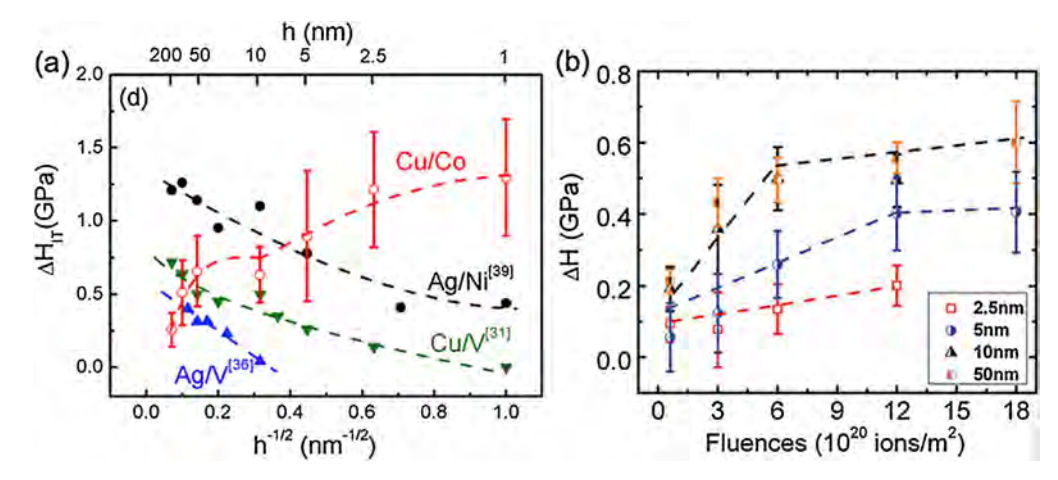


Fig. 3.19. (a) Less irradiation hardening in He ion irradiated Ag/V, Ag/Ni, Cu/V nanolayers with smaller *h* [463]. (b) Fluence dependence of irradiation hardening in He ion irradiated Cu/V nanolayers [444]. Irradiation hardening approaches saturation at lower fluences in multilayers with greater *h*. Reprinted with permission from Ref. [444,463].

nanolayers were performed on the He ion irradiated Cu/V system [443] prepared with various h and fluences, and the Cu/V system showed size-dependent irradiation hardening in which the magnitude of the irradiation hardening decreased with decreasing h (Fig. 3.19a). Correlated microscopy studies show that for multilayers with smaller h, the density of He bubbles is significantly reduced, and hence irradiation hardening in these fine nanolayers (primarily due to He bubbles) is expected to be less prominent than that in multilayers with greater h. This size dependent hardening phenomena have also been observed in a variety of other He ion irradiated nanolayers, including Ag/V [452] and Ag/Ni [463] (Fig. 3.19a). Notice that in these immiscible nanolayer systems with incoherent FCC/BCC or FCC/FCC interfaces, radiation hardening typically decreases in nanolayers with smaller h. Surprisingly, in He ion irradiated immiscible (100) FCC Cu/Co nanolayers with coherent interface, an opposite trend was observed: the magnitude of irradiation hardening increases with decreasing h [463]. In the as-deposited FCC Cu/Co nanolayers, mobile Shockley partials are the predominant plasticity carriers as both Cu and Co have low SFE. The peak strength of Cu/Co multilayers is determined by the interface barrier strength to the transmission of the partials. After He ion irradiation, however, He bubbles align preferentially along the Cu/Co layer interface. Consequently, the partials may have to undergo constriction (to become full dislocations) at the interface before transmission across the layer interface, leading to a significant increases in the yield strength of irradiated multilayers with smaller h [463]. There are a limited number of studies on dose- and size-dependent radiation damage in nanolayers. An example of He ion irradiated Cu/V nanolayers in Fig. 3.19b shows that irradiation hardening reaches saturation at lower fluence for multilayers with greater h [444].

Although nanoindentation is useful for probing irradiation hardening in irradiated nanolayers, it applies nonuniform stress and strain under the probe tip, thereby leading to the complication of interpreting plastic flow behavior. The development of the micropillar compression test technique has enabled new routes to acquire stress-strain curves from nominally uniaxial compression tests of small-volume specimens [493–495]. Li et al. studied compressive flow behaviors of He ion irradiated Cu/Nb nanolayers containing uniformly distributed He bubbles [418]. The flow stress of the irradiated Cu films increases by more than a factor of 2 owing to the introduction of high-density He bubbles (Fig. 3.20a). In contrast in He ion irradiated Cu/Nb nanolayers, the magnitude of irradiation-induced strengthening (increase in yield strength) was much less and decreased with decreasing h (Fig. 3.20c and d). When h decreases to 2.5 nm, the 2.5-nm-thick Cu/Nb nanolayer shows insignificant hardening and very little loss in deformability. SEM images of Cu/Nb 70 nm micropillars (in Fig. 3.20e) show the morphological evolution of the as-deposited and irradiated pillars before and after compression. The irradiation induced increase in shear strength has also been studied via *in situ* compression of Cu [496] and Cu-Nb alloy and Cu/Nb nanolaminate pillars in TEM [423].

The irradiation induced hardening mechanisms of nanolayers are complicated as they are not only determined by the type, dimension, and density of irradiation induced defect clusters, but also by h and the nature of layer interfaces. Before we discuss the details of the irradiation hardening in nanolayers, the mechanical behaviors correlated with various layer thicknesses will be briefly described. Generally, three regimes describe size-dependent strengthening in as-deposited nanolayers. (1) When h is large (typically > 50 nm), the strengthening depends on the pile-up of gliding dislocations, and thus follows the classical Hall-Petch strengthening model. (2) At intermediate layer thicknesses (when h = 10-50 nm), the flow strength of nanolayers is determined by the confined layer slip model, and typically follows the Orowan bowing mechanism. (3) When h is small (≤ 5 nm), the interface barrier strength for a single glide dislocation dominates the strength of the film (refer to Ref. [396] in the literature for more details). Thus, understanding the fundamental mechanisms of irradiation hardening in nanolayers should couple together multiple strengthening mechanisms.

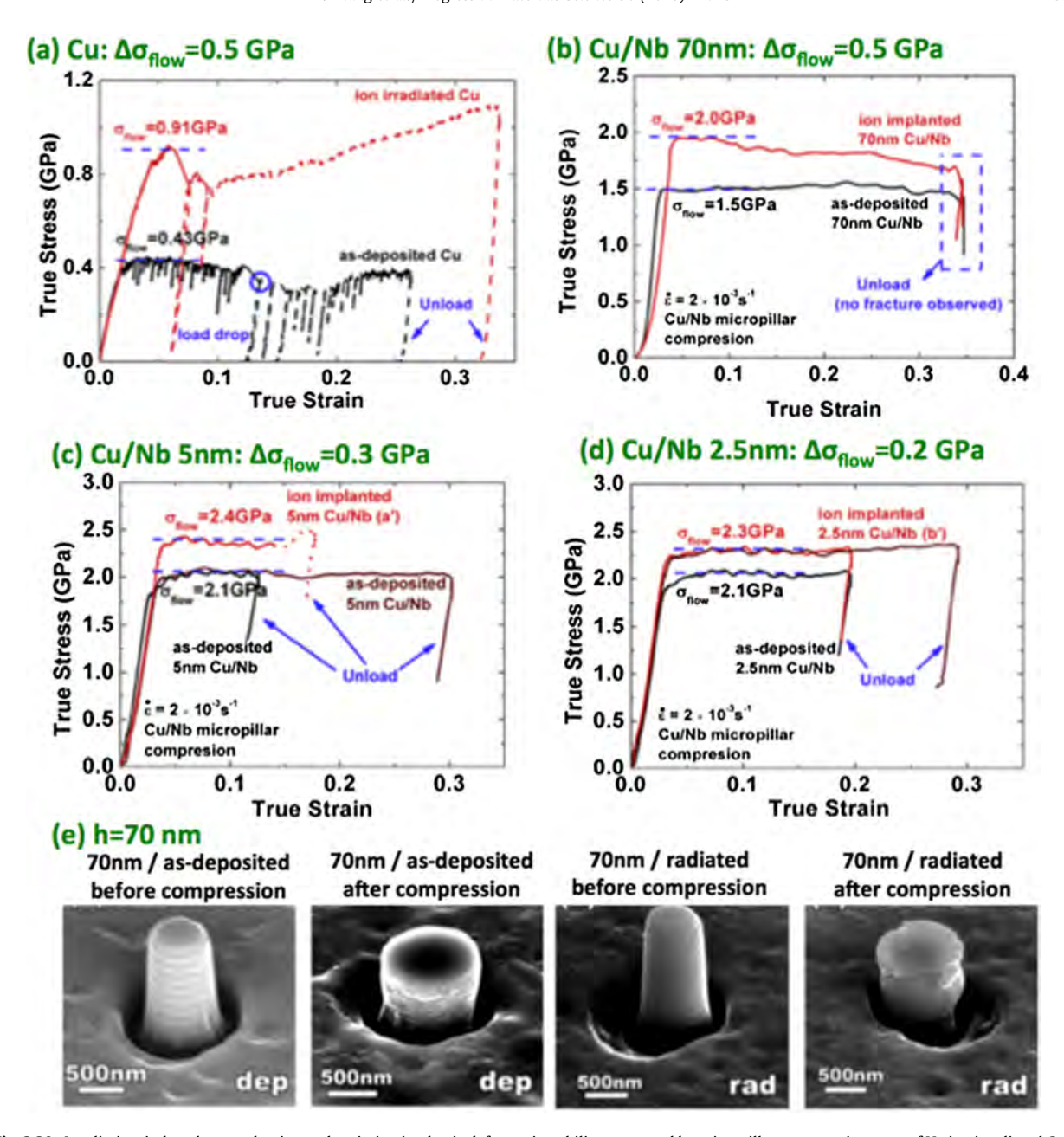


Fig. 3.20. Irradiation-induced strengthening and variation in plastic deformation ability measured by micropillar compression tests of He ion irradiated Cu/Nb nanolayers. True stress-strain behaviors of (a) single-crystal Cu pillar, (b) 70-nm-thick Cu/Nb, (c) 5-nm-thick Cu/Nb, and (d) 2.5-nm-thick Cu/Nb nanolayer pillars before and after He ion irradiation. (e) SEM images of 70-nm-thick Cu/Nb micropillars before and after irradiation and pillar compression [418]. Reprinted with permission from Ref. [418].

Irradiation hardening of nanolayers is contributed by both layer constituents and interfaces. At large layer thickness, (h > 5 nm), the hardening behavior of nanolayers is similar to that of monolithic metals. Radiation induced dislocation loops and He bubbles are generally treated as weak obstacles to the migration of dislocations. The Friedel-Kroupa-Hirsch (FKH) model is commonly used to describe irradiation strengthening ($\Delta \sigma$) arising from weak obstacles as follows [497–499]:

$$\Delta \sigma = \frac{1}{8} M \mu b dN^{2/3},\tag{3.16}$$

where M is the Taylor factor (\sim 3 for polycrystalline FCC and BCC metals), μ is the shear modulus, b is the magnitude of the Burgers vector of the primary glide dislocations, and d and N are the respective average defect diameter and density and can be determined from TEM experiments. Although the model was initially developed to account for the interactions between

(a) dislocation-bubble interaction dislocation line bubble (b) large h (c) small h

Fig. 3.21. Schematic illustration of glide dislocation interaction with obstacles (He nanobubbles) of spacing l. Φ_C is the semicritical angle at which the dislocation breaks away from the pinning obstacle. (b and c) Schematic illustration of the bubble distribution in nanolayers (the circles indicate the bubbles). (b) When h is a few tens of nm, h >> l, and the strengthening mechanism is dominated by the confined layer slip model. Glide dislocations in a given layer are confined by the interfaces and nanobubbles, resulting in a term that adds to the barrier strength; (c) When h is a few nm, h < l, and the yield strength is determined by the crossing of single dislocations across interfaces containing He nanobubbles [452]. Reprinted with permission from Ref. [452].

gliding dislocations and dislocation loops or small cavities without He atoms [497], it still works well for describing He bubble induced hardening.

A more sophisticated hardening model can be derived from the Orowan model. For strong (impenetrable) obstacles with a separation spacing l, the Orowan model assumes that the glide dislocation bows to a semicircle with a radius of l/2 between obstacles. However, it has been shown that the model overestimates the strengthening due to weak obstacles, and thus the Orowan model is modified to [452,500]:

$$\tau = \frac{\mu b}{2\pi l} \ln\left(\frac{l}{r}\right) (\cos\varphi_c)^{1/2},\tag{3.17}$$

where φ_c is half of the critical bow-out angle between the lines of a dislocation cutting an obstacle, as shown schematically in Fig. 3.21a. When φ_c = 0, this equation reduces to the Orowan formula. The average obstacle spacing l_s is then given by:

$$l_{s} = \frac{1}{\sqrt{2Nr}},\tag{3.18}$$

where r is the radius of the defect cluster, and N is the defect density. For weak obstacles, $0 < \varphi_c < \pi/2$, the spacings of the obstacles only involves the two adjacent obstacles on the dislocation line, and Friedel [498] proposes that l is given by:

$$l = \frac{l_s}{\sqrt{\cos \varphi_c}},\tag{3.19}$$

Substitution of Eq. (3.19) into Eq. (3.17) yields the Friedel equation [498]:

$$\tau = \frac{\mu b}{2\pi l_{\rm s}} \ln\left(\frac{l}{r\sqrt{\cos\varphi_c}}\right) (\cos\varphi_c)^{3/2},\tag{3.20}$$

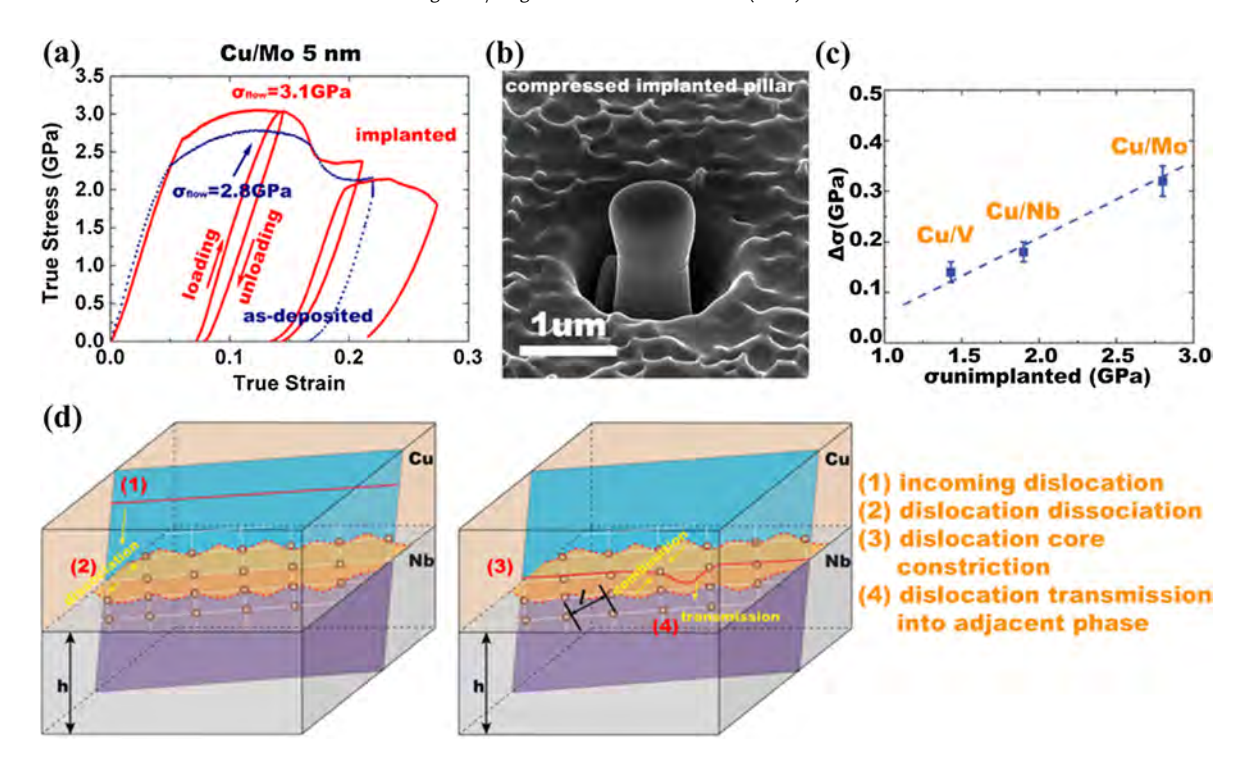


Fig. 3.22. (a) Compressive stress versus strain curves of a 5-nm-thick Cu/Mo nanolaminate pillar before (blue) and after (red) 0.8 at.% He implantation. (b) The corresponding SEM image of a compressed implanted nanopillar. (c) Flow stress enhancement introduced by interfacial He bubbles in He ion irradiated 5-nm-thick Cu/Mo, Cu/V, and Cu/Nb nanolaminates is proportional to the strength of the nonimplanted sample. (d) Schematic illustration of the interaction behaviors of interfacial bubbles with incoming gliding dislocations. Step 1: When the dislocation glides toward and reaches the interface, its core dissociates. (The circles indicate bubbles.) Step 2: The dissociated core spreads along the interface to an extent dependent upon the interfacial shear strength, marked in orange. Step 3: The dislocation trapped at the interface must collapse its core to transmit into the adjacent phase with higher applied stress, which will be affected by the shear strength of the interface as well as the interactive forces from interfacial He bubbles [425]. Reprinted with permission from Ref. [425].

which is used to predict irradiation hardening for known critical bow-out angles between lines of a dislocation cutting an obstacle. The bow-out angle can be estimated by [501]:

$$\cos \varphi_c = \frac{\ln(\alpha \bar{D}/b)}{\ln(l/b)},\tag{3.21}$$

where $\alpha = 1-4$, and is the harmonic mean of *l* and *d* and is given by:

$$\frac{1}{\overline{D}} = \frac{1}{d} + \frac{1}{L},\tag{3.22}$$

where d is the bubble diameter. Theoretically, this model can be used to treat most irradiation-induced defects. For example, interstitial loops could be treated as strong obstacles and φ_c = 0. A simplified Orawan model can be written as follows [502]:

$$\Delta \sigma = M \omega \mu b \sqrt{Nd}, \tag{3.23}$$

where b, N, and d carry the same physical meanings as defined previously. α' is the average barrier strength of the radiation-induced defect clusters [502]. This model is acceptable only when all the obstacles have identical strength and are, arranged on a square lattice in the slip plane [For details see [5 0 0]]. In conclusion, irradiation hardening originating from defects, such as bubbles, dislocation loops and SFTs, can be appropriately tackled by a dispersed-barrier hardening model.

When the individual layer thickness is small (h < 5 nm), in pristine nanolayers, the strength of the nanolayers is determined by the transmission of a single dislocation across the interface. In He ion irradiated nanolayers, a high density of He bubbles decorate the layer interfaces and are therefore, responsible for irradiation hardening. Multiple factors, including interface shear strength and bubble distributions at interfaces, contribute to the flow stress enhancement after irradiation. Recently, a series of micropillar compression tests have been performed on He ion implanted Cu/Mo, Cu/V and Cu/Nb nanolayers with an individual layer thickness of 5 nm, wherein the implanted He concentration was tuned to correlate with the MDI density, so that the average He concentration at each MDI was approximately the same (Fig. 3.22) [425]. After He implantation, the flow stress enhancement was proportional to the strength of the nonimplanted nanolayer system. Interfaces with higher densities of MDIs and lower shear resistances tend to provide enhanced hardening [425].

Table 3.1 A summary of current studies on radiation damage in nanolayers.

	Miscibility	Coherent/incoherent	Radiation source	Modeling
Metallic nanolayers FCC/BCC systems				
Cu/Nb	Immiscible	Incoherent	He ion [305,396,414,416-422,424,425,430,438]; Kr ion [409,423,426]	MD [361,416,428,430–438,441,503]; Reaction-diffusion model [407]; O-lattice theory [440]; OKMC [442]
Cu/V	Immiscible	Incoherent	He ion [123,443,444]; Kr ion [426]	MD [430]
Cu/Mo	Immiscible	Incoherent	He ion [445,446]	
Cu/W	Immiscible	Incoherent	He ion [447,448,450]	DFT [449]
Cu/Fe	Immiscible	Incoherent	He ion [451]; Cu ion [77]	
Ag/V	Immiscible	Incoherent	He ion [205,452,453]	Monte Carlo [361]
Ni/Fe	Miscible	Incoherent	Fe ion [455]	MD [454]
Cu/Ni	Miscible	Coherent/incoherent	Kr ion [426]	MD [464]
Al/Nb	Miscible	Incoherent	He ion [465]	
FCC/FCC systems				
Ag/Ni	Immiscible	Incoherent	He ion [453];	
715/111	miniscibic	meonerene	Proton [453];	
			Kr ion [408]	
Cu/FCC Co	Immiscible	Coherent/incoherent	He ion [463]	
Cu/FCC Fe	Immiscible	Coherent	He ion [451]	
			110 1011 [1001]	
BCC/BCC systems	N #1 11-1 -	I	He less [400]	Manta Carla [201]
Fe/W	Miscible	Incoherent	He ion [468]	Monte Carlo [361]
Cr/W	Miscible	Incoherent	Xe ion [504]	
BCC/HCP systems				
Zr/Nb		Incoherent	γ-ray [505]	
Ta/Ti	Miscible	Incoherent	Ar ion [506]	Monte Carlo [361]
FCC/HCP systems				
Al/Ti	Miscible	Incoherent	Ar ion [466,467]	MD [507]
Metal/Amorphous (Cr.	ystal/Amorpho	us)		
Fe/SiOC	-		He ion [508–510]	
			Kr ion [509]	
Cu/Ta	Immiscible	Incoherent	He ion [508]	
Fe/Y ₂ O ₃			He ion [487];	DFT [398]
			Kr ion [511]	
Cu/CuZr			He ion [492]	
Fe/TiO ₂			He ion [512]	
Metal/Ceramics (Cryst	tal/Crvstal)			
FeCr/MgO	,,		Ni ion [513]	
FeCr/TiO ₂			Ni ion [513]	
FeCr/Y ₂ O ₃			Ni ion [514]	
W/ZrO ₂			Au ion [515]	
Zr/SiC			Xe ion [516]	
Commission				
Ceramic nanolayers			An ion [472 474]	
CrN/AlTiN			Ar ion [473,474]	
TiN/MgO			He ion [475]	MD [470]
CeO ₂ /SrTiO ₃ TiN/AlN			He ion [476];	MD [479]
I III/AIIN			He ion [4/6]; Ar ion [481,482];	
			Ar ion [481,482]; Xe ion [483]	
BaTiO ₃ /STO			Ne ion [478]	Reaction-diffusion model [484]
				reaction-unitusion model [404]
(Ti,Al)N/Ti ₂ AlN _x			Ar ion [517]	

Note: Miscibility and coherency are marked for metal/metal systems only.

In summary, the irradiation hardening in nanolayers relies on the relationship between bubble spacing and layer thickness. The increase in shear stress ($\Delta \tau$) due to He bubbles is obtained by the balance between the dislocation line force and resistance from all obstacles with separation distance l and layer thickness h. The dependence of hardening increment due to bubbles ($\Delta \tau$) on the interface spacing (h) for a variety of multilayers was found to follow a simple analytical form:

$$\Delta \tau = \tau_i \left(1 - \frac{l}{\sqrt{2}h} \right). \tag{3.24}$$

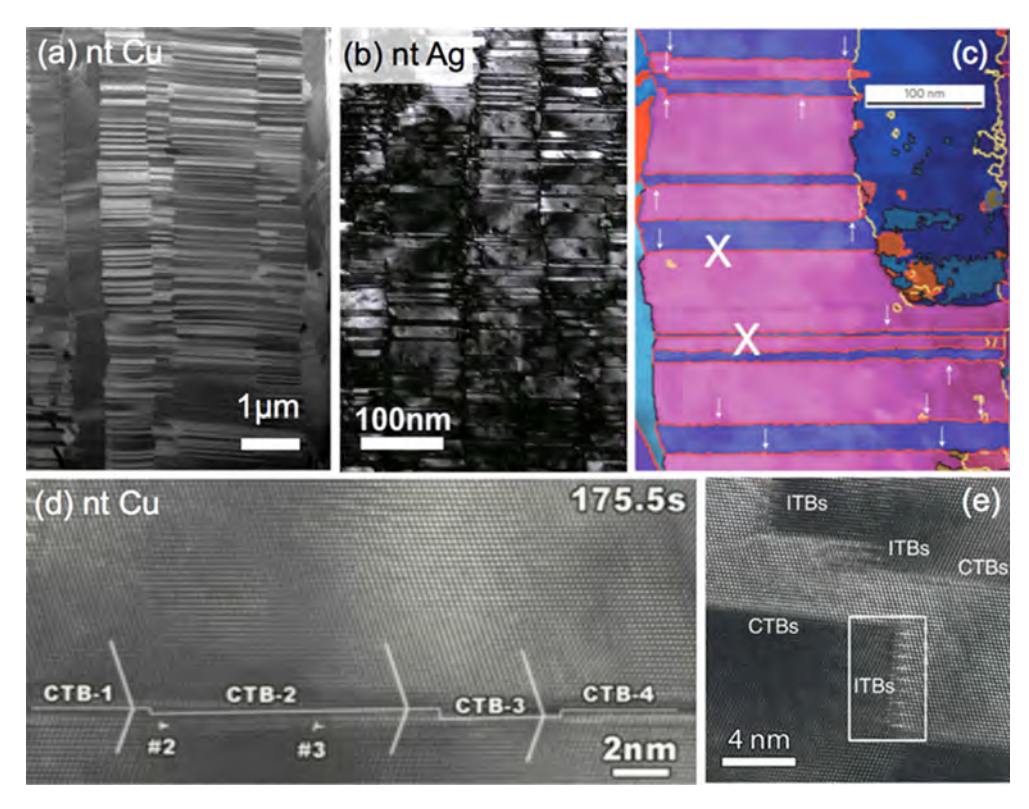


Fig. 4.1. TEM micrographs of (a) NT Cu [546] and (b) NT Ag [526]; (c) defective CTBs prevailing in deformed NT structure [547]; (d) the interaction of lattice glide dislocation with a CTB, forming defective CTB [548]; (e) CTB-ITB junctions in NT Cu [545]. Reprinted with permission from Ref. [526,545–548].

where τ_i is the average shear strength owing to obstacles. When the average bubble spacing is equal to or greater than the layer thickness, bubble hardening is negligible compared to the confined layer slip stress for single dislocations in multilayers. Finally, we summarize the majority of the literature to date on radiation damage in nanolayers in Table 3.1.

3.8. Challenges and future outlook

Although radiation studies on nanolayer systems have been conducted for over a decade, there are still many unexplored subjects. First, most studies on nanolayers focus on He ion irradiation to a dose of several dpa. More comprehensive studies should be conducted by neutron irradiation and heavy ion irradiation, especially to a high dpa level.

Second, most current radiation studies on nanolayers are performed at room temperature. The stabilities of interfaces subjected to radiation at elevated temperatures (relevant to the service temperatures of materials in nuclear reactors) must be examined. Radiation induced dimension and density of defects are expected to be temperature-dependent. Radiation damage in nanolayers at elevated temperatures remains a poorly understood subject.

Third, the combined effects of layer interfaces and MDIs on defect (such as He) management should be considered from a comprehensive point of view. A recent study [361] has shed some light on the radiation tolerance of irradiated Cu/Nb, Ag/V, Fe/W, and Ti/Ta interfaces.

Fourth, there are a limited number of experimental studies on radiation damage in HCP-based nanolayers. Meanwhile, mechanical testing of irradiated nanomaterials is limited mostly to nanoindentation and a few micropillar compression studies. Tensile tests on irradiated nanomaterials are necessary to validate their application as structural materials in reactor environments.

Finally, the majority of theoretical studies on radiation damage in nanolayers focus on point defects. The interaction of dislocation loops and 3D defects, such as voids/bubbles with layer interfaces should also be considered in future simulation studies.

4. Radiation damage in nanotwinned metals

Nanotwinned (NT) metals can be synthesized by pulsed electrodeposition [518] or magnetron sputtering techniques [519–522]. By controlling the deposition temperature, deposition rate, and orientation of growth twins, the average twin spacing can be tailored from a few to tens of nanometers. Twin boundaries (TBs) strengthen metallic materials significantly

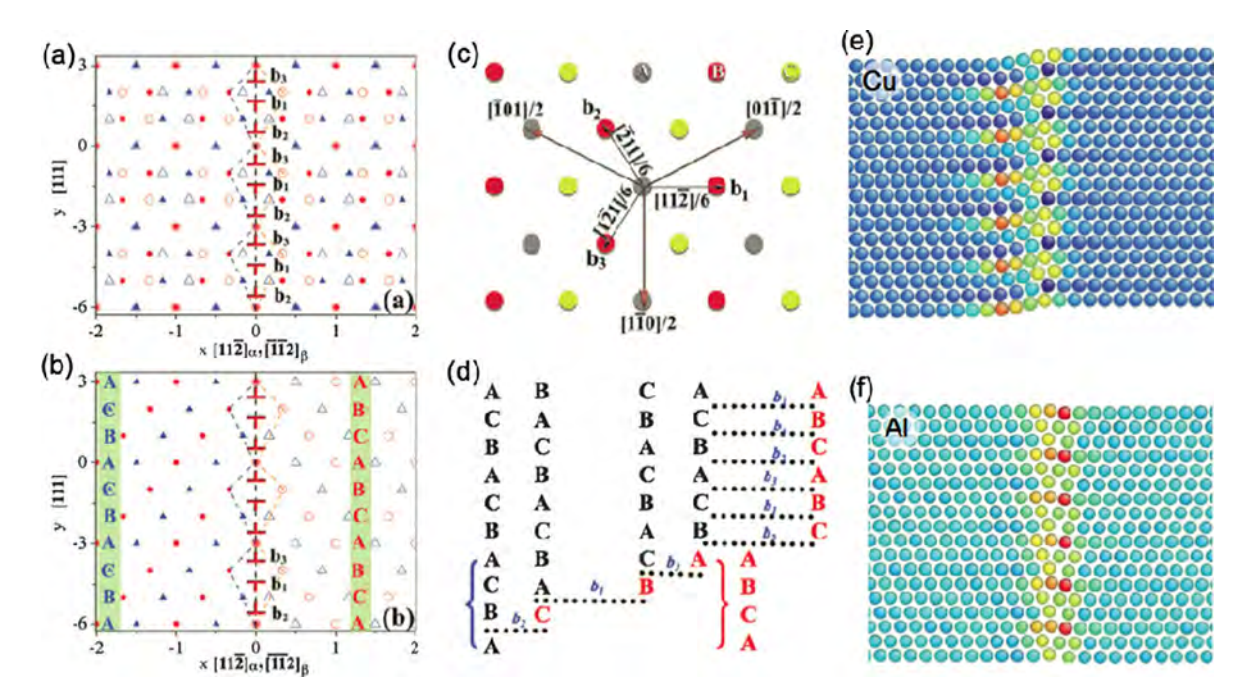


Fig. 4.2. (a–d) Dichromatic pattern of a [110] $\Sigma 3\{1\ 1\ 2\}$ ITB showing the atomic structure of the boundary: (a) Dichromatic pattern of an ITB containing a set of partial dislocations on every (1 1 1) plane with a repetitive sequence $b_2:b_1:b_3$, and (b) the equivalent bicrystal structure of an ITB. The dashed lines indicate the boundary atoms belonging to two grains. (c) Plan-view of (1 1 1) plane stacking and three partials, where b_1 is a pure edge dislocation, b_2 and b_3 are mixed partial dislocations with opposite sign screw components. (d) Schematic illustration of the glide of the three partials to create a twin. The solid symbols represent atoms in grain α and the open symbols represent atoms in grain β. The repeatable pattern with a unit involving three {1 1 1} planes is indicated by solid lines. (e) and (f) show relaxed atomic structures of $\Sigma 3\{1\ 1\ 2\}$ in Cu and Al, respectively [557]. Reprinted with permission from Ref. [557].

by impeding dislocation motion because of slip discontinuity, without losing ductility and work-hardening capability owing to symmetrical slips across the twin boundaries [523–525]. As a result, NT metals have a combination of high strength and strong work hardening capabilities [515,518,526–533]. Moreover, TBs have long been recognized as effective defect sinks in irradiated materials as demonstrated decades ago in a series of works by Makin [534], Norris [535], King [536,537], Smith [537] and Zinkle [3] et al. Different mechanisms for the defect-TB interactions have been proposed; however, questions remain regarding whether a defect denuded zone can form near a coherent twin boundary (CTB) [534,535,538]. Some experiments and simulations suggest that CTBs have limited effects on alleviating radiation damage [462,539], while others provide real time evidence that shows TBs can act as effective sinks and diffusion channels for radiation induced defects, and consequently, enhance the radiation tolerance of the NT materials [29,540,541].

This section begins with the review of the atomic structure of TBs. In particular, the structure and behavior of incoherent twin boundaries (ITBs) are emphasized because increasing evidence indicates that CTBs are often defective and contain ITB steps. Several recent reports on the ion irradiation response of NT metals are highlighted and open questions are summarized.

4.1. Twin boundaries in FCC metals

TBs are often classified into two major types: CTBs and ITBs. A CTB is generally atomically flat without intrinsic dislocations, while an ITB contains twinning dislocations. Corresponding to the crystallography of the Σ 3 twin in the FCC structure, Σ 3{1 1 1} CTBs and Σ 3{1 1 2} ITBs are commonly observed (Fig. 4.1a and b). Given that the mechanisms of defect-TB interactions are inevitably built on the structures of CTBs and ITBs, a brief introduction to the atomic configuration of these TBs is necessary.

4.1.1. Defective CTBs

CTBs were widely described as crystallographically perfect interfaces in early studies and the role of CTBs in strengthening, maintaining the ductility and minimizing electron scattering is well documented [518–521,524,526]. Recently, Li et al. performed *in situ* HRTEM nanoindentation and MD simulations to demonstrate that CTBs not only resist slip transmission [542–544], but also interact with lattice dislocations to facilitate the multiplication of partial dislocations, and form imperfect/defective CTBs (Fig. 4.1d and e) [419,545]. A further study by Wang et al. pointed out that as-grown CTBs in NT Cu are

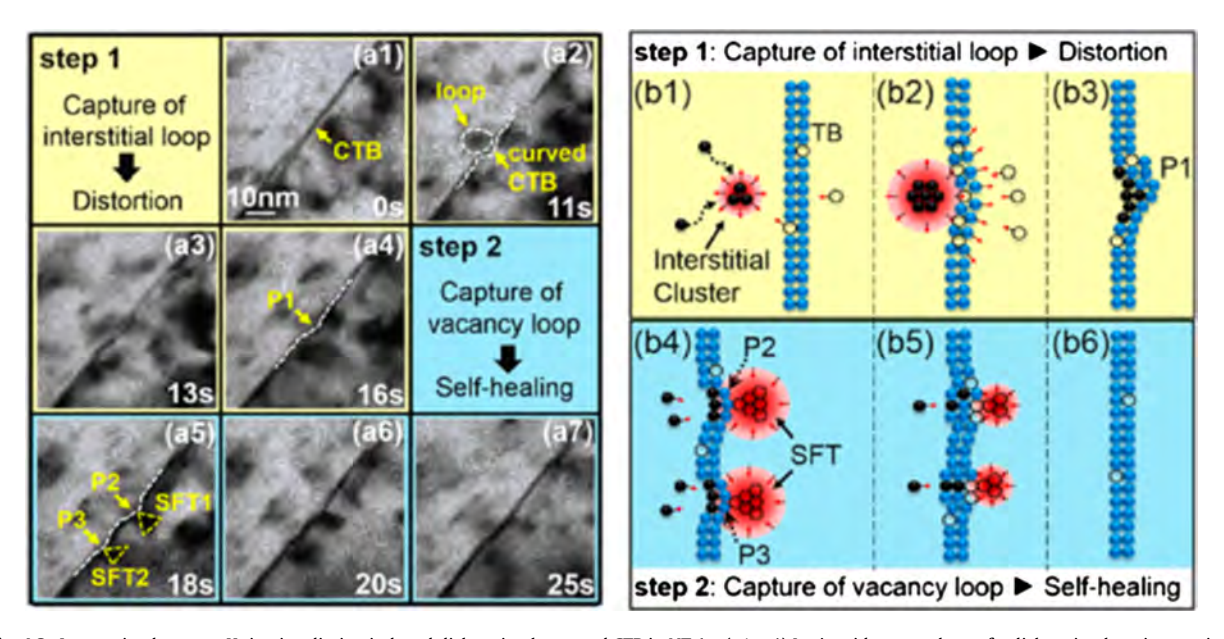


Fig. 4.3. Interaction between Kr ion irradiation induced dislocation loops and CTB in NT Ag. (a1-a4) In situ video snapshots of a dislocation loop interacting with a CTB. The CTB was curved during the interaction from 11 to 16 s, as indicated by P1. (a5-a7) In situ video snapshots of the self-healing of the CTB via absorption of SFTs. At 18 s, P1 transformed into two smaller curved sections, labeled P2 and P3. At 20 s, two SFTs approached to the curved CTB, causing gradual evolution of the boundary. The CTB eventually recovered (self-healed) at 25 s. (b1-b6) Schematics of the self-healing mechanism of a CTB. The stress field of the interstitial loop firstly curved the CTB and the formation of SFTs later changed the distribution of interstitials at CTB, generating two smaller puddles close to each SFT. Finally, the annihilation of interstitials with SFTs resulted in the self-healing of the CTB [562]. Reprinted with permission from Ref. [562].

inherently defective with kink-like steps and curvature. The imperfections on CTBs consist of incoherent segments and partial dislocations, which play a crucial role in the deformation mechanisms and defect-TB interactions.

4.1.2. Dislocation structures of ITBs

 Σ 3{1 1 2} ITBs are of great interest as they are low-energy, thermally stable boundaries that separate one column from the others in NT metals. Atomistic simulations were employed to investigate the structure and stability of Σ 3 GBs in FCC metals, such as Cu with low SFE and Al with high SFE [419,528,529,549–556]. Taking Cu as an example, three sets of tilt Σ 3 GBs have been studied with respect to the tilt axis parallel to $\langle 1 1 1 \rangle$, $\langle 1 1 2 \rangle$, and $\langle 1 1 0 \rangle$, respectively. The results show

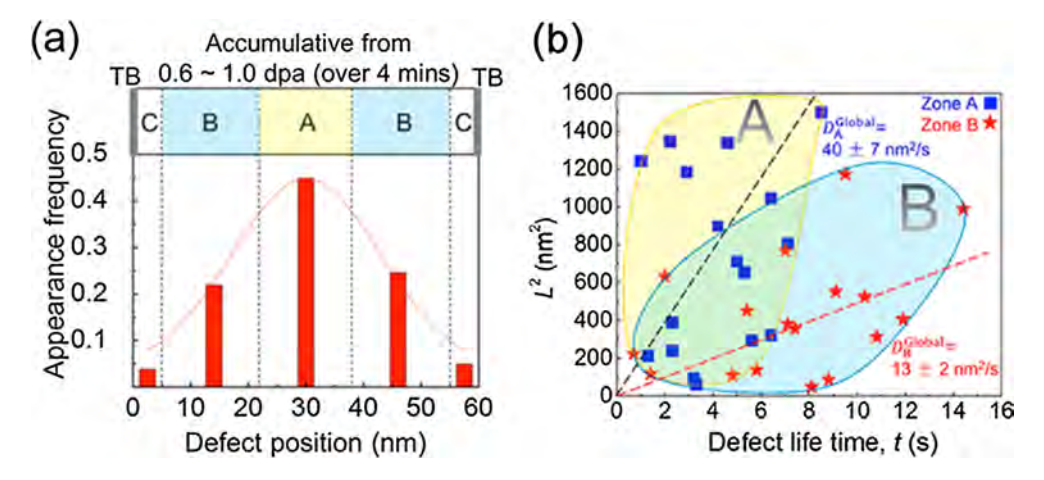


Fig. 4.4. (a) Existence of TBAZ in irradiated NT Ag. The accumulative defect concentration (0.6–1.0 dpa over 4 min) in Zone A (shown as the appearance frequency) was significantly higher than those in Zone B. Zone C (closest to TBs) had the lowest accumulative defect concentration. (b) Different defect migration kinetics in Zone A and B in irradiated NT Ag. The global diffusivity, derived by fitting the plot of L^2 as a function of defect lifetime (t) as indicated by the dashed lines was $40 \pm 7 \text{ nm}^2/\text{s}$ for defect clusters in Zone A, around three times larger than that in Zone B, $13 \pm 2 \text{ nm}^2/\text{s}$ [562]. Reprinted with permission from Ref. [562].

that only $\Sigma 3\{1\ 1\ 1\}$ and $\Sigma 3\{1\ 1\ 2\}$ GBs are thermodynamically stable and the others tend to dissociate into terraced interfaces, consistent with TEM observations [520].

 $\Sigma 3\{1\ 1\ 2\}$ ITBs show different structures with respect to their SFE [542] and play a crucial role in determining the mechanical response of NT metals [515,557], in particular when the height of ITBs is a few nanometers thick [525,558]. $\Sigma 3\{1\ 1\ 2\}$ ITBs can be represented as a set of partial dislocations on every $\{1\ 1\ 1\}$ plane with a repeatable sequence b_1 : b_2 : b_3 , where the Burgers vector of a pure edge dislocation b_1 is $1/6[1\ 1\ 2]$, and the Burgers vectors of two mixed partial dislocations (b_2 and b_3) are $1/6[1\ 1]$ and $1/6[1\ 2]$, respectively, and have screw components of opposite sign (Fig. 4.2) [525]. The sum of the Burgers vectors in one triple unit is zero.

In the absence of external stress, the dissociation of partial dislocations in ITBs can occur spontaneously due to a reduction in the core energy. Molecular statics calculations for ITBs in FCC metals under zero applied stress [557] revealed that ITBs can dissociate into two phase boundaries (bounding the 9R phase) that contain different arrays of partial dislocations. The separation distance between the two phase boundaries scales inversely with increasing SFE (Fig. 4.2e and f) [525,557]. The study of the shear response of ITBs in FCC metal also reveals possible migration mechanisms of ITBs [557]. For FCC metals with low SFE, one of the two phase boundaries migrates through the collective glide of partials, referred to as the phase-boundary-migration mechanism, which has been observed by *in situ* nanoindentation test in TEM [525]. For metals with high SFE, ITBs experience a coupled motion (migration and sliding) through the glide of interface disconnections, which is referred to as the interface-disconnection-glide mechanism [557] that has been recently confirmed in NT Al [515].

4.2. Radiation effects of CTBs

4.2.1. Defect-CTB interactions

Annihilation of point defects by GBs gives rise to denuded zones of point defects or precipitates upon irradiation or quenching [535,538,559,560] since it is energetically favorable for point defects to nucleate at or migrate to GBs. In contrast, the formation energies of vacancies and interstitials at CTBs are close to those in perfect lattices [462]. Thus the defect denuded zones (DDZs) at the vicinity of CTBs are generally not expected. A previous work by Makin et al. showed that CTBs have no DDZs [534]. However, by quenching Au from a temperature close to its melting point, Segall identified that a CTB can act as a very effective vacancy sink to annihilate SFTs [538]. In case of irradiation, Norris has pointed out that TBs may be effective in capturing vacancies [535]. Later a systematic study by King and Smith showed that defect evolution near CTBs is different from that in matrix [537]. Debates remain regarding the validity of the sink effect of CTBs in irradiation environments [462,539]. Conceptually, a perfect CTB is not a energetically favorable sink to absorb defects. However this perception no longer holds for a defective CTB. Recent studies have shown that the interaction between CTBs and defects can introduce steps at TBs containing dislocations [548,561]. The formation energy of a point defect at these twin steps is generally lower than that in a perfect lattice/CTB. Taking NT Cu as an example, the interstitial formation energy decreases from 3.06 eV in the Cu lattice to 0.98 eV at a twin step with a Frank dislocation [29]. These steps provide fast-diffusion channels to promote defect migration and annihilation mainly due to the confinement of migration path from 3D to 1D along a dislocation line.

Interactions between CTBs and point defects (or clusters) were recently investigated in real time by Li et al. [562]. NT Ag was irradiated in an electron microscope at room temperature (RT) using 1 MeV Kr ions and the microstructural evolution was observed [562]. As shown in Fig. 4.3a1, a nearly perfect CTB is originally straight. At 11 s, a mobile interstitial loop formed near the CTB (Fig. 4.3a2), causing distortion (curvature) of the CTB. Later the loop was captured by the curved

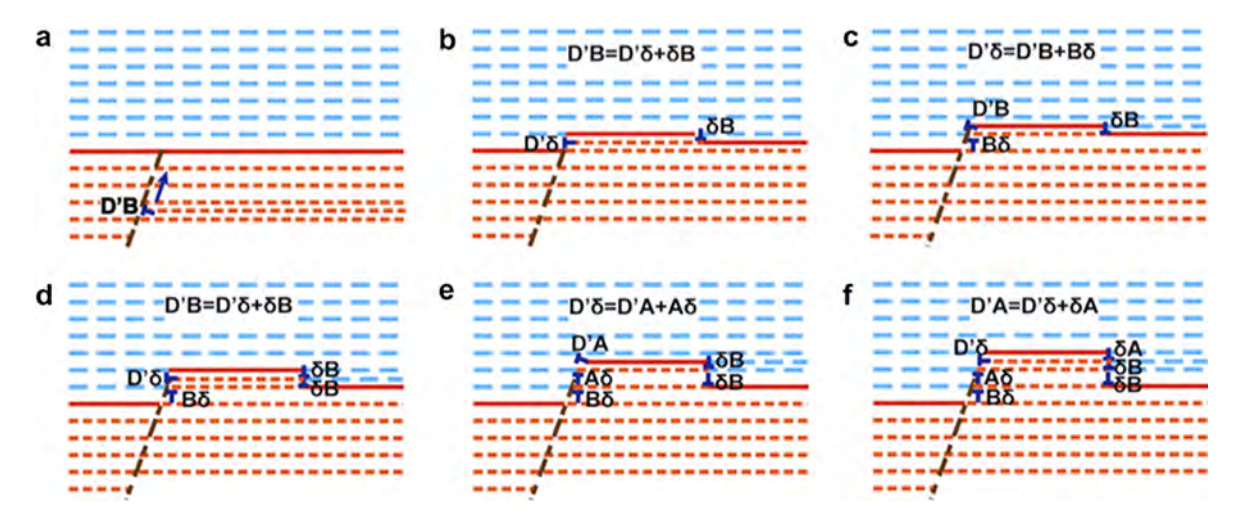


Fig. 4.5. (a-f) Schematic illustration of the dislocation multiplication mechanism through the interaction of a mixed dislocation D'B with the TB. A detailed description of the propagation process was given previously [548]. Reprinted with permission from Ref. [548].

CTB at 13 s (Fig. 4.3a3) and eventually absorbed by the CTB at 16 s (Fig. 4.3a4). As shown in Fig. 4.3a5, the P1 puddle on the CTB was later replaced by two neighboring curved sections, labeled as P2 and P3 at 18 s, and the two SFTs were then gradually absorbed before the CTB recovered, to become a straight TB at 25 s (Fig. 4.3a7).

Based on these observations, a hypothetical mechanism of point defect–CTB interaction is illustrated in Fig. 4.3b. It was proposed that the nature and content of point defects on each side of the boundary determine the morphological evolution of the CTB. First, the local stress field generated by the small interstitial loop deforms the CTB. The estimated magnitude of shear stress introduced by a dislocation loop has also been shown to be sufficient to drive partials along CTBs. Second, the absorption of the interstitials results in a locally interstitial-rich boundary. Third, when the vacancy-rich SFTs approach the CTB, the interstitial-rich CTB prompts the interstitials to rapidly redistribute themselves along the CTB into two smaller puddles adjacent to each SFT. Eventually, the recombination of vacancies and interstitials restores the local structure of the CTB, i.e., the CTB self-heals via this process.

The fact that the CTBs can be defect sinks brings up other questions, such as whether there are defect denuded zones near TBs and will TBs alter the migration kinetics of nearby defects. Statistical analyses of defect activities near CTBs have been reported [562]. The accumulative defect concentration within a twin in Kr ion irradiated Ag was evaluated using an *in situ* irradiation video captured in the dose range of 0.6 to 1 dpa. As shown in Fig. 4.4a, Zone C exhibited the lowest defect density

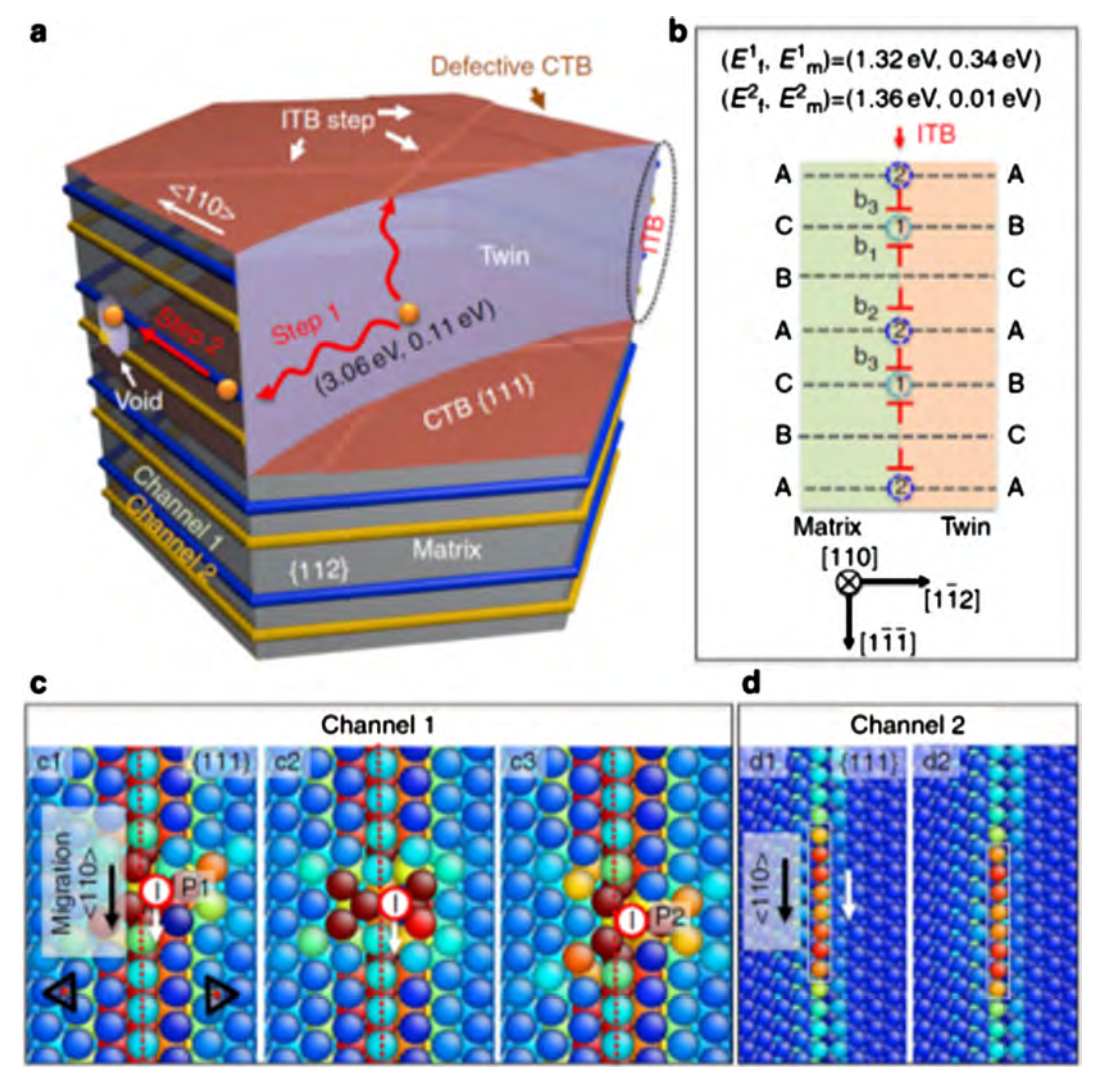


Fig. 4.6. Absorption and diffusion of interstitials in nanovoid-nanotwinned Cu. (a) Fast interstitial diffusion pipes enabled by ITB-CTB networks in NT Cu. (b) Two fast diffusion channels at ITBs and (c, d) the corresponding diffusion mechanisms. (c) For channel 1, an interstitial initially stays at a dislocation core in an $\{1\ 1\ 1\}$ layer sandwiched between b_1 and b_3 . The interstitial then migrates downward to another low-energy site, with energy at the same level as its initial low-energy site. (d) For channel 2, an interstitial has a spreading core associated with the distributed free volume along a dislocation line. The migration of the distributed interstitial requires a very low energy barrier $(0.01\ eV)$ and shows a crowdion-type behavior [29]. Reprinted with permission from Ref. [29].

after overlapping numerous video frames, indicating the existence of the TB affected zone (TBAZ), which is analogous to the DDZs near GBs. The width of the TBAZ was 2–5 nm. By tracking dozens of distinguishable defects, the global diffusivity D^{Global} was calculated as $D^{\text{Global}} = L^2/4t$, where $\textbf{\textit{L}}$ is the average of accumulative diffusion distance of the defects and t is the defect lifetime. Note that the lifetime is the sum of the migration and dwell time. Fig. 4.4b shows that D^{Global} in Zone A $(D_{\text{A}}^{\text{Global}})$ is $40 \pm 7 \text{ nm}^2/\text{s}$, which is ~ 3 times larger than that in Zone B $(D_{\text{B}}^{\text{Global}}) = 13 \pm 2 \text{ nm}^2/\text{s}$). The defect clusters in Zone B are more remotely distributed from one another, and therefore their interactions become less active, resulting in a longer dwell time.

Similar to the previous sections, here we attempt to derive the defect sink formula for TBs. Following the derivation of the sink strength for thin foils with free surfaces, the sink strength of CTBs with an average twin spacing, *t*, can be written as follows:

$$k_{t}^{2} = \frac{k_{sc}/t}{\left[\frac{k_{sc}t}{4} \coth(k_{sc}t/2) - \frac{1}{k_{sc}t}\right]}$$
(4.1)

When $k_{sc}t \rightarrow 0$:

$$k_t^2 = \frac{12}{t^2} \tag{4.2}$$

Furthermore, as there are different types of TBs, we assume that the sink strength of TBs is related to their coherency and energy, and can be described as follows:

$$k_t^2 = \frac{12f(\gamma_t, \rho_{step})}{t^2}$$
 (4.3)

where γ_t is the TB energy. f may also be related to TB characteristics, such as the density of ITB steps, ρ_{step} . Note that other factors such as excess free volume near the ITBs may also affect f and in turn the sink strength. Furthermore, as CTBs may continuously evolve by forming more ITB steps during radiation, the sink strength of TBs may vary correspondingly. The following section discusses the formation of ITBs due to dislocation–CTB interactions.

4.2.2. The formation of ITB steps due to dislocation-CTB interactions

ITB steps on CTBs are active defect sinks. Previous studies (as shown in Fig. 4.3) have shown that dislocation loop–CTB interactions may lead to ITB steps [562]. Here we show another example as revealed by *in situ* nanoindentation, that dislocation–CTB interactions may also lead to the generation of ITB steps by applied stress. It has been shown that depending on the characteristics of the dislocations and driving stress, dislocations can interact with CTBs in several configurations, including cross-slip into the twinning plane to cause twin growth or detwinning, formation of sessile stair–rod dislocations at the CTB, and transmission across the CTB [520,527,530,540,544,546–548,552,563–587]. After transmission, a Shockley partial dislocation is left at the CTB and a set of partials finally form an ITB [588–590]. Fig. 4.5 illustrates the possible dislocation multiplication mechanisms [548].

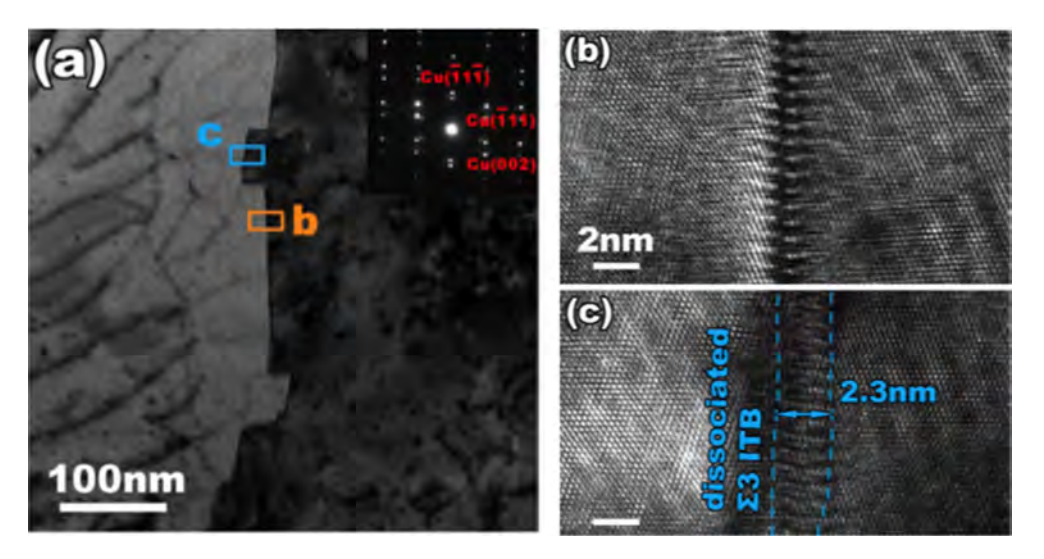


Fig. 4.7. (a) Bright field TEM image of an ITB generated after irradiation to 8.5 dpa. The inset shows the corresponding SAD pattern, which confirmed the $\Sigma 3$ ITB orientation. (b–c) HRTEM images of the boundary before and after migration, respectively. After migration, the width of the boundary was ~ 2.3 nm. The Cu films were fabricated by e-beam evaporation on a sapphire substrate at 300 °C and irradiation was performed using 4.5 MeV Cu³⁺ ions to a dose of 5.55 dpa at a rate of 27.9 × 10¹⁴ ions/cm² [592]. Reprinted with permission from Ref. [592].

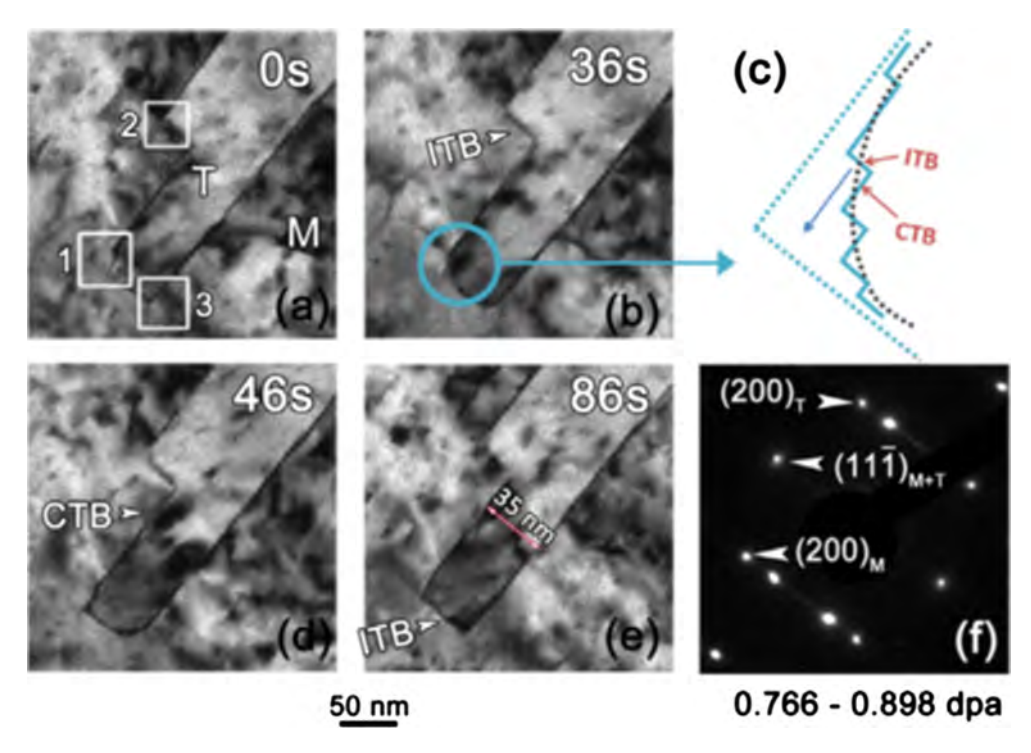


Fig. 4.8. Continuous migration and recovery of TBs in Kr ion irradiated NT Ag. Snapshots recorded during *in situ* irradiation in TEM and corresponding schematics showing the continuous evolution of twin boundaries over a dose range of 0.766–0.898 dpa. The observation was performed along the [0 1 1] direction. (a) At 0 s, box 1 indicates a region with a small kink at the junction between an ITB and a CTB, while boxes 2 and 3 each outline a right-angular corner consisting of an ITB and CTB pair. (b) By 36 s, the sharp corners in boxes 2 and 3 became blunted, and the kink in box 1 evolved into a curved boundary. (c) Schematic diagram showing a magnified view of box 1, where the curved corner consists of numerous tiny steps of ITBs and CTBs. (d) At 46 s, the corner in box 1 has become sharp again, while the bottom corner in box 3 was blunter (with mixtures of ITB and CTB steps). (e) The kink in box 1 had nearly disappeared by 86 s. (f) SAD pattern indicating the existence of twins with $\Sigma 3$ {1 1 1} CTBs [593]. Videos are available online in the original reference. Reprinted with permission from Ref. [593].

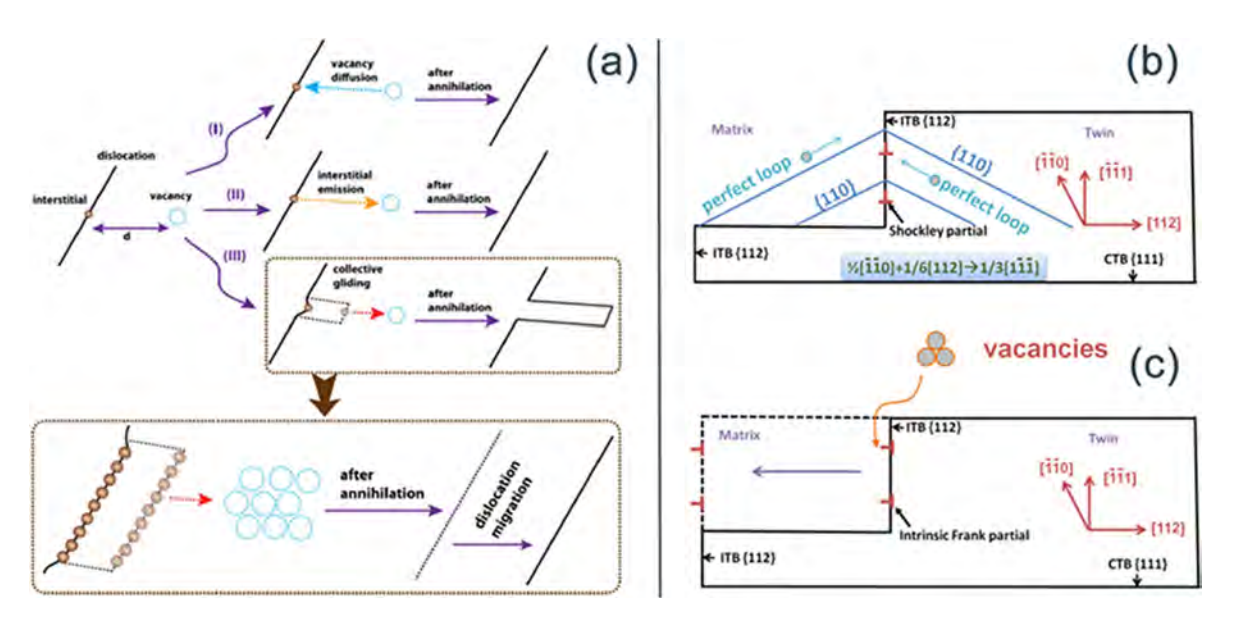


Fig. 4.9. (a) Schematic illustration representing three interstitial-vacancy annihilation mechanisms [592]. (b and c) Schematics of ITB migration mechanisms during irradiation showing the interaction of a dislocation loop on the {1 1 0} plane with Shockley partials on an ITB, leading to the formation of Frank partials at the ITB. The ITB is decorated by an array of 1/3 (1 1 1) intrinsic Frank partials (due to perfect loop-Shockley partial interactions). The absorption of vacancies can result in the ITB moving leftwards via dislocation climb. The Frank partials can then interact with perfect loops and form mobile Shockley partials, which usually dominate migration of the ITB. Shockley partials can migrate under local stress induced by irradiation [593]. Reprinted with permission from Refs. [592,593].

During irradiation, a large number of dislocations are generated and frequently interact with the high density of CTBs, possibly through the mechanisms as described above. As a result, large quantities of ITB steps form and continue to interact with defects. A recent study showed that point defects were not absorbed by CTBs due to their coherent nature [591]. However, simulations showing dislocation loop—TB interactions during radiation remain lacking.

4.3. Effects of ion irradiation on ITBs

4.3.1. Point defect-ITB interactions

ITBs separate one column from the others in NT metals. Corresponding to dislocation structure of ITBs, Fig. 4.6a illustrates the defect structures associated with a twinned column [29]. In contrast to the CTB, the formation and transportation of point defects at the ITB is more energetically favorable. Molecular statics simulations on NT Cu have shown that defects prefer to nucleate at ITBs and migrate faster than those in the crystal lattice. The formation energy for an interstitial at ITBs (\sim 1.3 eV) is much lower than that within the crystal lattice (\sim 3 eV) (Fig. 4.6b), implying that interstitials prefer to stay at TBs [29]. Furthermore, interstitials in the grain interior experience a very low migration energy (\sim 0.11 eV), permitting their rapid migration to nearby TBs. Once defects arrive at ITBs, they can be transported rapidly (similar to 1D diffusion) along fast diffusion channels and the recombination/neutralization of defects with opposite types is significantly enhanced. For ITBs consisting of sets of three adjacent Shockley partials, there are two fast diffusion paths for interstitials along dislocation lines, including channel 1 at tensile sites sandwiched by two partial dislocations (b_1 and b_3) with a kinetic barrier of 0.34 eV (Fig. 4.6b and c), and channel 2 with an energy barrier of merely 0.01 eV for expedited 1D crowdion diffusion (Fig. 4.6b–d). In addition, if nanovoids exist at ITBs to store radiation-induced defects, the radiation tolerance is further enhanced, as recently reported in NT Cu with nanovoids [561]. It is worth mentioning that the kinetic energy barrier is as low as 0.01–0.16 eV for channels along ITB-CTB junctions in NT Cu, which is significant in an NT structure with abundant ITB-CTB junctions.

4.3.2. Irradiation-induced ITB migration and dislocation-ITB interactions

Besides point defects, ITBs frequently interact with dislocations, resulting in the change in the dislocation content within ITBs. Previous *in situ* nanoindentation studies have revealed that repetitive dislocation–ITB interactions can induce steps [515,586], where dislocation transmission eventually occurs, and ITB steps migrate to further accommodate plasticity under high stress conditions [571,586]. MD simulations show that before absorption of the lattice dislocations, ITBs migrate and dissociate into two tilt walls bounding a 9R phase due to applied shear stress. The dissociation of ITBs is associated with crystal rotation [557]. Continued dislocation–ITB interactions in twinned Al lead to the accumulation of residual dislocations,

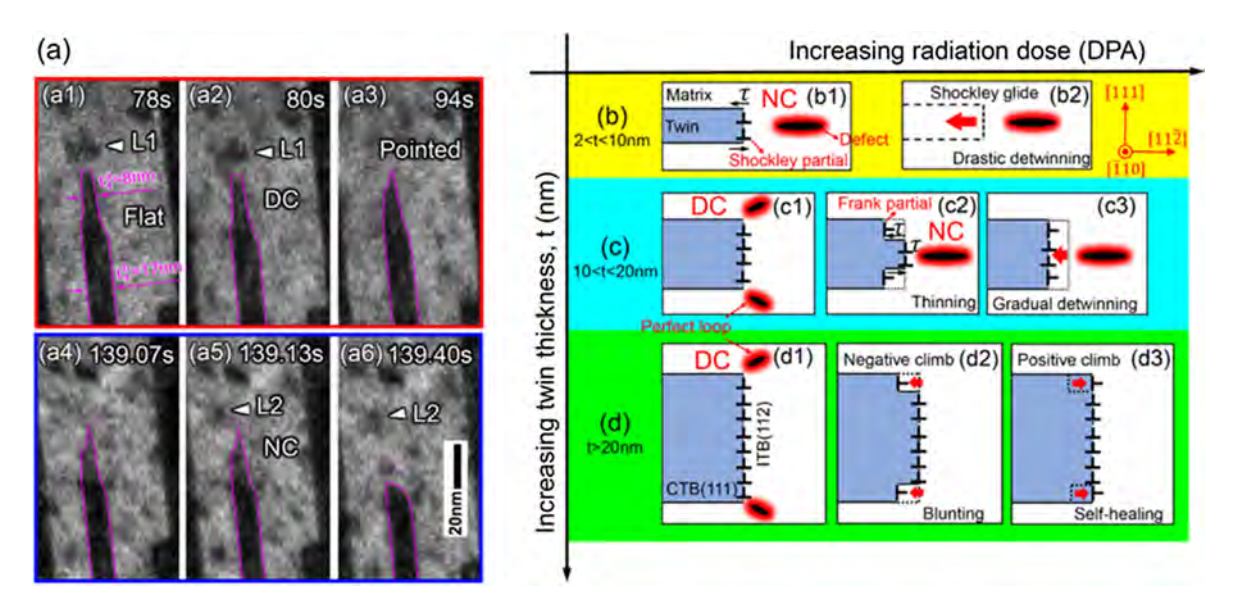


Fig. 4.10. (a) A series of TEM snapshots taken during in situ irradiation of NT-Cu over 0.1–0.2 dpa, showing the detwinning process for a 17 nm-thick twin with a 8 nm-thick tip. Two irradiation-induced dislocation loops interacting with the ITB are indicated by L1 and L2 [594]. The sharpening (a1–a5) and the subsequent collapsing (a6) processes of the twin are the consequences of dislocation-ITB interactions. (b-d) Schematic illustration of twin thickness-dependent detwinning during radiation. (b1)–(b2) When the twin thickness t < 10 nm, drastic detwinning occurred due to the glide of Shockley partials on ITBs. (c1)–(c3) For intermediate thickness (10 < t < 20 nm), gradual detwinning started from the corner, and was followed by the collapse of the sharpened tip. (d1)–(d3) In thick twins (t > 20 nm), the corner of twins can migrate back and forth due to climbing of Frank partials or gliding of Shockley partials [594]. This phenomenon was observed through in situ TEM studies as shown in Fig. 4.8. Reprinted with permission from Ref. [594].

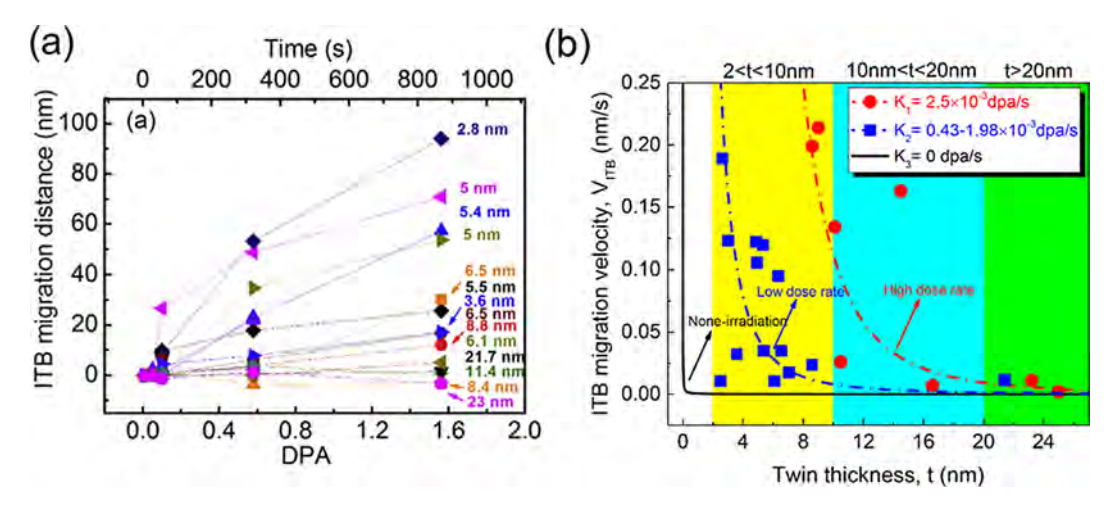


Fig. 4.11. Dependence of ITB migration on twin thickness and dose rate at RT. (a) Twin length vs. radiation dose for various twins. The migration velocity of ITBs (the slope of each data set) decreases progressively with increasing twin thickness. The critical film thickness was \sim 10 nm [558]. (b) V_{ITB} decreased rapidly with increasing twin thickness at a high dose rate ($K_1 = 2.5 \times 10^{-3}$ dpa/s; red data) compared to that at a low dose rate ($K_2 = 0.43 - 1.98 \times 10^{-3}$ dpa/s, blue data) [594]. Data calculated for non-irradiation condition [595] ($K_3 = 0$ dpa/s) are also plotted (black line) as a reference. Reprinted with permission from Refs. [558,594,595].

which appear as steps along the initially straight ITBs [515]. These steps eventually become pronounced enough to provide sites for dislocation transmission across the ITB or the nucleation of dislocations in adjacent grains.

The local variation of the ITB structure during irradiation can trigger migration of the ITB, in contrast to morphological variations of the CTB as discussed previously. Li et al. examined the migration of vicinal ITBs in self-ion irradiated Cu, as shown in Fig. 4.7, and ascribed the ITB migration to collective glide of an array of mobile partials due to defect–ITB interactions [592]. In addition, Yu and coworkers presented *in situ* evidence of ITB migration for Kr ion irradiated NT Ag as shown in Fig. 4.8 [593]. The tiny kink indicated by box 1 disappeared due to ITB migration after 86 s.

The mechanisms of ITB migration due to the interaction between ITB and irradiation-induced defects have been described as follows. Considering point defect–ITB interactions, irradiation leads to supersaturated vacancies close to the ITBs, and interstitials may be emitted from the TBs to annihilate neighboring vacancies [592]. As a result, the local stress between vacancies within the matrix and interstitials in the boundary can promote Shockley partials at ITBs to glide, leading to ITB migration, as shown in Fig. 4.9a. Energetically, the collective glide of Shockley partials within Σ 3 {1 1 2} ITBs generate zero strain, thus the strain energy remains constant during ITB migration.

From the perspective of dislocation and ITB interactions, as shown in Fig. 4.9b [593], a perfect dislocation loop can be absorbed by an ITB, forming of a Frank partial by:

$$\frac{1}{2}[\bar{1}\,\bar{1}\,0] + \frac{1}{6}[1\,12] \to \frac{1}{3}[\bar{1}\,\bar{1}\,1] \tag{4.4}$$

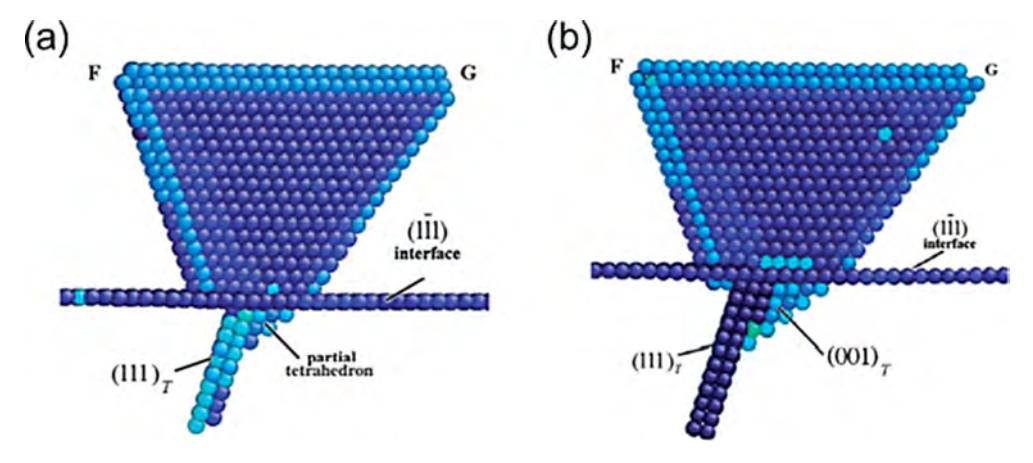


Fig. 4.12. MD simulation results showing the destruction of a large SFT in apex-down configuration by a growing twin [541]. (a) The parent SFT partially incorporated into the twin lattice. (b) Destruction of the parent SFT during further twin growth. Reprinted with permission from Ref. [541].

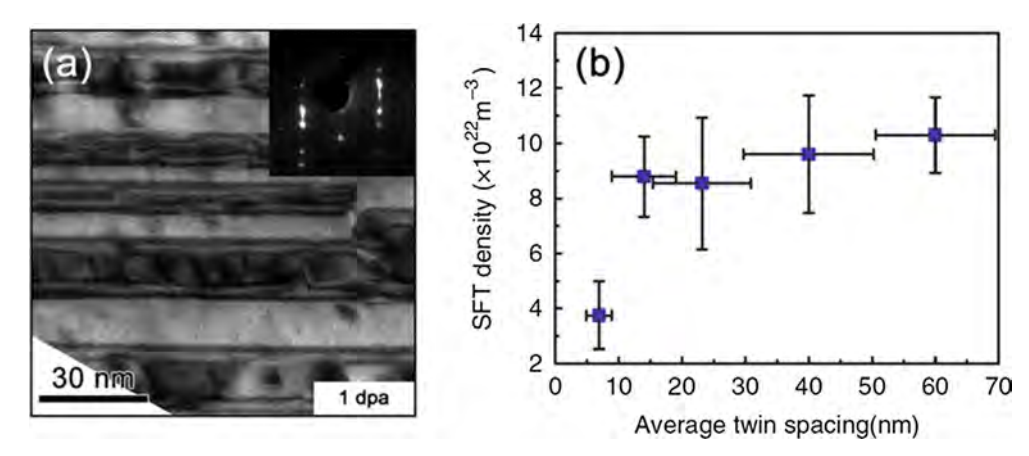


Fig. 4.13. (a) XTEM of fine twinned Ag (t = 8 nm) irradiated by 1 MeV Kr ions at RT up to 1 dpa, showing a relatively low defect density. The inset SAD pattern shows a strong intensity of streaked lines, implying the formation of a high density of stacking faults, which were observed along TBs. (b) The density of SFTs decreased sharply at smaller average twin spacings. All specimens were irradiated up to 1 dpa [39]. Reprinted with permission from Ref. [39].

As a result, an array of parallel Frank partials could form during irradiation along ITBs. These partials could grow by absorbing vacancies if they are intrinsic faults (vacancy-type), causing the ITB to migrate leftwards as shown in Fig. 4.9c. Equivalently, the intrinsic Frank partials could also shrink by absorbing interstitials to propagate to the right. Therefore, the ITBs in a NT metal could migrate back and forth via dislocation climb by absorbing interstitials or vacancies. In addition, it is likely that the migration of 1/6[1 1 2] Shockley partials at the ITB could be directly driven by local stress field formed by excessive defects, which is analogous to the mechanism of ITB migration under applied stress. In summary, the glide of Shockley partials and climb of Frank partials, may operate alternatively or simultaneously to advance or retreat ITBs during irradiation.

In addition to the continuous migration of ITBs during irradiation, Fan et al. recently reported an observation of the rapid migration of sharp ITB tips [594]. A series of TEM snapshots taken during $in\ situ$ irradiation of twinned Cu over 0.1–0.2 dpa (Fig. 4.10a) showed detwinning process through the sharpening and subsequent collapse of a TB due to dislocation loop - ITB interactions. Furthermore, ITB migration has a strong correlation with the twin thickness (t). Fig. 4.10b–d shows several scenarios for ITB migration in twins with different t values. When t is small (<10 nm), the stress field of a dislocation loop (not in direct contact with the ITB) may be sufficient to drive a rapid detwinning event (Fig. 4.10b). However, for thicker twins $(t > 20\ nm)$, the corner of twins (ITB corners) can migrate back and forth due to the climb of Frank partials or glide of Shockley partials, leading to self-healing of ITBs (Fig. 4.10d). For twins with intermediate thickness (10–20 nm), a gradual "sharpening" of ITBs from corners occurs (Fig. 4.10c), followed by detwinning [594].

During irradiation, energetic ITBs tend to migrate to reduce the area of CTBs (and consequently the energy stored in the CTBs) with the driving force $F = 2\gamma_T/t$, where γ_T is the excess energy of the CTB and t is the twin thickness). The friction force (F_P , or Peierls barrier), for the migration of ITBs increases with twin thickness, as partial dislocations in the ITB migrate collectively [525]. When t is small, the driving force is greater than the friction stress ($F > F_P$), hence the ITB can migrate to reduce the area of CTBs (Fig. 4.10b and c) [558]. In the case of thicker twins, the ITB cannot migrate. Clearly, the migration velocity is dependent on the twin thickness. As shown in Fig. 4.11a, Chen et al. showed that the velocity of ITBs decreased progressively with increasing twin thickness, where the critical thickness (t^*) for ITB migration is \sim 10 nm [558]. They showed that when $t > t^*$, detwinning could begin from the corner, but would easily reverse back. This is due to a negligible driving force for ITB migration in this case, as detwinning does not change the total area of the CTBs (*i.e.*, does not reduce the energy stored at TBs). In addition, if ITB migration is induced by interaction with defects, then it is natural to speculate that the ITB migration velocity is also affected by the defect generation rate controlled by the dose rate during irradiation experiments. Fig. 4.11b shows the dependence of ITB migration on the dose rate at room temperature. The average ITB migration velocity (V_{ITB} , nm/s) decreased rapidly with increasing twin thickness at a high dose rate (2.5×10^{-3} dpa/s) compared to that at lower dose rates (2.5×10^{-3} dpa/s) compared to that at lower dose rates (2.5×10^{-3} dpa/s) is also shown (black line) as a reference.

4.4. 3D defect-TB interactions

4.4.1. SFT-TB interactions: mechanisms and experiments

SFTs are a dominant type of vacancy clusters in irradiated FCC metals with low-to-intermediate SFE [596–598]. Once formed, SFTs are very stable [44,599], but can be annihilated during interaction with interstitials or dislocations [600–603]. Based on MD simulations as shown in Fig. 4.12, Niewczas and Hoagland [541] suggested that Σ 3 {1 1 } CTBs

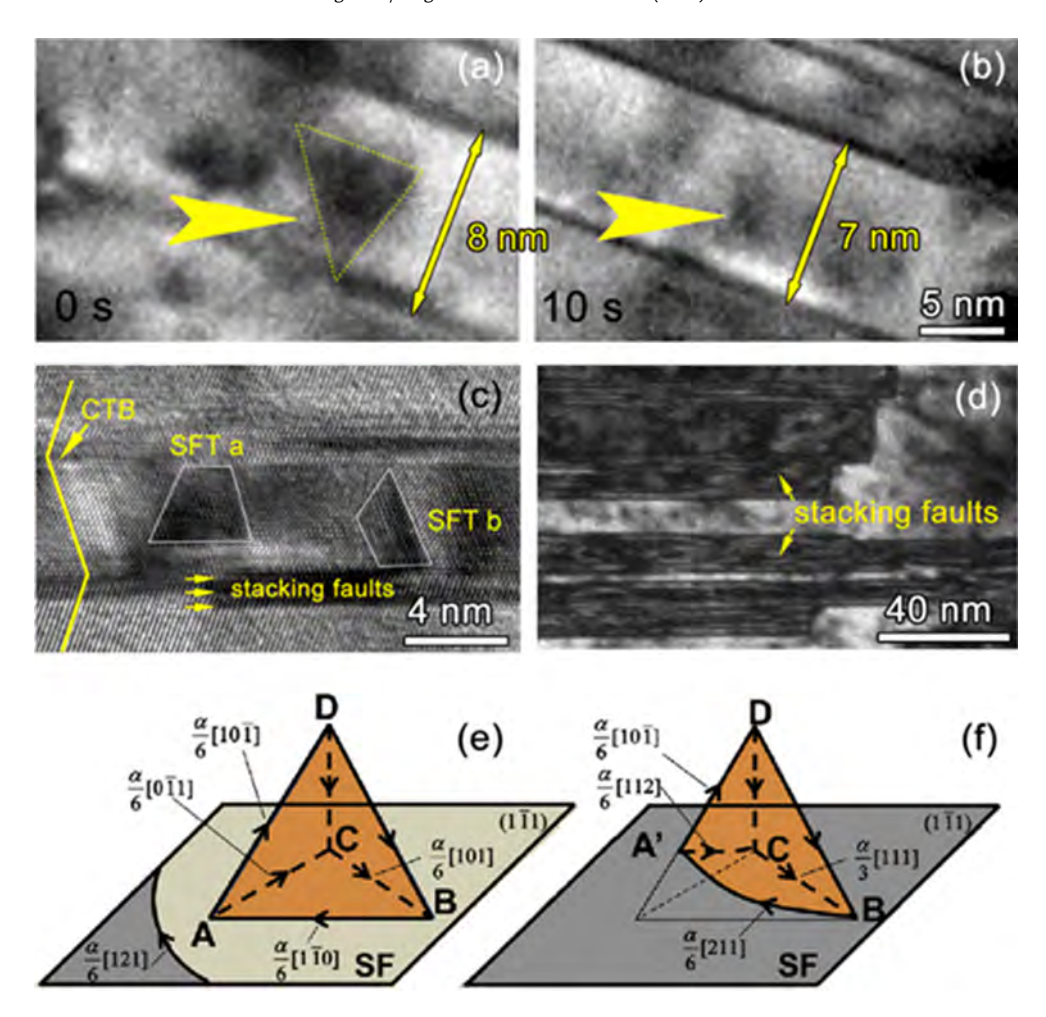


Fig. 4.14. (a-b) *In situ* observation of an SFT interacting with TBs over a dose range of 0.075–0.081 dpa. The apex of the SFT was in contact with a TB at 0 s and started to evolve. At 10 s, the SFT had a barely discernible core and the twin spacing shrank by 1 nm. (c) HRTEM image of two truncated SFTs at TBs. SFT-a was truncated from its apex, whereas SFT-b was destructed from its base. (d) TEM micrograph showing high density stacking faults induced by SFT-TB interactions residing along CTBs and within the twin interior [39]. (e and f) Schematic illustration of a Shockley partial migrating on the base plane of the SFT. The mobile Shockley partial interacted with two sessile stair-rod dislocations, AB and AC, generated two mobile Shockley partials on the surfaces of the SFT, ABD and ACD, which continued to glide on the SFT surface and resulted in the collapse of the SFT [604]. Reprinted with permission from Refs. [39,604].

could lead to the destruction of SFTs via interaction with partial dislocations (on CTBs). King and Smith studied the mechanism of point defect absorption by GBs and $\Sigma 3$ {1 1 1} CTBs in electron-beam irradiated Al and Cu, and showed that TBs may be biased sinks for dislocation loops [537]. It is likely that these CTBs are defective, and SFTs actually interact with tiny ITB steps at the CTBs. To investigate the interaction between TBs on SFTs, NT Ag was irradiated by Kr ions at RT inside a TEM microscope (Fig. 4.13a) [39]. A clear twin-size-dependence has been shown, *i.e.*, fewer SFTs formed in Ag with finer twins after irradiation to 1 dpa (Fig. 4.13b). It was also proposed that SFT-TB interactions result in a large number of truncated SFTs and a high-density of SFs at TBs and within twin matrix [604], consistent with prior MD simulations. The existence of SFs was confirmed by both the elongated diffraction dots and streaked lines in the inset SAD pattern of Fig. 4.13a.

The *in situ* evidence for annihilation of SFTs by TBs is shown in Fig. 4.14a and b, wherein the apex of an SFT approached a CTB at 0 s and disappeared by 10 s. In the meantime, the twin thickness was reduced from 8 to 7 nm. After post-irradiation analyses, as shown by the HRTEM image in Fig. 4.14c, two typical SFT morphologies have been revealed. SFT-a was truncated from its apex and SFT-b lost part of its base. The consequence of such interactions is the generation of high-density SFs as shown in Fig. 4.14c and d. The volume fraction of irradiation-induced SFs was estimated to be \sim 10%. Similar results were reported in Kr irradiated NT Cu [604].

The interaction mechanisms have been shown schematically although the knowledge of what is occurring at the atomic level is limited by the time and space resolution of current techniques [39]. When the SFT is approached by a TB from its base as shown in Fig. 4.14e, a $1/6[1\ 2\ 1]$ Shockley partial at the TB could interact with the stair-rod dislocations $1/6\langle 1\ 1\ 0\rangle$ in the

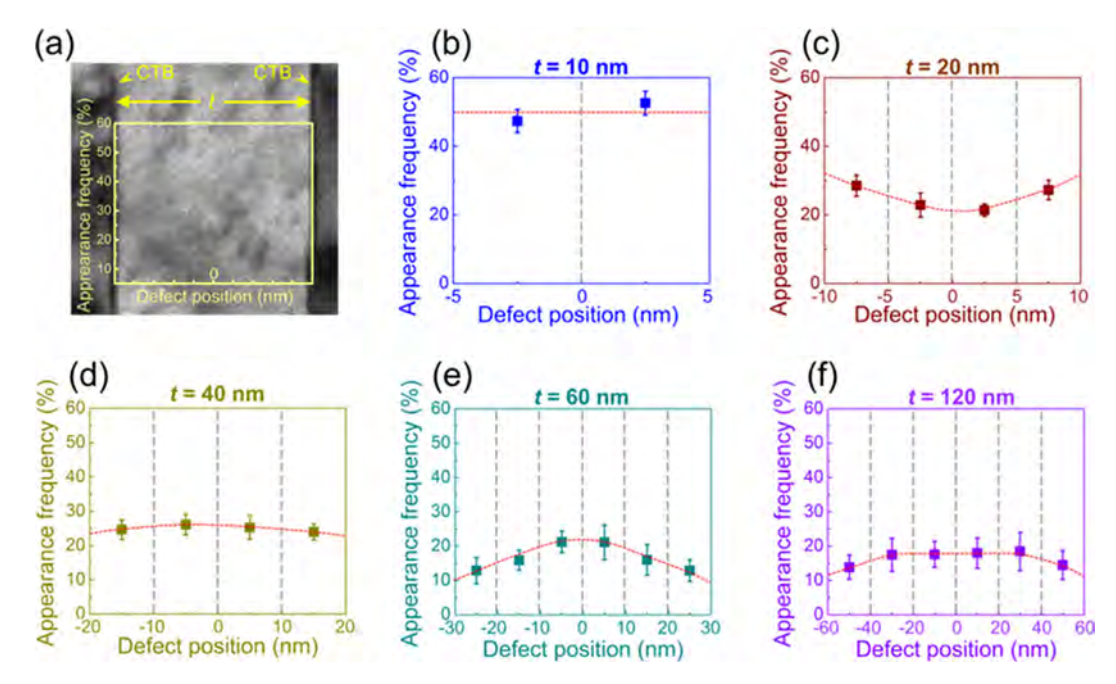


Fig. 4.15. Accumulative appearance frequency of defect clusters in NT Ag during 0.025 dpa Kr ion irradiation with respect to defect position for twins with different thicknesses. (a) The position 0 (center axis) was defined as the center of the twinned crystals. The left and right y axes represent the two twin boundaries. (b) For t = 10 nm, the defect clusters were distributed nearly uniformly. (c) For t = 20 nm, more defects appeared close to twin boundaries. (d-f) For t > 20 nm, the center of the twins tended to accumulate more defects than the areas near TBs [606]. Reprinted with permission from Ref. [606].

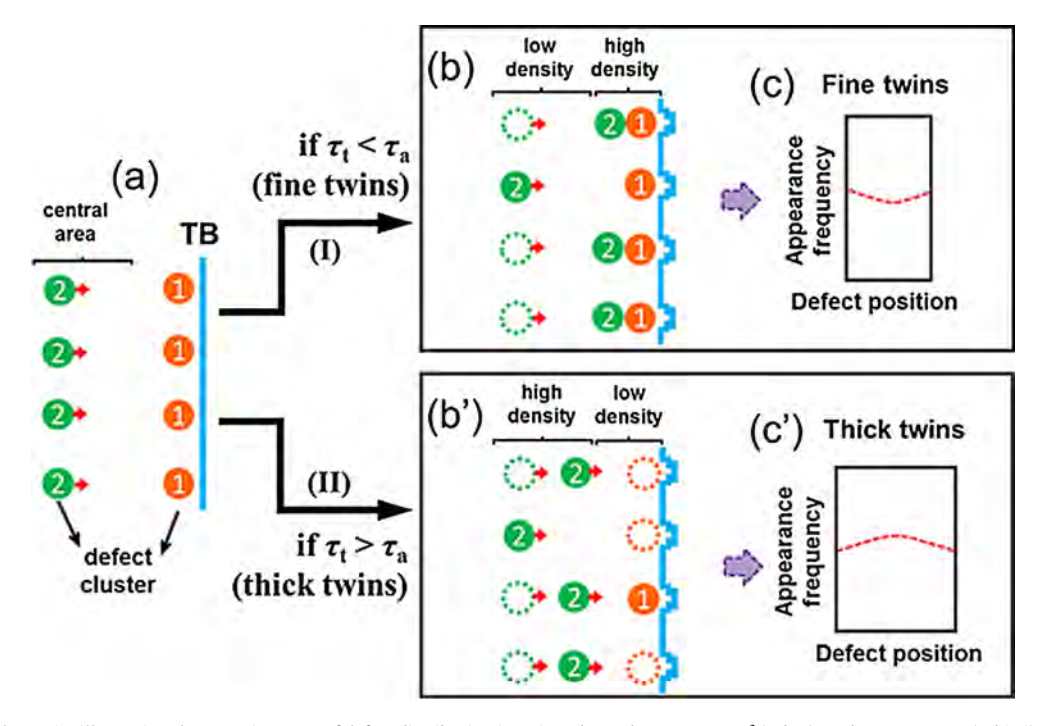


Fig. 4.16. Schematics illustrating the opposite types of defect distribution in twinned metals. Case I: $\tau_t < \tau^a$ (a-b-c); and case II: $\tau_t > \tau_a$ (a-b'-c'). τ_t is the time for a defect cluster to travel (migrate) to twin boundaries (defect sinks), and τ_a is the time it takes for a twin boundary to absorb adjacent defect clusters. (b) In case I (a-b-c), when twins are very fine, as $\tau_t < \tau_a$, defects (labeled by "2") arrive at twin boundaries before their predecessors (marked by "1") can be absorbed, thus, defect clusters pile-up near the TBs, resulting in a higher defect density near the TBs (c). Note that the TBs are distorted while attempting to absorb adjacent defect clusters. In Case II, the scenario is the opposite for thick twins and it is likely that $\tau_t > \tau_a$, *i.e.*, the arrival of group 2 defect clusters takes a longer time than the absorption of group 1 defect clusters adjacent to TBs. (c') Thus the central area exhibits a higher defect density [606]. Reprinted with permission from Ref. [606].

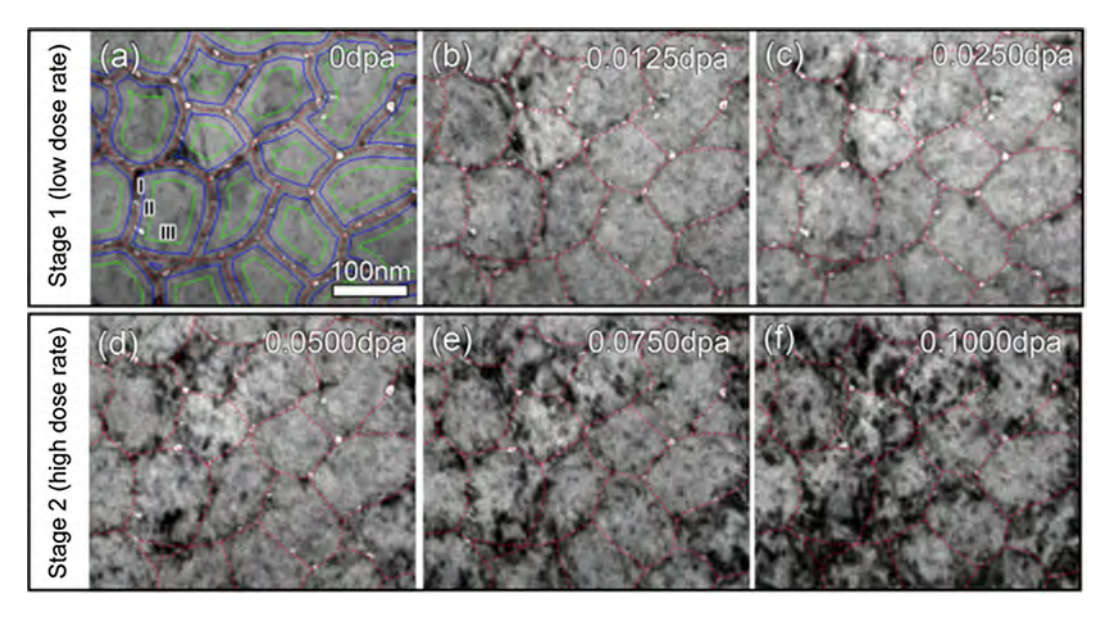


Fig. 4.17. Bright-field TEM snapshots showing the accumulation and distribution of defect clusters during *in situ* Kr⁺⁺ ion irradiation of nanovoid-nanotwinned Cu up to a dose of 0.1 dpa. Each domain is divided into three regions of equal area, marked in (a) by I, II and III that are bounded by red, blue and green lines, respectively. The irradiation-induced defects showed preferential distribution in Region IIII. (a–c) The defect evolution in stage 1 of low dose rate from 0 to 0.025 dpa. (d–f) The defect evolution in stage 2 of high dose rates from 0.025 to 0.1 dpa [607]. Reprinted with permission from Ref. [607].

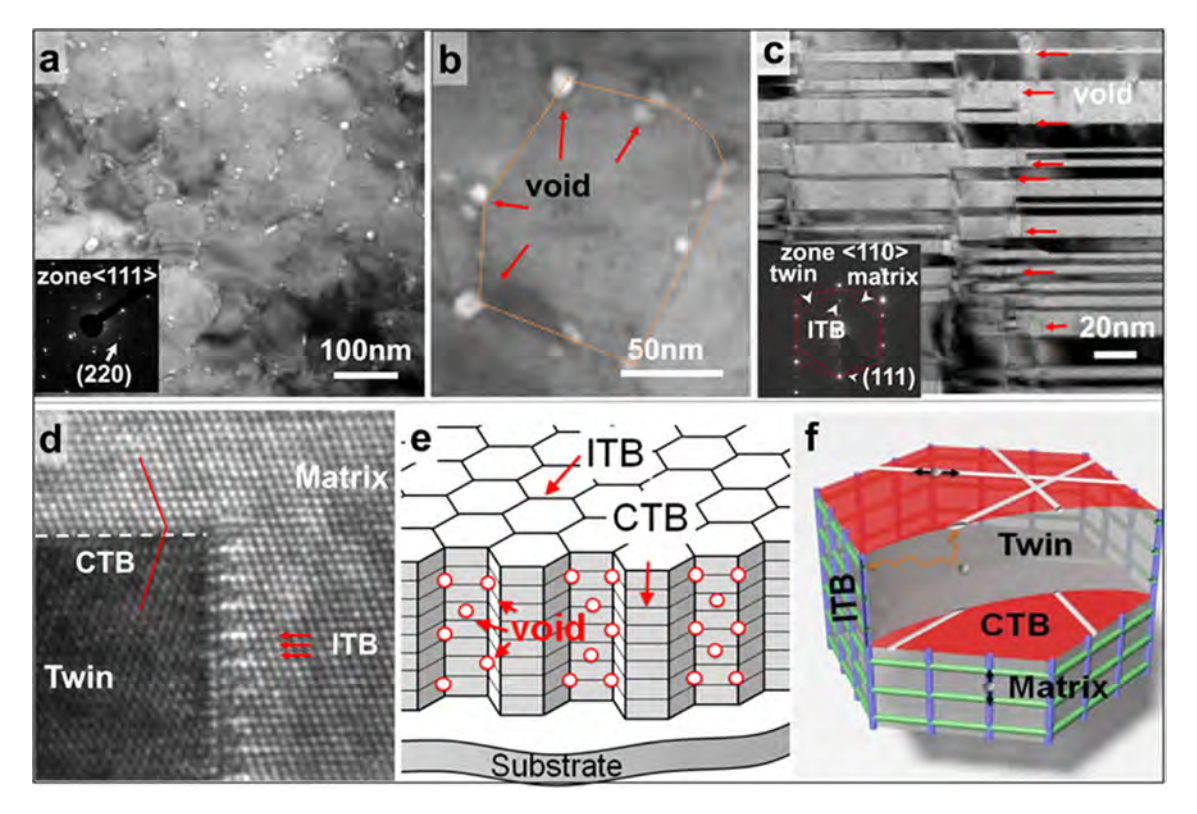


Fig. 4.18. (a and b) Plan-view TEM micrograph showing an as-prepared nanovoid-nanotwinned Cu film containing abundant nanovoids primarily surrounding columnar domain boundaries. (c) X-TEM micrograph showing high-density $\Sigma 3\{1\ 1\ 1\}$ CTBs with an average twin thickness of ~ 15 nm, and $\Sigma 3\{1\ 1\ 2\}$ ITBs decorated with many nanovoids with an average diameter of ~ 10 nm. The SAD pattern confirmed the formation of epitaxial NT Cu. (d) HRTEM image of CTBs and ITBs. (e) A conceptual schematic of metals with CTB and ITB networks and nanovoids. (f) Inside a typical columnar grain radiation-induced interstitials or their loops can rapidly migrate towards ITBs, where they can migrate rapidly to nanovoids [29]. Videos are available online in the original reference. Reprinted with permission from Ref. [29].

SFT, forming new mobile Shockley partials (1/6[2 1 1] and 1/6[1 1 2]), which propagate on ABD and ACD faces of the SFT. Consequently, Frank loops on the faces are unfaulted and the SFT eventually collapsed [598]. These studies might have brought up potential approaches to eliminate SFTs in irradiated FCC metals, *i.e.*, introducing a large density of ITBs or defective CTBs.

4.4.2. Helium bubbles in nanotwinned metals

The previous sections revealed that TBs can serve as active defect sinks by facilitating the recombination of point defects and favoring interactions between TB dislocations and defect clusters. It is thus natural to hypothesize that TBs might exert similar effects on the nucleation and distribution of helium bubbles. However, unlike high angle GBs, CTBs in NT Cu subjected to high doses of He ion irradiation were not found to curtail the formation of vacancy and interstitial clusters [462]. These observations have been rationalized using atomistic simulations, which show that the formation energies of vacancies and interstitials at CTBs were nearly identical to those of the Cu matrix, in contrast to the heterophase interfaces in nanolayers [428] or high-angle GBs in NC metals [605]. In addition, SFTs and loops were not observed in the specimens as He prevents vacancies from forming such clusters. Systematic studies by Han et al. on GB sink efficiencies of He irradiated Cu showed that variations in the width of the bubble-free zone was related to the misorientation angle and GB plane normal [236]. CTBs show only very small bubble free zones as their inclination angle is 0° (Fig. 2.17g and h). It should be noted that these studies focused solely on CTBs. Given that the excess volume at ITBs can store He atoms during irradiation, it is likely

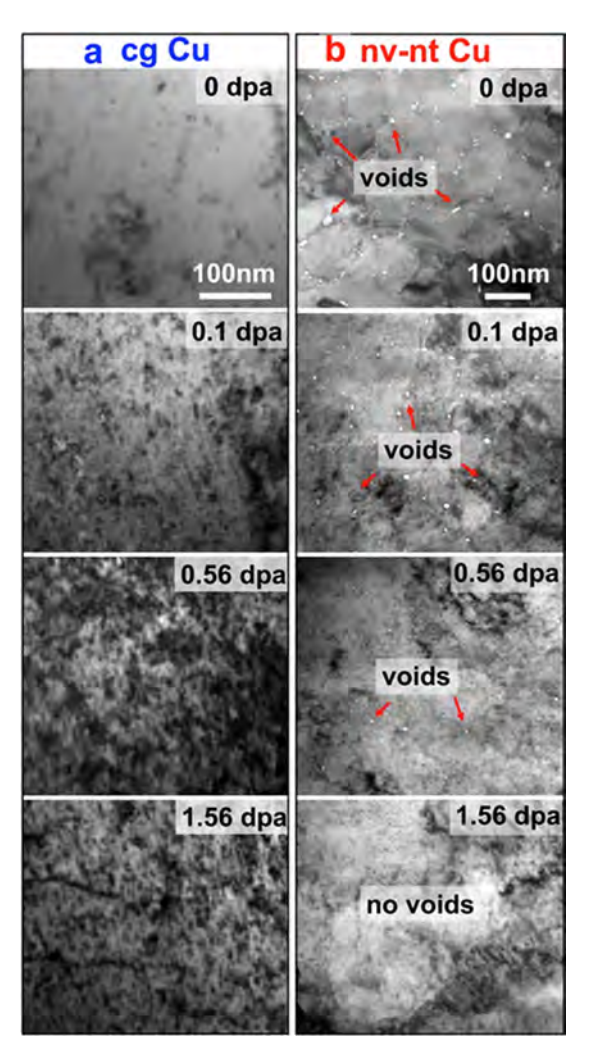


Fig. 4.19. Superior radiation tolerance and void shrinkage in nanovoid-nanotwinned Cu as evidenced by *in situ* Kr ion irradiation studies. The TEM snapshots in (a) and (b) show the drastically different evolution of the microstructure during *in situ* Kr ion irradiation of CG and nanovoid-nanotwinned (nv-nt) Cu. (a) During initial radiation of CG Cu by 0.1 dpa, there was a rapid and prominent increase in the density of defect clusters, while the density of dislocation loops increased monotonically with increasing dose and a high density of dislocation segments were observed by 1.56 dpa (b) In contrast, in nv-nt Cu, the density of dislocation loops increased slightly with increasing dose accompanied by a gradual elimination of nanovoids [29]. Reprinted with permission from Ref. [29].

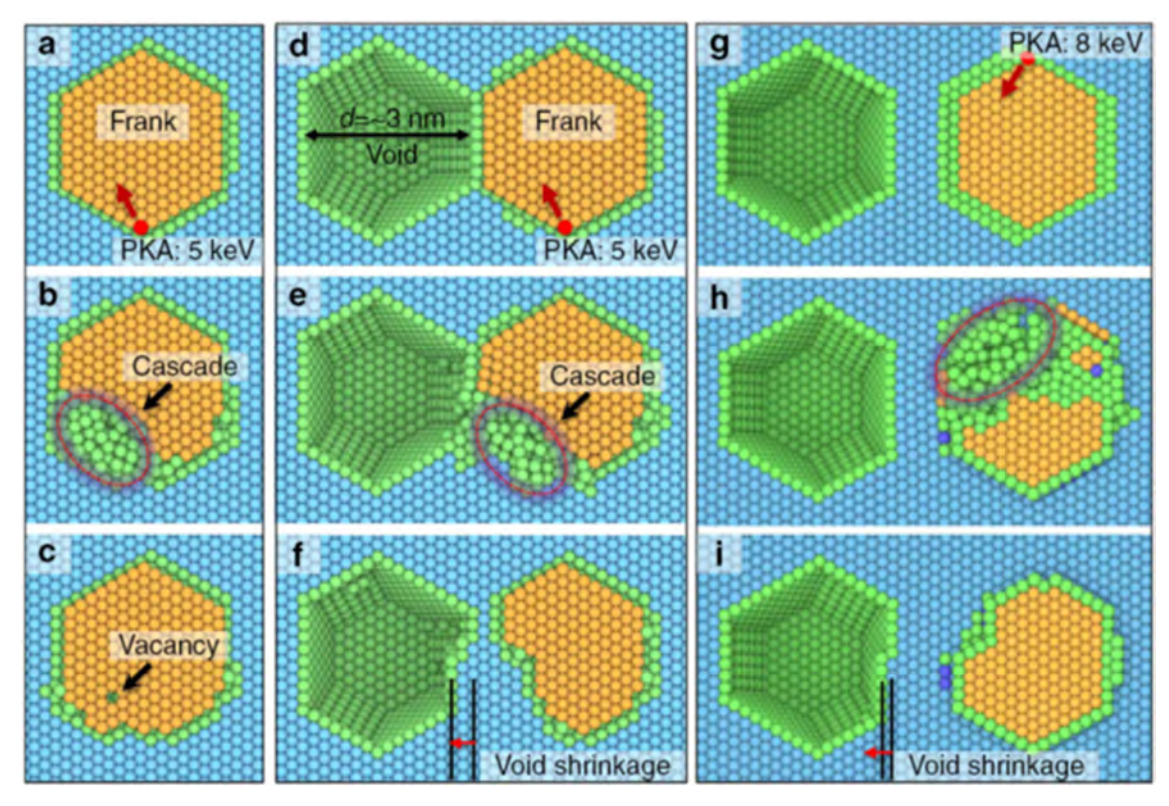


Fig. 4.20. Two-dimensional projected view of interstitial loop–nanovoid interactions. (a) For a stand-alone Frank loop, a 5 keV PKA generates a cascade at one corner of the loop (b). During the quenching process, the cascade shrinks, accompanied by recovery of the Frank loop. After retreat of the cascade, the Frank loop evolves back to its original configuration, apart from a vacancy at the loop and an interstitial out of the loop (a Frenkel pair) (c). (d) For a Frank loop immediately next to a void (d = 3 nm), a similar cascade was performed. (e) Accompanying retreat of the cascade, interstitials are absorbed into the void (f), leading to a shrinkage of the void and substantial removal of the Frank loop. No defects appeared outside the Frank loop (g) For a Frank loop ~1 nm away from a void (d = 3 nm), a similar cascade generated by an 8 keV PKA was performed (h). The interstitials of the Frank loop were attracted into the void (i), leading to shrinkage of the void and Frank loop. No defects appeared outside the Frank loop in cases (d) and (h) [561]. Reprinted with permission from Ref. [561].

that bubble nucleation at ITBs is different from that at CTBs. However, the correlation between He bubbles and ITBs remains unclear.

4.5. Anomalous defect distribution in nanotwinned metals

The statistics of the defect distribution in a 60-nm-thick twin in NT Ag irradiated at RT up to 0.6–1.0 dpa is shown in Fig. 4.4 [562]. The accumulative defect concentration was higher in the center of twins, as the defect density could be lower near defect sinks. However, in a follow-up study, Li et al. reported that the distribution of defects in NT Ag depended on the twin spacing. When a 20 nm-thick twin in NT Ag was irradiated at an ultra-low dose (<0.025 dpa) the defect concentration was greater near TBs [606], as shown in Fig. 4.15. At such an early stage of irradiation, well before the steady-state defect concentration is established, the distribution of defects is controlled more by kinetics than thermodynamics. To explain the anomalous defect concentration distribution in NT Ag, a hypothesis was proposed as shown in Fig. 4.16 [606]. A defect cluster was assumed to be in one of two stages, migration and absorption, before being annihilated. Therefore, the competition between defect migration time (τ_t) and absorption time (τ_a) determines the defect concentration distribution at an early stage of irradiation, where kinetics play an important role. For instance, in fine twins (Fig. 4.16b) defects are closer to TBs compared to thick twins (Fig. 4.16c), so τ_t is likely to be smaller than τ_a . As a result, defect clusters build up near the TBs as shown in Fig. 4.16b.

The anomalous defect concentration distribution has also been observed in Kr ion irradiated nanovoid-nanotwinned Cu [607]. Radiation damage in such an interesting structure is discussed in detail in Section 4.7. A series of *in situ* TEM snapshots in Fig. 4.17 demonstrate the evolution of defect morphology up to 0.1 dpa at low and high dose rates in irradiated NT Cu with nanovoids. Qualitatively, the TEM micrographs show that a majority of the irradiation-induced defect clusters (black dots) were located near domain boundaries, especially in stage 1 of low dose radiation (Fig. 4.17a–c). The anomalous phenomenon observed further proves that TBs are effective defect sinks and may significantly enhance radiation tolerance.

4.6. Healing of nanovoids and alleviation of irradiation damage by nanovoid-nanotwinned architecture

Previous studies showed that NT Ag [39] and Cu [604] exhibited improved irradiation tolerances compared with their CG counterparts due to unique features of the NT structure. In this section, we discuss the possibility of void healing enabled by nanotwins. In general, continuous intense radiation leads to a high density of voids with increasing void size. Some voids can be removed by annealing at elevated temperatures, where plenty of mobile interstitials are activated. Hence, void shrinkage can be used as a measure of the mobility of interstitials within the materials. In a recent work by Chen et al., nanovoids were introduced into NT Cu, forming nanovoid-nanotwinned Cu [29]. Fig. 4.18a and b show that as-prepared Cu contained abundant nanovoids primarily surrounding columnar domain boundaries. Fig. 4.18c shows high-density CTBs with an average twin thickness of ~15 nm and ITBs decorated with many nanovoids with an average diameter of ~10 nm. These 3D voids distributed at different depths in the film were introduced during a magnetron sputtering process, and where void density can be controlled by tailoring the deposition rate, substrate temperature, and epitaxy between the film and substrate. The HRTEM image shown in Fig. 4.18d shows the atomic structure of CTBs and ITBs. Fig. 4.18e displays a conceptual schematic of nanovoid- nanotwinned metals containing ITB-CTB networks and nanovoids along ITBs. Fig. 4.18f shows diffusion channels associated with dislocations at CTBs and ITBs that could potentially transport interstitials and their clusters towards nanovoids.

The radiation response of nanovoid- nanotwinned Cu was investigated via *in situ* Kr ion irradiation studies. TEM snapshots compare the drastic difference in the microstructure evolution between the coarse grained (CG) (Fig. 4.19a) and nanovoid-nanotwinned Cu (Fig. 4.19b). During initial radiation of CG Cu up to 0.1 dpa, there was a rapid, prominent increase in the density of defect clusters; the density of dislocation loops increased monotonically with increasing dose and a high density of dislocation segments were observed by 1.56 dpa. In contrast, in nanovoid-nanotwinned Cu, the density of dislocation loops increased slightly with increasing dose, accompanied by a gradual elimination of nanovoids. By 0.56 dpa, a significant decrease in the void density was observed. By 1.56 dpa, the voids were mostly removed.

Superior irradiation tolerance of such materials has been ascribed to the ITB-CTB network and nanovoids. The significance of such ITB-CTB networks has been covered previously in Section 4.1 (Fig. 4.6), and thus we focus on the role of nanovoids. During *in situ* irradiation experiments, the absorption of interstitial loops by nanovoids was frequently observed. MD simulations revealed the dynamic process by which a void absorbs a neighboring dislocation loop (Fig. 4.20). Three scenarios subjected to self-ion irradiation, were compared, including a stand-alone Frank (interstitial) loop, a nanovoid and Frank loop pair in immediate contact, and a similar pair separated by ~1 nm. During irradiation, the individual Frank loop was disturbed, but only slightly changed its shape after a cascade (Fig. 4.20a-c). Meanwhile, the Frank loops immediately contacting the void (Fig. 4.20d-f) or slightly separated from the void (Fig. 4.20g-i) were absorbed by the void after radiation. The amount of net interstitials (inside a Frank loop) absorbed by a void depends on the energy and fluence of primary knock-on atoms (PKA) and the detailed absorption mechanisms, as discussed in [561].

4.7. Summary and future outlook

In this section, we briefly summarized several significant characteristics of the ion irradiation response of NT metals. First, there are *in situ* irradiation studies showing that both CTBs and ITBs can effectively engage and eliminate irradiation-induced defects, and that TB affected zones clearly exist in heavy ion irradiated NT metals. Second, a direct consequence of these interactions is TB migration, which may have profound impacts on the design of irradiation tolerant materials. Meanwhile the migration of TBs leads to detwinning, a process that depends on twin thickness, which may however reduce the twin density and in turn the radiation tolerance. So there is a need to explore methods for enhancing the stability of TBs under irradiation. Third, TBs can destruct SFTs, which are typically considered as very stable defect clusters. Fourth, the influence of TBs on the resistance to He ion irradiation remains a topic that needs further investigation. The role of CTBs and ITBs on He bubble nucleation and growth may be an interesting subject for future studies. Fifth, despite the abundant *in situ* evidence of defect—TB interactions, simulations revealing the underlying physics remain limited. Finally, there are abundant opportunities to investigate the mechanical behavior of irradiated NT metals and alloys towards the design of mechanically reliable structural metals in nuclear reactors.

5. Radiation damage in nanoporous materials, nanowires and nanoparticles

Metallic nanoporous (NP) materials, nanowires and nanoparticles as shown in Fig. 5.1a–c with a large surface-to-volume ratio exhibit unique properties that enable potential applications, such as energy storage, catalysts, filters, and gas sensors [523,608–615]. For instance, NP Au possesses remarkable catalytic activity for oxidation reactions compared to its bulk counterpart [616]. It has also been reported that the strength of NP materials can be dramatically improved by reducing the length scale of ligaments and pores. NP Au with high porosity can be as strong as bulk Au and the ligaments in NP Au can approach the theoretical yield strength when the ligament diameter reduces to approximately 10 nm, as shown in Fig. 5.1d and e [617]. In addition, the Young's modulus of ZnO nanowires increases with decreasing wire diameter as shown

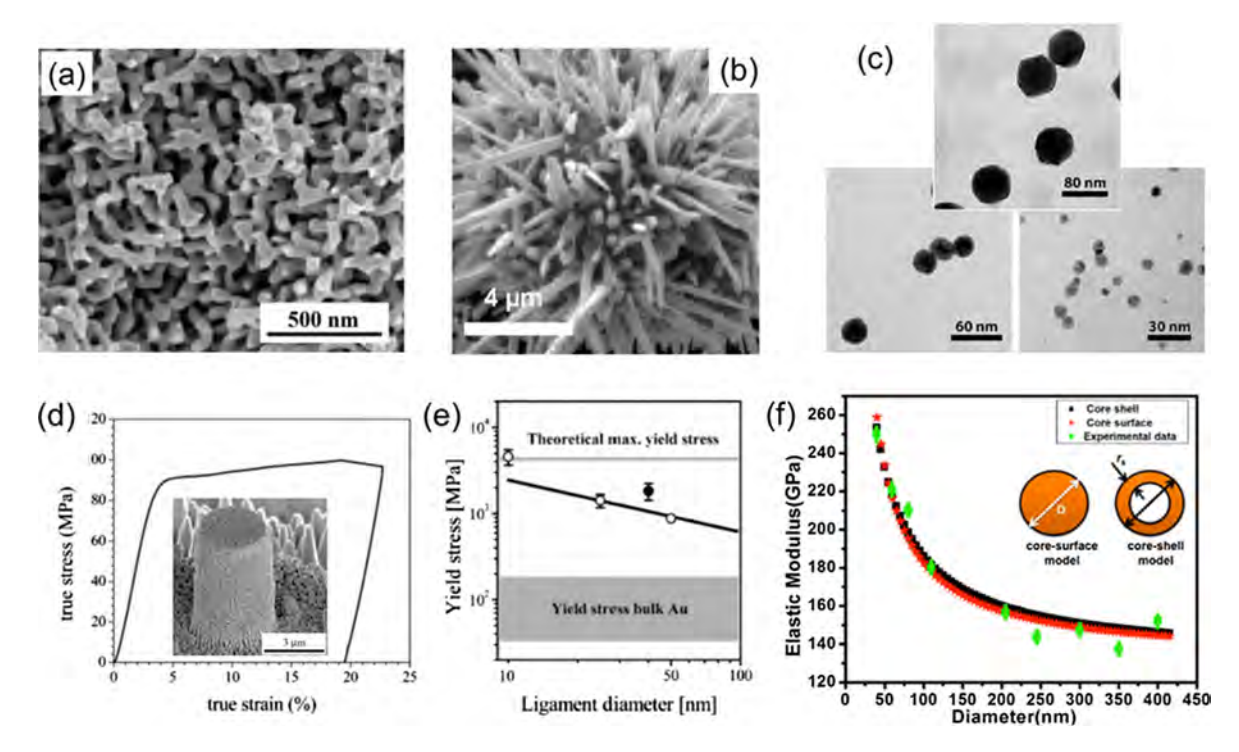


Fig. 5.1. SEM micrographs of (a) open-cell foam morphology of NP Au [617] and (b) as-received ZnO nanowires [450]. (c) *In situ* TEM images of as-deposited Au nanoparticles on carbon grids [629]. (d) Stress-strain curve of an NP Au pillar. The embedded SEM micrograph shows the NP Au pillar used for uniaxial microcompression tests. Despite its high porosity, the NP Au is as strong as bulk Au (10–200 MPa) [617]. (e) The yield strength of NP Au increased with decreasing ligament diameter [617]. (f) The elastic modulus as a function of wire diameter for ZnO nanowires [618]. Reprinted with permission from Refs. [450,617,618,629].

in Fig. 5.1f; when the wire diameter is \geq 200 nm, the elastic modulus reaches that of bulk ZnO [618]. These unique properties are ascribed to the high surface-to-volume ratios of nanopores, nanowires and nanoparticles. This section will examine the radiation tolerance of these surface-dominated nanomaterials.

5.1. The sink strength of nanoporous materials

We begin the discussion of the radiation response of NP materials by revisiting the sink strength for voids. A cellular model and embedding model have been developed to describe the sink strength of a void [137]. The cellular model is appropriate for an array of uniformly distributed voids, whereas the embedding model is applicable when voids are randomly distributed. The results derived from the two models were in qualitative agreement with each other. Here, to simplify the

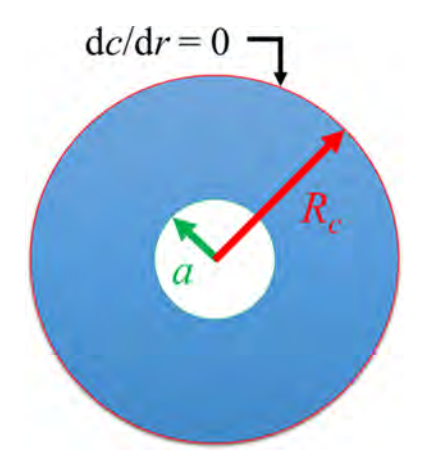


Fig. 5.2. Schematics of a void and the boundary of a void-influenced zone. The void radius is a. When r = a, c = 0 and when $r = R_c$, dc/dr = 0.

discussion, we briefly summarize the major conclusions derived from the cellular model. When voids are the only defect sinks in materials, the concentration of radiation-induced defects can be described as follows:

$$D\left[\frac{d^2c}{dr^2} + \frac{2}{r}\frac{dc}{dr}\right] + K = 0 \tag{5.1}$$

We assume voids are uniformly distributed within a material. Fig. 5.2 shows a void and corresponding void-influenced zone, where a is the void radius. When r = a, c = 0; and when $r = R_c$, dc/dr = 0. Hence, R_c can be approximated as the void-to-void distance. The solution for c becomes:

$$c(r) = \frac{K}{D} \frac{(r-a)}{6ar} [2R_c^3 - (r+a)ar]$$
 (5.2)

The sink strength for voids can thus be calculated as [137]:

$$k_V^2 = 4\pi a C_V^0 f_c, \tag{5.3}$$

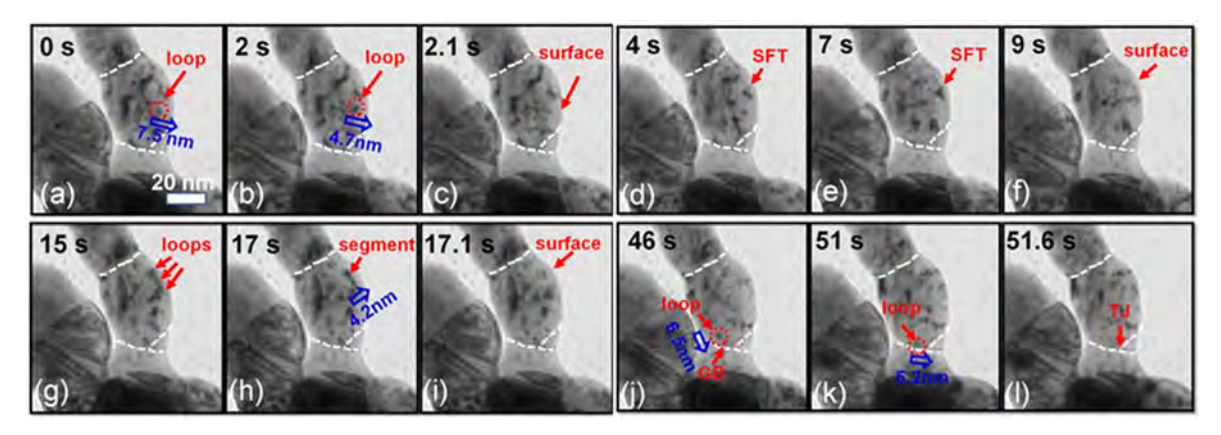


Fig. 5.3. *In situ* video snapshots showing several representative events during defect capture by free surface or TJs during Kr ion irradiation of NP Ag at RT over 1.18–1.27 dpa. (a–c) Evidence of rapid absorption of individual dislocation loops by the free surface. A loop migrated towards the free surface and was immediately removed by it within 0.1 s. (d–f) An SFT was gradually removed by the free surface from 7 to 9 s. (g–i) A dislocation segment was rapidly absorbed by the free surface. (i–l) Absorption of a dislocation loop by a TJ in the ligament [619]. Reprinted with permission from Ref. [619].

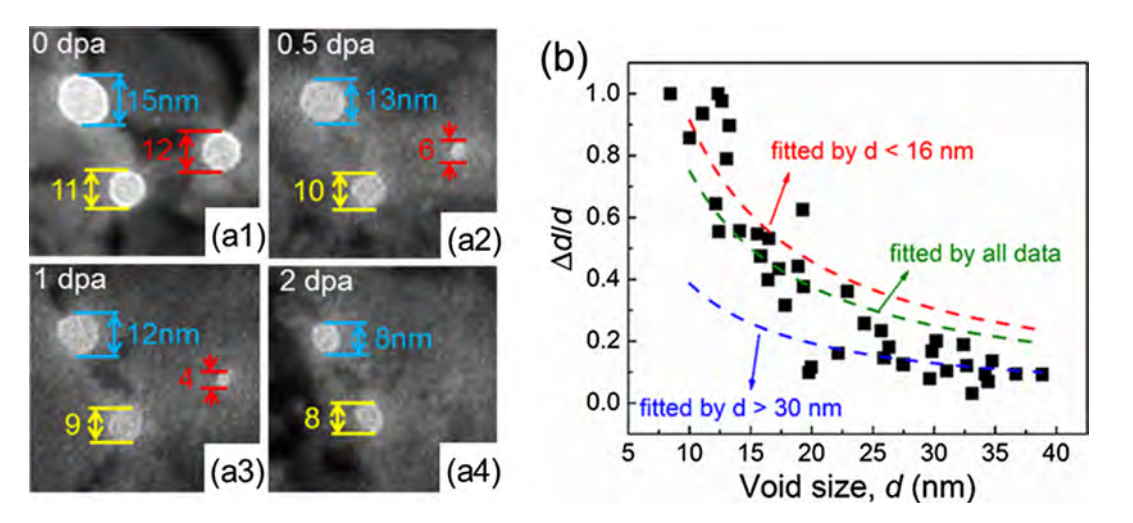


Fig. 5.4. *In situ* irradiation snapshots showing the shrinkage of nanopores in Au under Kr irradiation at RT. (a1) Three pristine pores with diameters of 15, 12 and 11 nm before irradiation. (a2-a3) Under irradiation up to 1 dpa, defects migrated towards the nanopores, and the size of pores continuously decreased. (a4) At 2 dpa, the 12 nm-large void disappeared and the size of the other two nanopores decreased from 15 to 8 nm and from 11 to 8 nm, respectively. (b) The normalized diameter reduction, Δ d/d, as a function of pore size. The olive dashed line is the result of fitting all data, while the red and blue dashed lines are fitting results for data in the range of d < 16 nm and d > 30 nm, respectively [40]. Reprinted with permission from Ref. [40].

where: $C_V^0 = \frac{3}{4\pi R_c^3}$, $R_0^3 = R_c^3 - a^3$, and:

$$f_c = \frac{5(R_c^3 - a^3)^2}{[5R_c^6 - 9aR_c^5 + 5a^3R_c^3 - a^6]}$$
 (5.4)

5.2. Free surface – defect interactions in nanoporous materials

5.2.1. Capture of radiation-induced defect clusters by free surface

The superior radiation tolerance of NP structures arises from abundant free surfaces, which are considered as effective defect sinks. *In situ* irradiation experiments were performed to directly examine the nucleation, growth and absorption of defect clusters in NP Ag [619] and NP Au [40]. Fig. 5.3 shows direct evidence of the removal of defect clusters by the free surface of NP Ag. Irradiation-induced defect clusters, including individual dislocation loops, SFTs and dislocation segments, in NP Ag were absorbed by either the free surfaces or TJs.

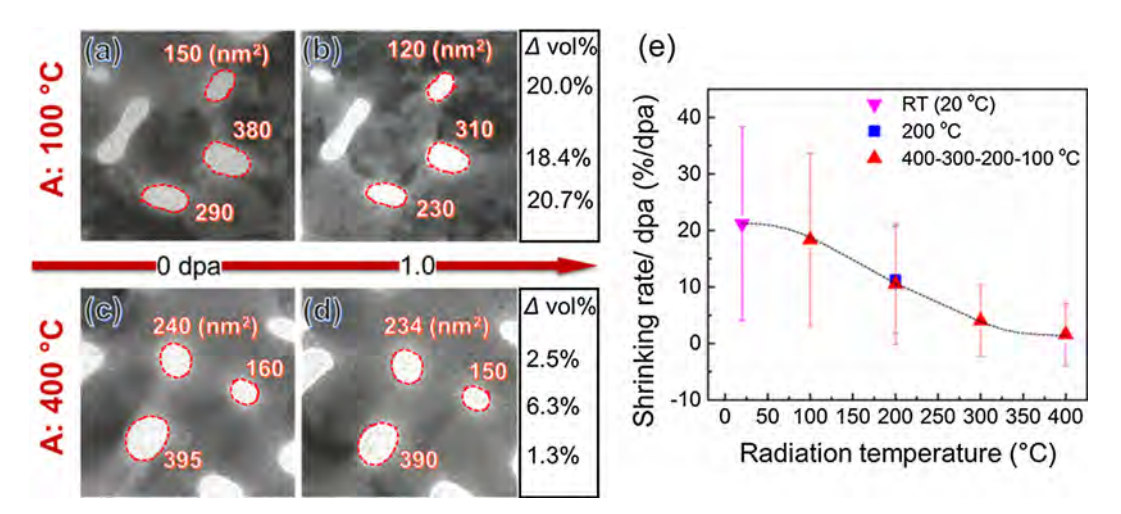


Fig. 5.5. (a–d) *In situ* TEM video snapshots showing the temperature-dependent pore shrinkage in Kr ion irradiated NP Au at two different temperatures, $100 \,^{\circ}$ C (a and b) and $400 \,^{\circ}$ C (c and d). At $100 \,^{\circ}$ C, three nanopores with areas of 150, 380 and $290 \, \text{nm}^2$ decreased in volume by 20%, 18.4%, and 20.7%, respectively after irradiation to 1 dpa. In comparison, at $400 \,^{\circ}$ C three nanopores only shrank by 2.5%, 6.3% and 1.3%. (e) Statistical data showing the temperature-dependent shrinkage of nanopores during irradiation of NP Au. The average pore shrinkage rate (%/dpa) decreased with the increasing irradiation temperature, from $\sim 21\%$ /dpa at RT [40] to 1.6%/dpa at $400 \,^{\circ}$ C [620]. Reprinted with permission from Ref. [40,620].

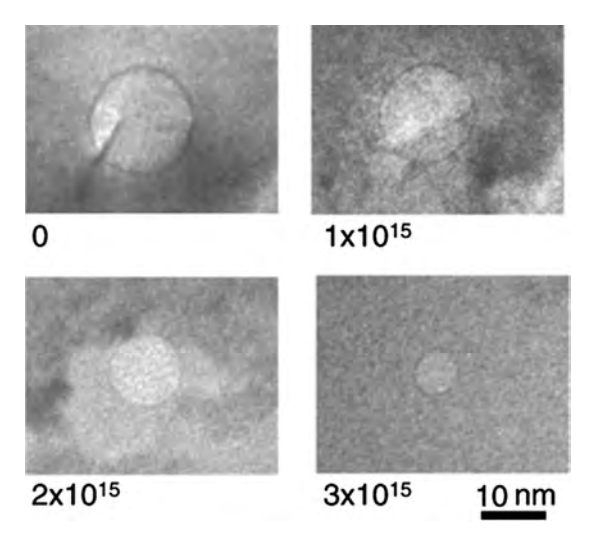


Fig. 5.6. In situ TEM micrographs showing the shrinkage of a single nanocavity in Si during self-ion irradiation at \sim 21 °C up to a fluence of 3 \times 10¹⁵ ions/cm² [621]. Reprinted with permission from Ref. [621].

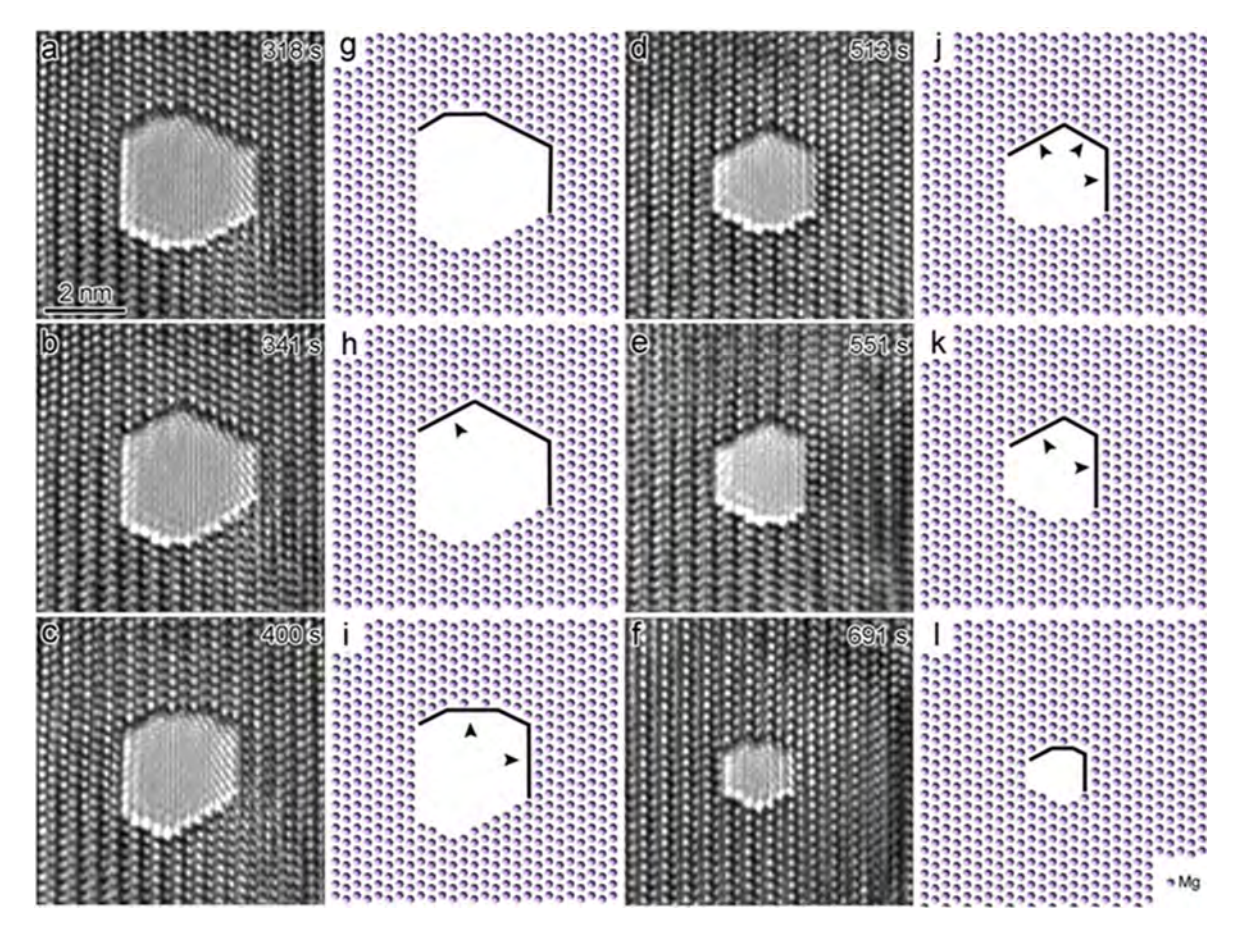


Fig. 5.7. Electron-beam-assisted healing of nanopores in magnesium alloy (86 wt.%Mg, 9 wt.%Al, 1 wt% Zn and 4 wt% Sn). (a–f) Sequential high-resolution TEM images showing the changes in the of nanopore morphology during continuous e-beam irradiation. (g–l) Schematic illustration corresponding to (a–f), respectively [615]. Reprinted with permission from Ref. [615].

5.2.2. Radiation induced void shrinkage

Void swelling in irradiated metallic materials has been widely observed at elevated temperatures [72–75]. Hence, it is surprising that void shrinkage was observed in NP Au by *in situ* Kr ion irradiation [84]. Fig. 5.4a shows the shrinkage of nanovoids in NP Au with diameters of 15, 12 and 11 nm during Kr ion irradiation at RT. The void shrinkage was explained as a consequence of two processes: one is the lack of vacancies to feed the growth of voids, as the majority of vacancies could be bound in the form of sessile vacancy clusters; the other is the biased flock of interstitials and their clusters to nanovoids during irradiation. A recent study of nanovoid-NT Cu shows the existence of significant tensile stress around nanovoids, where smaller voids generated higher stress fields near void surfaces compared to larger voids [29]. Consequently, smaller voids may capture defects more rapidly during irradiation, leading to their higher shrinkage rate. This rationale is consistent with experimental observations (Fig. 5.4b) that show the normalized void diameter reduction, $\Delta d/d$, is inversely proportional to the initial void diameter in NP Au. The green dashed line is the result of fitting all data, while the red and blue dashed lines are fitting results for the data in the range of d < 16 nm and d > 30 nm, respectively. The difference between the fitting results indicates that the smaller voids contract faster than the larger voids [40].

The irradiation-temperature-dependent void shrinkage has also been studied [620]. The shrinkage rate of voids in NP Au decreases with the increasing irradiation temperature as shown in Fig. 5.5. For Au irradiated at RT most vacancies are tied to sessile vacancy clusters (SFTs, vacancy loops) formed directly in the displacement cascades. Consequently, the mobility of vacancies and the nucleation and growth of voids are strongly suppressed. Thus, more interstitials migrate towards the free surface of the nanopores, leading to nanopore shrinkage. At higher irradiation temperatures, the vacancy mobility, and the recombination rate between interstitials and vacancies increase. The nanopores shrinkage rate decreases at high temperature as the nanopores absorb fewer defects. No obvious growth of nanopores was observed at elevated temperatures up to 400 °C.

Void shrinkage has also been observed in other material systems during irradiation, including self-ion irradiated Si [621] and e-beam irradiated Mg [615]. For instance, the *in situ* TEM micrographs in Fig. 5.6 show the shrinkage of a single nanocavity in Si during self-ion irradiation at \sim 21 °C up to a fluence of 3 \times 10¹⁵ ion/cm². Xu et al. performed *in situ* TEM studies on

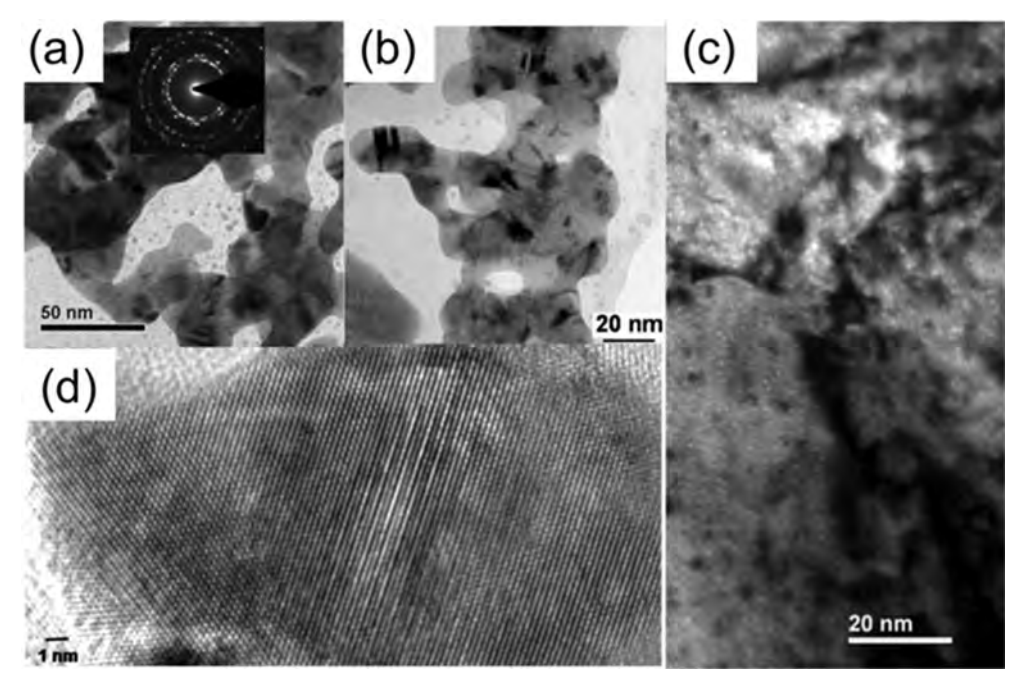


Fig. 5.8. Microstructural evolution of NP Au under irradiation. Irradiation of NP Au was performed with 45 keV Ne * to a dose of 4.5×10^{14} /cm 2 at 300 K. (a) Unirradiated NP Au showing that the ligaments are polycrystalline. (b) Microstructure of irradiated NP Au. (c) Under-focus bright-field TEM images of single crystal Au film after irradiation at the same condition, showing the formation of Ne bubbles and dislocation loops. (d) HRTEM image of irradiated NP Au. Little radiation damage was observed in (b) and (d) [623]. Reprinted with permission from Ref. [623].

pure Mg under electron-beam irradiation at RT [621]. Voids first formed a platelet shape and then gradually evolved into a nearly equiaxial geometry. The atomistic simulations suggested that the initial growth along the longitudinal direction is controlled by slow nucleation kinetics of vacancy layers on basal facets and anisotropic vacancy diffusivity [622]. The subsequent growth along the platelet thickness direction was driven by thermodynamics to reduce its surface energy. Zheng et al. used *in situ* HRTEM techniques to demonstrate layer-by-layer growth of atomic planes at the nanopore periphery, and observed that the spreading of the electron-beam leads to shrinkage and removal of nanopores, as shown in Fig. 5.7 [615]. The authors attributed the healing of nanopores in Mg-based alloys to the e-beam-induced anisotropic diffusion of Mg atoms near nanopore edges.

5.3. Size effect in irradiated nanoporous materials and nanowires

5.3.1. Size effect in nanoporous materials

It has been previously reported that the radiation resistance of NP metals depends on the ligament size of NP metals and the irradiation conditions [623]. Ion irradiation experiments on Au nanofoams have been performed to select the microstructure window of radiation tolerant NP Au in terms of ligament size at different dose rate [623]. Au nanofoams were synthesized by electrochemically dealloying Si from evaporated amorphous Si-Au thin films. The TEM image in Fig. 5.8a shows that a ligament diameter of 10–20 nm and a pore size of 20–50 nm resulted in a density of \sim 35–45% [623]. The ion irradiation experiments were performed at RT with 45 keV Ne ions up to a dose of 4.5 \times 10¹⁴/cm² at a dose rate of \sim 1 \times 10¹³ ions/cm²/s. The foam structure showed excellent radiation tolerance, without notable microstructural changes (Fig. 5.8b), in contrast to the formation of significant irradiation damage in single crystal Au (Fig. 5.8c) under the same irradiation conditions. The HRTEM micrograph in Fig. 5.8d reveals little defect clusters in the irradiated NP Au.

In situ irradiation experiments have been performed to study NP Ag synthesized by dealloying of the sputtered $Ag_{23}Cu_{77}$ film [619]. As shown in Fig. 5.9a and b, the average ligament size in NP Ag was ~40 nm, with an average island size of ~150 nm. Fig. 5.9c-h compare the microstructural evolution in NP and CG Ag under Kr ion irradiation at RT. At 0.02 dpa, a large number of defect clusters were formed in CG Ag (Fig. 5.9d), whereas NP Ag remained intact (Fig. 5.9g). At 0.25 dpa, both the size and density of defect clusters were significantly increased in CG Ag (Fig. 5.9e), while only a few small defect clusters formed in the ligaments of NP Ag (Fig. 5.9h). Similar results have been reported in NP Au prepared by dealloying of rolled $Ag_{65}Au_{35}$ leaves (Fig. 5.10a) [40]. In situ Kr ion irradiation at RT was performed for both NP and CG Au, and TEM snapshots from *in situ* videos compared the microstructural evolution of CG and NP Au irradiated under the same conditions. From 0 to 0.02 dpa, a few defect clusters formed in NP Au (Fig. 5.10b), whereas the defect density increased rapidly in CG Au (Fig. 5.10b'). At 0.2 dpa, both the diameter and density of defect clusters in CG Au increased significantly (Fig. 5.10c'), while

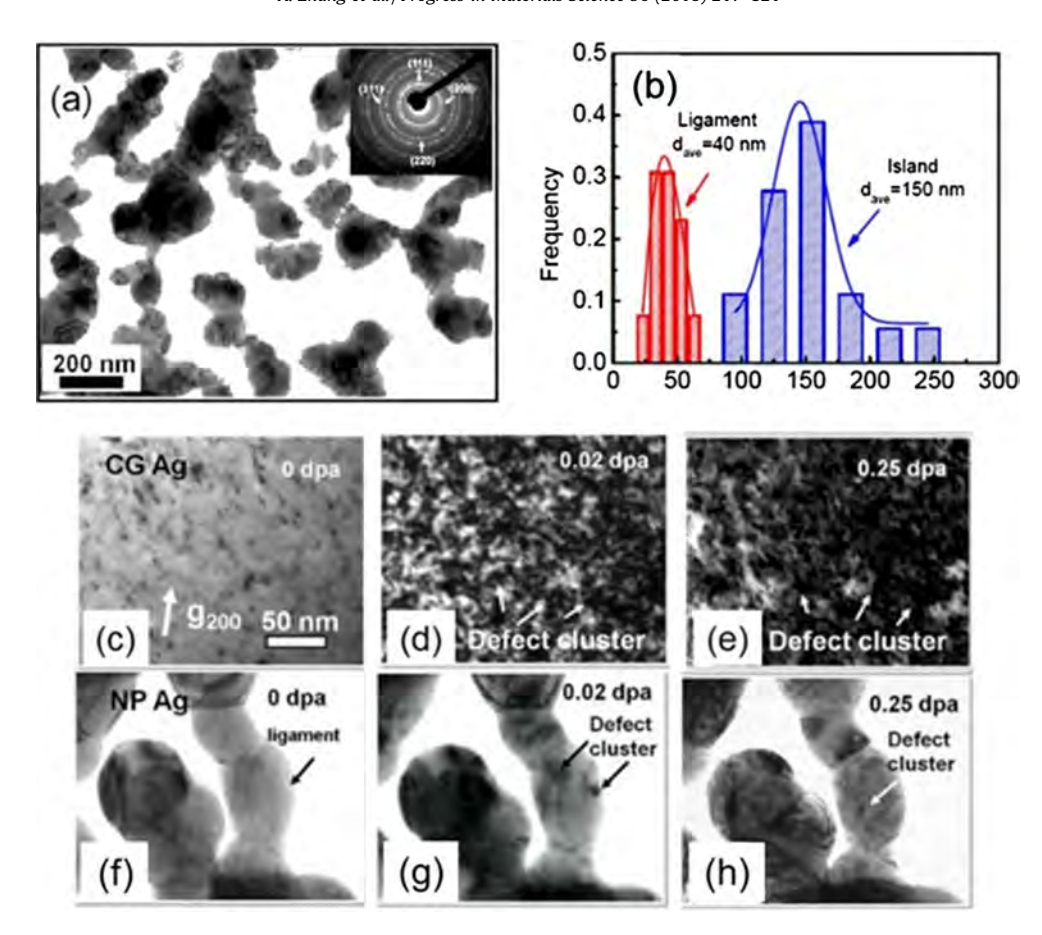


Fig. 5.9. (a) Bright-field TEM micrograph of NP Ag. (b) Frequency statistics showing an average ligament size of ~40 nm, and average island size of ~150 nm. (c-h) There were obvious differences between the microstructures of CG (c-e) and NP (f-h) Ag subjected to Kr ion irradiation at RT at different doses. (d, g) After irradiation at 0.02 dpa, CG Ag contained a high density of defect clusters, whereas NP Ag remained intact. (e, h) By 0.25 dpa, there was a significant increase in both the size and density of defect clusters in CG Ag, while only a few defect clusters were observed in the ligaments of NP Ag [619]. Reprinted with permission from Ref. [619].

only a few defect clusters were generated in NP Au (Fig. 5.10c). Kr ion irradiation caused a gradual and moderate increase in the defect density of NP Au up to 0.5 dpa (Fig. 5.10b–d). Under the same irradiation condition, CG Au accumulated significantly more defects at 0.5 dpa (Fig. 5.10b'–d'). At this dose level (Fig. 5.10d and d'), the average diameter of defect clusters in NP Au was much smaller than that in CG Au.

In a follow-up study, Li et al. performed temperature dependent *in situ* Kr ion irradiation studies with NP Au via a series of isothermal experiments (Fig. 5.11a) [620]. Such a temperature-jump test has the advantage of obtaining defect accumulation statistics during a single *in situ* experiment, and thus significantly increasing the efficiency of an *in situ* study. As shown in Fig. 5.11b, the defect density in NP Au decreased at elevated temperatures. In addition to the studies of NP Au and Ag, an *in situ* Kr ion irradiation study of porous Mg has also been performed [624]. Although the Mg did not have nanoscale pores, the results were similar; *i.e.*, defects accumulate rapidly in irradiated CG Mg, but gradually and moderately in porous Mg as shown in Fig. 5.12 [624].

Fig. 5.13 shows the evolution of the size and density of defect clusters in NP and CG Au at RT and during the temperature-jump test. The average saturation size of the defect clusters was \sim 10 and 4 nm in CG and NP Au, respectively (Fig. 5.13a). The defect density in both CG and NP Au reached saturation at a similar dose, \sim 0.1 dpa (Fig. 5.13b) [40]. Clearly, the free surface plays a major role in removing irradiation-induced point defects and defect clusters in NP Au. Although statistical studies showed a moderate reduction of the defect cluster density (a factor of 2) and cluster size (a factor of \sim 2.5) in irradiated NP Au compared to CG Au, the difference in the point defect concentration between CG and NP Au can be substantial. Fig. 5.13c and d show statistical results obtained from temperature-based jump tests of NP Au and CG Au. The saturation defect size in NP Au (Fig. 5.13c) was \sim 4 nm and showed only slight temperature dependence. In contrast, for irradiated CG Au, the defect size reached \sim 10 nm at RT, and decreased monotonically to \sim 4 nm with increasing irradiation temperature up to 400 °C. The large difference in defect size between CG Au and NP Au irradiated at RT indicates that the free surface inhibits the growth of defect clusters in NP Au by absorbing both vacancies and interstitials. However, the average defect size in NP Au and CG Au irradiated at 400 °C was similar (\sim 4 nm), presumably due to accelerated vacancy-interstitial

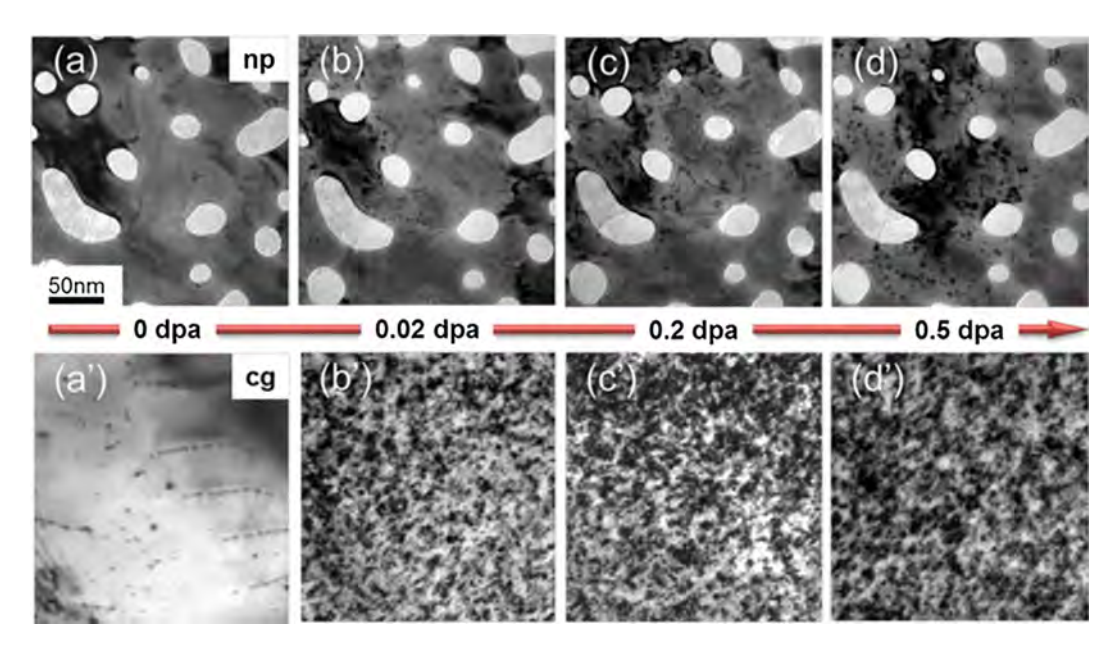


Fig. 5.10. TEM snapshots obtained from videos revealing drastically different irradiation responses of NP and CG Au subjected to *in situ* Kr ion irradiation at RT. (a–a′) Before irradiation, both NP and CG Au had few preexisting defects. (b–d) TEM snapshots showing a gradual and moderate increase in the defect density of irradiated NP Au, up to 0.5 dpa. (b′–d′) In contrast, CG Au rapidly accumulated many more defects by 0.5 dpa [40]. Reprinted with permission from Ref. [40].

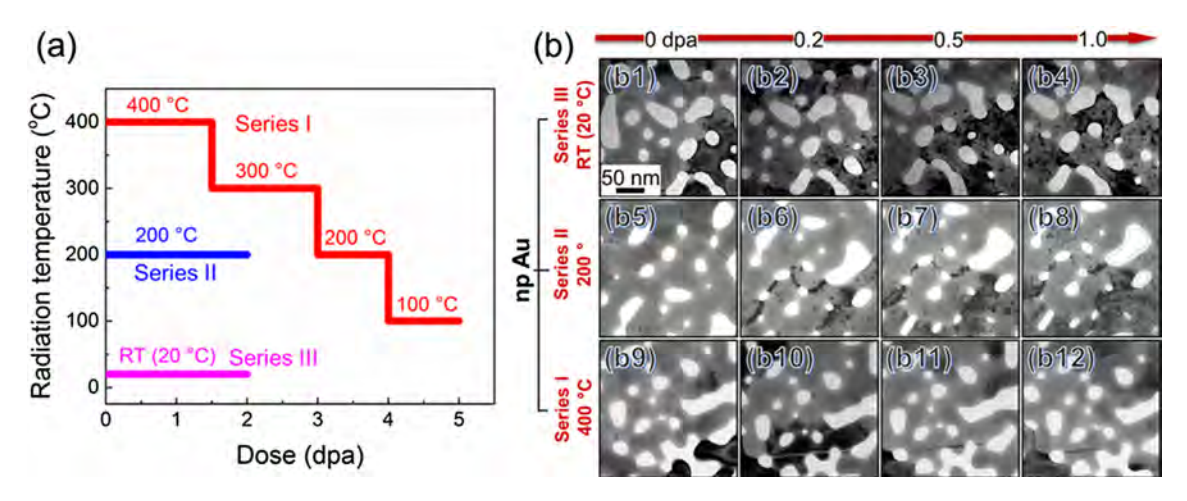


Fig. 5.11. (a) The summary of in situ irradiation experiments on NP Au reported in [620]. Series I: temperature-jump tests $(400 \rightarrow 300 \rightarrow 200 \rightarrow 100 \,^{\circ}\text{C})$, Series II: at constant 200 °C and Series III: at RT. (b) Corresponding TEM snapshots obtained from in situ videos showing the irradiation response of NP Au at various irradiation temperatures. Before irradiation, NP Au contained few defects (b1, b5, b9). (b2-b4) During irradiation, many defects accumulated in NP Au at RT with doses up to 1 dpa. (b5-b8) At 200 °C, irradiation induces fewer defects in NP Au, and much fewer defects in NP Au at 400 °C (b10-b12). Therefore, the defect density decreased with increasing irradiation temperature. Reprinted with permission from Ref. [620].

recombination. The saturated defect density in both NP and CG Au decreased gradually with increasing irradiation temperature (Fig. 5.13d).

It could be speculated that most of the nanovoids are removed during irradiation, indicating that the irradiation resistance of NP metals may degrade during subsequent irradiation. However, numerous studies showed that the presence of nanovoids significantly delays damage accumulation in NP metals by more than an order of magnitude. Furthermore, the void shrinkage rate significantly decreases at the dose rate relevant to nuclear reactors, and hence nanovoids may operate as defect sinks to mitigate radiation damage over a much longer period of time under low-dose radiation. In addition, deliberate introduction of nanovoids with a desired distribution of sizes and various densities may significantly prolong the radiation stability of irradiated metallic materials. Further investigations on the stability of nanovoids are necessary before this concept can used in practical reactor applications.

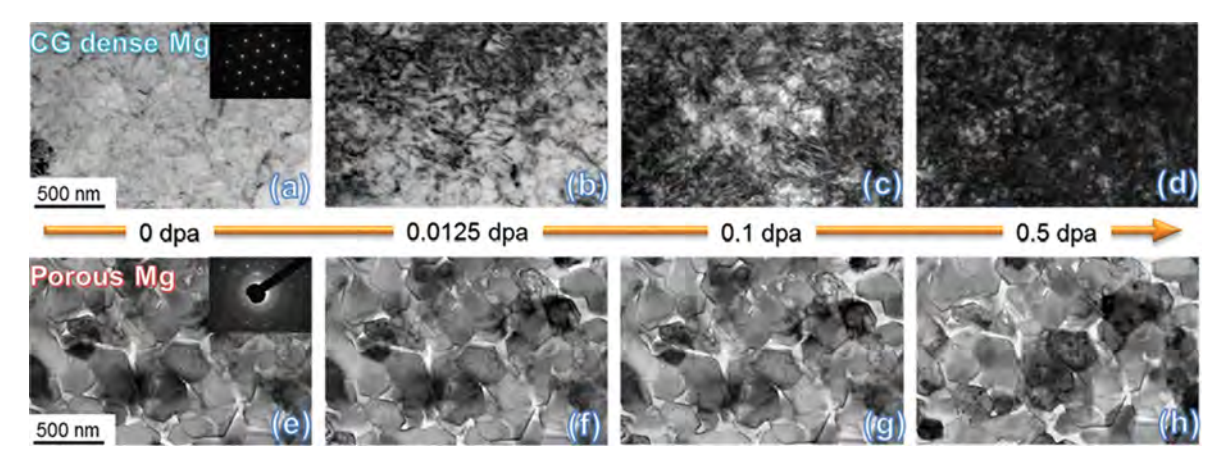


Fig. 5.12. TEM snapshots extracted from an *in situ* irradiation video showing drastically different irradiation responses between CG and porous Mg subjected to Kr ion irradiation at RT [624]. (a–d) During irradiation of CG Mg, the number of defects increased rapidly by 0.0125 dpa. After 0.5 dpa, abundant defects were introduced. (e–h) In contrast, a gradual and moderate increase in the defect density was observed in irradiated porous Mg. Reprinted with permission from Ref. [624].

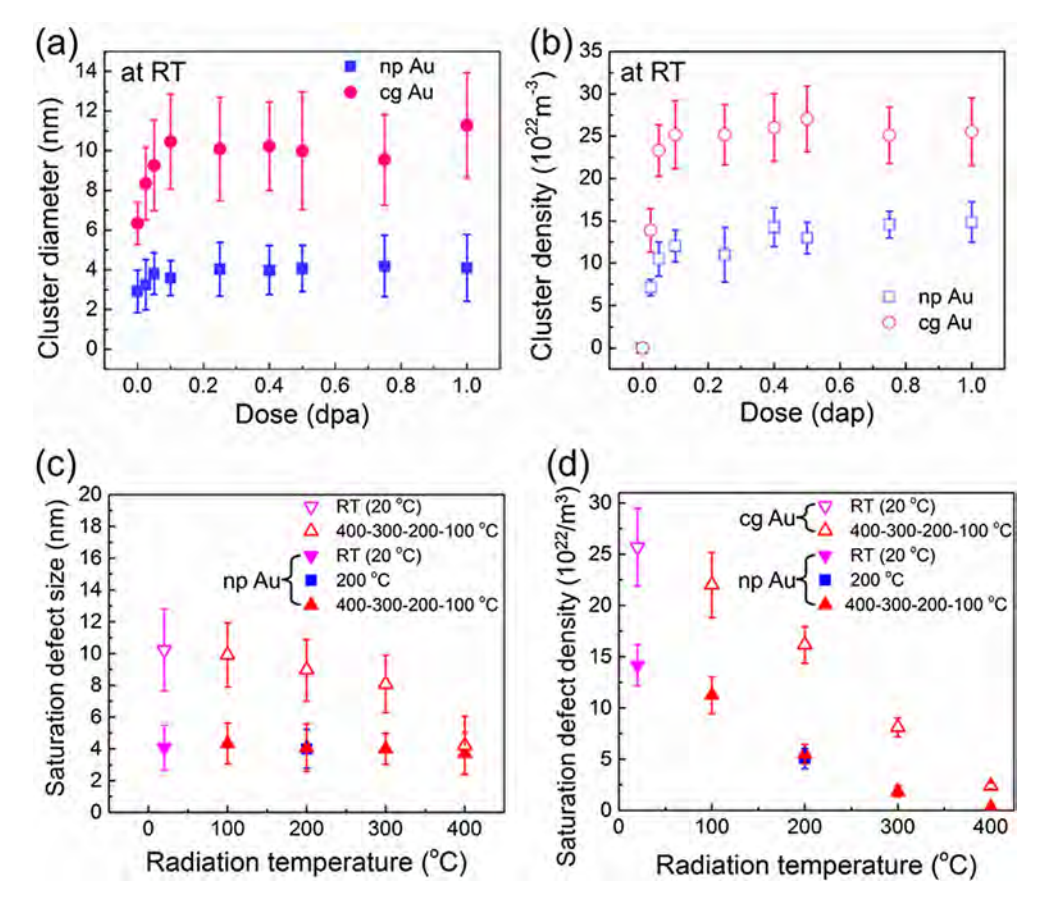


Fig. 5.13. (a and b) Statistical results of defect size and density as a function of dose in NP Au and CG Au *in situ* irradiated by Kr ions at RT [40]. (a) The average defect cluster diameters were \sim 10 nm and \sim 4 nm for CG and NP Au, respectively. (b) The saturated defect density in NP Au was half of that in CG Ag. (c and d) Statistical results of defect size and density vs. irradiation temperature for NP and CG Au. (c) The saturation defect size in NP Au was \sim 4 nm and showed only minor temperature dependence. In contrast, in irradiated CG Au, the defect size reached a plateau at \sim 10 nm at RT, then decreased monotonically to \sim 4 nm with increasing temperature to 400 °C. (d) The saturation defect density in NP Au and CG Au decreased gradually with increasing irradiation temperature [620]. Reprinted with permission from Ref. [620].

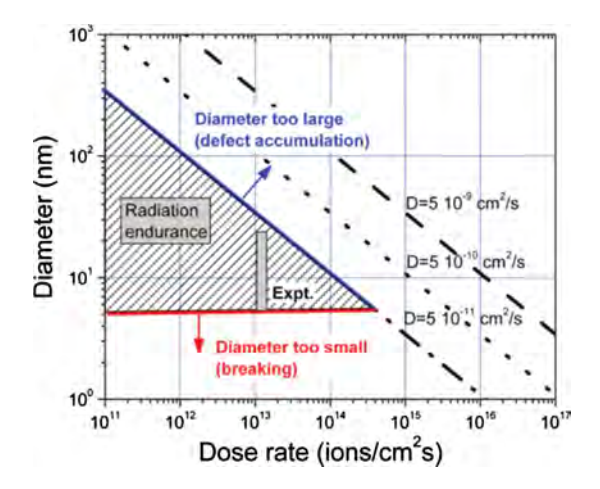


Fig. 5.14. Size effect on stability and design of radiation-tolerant NP metals. Irradiation resistant ligaments are predicted to be those within the triangular area. The upper critical limit was estimated for three diffusivities (D) of defect clusters [623]. Reprinted with permission from Ref. [623].

MD simulations showed that the radiation resistance of NP Au depends on the ligament size compared to that of the collision cascade size and the defect migration distance in the time interval between collision cascades [41]. Fig. 5.14 shows the radiation response of Au foam at RT (ligament size vs. dose-rate). When the ligament size was similar to or smaller than the cascade size, ligament melting and breaking were observed. When the ligament size was larger than the migration distance of defects between consecutive cascades, irradiation damage accumulated in a similar way as for conventional materials. In between these dimensions, the foam was more resistant to irradiation damage by the annihilation of defects at free surfaces.

5.3.2. Size effect in nanowires

In addition to NP materials, a size effect on the irradiation tolerance has also been observed in nanowires. Sun et al. showed that ZnO nanowires have distinct DDZs under *in situ* Kr ion irradiation [450]. As shown in Fig. 5.15a–d, the width of the DDZ is \sim 25 nm. The core of nanowires with a diameter of 70 nm contained a high-density dislocation loops

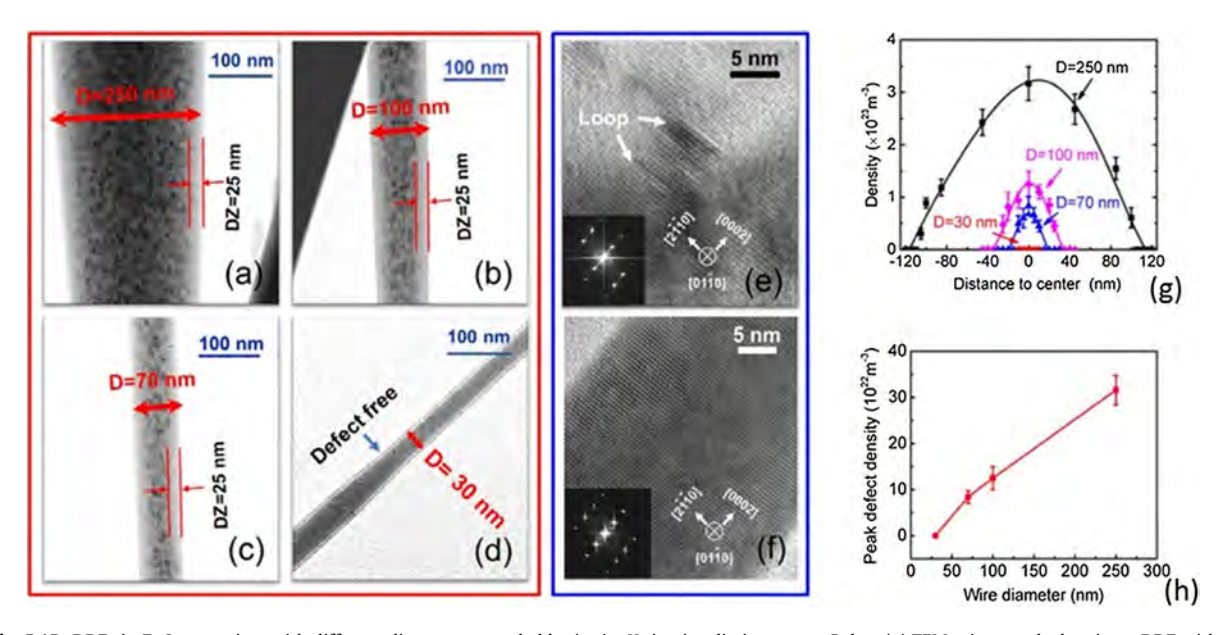


Fig. 5.15. DDZs in ZnO nanowires with different diameters revealed by *in situ* Kr ion irradiations up to 5 dpa. (a) TEM micrograph showing a DDZ with a width of ~25 nm in a ZnO nanowire with an average diameter D of ~250 nm; a similar DDZ width was also observed for nanowires with D of 100 nm (b) and 70 nm (c). The density of defect clusters reduced with decreasing wire diameters. (d) When D = 30 nm, no clear evidence of dislocation loops was observed; this wire was nearly immune to irradiation damage. (e) HRTEM image showing dislocation loops in irradiated nanowire with D of 70 nm. Dislocation loops, with D of ~5 nm, were located on $\{0\ 0\ 0\ 1\}$ planes. (f) HRTEM image of the irradiated nanowire (D = 30 nm) showing the absence of dislocation loops. (g) Defect cluster density vs. the distance to the center of wires with D = 30–250 nm. (h) ZnO nanowires with smaller diameter have lower peak defect density [450]. Reprinted with permission from Ref. [450].

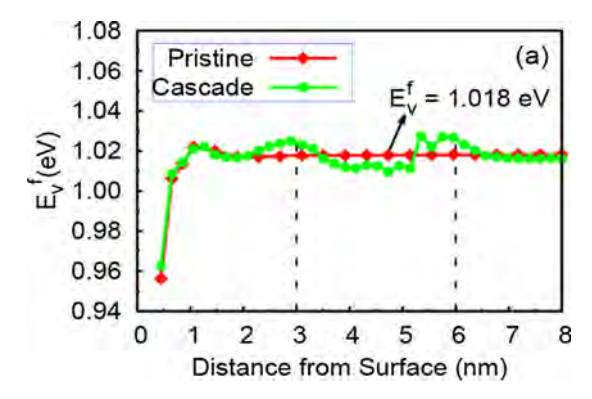


Fig. 5.16. Vacancy formation energy vs. vacancy-to-surface distance in Au nanowires [625]. Reprinted with permission from Ref. [625].

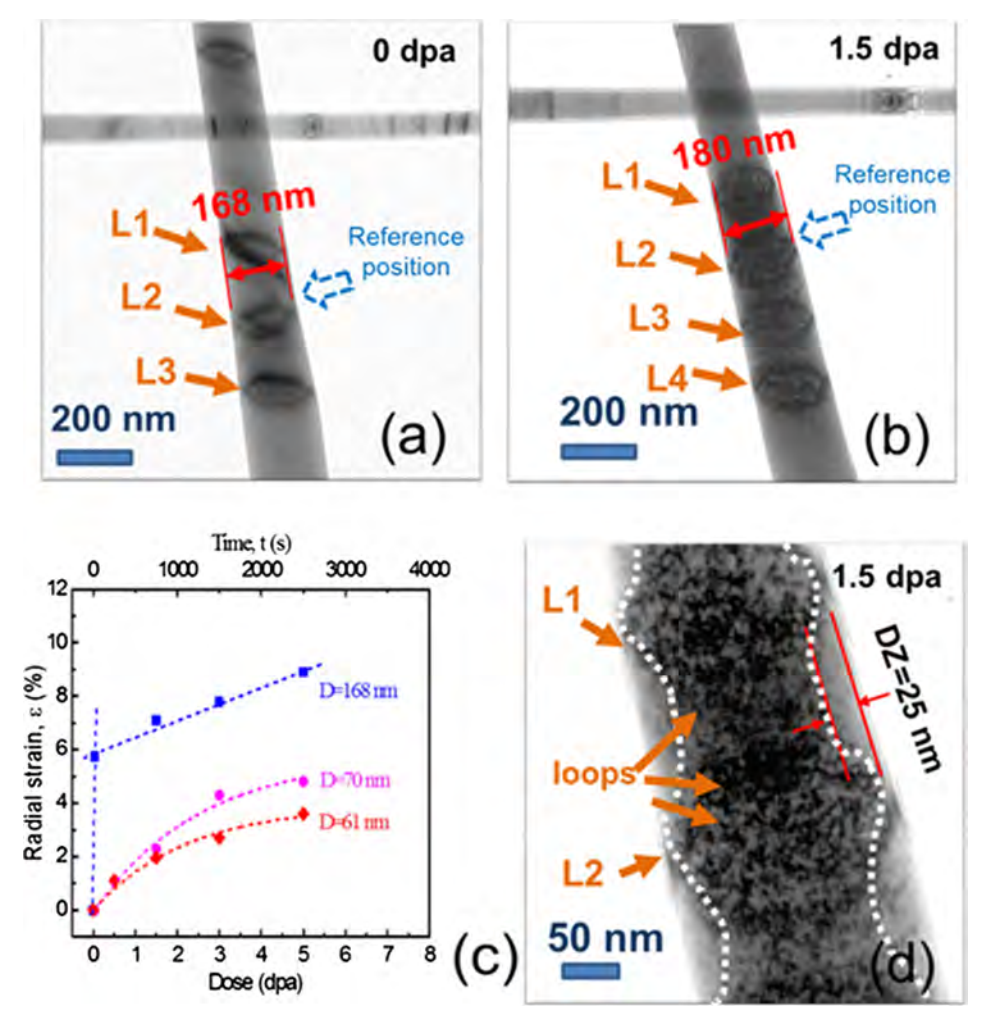


Fig. 5.17. Radiation-induced strain and the influence of internal defect sinks on loop distribution. (a) Bright field TEM image of several preexisting dislocation loops (L1–L3) in a ZnO nanowire prior to irradiation. (b) After Kr ion irradiation up to 1.5 dpa, a high density of defect clusters was observed near an array of hexagonal preexisting dislocation loops (L1–L3). The wire diameter (measured from the same location) swelled from 168 to 180 nm, where the dashed arrows show the reference position for the measurements. Notice that another loop (L4) migrated upward along the axial direction of the wire during radiation. (c) Comparison of irradiation-induced swelling (radial strain) in wires of various diameters shows that broader wires (D = 168 nm) swelled rapidly to \sim 9.0% by 5 dpa. In contrast, wires with smaller initial diameter (61 nm) swelled to only \sim 3.6%. (d) Magnified TEM micrograph of the loops L1 and L2 showing that a large number of small dislocation loops were trapped by pristine dislocation loops. Hence, consequently a dumbbell-shaped distribution of small loops was observed [450]. Reprinted with permission from Ref. [450].

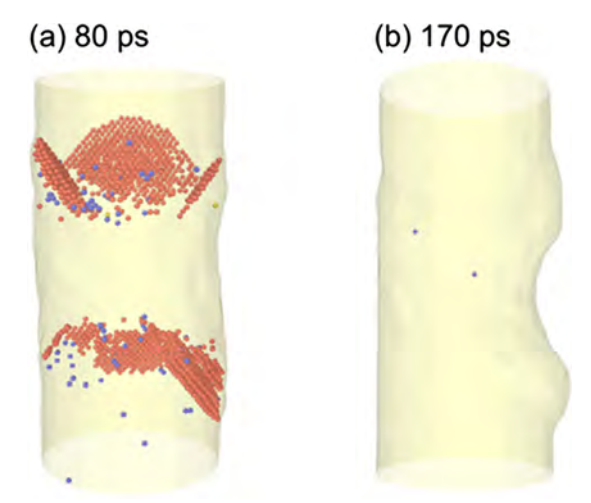


Fig. 5.18. MD simulations illustrating the surface roughening in an 8.2 nm-thick Au nanowire after 20 keV self-ion irradiation [627]. (a) Irradiation process at 80 ps, and (b) a crater formed on the surface of the Au nanowire after 170 ps, leading to a rough surface. Reprinted with permission from Ref. [627].

(Fig. 5.15e), whereas in nanowires with a diameters of \sim 30 nm, a much lower density of defects was observed (Fig. 5.15f). The defect density as a function of distance across the wire diameter (Fig. 5.15g) showed that the maximum density occurred in the center of the irradiated ZnO nanowires, and decreases rapidly towards free surfaces. The peak defect density decreased with decreasing wire diameters (Fig. 5.15h) [450].

Using MD simulations (selected results shown in Fig. 5.16), Zhang et al. showed that the vacancy formation energy decreased from 1.02 to 0.96 eV from the bulk region to the surface, respectively, in Au nanowires [625]. At a region of \sim 3–6 nm from the surface, the vacancy formation energy decreased. When the vacancy-surface distance was <1 nm, the vacancy formation energy quickly decreased, providing the driving force for vacancies to migrate toward the surfaces. Consequently, a gradient distribution of vacancy clusters emerged. It is worth mentioning that the formation energy of point defects in certain nanolayer systems, such as immiscible Cu/Nb multilayers [626], shows a larger decrease (from \sim 1.25 to \sim 0.2 eV in Cu and \sim 2.75 to \sim 1.1 eV in Nb) from the bulk region to the layer interface, respectively, as compared to nanowires.

In addition to the expected DDZs that affect the overall defect density in the nanowires, an *in situ* Kr ion irradiation study of ZnO nanowires showed size-dependent swelling and a non-uniform DDZ that were influenced by preexisting defect clusters in the wires [450]. Under irradiation, large preexisting dislocation loops (L1–L3 in Fig. 5.17a) migrated along the prismatic plane of the ZnO nanowire at \sim 2 nm/s during radiation before becoming stationary. By 1.5 dpa (Fig. 5.17b), these preexisting dislocation loops were pinned by small radiation-induced dislocation loops. Swelling of the ZnO nanowires along the radial direction was observed. Radiation-induced radial strain (ϵ), (ϵ = (d – d_0)/ d_0 , where d_0 and d are the wire diameter before and after radiation, respectively) increased with increasing doses, where the magnitude of strain decreased for nanowires with smaller diameters (Fig. 5.17c). Interestingly nanowires with diameters of \leq 30 nm showed no swelling. Fig. 5.17d shows that a large number of radiation-induced small dislocation loops were trapped by large preexisting dislocation loops, leading to a dumbbell-shape distribution of defect clusters, accompanied by DDZs near the surface.

MD simulations have also shown an interesting phenomenon, surface roughening after 20 keV self-ion irradiation of Au nanowires [627]. As shown in Fig. 5.18, a Au nanowire with a diameter of 8.2 nm had a relatively smooth surface after ion bombardment of 80 ps (Fig. 5.18a). After 170 ps, a large crater was formed on the nanowire surface. It was proposed that the formation of craters at the surface of Au nanowires was due to a microexplosion of hot atoms when the PKA energy was sufficiently high (>10 keV for Au nanowires). The formation of surface craters is likely to affect the stability of metallic nanowires during irradiation. However, there is no experimental evidence to validate this prediction.

5.4. Irradiation-induced structural change of nanoparticles

In addition to nanoporous metals and nanowires, the size dependent radiation damage in nanoparticles has also been investigated. The size effect of radiation damage in metallic nanoparticles is dominated by the increased sputtering present in the particles due to the increased surface-to-volume ratio. A simple analytical model accounting for the local curvature and depth of the damage in the particles as a function of sputtering yield showed a good fit and was valid at least to a first order [628]. The size effect on the sputtering yield and the corresponding fundamental mechanisms during self-ion irradiation were reported by Bufford et al. [629]. By investigating the radiation damage via *in situ* TEM technique, changes in the mechanism due to particle size were directly observed (Fig. 5.19). When the size of the particle decreases below a threshold of 10 nm, a transition from crater formation to particle disintegration was observed. In Fig. 5.19a (g'-i'), the violent

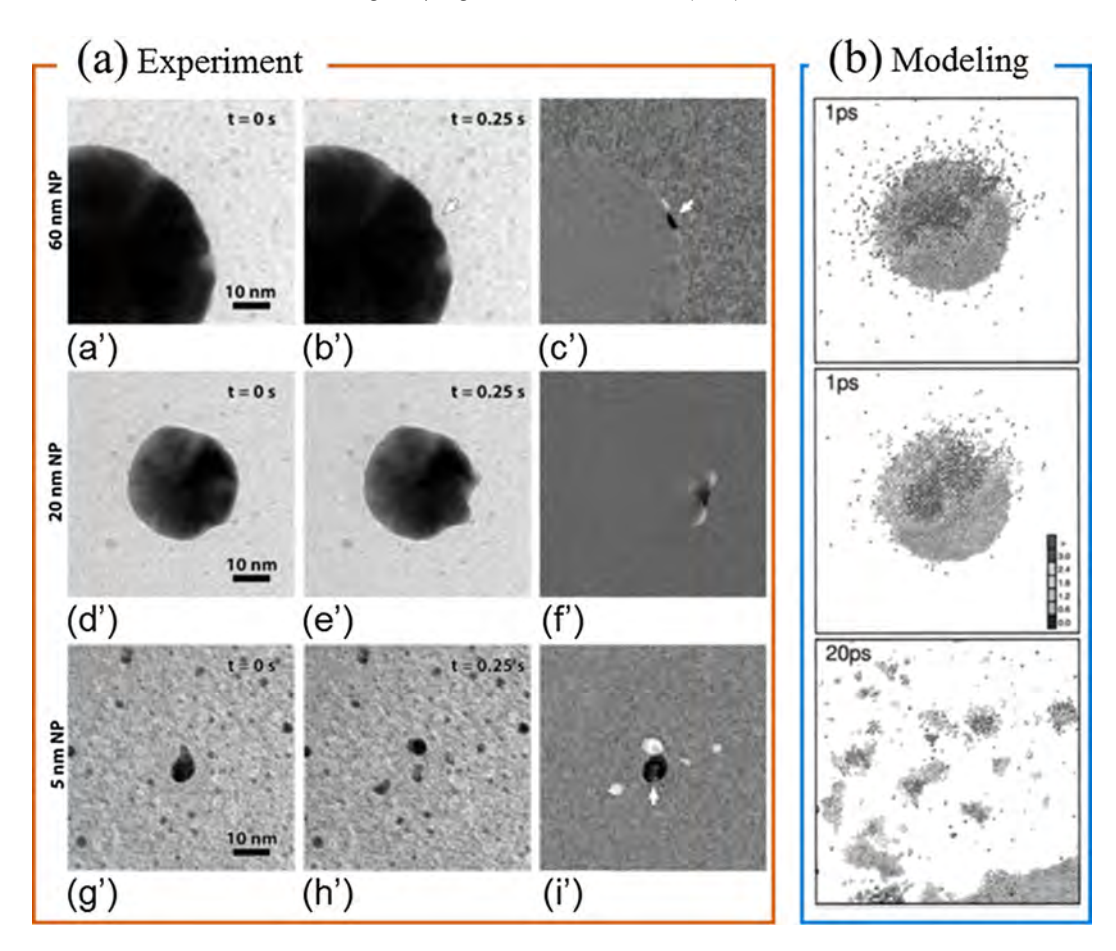


Fig. 5.19. Irradiation-induced nanoparticle disintegration (experiment (a) and modeling (b)). (a) Effects of single 46 keV Au ions on the evolution of Au nanoparticles of decreasing size (the magnification is same for all micrographs. Each pair of micrographs was separated by 1 frame, about 0.25 s. (a'-c') A single ion strike on a 60 nm nanoparticle created a surface crater, marked by the white arrow. (c') The difference image highlights the change between (a') and (b'); features present only in (a) are dark and newly formed features present only in (b') appear light. (d'-f') A single ion creating a crater in a 20 nm nanoparticle. (f') The difference image. (g') A teardrop-shaped nanoparticle (\sim 5 nm) was initially surrounded by a number of previously sputtered particles. (h') The nanoparticle exploded, leaving several particles nearby. (i') Difference image showing the locations of the old and new particles. The white arrow indicates a fragment from (h') that is difficult to see in (i') as it overlapped with the original nanoparticle location [629]. (b) Perspective (top) and cross-sectional (middle) view of the Au nanoparticle at t = 1 ps after atom bombardment. Bottom: Perspective view at t = 20 ps. Atoms are shaded according to their local temperature in units of the melting temperature of Au [632]. Reprinted with permission from Refs. [629,632].

disintegration of a single 5 nm particle to form five smaller nanoparticles was observed due to a single ion strike. Although these mechanisms may be related to those seen in the surface reconstruction occurring in bulk and thin films exposed to ionizing radiation [630,631], the detailed mechanisms seem to be very different due to free surfaces in multiple directions. Hence, these two dominant mechanisms (cratering and disintegration) warrant further investigation.

In a complementary modeling work, Kissel and Urbassek used MD simulations to predict the disintegration of 4 nm Au particles bombarded with 100 keV Au ions (Fig. 5.19b) [632]. This study explored the role of ion energy on the particle evolution showed that classical linear-cascade sputtering was active, in addition to a thermal aspect resulting in an enhanced sputtering yield from the Au nanoparticle. In such small particles, sputtering can result in the disintegration of Au particles in less than 20 ps and release of Au clusters of up to 100 atoms [632]. The results of this simulation agreed well with the structural evolution observed experimentally for 5 nm nanoparticle irradiated by a single 46 keV Au ion (Fig. 5.19a) [629].

Although ceramic nanoparticles often have novel size-dependent optical, magnetic, electrical and piezoelectric properties, their behavior in radiation environments remains poorly understood due to the few existing studies performed to determine the evolution of their microstructures, mechanical and physical properties, and band gap stability. In addition to the sputtering effects seen in metallic nanoparticles, nanoscale ceramics generally appear to undergo considerable microstructural evolution during irradiation. Fig. 5.20 shows the disintegration of SnO_2 exposed to 4.6 MeV Pb ions at a dose of 5×10^{12} ions/cm². The drastic structural changes from 100 nm single-crystal particles to interconnected and much smaller (few nm) nanoparticles were the result of the thermal spike in SnO_2 particles [633]. The extremely fine nanoparticles formed in the SnO_2 may have unique properties worthy of further study.

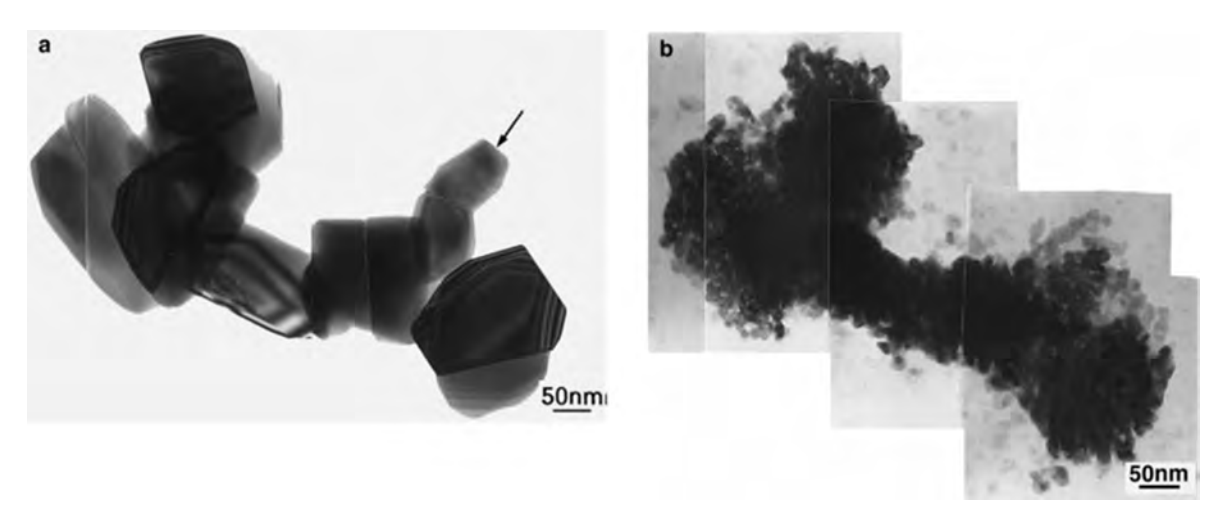


Fig. 5.20. Disintegration of SnO₂ nanoparticles after irradiation. The Pb ion beam induced microstructural evolution in SnO₂ nanograins: (a) Before irradiation, the SnO₂ nanoparticles were faceted with dimension of \sim 100 nm. (b) After the Pb ion irradiation to a dose of 5 \times 10¹² ion/cm², extremely fine SnO₂ nanoparticles formed. The arrow shows a small grain that mostly disappeared after ion irradiation [633]. Reprinted with permission from Ref. [633].

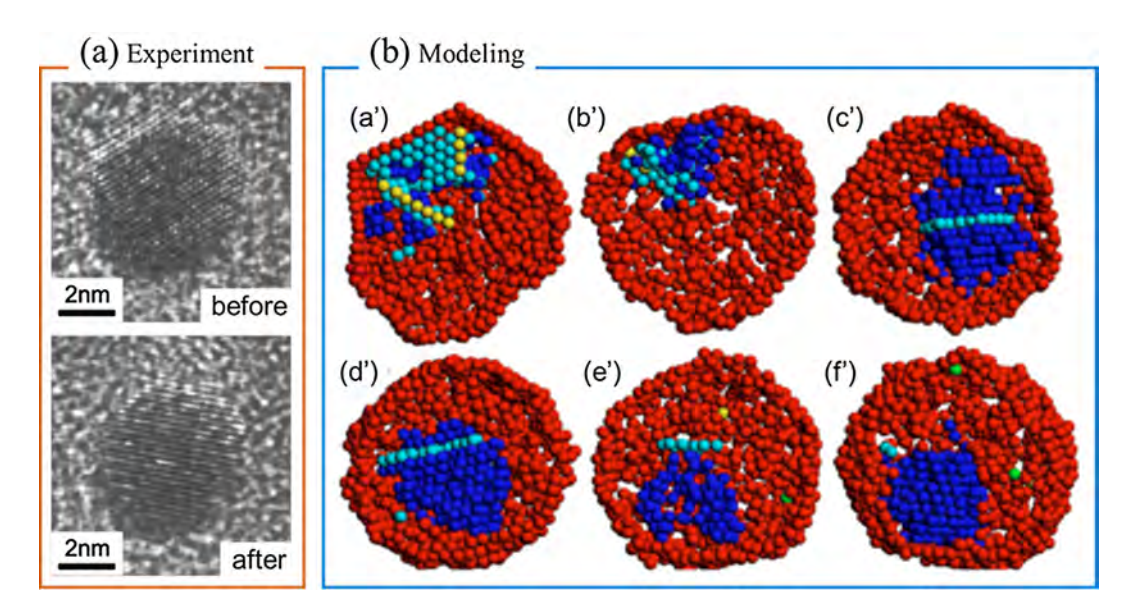


Fig. 5.21. Radiation-induced crystal structure changes of FePt nanoparticles (experiment (a) and modeling (b)). (a) An FePt nanoparticle, which exhibited multiple twinned structure before irradiation (top) transformed into an FCC single crystal particle (bottom) after 5 keV He irradiation at a fluence of 3×10^{17} ions/cm² [641], (b) MD simulation results show the transition from icosahedral to single-crystal morphology in a partly molten cluster. The upper part shows images of the transition. The atoms are FCC (blue), surface (red), HCP (light blue), and fivefold symmetry axis (yellow); liquid atoms are not shown. Initially (a'), the cluster was a partly molten icosahedron. After some point the liquid part almost completely absorbed the solid (b'). The solid then recrystallized with only one TB between two FCC components (c'). The boundary existed for several nanoseconds (d') but migrated in the crystalline part of the cluster. After some time, it reached the liquid boundary (e') and vanished, leaving a single-crystal solid (f') [643]. Reprinted with permission from Ref. [641,643].

In addition to foregoing discussions, numerous other *in situ* irradiation studies were performed to investigate the effect of particle size [629,634], dimensional ratio [635,636], and orientation. For example, a swift heavy ion study, using 1 GeV Pb, found an inverse relationship between the initial nanocluster on the target and the average sputtered particle size collected [637]. In contrast, Jarvi et al. predicted that during light ion irradiation the size of the particle did not have a significant effect on the sputtering yield [638]. Another MD simulation by Kissel et al. probed the interaction of irradiated Au with an underlying Au substrate during a cascade event [639]. This simulation performed as a function of energy showed that the particle could be sputtered rapidly, and also ejected from the surface due to the thermal spike, producing a crater on the substrate [639]. It should be noted that, although it appears generally accepted that the sputtering yield of nanoparticles is enhanced compared to bulk and thin film systems, it remains unclear what term and modifications should be added to the classical

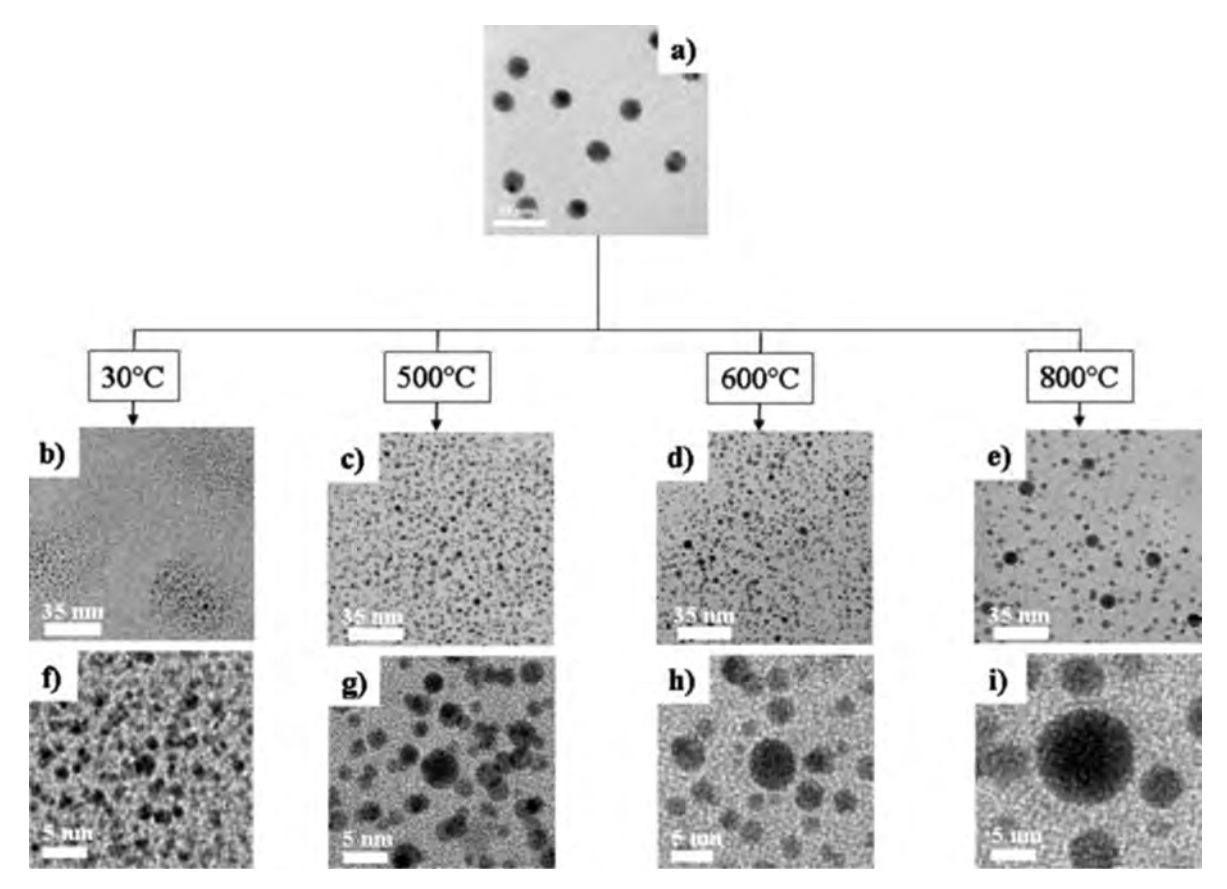


Fig. 5.22. Irradiation-induced microstructural change of nanoparticles at high temperatures. (a) Bright field TEM micrograph of an as-prepared sample. Bright field TEM micrographs of samples irradiated with 4 MeV Au ions at a fluence of 8×10^{16} ions/cm² at increasing temperatures: (b) and (f) 30 °C, (c) and (g) 500 °C, (d) and (h) 600 °C, and (e) and (i) 800 °C. The ion irradiation direction was normal to the plane [682]. Reprinted with permission from Ref. [682]

Thompson distribution to best represent the observed phenomena. The subject of enhanced sputtering yield in nanoparticles is an area that requires further research. Summarizing these experimental and modeling efforts on radiation damage of Au nanoparticles has showed three active regimes.

- (1) For particles with diameters less than \sim 10 nm, radiation results in atomization and violent disintegration of the fine nanoparticles.
- (2) Radiation of particles with dimensions of \sim 10–100 nm leads to craters with filaments and cluster sputtering.
- (3) When the particle diameter is greater than \sim 100 nm, radiation results in internal defect formation and sputtering yields reach near normal rates.

Although the majority of the work to date has focused on Au nanoparticles, some studies has been performed using other metallic nanoparticle systems. A few models have considered Fe nanoparticles to determine the size at which enhanced radiation stability may be achieved [640]. Beyond pure metal systems, an interesting example of internal structural evolution due to a 5 keV He ion beam was observed in the irradiation-induced destabilization of icosahedral structures in FePt nanoparticles [641]. Such low energy light ion implantation at a dose as low as 10^{17} ions/cm² was sufficient to drastically alter the structure of the icosahedral particles, but surprisingly, not that of the L1₀ particles [641]. Fig. 5.21a shows that an FePt nanoparticle, which was a previously multiply-twinned particle, transformed into an FCC single crystal particle after 5 keV He ion irradiation to a maximum fluence of 3×10^{17} ions/cm² [641]. However, He implantation was found to reduce the L1₀ ordering temperature of the FePt nanoparticles. This minor change in the structure and transition temperatures from a relatively minimal radiation exposure had notable changes on the properties of the irradiated FePt nanoparticles [642]. Javri et al. used MD simulations to highlight how the transition from icosahedral to single-crystal morphology can occur from only a single cascade event. The results showed that this transition occurred due to the melting and resolidification of the entire nanoparticle, as shown in Fig. 5.21b [643]. The evolution from icosahedral to single crystal nanoparticles appears to be a common response to ionizing irradiation; it has also been observed in a similar transition mechanism through a disordered phase [644].

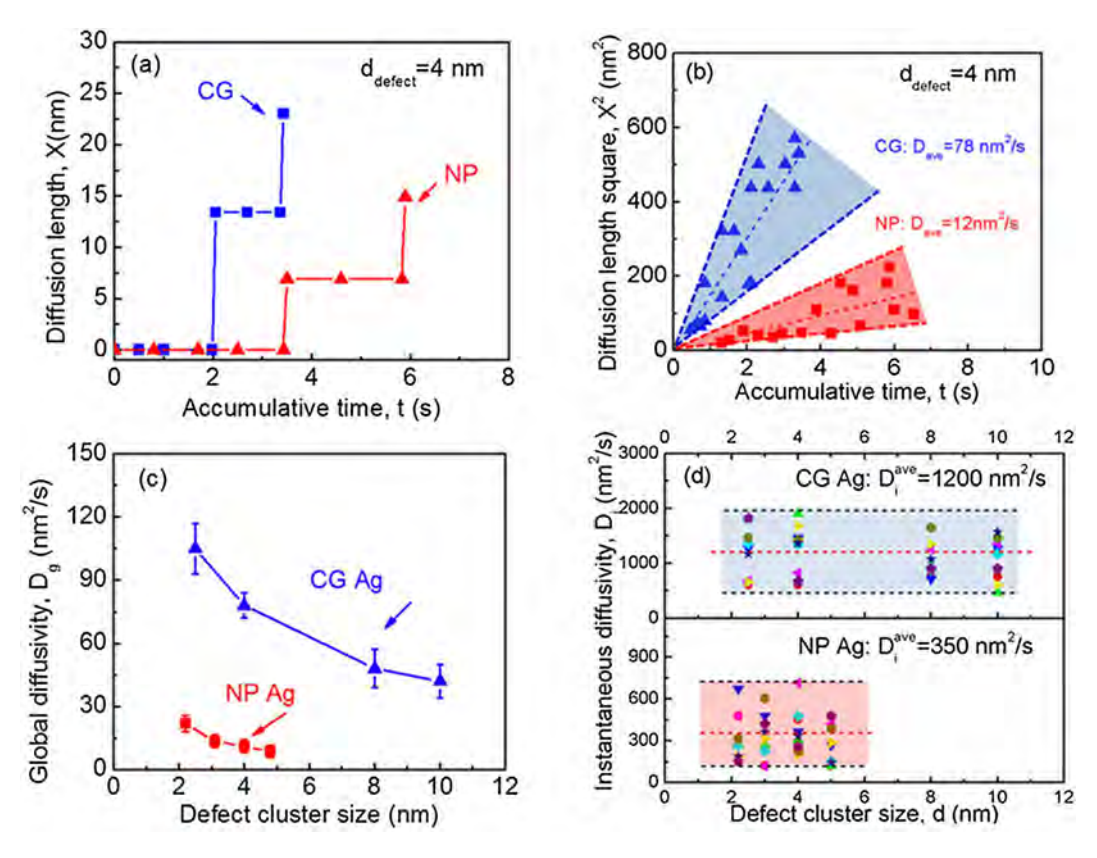


Fig. 5.23. Determination of global and instantaneous diffusivities of defect clusters in CG and NP Ag. (a) A representative plot of diffusion length (X) versus accumulative time for individual defect clusters with a diameter of 4 nm in CG and NP Ag. (b) Plots of the diffusion length squared (X^2) vs. accumulative time for a large number of defect clusters with a similar average size of 4 nm. The average value of D_g was ~ 78 and $12 \text{ nm}^2/\text{s}$ in CG and NP Ag, respectively. (c) The D_g of defect cluster in NP Ag was smaller than that in its CG counterpart. (d) The D_i values in CG and NP Ag were 1200 and 350 nm²/s, respectively [619]. Reprinted with permission from Ref. [619].

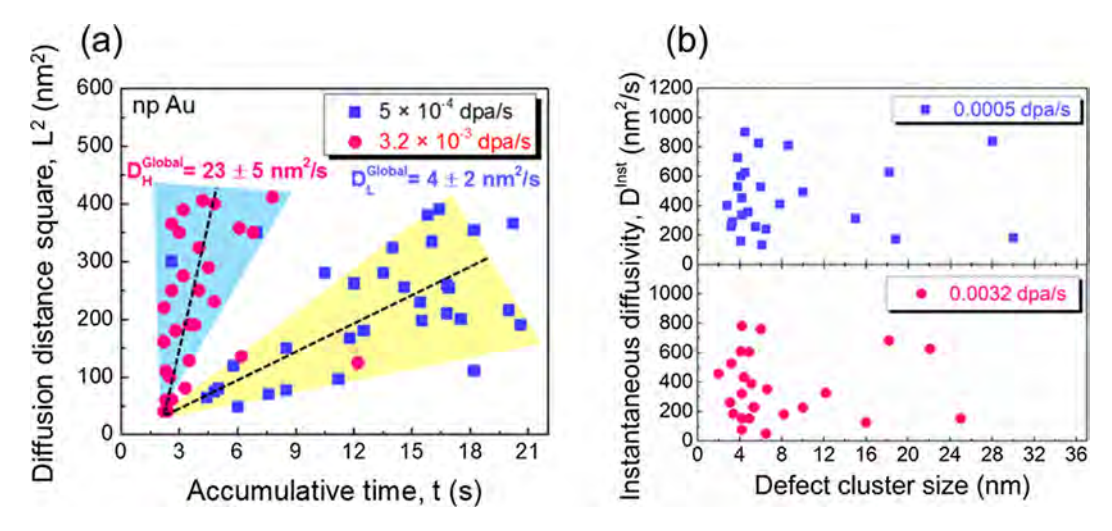


Fig. 5.24. Determination of global and instantaneous diffusivities of defect clusters in NP Au under irradiation at dose rates of 5.0×10^{-4} and 3.2×10^{-3} dpa/s. (a) The D_g of defect clusters in NP Au decreased significantly when the dose-rate decreased from 3.2×10^{-3} to 5×10^{-4} dpa/s. (b) D_i of defect clusters in irradiated NP Au varies from 200 to 800 nm²/s, and the average value of D_i showed little dependence on dose-rate and cluster diameter [40]. Reprinted with permission from Ref. [40].

In addition to free-standing nanoparticles, nanocomposites embedded with nanoparticles have demonstrated enhanced performance under radiation environments. These low-dimensional structures can be produced in large quantity by bulk processing [6], film deposition [645], or ion implantation [151,646,647]. This system will not be discussed as an embedded nanoparticle system in this review as there already exists extensive studies [6,13,280,487,511,648–680], an excellent review on the response of ODS steels to radiation environments [6], and models specifically discussing the radiation response of yttria nanoparticles [681]. The reader is referred to overviews by Meldrum et al. that nicely describe the potential for forming nanoparticles in bulk systems by ion implantation and future opportunities in this field [647].

The most common application of embedded nanoparticles in radiation environments, in addition to ODS steel, is metal nanoparticles embedded in glass. An example from Ramjauny et al. can be seen in Fig. 5.22 [682]. In this work, it was shown that the initial embedded Au nanoparticles can be destroyed by 4 MeV heavy ion irradiation at a dose of 10^{16} ions/cm². This can also result in the formation of a new precipitate phase. It was also shown that by controlling the temperature or nuclear stopping power, a bimodal size distribution of the particles was achievable [682].

The large variation in the structure of embedded Au nanoparticles was thoroughly investigated to control the particle size and distribution [683]. It was also shown that subsequent ion irradiation under limited conditions resulted in the elongated Au particles in a mica matrix [646]. Ridgway et al. proposed a thermodynamic argument for the elongation of Au nanoparticles due to swift heavy ions [684], despite conditions far from equilibrium. In addition to the work on Au, it was shown that embedded particles with a range of compositions can be formed or tailored via controlled ion beam modification. These systems include embedded Ag [685], Pt [686], Co [684], amorphous Cu [687], ZnO [688], solid state Xe [689], and many others [647] under appropriate irradiation conditions. In addition to amorphous silica and mica most commonly used in these studies, a range of other matrices with intriguing properties were used, including exotic matrices such as CdNbO₃ [690] or poly vinylidene fluoride (PVDF) [691]. In theory, embedded nanoparticles can be produced using an immiscible pair of implanted species and matrix, as well as many other systems that will be kinetically limited. Once created, the structure of these embedded particles can be tailored via a combination of ion irradiation and thermal processing. Systems containing embedded nanoparticles have already been used in harsh radiation environments, e.g., the use of erbium-doped-nanoparticle optical fibers for space applications [692]. Ridgway et al. published a nice reviewing of the potential of tailoring the size and shape of embedded nanoparticles [693]. It should be noted that radiation damage in metallic materials with nanoprecipitates has also been intensively studied [13,694-707], but not covered in the current review due to space and time limitations. With an improved fundamental understanding on the subject, a multitude of engineering applications ranging from quantum bridges [708] to color changing artwork [709] is possible.

5.5. The influence of free surfaces on the defect migration kinetics

In situ radiation studies provides abundant information regarding the defect migration kinetics in materials under irradiation. Global and instantaneous diffusivities of defect clusters under irradiation have been determined in NP metals. The global diffusivity (D_g) is averaged over a long period of time (including migration and dwell time) for numerous defect clusters, whereas instantaneous diffusivity (D_i) is measured only during the migration process [619]. Fig. 5.23a shows typical examples of measured migration distance (diffusion length X) of individual defect clusters (4 nm in diameter) in both CG and NP Ag [619]. In order to determine the D_g of defect clusters, the migration of a large number of defect clusters was statistically studied. Fig. 5.23b shows the diffusion length squared (X^2) vs. accumulative time for numerous defect clusters with similar size (4 nm in diameter) for both CG and NP Ag [619]. Assuming 1-D diffusion, the diffusivity of defect clusters (D) can be estimated by:

$$D = X^2/2t, (5.5)$$

where t is the diffusion time. A linear fit of these data shows that D_g of defect clusters (d_{defect} = 4 nm) in CG Ag is 78 nm²/s, much greater than that in NP Ag, \sim 12 nm²/s. Fig. 5.23c compares the size-dependent variation of D_g for CG and NP Ag. The value of D_g reduces rapidly from 105 to 45 nm²/s with increasing size of defect clusters in CG Ag. A similar trend was observed in NP Ag. However, for the same dimension of defect clusters, D_g in NP Ag was much lower than that in CG Ag. Similar techniques were applied to determine D_i , as shown in Fig. 5.23d. Interestingly, there was no clear size-dependent variation of D_i for CG and NP Ag. Nonetheless, the average value of D_i in NP Ag (\sim 350 nm²/s) was much lower than that in CG Ag (\sim 1200 nm²/s). The D_i values in both CG and NP Ag were at least an order of magnitude greater than their respective D_g values.

The migration kinetics of defect clusters has been examined in NP Au under irradiation at different dose-rates [40]. The D_g of defect clusters was determined using the same estimation method [40]. Similar to NP Ag [619], most defect clusters in NP Au migrate in a 'stick-slip' manner, where a defect cluster migrates instantaneously within a fraction of a second, and then stay steady for a while (dwell time) before its next movement. Fig. 5.24a shows D_g of defect clusters in NP Au at two dose-rates, 3.2×10^{-3} and 5.0×10^{-4} dpa/s. The value of D_g was greater at a higher dose-rate. Fig. 5.24b shows the value of D_i of the defect clusters in the irradiated NP Au varied from 200 to 800 nm²/s, and the average value of the D_i does not show a clear dependence on the dose rate.

5.6. Summary and future work

Understanding the response of low-dimensional nanomaterials to radiation environments has become the cornerstone of modern electronics and has been essential for the development of advanced materials for nuclear systems. Despite enormous research efforts in the development of nanomaterials with novel physical properties, fundamental understanding of the irradiation tolerance of NP materials, nanoparticles, and nanowires remains limited. Free surfaces can act as defect sinks and remove radiation-induced defect clusters, including dislocation loops, segments and SFTs. However, the radiation response of these low-dimensional nanomaterials in harsher environments, such as high-flux neutron radiation at elevated temperatures, is largely unknown. The diffusivities of defect clusters in monolithic NP metals under irradiation have been measured by *in situ* techniques. It is shown that the response of nanoparticles to irradiation conditions cannot be entirely predicted from the bulk response, and varies drastically among these low-dimensional materials. Further work on the solute redistribution of low-dimensional alloys and the corresponding mechanical properties evolution under irradiation is necessary, where the window of radiation tolerance of low-dimensional materials under various irradiation conditions needs to be further established. Coupling of multiscale modeling and experimental observations improves our understanding of the irradiation response of low-dimensional materials and predicts the performance of such materials in harsh irradiation environments.

6. Summary and future outlook

Radiation damage in nanostructured materials has emerged as a new research arena that bridges among the communities of nanostructured materials, radiation effects, physics, mechanics as well as modeling and simulation. As this review shows, there are significant challenges and opportunities ahead.

A paramount challenge remains how to discover and design advanced materials that are eventually "immune" to radiation into the hundreds of dpa range. Significant progress has been made to explore the impacts of various types of defect sinks in nanostructured materials. However there are abundant scientific questions that remain to be addressed. The followings are some outstanding issues from a long list of scientific problems that deserve prompt attention.

It is well known that most defect sinks evolve during interaction with radiation induced defects. Consequently these defect sinks may lose their capability to continuously absorb or eliminate radiation induced defect clusters. Perhaps the ideal defect sinks should have "self-healing" capabilities, so that these sinks can retain their ability to eliminate radiation induced damage while recovering at the same time. Although there has been some limited success in using precipitate (such as TiC) to alleviate radiation damage in austenitic stainless steels, and ODS steels, there is a need to design advanced radiation resistant materials with progressively greater sink strength and self-healing ability. The concept of work hardening and dislocation recovery for superior plasticity is, to some extent, analogous to the search for ideal defect sinks to accomplish outstanding radiation resistance.

In each of the previous sections, a particular type of defect sink is treated as the primary defect absorber in nanostructured materials. It is natural to suspect that an innovative combination of these defect absorbers into defect networks may be an effective approach to tackle irradiation induced damage. There are numerous successful examples in the literature already, including ODS alloys with grain boundaries and phase boundaries, NT metals with nanopores, etc. Clearly much work is needed to design nanomaterials with defect networks to handle the transportation and elimination of radiation induced defects.

The introduction of defects put materials into a state further away from equilibrium, as these defects store excess energy. Thermodynamically, most of these defects can be removed at elevated temperature (by annealing) with few exceptions (such as oxides nanoprecipitates in ODS steels). As most radiation environments encounter intermediate-to-high temperatures, the thermal stability of most defect sinks in nanomaterials is clearly a major concern. There are increasing studies on enhancement of thermal stability of grain boundaries and interfaces in nanostructured materials. A combination of various defect sinks with outstanding thermal and radiation stability may enable unprecedented radiation tolerance in nanomaterials.

Although there are abundant experimental evidence showing the significant reduction of defect density in nanomaterials, fundamental questions remain on how defect sinks interact and eliminate these defect clusters. To date modeling studies on radiation induced damage in nanomaterials remain rather limited. Various computational and simulation tools can make significant impact in studying radiation response of nanomaterials.

In situ radiation inside a transmission electron microscope remains a critical tool to answer this question. The *in situ* radiation facilities worldwide have produced a significant amount of data in this aspect. Continuous upgrade of the existing facility and establishment of new facility worldwide are necessary to probe the evolution of defects and chemistry at nanoscale and even atomic scale during radiation. Combination of *in situ* studies with modeling is critical to understand and predict the kinetics of defect clusters in irradiated nanomaterials.

There is a lot of room to investigate the mechanical behavior of irradiated nanostructured materials. As the range of heavy ion irradiation damage is often limited to the surface and subsurface of the irradiated materials, advanced nanomechanical testing tools are necessary to evaluate the mechanical behavior of the heavy ion irradiated nanomaterials. In comparison, the

mechanical behavior of the neutron irradiated nanomaterials can be investigated with conventional mechanical testing methods.

The nanostructured material community has spent several decades to explore the synthesis of bulk nanostructured materials. Much of their success can be translated to the nanomaterials for nuclear application. Severe plastic deformation, such as equal channel angular pressing, can now process large quantity of materials in a short time. Consolidation of nanocrystalline powders (prepared by ball milling or chemical synthesis) by sintering can also produce bulk nanostructured materials.

Many of the previous chapters have discussed the radiation tolerance of nanostructured coatings consisting of metallic or ceramic materials. Fabrication of coatings on a large substrate is a possibility given the maturity of industry in using a variety of coating techniques, such as physical and chemical vapor depositions, thermal and plasma spray. The radiation resistance of nanostructured metallic and ceramics coatings fabricated using industrial coating techniques needs to be rigorously evaluated.

As described in the foregoing sections, the investigation of radiation damage in nanomaterials is an emerging and active research subject, rich in materials science, physics, chemistry and mechanics. Such a new research arena brings many aspects of nanomaterials together. Extensive and collaborative research on the radiation response of nanomaterials is necessary to design and implement novel radiation resistant nanomaterials for advanced nuclear energy applications.

Acknowledgements

We acknowledge Prof. Engang Fu from Peking University and Dr. Oing Su from University of Nebraska, Lincoln, for providing data and discussions. X.Z. and J.L. acknowledge financial support by NSF-DMR-Metallic Materials and Nanostructures Program under grant no. 1643915, and partial support by NSF under grant no. 1611380 and 1728419. Work by M.L.T. was supported by the U.S. Department of Energy, Office of Science, Basic Energy Sciences, under Award # DE-SC0008274. K.Y. acknowledges financial supports from Natural National Science Foundation of China (51501225), M.N., and L.S. acknowledge financial support from the DoE Office of Nuclear Energy, Nuclear Energy Enabling Technologies, award DE-NE0000533. L.S. also acknowledges financial support by NSF under award no. 1130589. H.W. acknowledges the funding support from the U.S. Office of Naval Research (N00014-17-1-2087 and N00014-16-1-2778), K.H. acknowledges partial support by the LDRD program at Sandia National Laboratories and the Division of Materials Science and Engineering, Office of Basic Energy Sciences, U.S. Department of Energy. Sandia National Laboratories is a multi-mission laboratory managed and operated by National Technology and Engineering Solutions of Sandia, LLC., a wholly owned subsidiary of Honeywell International, Inc., for the U.S. Department of Energy's National Nuclear Security Administration under contract DE-NA-0003525. This work was performed, in part, at the Center for Integrated Nanotechnologies, an Office of Science User Facility operated for the US Department of Energy (DOE) Office of Science by Los Alamos National Laboratory [Contract DE-AC52-06NA25396] and Sandia National Laboratories [Contract DEAC04-94AL85000]. The IVEM facility at Argonne National Laboratory is supported by DOE-Office of Nuclear Energy. C.S. acknowledges support through the INL Laboratory Directed Research & Development (LDRD) Program under DOE Idaho Operations Office Contract DE-AC07-05ID14517. The authors would like to thank M. Blair for assistance with preparation for the document. JW acknowledges the support by the Nebraska Center for Energy Sciences Research, N.L. acknowledges the support of the U.S. Department of Energy through the Los Alamos National Laboratory (LANL)/Laboratory Directed Research & Development (LDRD) Program.

References

- [1] Zinkle SJ, Was GS. Materials challenges in nuclear energy. Acta Mater 2013;61:735-58.
- [2] Zinkle SJ. 1.03 Radiation-Induced Effects on Microstructure* A2. In: Konings Rudy JM, editor. Comprehensive Nuclear Materials. Oxford: Elsevier; 2012. p. 65–98.
- [3] Zinkle SJ, Farrell K. Void swelling and defect cluster formation in reactor-irradiated copper. J Nucl Mater 1989;168:262-7.
- [4] Nastasi MA, Mayer JW. SpringerLink (Online service), Ion implantation and synthesis of materials.
- [5] Zinkle SJ, Busby JT. Structural materials for fission & fusion energy. Mater Today 2009;12:12-9.
- [6] Odette GR, Alinger MJ, Wirth BD. Recent developments in irradiation-resistant steels. Annu Rev Mater Res 2008;38:471–503.
- [7] Ukai S, Fujiwara M. Perspective of ODS alloys application in nuclear environments. J Nucl Mater 2002;307:749–57.
- [8] El-Genk MS, Tournier J-M. A review of refractory metal alloys and mechanically alloyed-oxide dispersion strengthened steels for space nuclear power systems. J Nucl Mater 2005;340:93–112.
- [9] Hsiung LL, Fluss MJ, Tumey SJ, Choi BW, Serruys Y, Willaime F, et al. Formation mechanism and the role of nanoparticles in Fe-Cr ODS steels developed for radiation tolerance. Phys Rev B 2010;82:184103.
- [10] Alinger M, Odette G, Hoelzer D. On the role of alloy composition and processing parameters in nanocluster formation and dispersion strengthening in nanostuctured ferritic alloys. Acta Mater 2009;57:392–406.
- [11] Hirata A, Fujita T, Wen Y, Schneibel J, Liu CT, Chen M. Atomic structure of nanoclusters in oxide-dispersion-strengthened steels. Nat Mater 2011;10:922.
- [12] Odette GR, Hoelzer DT. Irradiation-tolerant nanostructured ferritic alloys: transforming helium from a liability to an asset. Jom 2010;62:84–92.
- [13] Marquis EA. Core/shell structures of oxygen-rich nanofeatures in oxide-dispersion strengthened Fe-Cr alloys. Appl Phys Lett 2008;93.
- [14] Odette GR. Recent progress in developing and qualifying nanostructured ferritic alloys for advanced fission and fusion applications. Jom 2014;66:2427–41.
- [15] Williams CA, Unifantowicz P, Baluc N, Smith GD, Marquis EA. The formation and evolution of oxide particles in oxide-dispersion-strengthened ferritic steels during processing. Acta Mater 2013;61:2219–35.
- [16] Aydogan E, Almirall N, Odette G, Maloy S, Anderoglu O, Shao L, et al. Stability of nanosized oxides in ferrite under extremely high dose self ion irradiations. J Nucl Mater 2017;486:86–95.

- [17] Anders A. Metal plasma immersion ion implantation and deposition: a review. Surf Coat Technol 1997;93:158-67.
- [18] Chu PK, Qin S, Chan C, Cheung NW, Larson LA. Plasma immersion ion implantation—A fledgling technique for semiconductor processing. Mater Sci
- [19] Gibbons JF. Ion implantation in semiconductors—Part II: Damage production and annealing. Proc IEEE 1972;60:1062–96.
- [20] Pearton S, Vartuli C, Zolper J, Yuan C, Stall R. Ion implantation doping and isolation of GaN. Appl Phys Lett 1995;67:1435-7.
- [21] Williams JS, Poate JM. Ion implantation and beam processing. Academic Press; 2014.
- [22] Ziegler JF. Ion Implantation Science and Technology 2e. Elsevier; 2012.
- [23] Erlebacher J, Aziz MJ, Chason E, Sinclair MB, Floro JA. Spontaneous pattern formation on ion bombarded Si (001). Phys Rev Lett 1999;82:2330.
- [24] Li J, Stein D, McMullan C, Branton D, Aziz MJ, Golovchenko JA. Ion-beam sculpting at nanometre length scales. Nature 2001;412:166-9.
- [25] Zinkle SJ, Singh BN, Microstructure of neutron-irradiated iron before and after tensile deformation. | Nucl Mater 2006;351:269-84.
- [26] Yu KY, Chen Y, Li J, Liu Y, Wang H, Kirk MA, et al. Measurement of heavy ion irradiation induced in-plane strain in patterned face-centered-cubic metal films: an in situ study. Nano Lett 2016;16:7481–9.
- [27] Wangyu H, Bangwei Z, Baiyun H, Fei G, David JB. Analytic modified embedded atom potentials for HCP metals. J Phys: Condens Matter 2001;13:1193.
- [28] Wolfer W. Fundamental properties of defects in metals. Compr Nucl Mater 2012;1:1–45.
- [29] Chen Y, Yu KY, Liu Y, Shao S, Wang H, Kirk M, et al. Damage-tolerant nanotwinned metals with nanovoids under radiation environments. Nat Commun 2015;6.
- [30] Sun C, Song M, Yu KY, Chen Y, Kirk M, Li M, et al. In situ evidence of defect cluster absorption by grain boundaries in Kr ion irradiated nanocrystalline Ni. Metall Mater Trans A 2013;44:1966–74.
- [31] Zinkle S, Sindelar R. Defect microstructures in neutron-irradiated copper and stainless steel. | Nucl Mater 1988;155:1196-200.
- [32] Kozlov A, Panchenko V, Kozlov K, Russkikh I, Kozlov AV. Evolution of radiation defects in nickel under low-temperature neutron irradiation. Phys Metals Metallogr 2014;115:39–45.
- [33] Packan NH. Voids in neutron irradiated aluminum; 1970.
- [34] Kiritani M. Similarity and difference between fcc, bcc and hcp metals from the view point of point defect cluster formation. J Nucl Mater 2000;276:41–9.
- [35] Zinkle S, Singh B. Analysis of displacement damage and defect production under cascade damage conditions. J Nucl Mater 1993;199:173-91.
- [36] Averback R, de La Rubia TD. Displacement damage in irradiated metals and semiconductors. Solid State Phys 1997;51:281-402.
- [37] Stoller R, Odette G, Wirth B. Primary damage formation in bcc iron. J Nucl Mater 1997;251:49-60.
- [38] Averback R. Atomic displacement processes in irradiated metals. J Nucl Mater 1994;216:49-62.
- [39] Yu KY, Bufford D, Sun C, Liu Y, Wang H, Kirk MA, et al. Removal of stacking-fault tetrahedra by twin boundaries in nanotwinned metals. Nat Commun 2013;4.
- [40] Li Jin, Fan C, Ding J, Xue S, Chen Y, Li Q, et al. In situ heavy ion irradiation studies of nanopore shrinkage and enhanced radiation tolerance of nanoporous Au. Sci Rep 2017;7.
- [41] Silcox J, Hirsch P. Direct observations of defects in quenched gold. Phil Mag 1959;4:72–89.
- [42] Wirth B, Bulatov V, De La Rubia TD. Atomistic simulation of stacking fault tetrahedra formation in Cu. J Nucl Mater 2000;283:773-7.
- [43] Voskoboinikov RE, Osetsky YN, Bacon DJ. Computer simulation of primary damage creation in displacement cascades in copper. I. Defect creation and cluster statistics. J Nucl Mater 2008;377:385–95.
- [44] Uberuaga BP, Hoagland RG, Voter AF, Valone SM. Direct transformation of vacancy voids to stacking fault tetrahedra. Phys Rev Lett 2007;99:135501.
- [45] Zarkadoula E, Daraszewicz SL, Duffy DM, Seaton MA, Todorov IT, Nordlund K, et al. The nature of high-energy radiation damage in iron. J Phys: Condens Matter 2013:25:125402.
- [46] Rieth M, Dudarev SL, Gonzalez de Vicente SM, Aktaa J, Ahlgren T, Antusch S, et al. Recent progress in research on tungsten materials for nuclear fusion applications in Europe. J Nucl Mater 2013;432:482–500.
- [47] Schilling W. Self-interstitial atoms in metals. J Nucl Mater 1978;69–70:465–89.
- [48] Ullmaier H. Atomic defects in metals, Landolt-Börnstein Group III Condensed Matter, vol. 25. Berlin: Springer-Verlag; 1991.
- [49] Marian J, Wirth BD, Perlado JM. Mechanism of formation and growth of <100> interstitial loops in ferritic materials. Phys Rev Lett 2002;88:255507.
- [50] Bacon DJ, Gao F, Osetsky YN. The primary damage state in fcc, bcc and hcp metals as seen in molecular dynamics simulations. J Nucl Mater 2000;276:1–12.
- [51] Jenkins ML, Yao Z, Hernández-Mayoral M, Kirk MA. Dynamic observations of heavy-ion damage in Fe and Fe-Cr alloys. J Nucl Mater 2009;389:197-202.
- [52] Kirk M, Yi X, Jenkins M. Characterization of irradiation defect structures and densities by transmission electron microscopy. J Mater Res 2015;30:1195–201.
- [53] Downey M, Eyre B. Neutron irradiation damage in molybdenum. Phil Mag 1965;11:53-70.
- [54] Loubeyre P, LeToullec R, Pinceaux J, Mao H, Hu J, Hemley R. Equation of state and phase diagram of solid He 4 from single-crystal x-ray diffraction over a large P-T domain. Phys Rev Lett 1993;71:2272.
- [55] Maher D, Eyre B. Neutron irradiation damage in molybdenum. Phil Mag 1971;23:409-38.
- [56] Lacefield K, Moteff J, Smith J. Neutron radiation damage in tungsten single crystals. Phil Mag 1966;13:1079-81.
- [57] Kiritani M, Maehara Y, Takata H. Electron radiation damage and properties of point defects in molybdenum. J Phys Soc Japan 1976;41:1575–83.
- [58] Fukuzumi S, Yoshiie T, Satoh Y, Xu Q, Mori H, Kawai M. Defect structural evolution in high purity tungsten irradiated with electrons using high voltage electron microscope. J Nucl Mater 2005;343:308–12.
- [59] Xu H, Stoller RE, Osetsky YN, Terentyev D. Solving the puzzle of <100> interstitial loop formation in bcc iron. Phys Rev Lett 2013;110:265503.
- [60] Marinica M-C, Willaime F, Crocombette J-P. Irradiation-induced formation of nanocrystallites with C 15 laves phase structure in bcc iron. Phys Rev Lett 2012;108:025501.
- [61] Bacon DJ. A review of computer models of point defects in hcp metals. J Nucl Mater 1988;159:176-89.
- [62] Bacon D. Point defects and clusters in the hcp metals: their role in the dose transition. J Nucl Mater 1993;206:249-65.
- [63] Griffiths M. Evolution of microstructure in hcp metals during irradiation. J Nucl Mater 1993;205:225-41.
- [64] Yamada S, Kameyama T. Observation of c-component dislocation structures formed in pure Zr and Zr-base alloy by self-ion accelerator irradiation. J Nucl Mater 2012;422:167–72.
- [65] Griffiths M. A review of microstructure evolution in zirconium alloys during irradiation. J Nucl Mater 1988;159:190-218.
- [66] Khan A, Yao Z, Daymond M, Holt R. Effect of foil orientation on damage accumulation during irradiation in magnesium and annealing response of dislocation loops. J Nucl Mater 2012;423:132–41.
- [67] Wolfenden A, Herschbach K, Müller K, Stober T. Neutron irradiation damage in magnesium single crystals. Radiation Effects 1978;39:177-80.
- [68] Griffiths M. Microstructure evolution in h.c.p. metals during irradiation. Phil Mag A: Phys Condens Matter, Struct, Defects Mech Prop 1991;63:835–47.
- [69] Levy V. Determining the nature of dislocation loops observed in Mg. J Microscopie 1974;19:1-16.
- [70] Jostsons A, Blake R, Napier J, Kelly P, Farrell K. Faulted loops in neutron-irradiated zirconium. J Nucl Mater 1977;68:267-76.
- [71] Griffiths M, Faulkner D, Styles R. Neutron damage in α-titanium. J Nucl Mater 1983;119:189-207.
- [72] Mansur LK. Void swelling in metals and alloys under irradiation: an assessment of the theory. Nucl Technol 1978;40:5–34.
- [73] Norris D. The use of the high voltage electron microscope to simulate fast neutron-induced void swelling in metals. J Nucl Mater 1971;40:66–76.
- [74] Little E, Stow D. Void-swelling in irons and ferritic steels: II. An experimental survey of materials irradiated in a fast reactor. J Nucl Mater 1979;87:25–39.

- [75] Garner F, Brager H, Gelles D, McCarthy J. Neutron irradiation of FeMn, FeCrMn and FeCrNi alloys and an explanation of their differences in swelling behavior. J Nucl Mater 1987:148:294–301.
- [76] Packan N, Farrell K, Stiegler J. Correlation of neutron and heavy-ion damage: I. The influence of dose rate and injected helium on swelling in pure nickel. J Nucl Mater 1978;78:143–55.
- [77] Sharafat S, Ghoniem NM, Anderson M, Williams B, Blanchard J, Snead L. Micro-engineered first wall tungsten armor for high average power laser fusion energy systems. I Nucl Mater 2005;347:217–43.
- [78] Garner FA, Toloczko MB, Sencer BH. Comparison of swelling and irradiation creep behavior of fcc-austenitic and bcc-ferritic/martensitic alloys at high neutron exposure. J Nucl Mater 2000;276:123–42.
- [79] Brailsford AD, Bullough R, Hayns MR. Point defect sink strengths and void-swelling. | Nucl Mater 1976;60:246-56.
- [80] Stubbins I, Garner F, Swelling and microstructure of high purity nickel irradiated with fast neutrons in EBR-II. | Nucl Mater 1992;191:1295-9.
- [81] Farrell K, Houston J. Suppression of radiation damage microstructure in aluminum by trace impurities. J Nucl Mater 1979;83:57-66.
- [82] Konobeev YV, Dvoriashin A, Porollo S, Garner FA. Swelling and microstructure of pure Fe and Fe–Cr alloys after neutron irradiation to~ 26dpa at 400°C. | Nucl Mater 2006;355:124–30.
- [83] Ohnuki S, Gelles D, Loomis B, Garner F, Takahashi H. Microstructural examination of simple vanadium alloys irradiated in the FFTF/MOTA. J Nucl Mater 1991;179:775–8.
- [84] Evans JH. Void swelling and irradiation-induced void shrinkage in neutron irradiated molybdenum and TZM. J Nucl Mater 1980;88:31-41.
- [85] Song M, Wu YD, Chen D, Wang XM, Sun C, Yu KY, et al. Response of equal channel angular extrusion processed ultrafine-grained T91 steel subjected to high temperature heavy ion irradiation. Acta Mater 2014;74:285–95.
- [86] Sun C, Zheng S, Wei CC, Wu Y, Shao L, Yang Y, et al. Superior radiation-resistant nanoengineered austenitic 304L stainless steel for applications in extreme radiation environments. Sci Rep 2015;5:7801.
- [87] Zinkle S, Farrell K, Kanazawa H. Microstructure and cavity swelling in reactor-irradiated dilute copper-boron alloy. J Nucl Mater 1991;179:994–7.
- [88] Garner F, Porter D. Reassessment of the swelling behavior of AISI 304 stainless steel. In: Hanford Engineering Development Lab.; 1982.
- [89] Dubuisson P, Gilbon D, Séran J. Microstructural evolution of ferritic-martensitic steels irradiated in the fast breeder reactor Phénix. J Nucl Mater 1993;205:178–89.
- [90] Toloczko M, Garner F, Eiholzer C. Irradiation creep and swelling of the US fusion heats of HT9 and 9Cr-1Mo to 208 dpa at~ 400 C. J Nucl Mater 1994;212:604-7.
- [91] Ghoniem NM, Kulcinski GL. The use of the fully dynamic rate theory to predict void growth in metals. Radiation Effects 1979;41:81-9.
- [92] McLaurin SK, Kulcinski GL, Dodd RA. Effects of temperature and helium on void formation in self-ion irradiated aluminum. J Nucl Mater 1983;117:208–12.
- [93] Singh BN, Evans JH. Significant differences in defect accumulation behaviour between fcc and bcc crystals under cascade damage conditions. J Nucl Mater 1995;226:277–85.
- [94] Budylkin NI, Mironova EG, Chernov VM, Krasnoselov VA, Porollo SI, Garner FA. Neutron-induced swelling and embrittlement of pure iron and pure nickel irradiated in the BN-350 and BOR-60 fast reactors. J Nucl Mater 2008;375:359–64.
- [95] Ryan TD, Taylor A. Heavy ion-induced void formation in pure nickel. In: Picraux ST, EerNisse EP, Vook FL, editors. Applications of ion beams to metals. US, Boston (MA): Springer; 1974. p. 675–85.
- [96] Garner FA, Stubbins JF. Saturation of swelling in neutron-irradiated molybdenum and its dependence on irradiation temperature and starting microstructural state. J Nucl Mater 1994;212:1298–302.
- [97] Elen JD, Hamburg G, Mastenbroek A. Voids in vanadium, niobium and molybdenum by fast neutron irradiation at high temperatures. J Nucl Mater 1971;39:194–202.
- [98] Kulcinski GL, Brimhal JL. High-temperature heavy ion bombardment of molybdenum, niobium and TZM, Belgium; 1972.
- [99] Loomis BA, Taylor A, Gerber SB. Void swelling of Nb and Nb-1% Zr induced by 58Ni+ bombardment. J Nucl Mater 1975;56:25–37.
- [100] Wiffen FW. The microstructure and swelling of neutron irradiated tantalum. | Nucl Mater 1977;67:119-30.
- [101] Yasunaga K, Watanabe H, Yoshida N, Muroga T, Noda N. Microstructure of tantalum irradiated with heavy ions. J Nucl Mater 1998;258–263(Part 1):879–82
- [102] Weber WJ, Kulcinski GL, Lott RG, Wilkes P, Smith HV. Ion simulation study of void formation in high purity vanadium, United States; 1976.
- [103] Matolich J, Nahm H, Moteff J. Swelling in neutron irradiated tungsten and tungsten-25 percent rhenium. Scripta Metall 1974;8:837-41.
- [104] Faulkner D, Woo CH. Void swelling in zirconium. J Nucl Mater 1980;90:307-16.
- [105] Jostsons A, Kelly PM, Blake RG, Farrell K. Neutron irradiation-induced defect structures in zirconium. American Society for Testing and Materials, Special Technical Publication; 1978. p. 46–61.
- [106] Cann CD, Faulkner D, Nuttall K, Styles RC, Shillinglaw AJ, Chow CK, et al. Irradiation growth in zirconium and zirconium alloys irradiated in the Dounreay fast reactor, Canada; 1986. p. 77.
- [107] Wolfer WG. Advances in void swelling and helium bubble physics. J Nucl Mater 1984;122:367-78.
- [108] Rokkam S, El-Azab A, Millett P, Wolf D. Phase field modeling of void nucleation and growth in irradiated metals. Model Simul Mater Sci Eng 2009:17:064002.
- [109] Li Y, Hu S, Sun X, Gao F, Henager CH, Khaleel M. Phase-field modeling of void migration and growth kinetics in materials under irradiation and temperature field. J Nucl Mater 2010;407:119–25.
- [110] Di S, Yao Z, Daymond MR, Zu X, Peng S, Gao F. Dislocation-accelerated void formation under irradiation in zirconium. Acta Mater 2015;82:94-9.
- [111] Dai Y, Odette G, Yamamoto T. The effects of helium in irradiated structural alloys-1.06; 2012.
- [112] Stoller RE. The influence of helium on microstructural evolution: implications for DT fusion reactors. J Nucl Mater 1990;174:289-310.
- [113] Packan N, Farrell K. Simulation of first wall damage: effects of the method of gas implantation. J Nucl Mater 1979;85:677-81.
- [114] Jostsons A, Farrell K. Structural damage and its annealing response in neutron irradiated magnesium†. Radiation Effects 1972;15:217–25.
- [115] Brimhall JL, Kulcinski GL, Kissinger HE, Mastel B. Microstructural analysis of neutron irradiated titanium and rhenium. Radiation Effects 1971;9:273–8.
- [116] Donnelly S. The density and pressure of helium in bubbles in implanted metals: a critical review. Radiation Effects 1985;90:1–47.
- [117] Han W, Fu E, Demkowicz MJ, Wang Y, Misra A. Irradiation damage of single crystal, coarse-grained, and nanograined copper under helium bombardment at 450 C. J Mater Res 2013;28:2763–70.
- [118] Zhang F, Wang X, Wierschke JB, Wang L. Helium bubble evolution in ion irradiated Al/B 4 C metal metrix composite. Scripta Mater 2015;109:28–33.
- [119] Hetherly J, Martinez E, Di Z, Nastasi M, Caro A. Helium bubble precipitation at dislocation networks. Scripta Mater 2012;66:17–20.
- [120] Yu KY, Liu Y, Sun C, Wang H, Shao L, Fu EG, et al. Radiation damage in helium ion irradiated nanocrystalline Fe. J Nucl Mater 2012;425:140-6.
- [121] Iwakiri H, Yasunaga K, Morishita K, Yoshida N. Microstructure evolution in tungsten during low-energy helium ion irradiation. J Nucl Mater 2000:283:1134-8.
- [122] Johnson P, Lawson F. Helium gas-bubble superlattice formation in molybdenum. Nucl Instrum Methods Phys Res Sect B: Beam Interact Mater Atoms 2006;243:325–34.
- [123] Fu E, Misra A, Wang H, Shao L, Zhang X. Interface enabled defects reduction in helium ion irradiated Cu/V nanolayers. J Nucl Mater 2010;407:178-88.
- [124] Carnahan NF, Starling KE. Equation of state for nonattracting rigid spheres. J Chem Phys 1969;51:635-6.
- [125] Driessen A, Van der Poll E, Silvera IF. Equation of state of solid He 4. Phys Rev B 1986;33:3269.
- [126] Mao H, Hemley R, Wu Y, Jephcoat A, Finger L, Zha C, et al. High-pressure phase diagram and equation of state of solid helium from single-crystal X-ray diffraction to 23.3 GPa. Phys Rev Lett 1988;60:2649.
- [127] Evans JH. An interbubble fracture mechanism of blister formation on helium-irradiated metals. J Nucl Mater 1977;68:129-40.

- [128] Mills R, Liebenberg D, Bronson J, Equation of state and melting properties of He 4 from measurements to 20 kbar. Phys Rev B 1980;21:5137.
- [129] Hirth JP, Lothe J. Theory of dislocations; 1982.
- [130] Wolfer W. Dislocation loop punching in bubble arrays. Phil Mag A 1989;59:87–103.
- [131] Schober T, Lasser R, Golczewski J, Dieker C, Trinkaus H. Dilatometric measurements of helium densities in bubbles arising from tritium decay in tantalum. Phys Rev B 1985;31:7109.
- [132] Zhang X, Fu E, Misra A, Demkowicz M. Interface-enabled defect reduction in He ion irradiated metallic multilayers. Jom 2010;62:75-8.
- [133] Kramer D, Brager HR, Rhodes CG, Pard AG. Helium embrittlement in type 304 stainless steel. J Nucl Mater 1968;25:121-31.
- [134] Gilbert MR, Dudarev SL, Zheng S, Packer LW, Sublet J-C. An integrated model for materials in a fusion power plant: transmutation, gas production, and helium embrittlement under neutron irradiation. Nucl Fusion 2012;52:083019.
- [135] Trinkaus H. On the modeling of the high-temperature embrittlement of metals containing helium. J Nucl Mater 1983;118:39-49.
- [136] Mansur LK. Theory and experimental background on dimensional changes in irradiated alloys. J Nucl Mater 1994;216:97-123.
- [137] Bullough R, Hayns MR, Wood MH. Sink strengths for thin-film surfaces and grain-boundaries. J Nucl Mater 1980;90:44–59.
- [138] Zinkle SJ, Snead LL, Designing radiation resistance in materials for fusion energy. Annu Rev Mater Res 2014;44:241–67.
- [139] Zinkle SJ, Moslang A. Evaluation of irradiation facility options for fusion materials research and development. Fusion Eng Des 2013;88:472–82.
- [140] Zinkle SJ, Fusion materials science: overview of challenges and recent progress. Phys Plasmas 2005;12.
- [141] Jenkins ML, Kirk MA, Phythian WJ. Experimental studies of cascade phenomena in metals. Nucl Mater 1993;205:16–30.
- [142] Dimitrov C, Sitaud B, Zhang X, Dimitrov O, Dedek U, Dworschak F. Radiation-induced defects in solid solutions and intermetallic compounds based on the Ni-Al system: I. Low-temperature electron-irradiation damage. J Phys: Condens Matter 1992;4:10199.
- [143] Arsenault RJ. The possibility of irradiation damage affecting the rate-controlling mechanism of slip in body-centered cubic metals and solid solutions. Acta Metall 1967:15:1853–9.
- [144] Schulson EM. The ordering and disordering of solid solutions under irradiation. J Nucl Mater 1979;83:239-64.
- [145] Venker H, Giesecke P, Ehrlich K. Influence of fast diffusing substitutional elements on the swelling behaviour of Ni-and Cu-alloys. In: Radiation effects in breeder reactor structural materials; 1977.
- [146] Osetsky YN, Rodney D, Bacon DJ. Atomic-scale study of dislocation-stacking fault tetrahedron interactions. Part I: mechanisms. Phil Mag 2006:86:2295–313.
- [147] Wirth BD, Bulatov VV, de la Rubia TD. Dislocation-stacking fault tetrahedron interactions in Cu. J Eng Mater Technol 2002;124:329–34.
- [148] Szelestey P, Patriarca M, Kaski K. Computational study of a screw dislocation interacting with a stacking-fault tetrahedron. Model Simul Mater Sci Eng 2005;13:541–51.
- [149] Osetsky YN, Stoller RE, Matsukawa Y. Dislocation-stacking fault tetrahedron interaction: what can we learn from atomic-scale modelling. J Nucl Mater 2004;329–333(Part B):1228–32.
- [150] Andrievskii RA. Effect of irradiation on the properties of nanomaterials. Phys Met Metallogr+ 2010;110:229-40.
- [151] Wang LM, Wang SX, Ewing RC, Meldrum A, Birtcher RC, Provencio PN, et al. Irradiation-induced nanostructures. Mater Sci Eng a-Struct 2000;286:72–80.
- [152] Wurster S, Pippan R. Nanostructured metals under irradiation. Scripta Mater 2009;60:1083–7.
- [153] Chao AW, Chou W. Reviews of accelerator science and technology, Volume 2: Medical applications of accelerators. World Scientific; 2010.
- [154] Beyerlein IJ, Caro A, Demkowicz MJ, Mara NA, Misra A, Uberuaga BP. Radiation damage tolerant nanomaterials. Mater Today 2013;16:443-9.
- [155] Adlakha I, Solanki KN. Atomic-scale investigation of triple junction role on defects binding energetics and structural stability in a alpha-Fe. Acta Mater 2016:118:64–76.
- [156] Dunn A, Dingreville R, Martinez E, Capolungo L. Identification of dominant damage accumulation processes at grain boundaries during irradiation in nanocrystalline alpha-Fe: a statistical study. Acta Mater 2016;110:306–23.
- [157] Valles G, Panizo-Laiz M, Gonzalez C, Martin-Bragado I, Gonzalez-Arrabal R, Gordillo N, et al. Influence of grain boundaries on the radiation-induced defects and hydrogen in nanostructured and coarse-grained tungsten. Acta Mater 2017;122:277–86.
- [158] Rajasekhara S, Ferreira PJ, Hattar K. Microstructural evolution of nanocrystalline nickel thin films due to high-energy heavy-ion irradiation. Aip Conf Proc 2013;1525;630–5.
- [159] Gruber J, Lim H, Abdeljawad F, Foiles S, Tucker GJ. Development of physically based atomistic microstructures: the effect on the mechanical response of polycrystals. Comp Mater Sci 2017;128:29–36.
- [160] Chen Z, Kecskes LJ, Zhu KG, Wei QM. Atomistic simulations of the effect of embedded hydrogen and helium on the tensile properties of monocrystalline and nanocrystalline tungsten. J Nucl Mater 2016;481:190–200.
- [161] El-Atwani O, Nathaniel JE, Leff AC, Muntifering BR, Baldwin JK, Hattar K, et al. The role of grain size in He bubble formation: Implications for swelling resistance. J Nucl Mater 2017;484:236–44.
- [162] Piaggi PM, Bringa EM, Pasianot RC, Gordillo N, Panizo-Laiz M, del Rio J, et al. Hydrogen diffusion and trapping in nanocrystalline tungsten. J Nucl Mater 2015:458:233-9
- [163] Samaras M, Derlet PM, Van Swygenhoven H, Victoria M. Atomic scale modelling of the primary damage state of irradiated fcc and bcc nanocrystalline metals. J Nucl Mater 2006;351:47–55.
- [164] Vetterick GA, El-Atwani O, Baldwin JK, Tonks MR, Taheri ML. Quantification of void pinning effects during grain growth of nanocrystalline iron. J Nucl Mater 2016;481:62–5.
- [165] Stoller RE, Kamenski PJ, Osetsky YN. Length-scale effects in cascade damage production in iron. Mater Res Soc Symp P 2009;1125:109-+.
- [166] Liu LL, Tang Z, Xiao W, Wang Z. Self-healing mechanism of irradiation defects near Sigma=11(113) grain boundary in copper. Mater Lett 2013;109:221-4.
- [167] El-Atwani O, Hinks JA, Greaves G, Allain JP, Maloy SA. Grain size threshold for enhanced irradiation resistance in nanocrystalline and ultrafine tungsten. Mater Res Lett 2017;5:343–9.
- [168] El-Átwani O, Nathaniel JE, Leff AC, Baldwin JK, Hattar K, Taheri ML. Evidence of a temperature transition for denuded zone formation in nanocrystalline Fe under He irradiation. Mater Res Lett 2017;5:195–200.
- [169] Muntifering B, Blair SJ, Gong C, Dunn A, Dingreville R, Qu JM, et al. Cavity evolution at grain boundaries as a function of radiation damage and thermal conditions in nanocrystalline nickel. Mater Res Lett 2016;4:96–103.
- [170] Park NY, Cha PR, Kim YC, Seok HK, Han SH, Lee SC, et al. Radiation damage in nano-crystalline tungsten: a molecular dynamics simulation. Met Mater Int 2009;15:447–52.
- [171] Misra A, Thilly L. Structural metals at extremes. Mrs Bull 2010;35:965-76.
- [172] Samaras M, Derlet PM, Van Swygenhoven H, Victoria M. Stacking fault tetrahedra formation in the neighbourhood of grain boundaries. Nucl Instrum Meth B 2003;202:51–5.
- [173] Voegeli W, Albe K, Hahn H. Simulation of grain growth in nanocrystalline nickel induced by ion irradiation. Nucl Instrum Meth B 2003;202:230-5.
- [174] Xu J, Liu JB, Li SN, Liu BX, Jiang Y. Self-healing properties of nanocrystalline materials: a first-principles analysis of the role of grain boundaries. Phys Chem Chem Phys 2016;18:17930–40.
- [175] Xiao XZ, Song DK, Chu HJ, Xue JM, Duan HL. Mechanical properties for irradiated face-centred cubic nanocrystalline metals. P Roy Soc a-Math Phy 2015;471.
- [176] Kilmametov A, Balogh A, Ghafari M, Gammer C, Mangler C, Rentenberger C, et al. Radiation effects in bulk nanocrystalline FeAl alloy. Radiat Eff Defect S 2012;167:631–9.
- [177] Andrievski RA. Behavior of radiation defects in nanomaterials. Rev Adv Mater Sci 2011;29:54-67.
- [178] Xiao XZ, Chu HJ, Duan HL. Effect of grain boundary on the mechanical behaviors of irradiated metals: a review. Sci China Phys Mech 2016;59.

- [179] Arjhangmehr A, Feghhi SAH. Irradiation deformation near different atomic grain boundaries in alpha-Zr: an investigation of thermodynamics and kinetics of point defects. Sci Reports 2016:6.
- [180] Cheng GM, Xu WZ, Wang YQ, Misra A, Zhu YT. Grain size effect on radiation tolerance of nanocrystalline Mo. Scripta Mater 2016;123:90-4.
- [181] El-Atwani O, Suslova A, Novakowski TJ, Hattar K, Efe M, Harilal SS, et al. In-situ TEM/heavy ion irradiation on ultrafine-and nanocrystalline-grained tungsten: Effect of 3 MeV Si, Cu and W ions. Mater Charact 2015;99:68–76.
- [182] Samaras M, Derlet PM, Van Swygenhoven H, Victoria M. Computer simulation of displacement cascades in nanocrystalline ni. Phys Rev Lett 2002:88:125505.
- [183] Bai XM, Voter AF, Hoagland RG, Nastasi M, Uberuaga BP. Efficient annealing of radiation damage near grain boundaries via interstitial emission. Science 2010;327:1631-4.
- [184] Chen D, Wang J, Chen TY, Shao L. Defect annihilation at grain boundaries in alpha-Fe. Sci Reports 2013;3.
- [185] Singh B. On the influence of grain boundaries on void growth. Phil Mag 1973;28:1409-13.
- [186] Skorvanek I, Gerling R. The influence of neutron irradiation on the soft magnetic and mechanical properties of amorphous and nanocrystalline Fe73. 5Cu1Nb3Si13. 5B9 alloys, J Appl Phys 1992;72:3417–22.
- [187] El-Atwani O, Hinks J, Greaves G, Gonderman S, Qiu T, Efe M, et al. In-situ TEM observation of the response of ultrafine-and nanocrystalline-grained tungsten to extreme irradiation environments. Sci Reports 2014;4.
- [188] Etienne A, Radiguet B, Cunningham N, Odette G, Valiev R, Pareige P. Comparison of radiation-induced segregation in ultrafine-grained and conventional 316 austenitic stainless steels. Ultramicroscopy 2011;111:659–63.
- [189] El-Atwani O, Efe M, Heim B, Allain JP. Surface damage in ultrafine and multimodal grained tungsten materials induced by low energy helium irradiation. J Nucl Mater 2013;434:170–7.
- [190] Nita N, Schaeublin R, Victoria M. Impact of irradiation on the microstructure of nanocrystalline materials. J Nucl Mater 2004;329:953-7.
- [191] Radiguet B, Etienne A, Pareige P, Sauvage X, Valiev R. Irradiation behavior of nanostructured 316 austenitic stainless steel. J Mater Sci 2008;43:7338–43.
- [192] Alsabbagh A, Valiev RZ, Murty KL. Influence of grain size on radiation effects in a low carbon steel. J Nucl Mater 2013;443:302-10.
- [193] Kilmametov AR, Gunderov DV, Valiev RZ, Balogh AG, Hahn H. Enhanced ion irradiation resistance of bulk nanocrystalline TiNi alloy. Scripta Mater 2008: 59:1077–30
- [194] Rose M, Balogh AG, Hahn H. Instability of irradiation induced defects in nanostructured materials. Nucl Instrum Meth B 1997;127:119-22.
- [195] Sun C, Yu KY, Lee JH, Liu Y, Wang H, Shao L, et al. Enhanced radiation tolerance of ultrafine grained Fe-Cr-Ni alloy. J Nucl Mater 2012;420:235-40.
- [196] Sun C, Garner FA, Shao L, Zhang X, Maloy SA. Influence of injected interstitials on the void swelling in two structural variants of 304L stainless steel induced by self-ion irradiation at 500 °C. Nucl Instrum Meth Phys Res Sect B: Beam Interact Mater Atoms 2017;409:323–7.
- [197] Abromeit C. Aspects of simulation of neutron damage by ion irradiation. J Nucl Mater 1994;216:78-96.
- [198] Vook F, Stein H. Relation of neutron to ion damage annealing in Si and Ge. Radiation Effects 1969;2:23–30.
- [199] Was GS, Busby JT, Allen T, Kenik EA, Jenssen A, Bruemmer SM, et al. Emulation of neutron irradiation effects with protons: validation of principle. J Nucl Mater 2002;300:198–216.
- [200] Kaoumi D, Motta AT, Birtcher RC. A thermal spike model of grain growth under irradiation. J Appl Phys 2008;104:073525.
- [201] Bufford DC, Abdeljawad FF, Foiles SM, Hattar K. Unraveling irradiation induced grain growth with in situ transmission electron microscopy and coordinated modeling. Appl Phys Lett 2015;107:191901.
- [202] Zhang YW, Jiang WL, Wang CM, Namavar F, Edmondson PD, Zhu ZH, et al. Grain growth and phase stability of nanocrystalline cubic zirconia under ion irradiation. Phys Rev B 2010;82:184105.
- [203] Zhang Y, Edmondson PD, Varga T, Moll S, Namavar F, Lan C, et al. Structural modification of nanocrystalline ceria by ion beams. Phys Chem Chem Phys 2011:13:11946–50.
- [204] Aidhy DS, Zhang YW, Weber WJ. A fast grain-growth mechanism revealed in nanocrystalline ceramic oxides. Scripta Mater 2014;83:9-12.
- [205] Jiao L, Yu KY, Chen D, Jacob C, Shao L, Zhang X, et al. Radiation tolerant nanocrystalline ZrN films under high dose heavy-ion irradiations. J Appl Phys 2015:117:145901.
- [206] Wang H, Araujo R, Swadener JG, Wang YQ, Zhang X, Fu EG, et al. Ion irradiation effects in nanocrystalline TiN coatings. Nucl Instrum Meth B 2007;261:1162–6.
- [207] Guglya A, Neklyudov I, Vasilenko R. Effect of helium ion irradiation on the structure and electrical resistivity of nanocrystalline Cr-N and V-N coatings. Radiat Eff Defect S 2007;162:643–9.
- [208] Shen TD, Feng S, Tang M, Valdez JA, Wang Y, Sickafus KE. Enhanced radiation tolerance in nanocrystalline MgGa2O4. Appl Phys Lett 2007;90:263115–500.
- [209] Rose M, Gorzawski G, Miehe G, Balogh AG, Hahn H. Phase stability of nanostructured materials under heavy ion irradiation. Nanostruct Mater 1995:6:731-4.
- [210] Jiang W, Wang H, Kim I, Bae IT, Li G, Nachimuthu P, et al. Response of nanocrystalline 3C silicon carbide to heavy-ion irradiation. Phys Rev B 2009;80.
- [211] Audren A, Monnet I, Leconte Y, Portier X, Thome L, Levalois M, et al. Structural evolution of SiC nanostructured and conventional ceramics under irradiation. Nucl Instrum Meth B 2008;266:2806–9.
- [212] Meldrum A, Boatner LA, Ewing RC. Nanocrystalline zirconia can be amorphized by ion irradiation. Phys Rev Lett 2001;88:025503.
- [213] Lu FY, Shen YO, Sun X, Dong ZL, Ewing RC, Lian J. Size dependence of radiation-induced amorphization and recrystallization of synthetic nanostructured CePO4 monazite. Acta Mater 2013;61:2984–92.
- [214] Weber WJ, Ewing RC, Wang LM. The radiation-induced crystalline-to-amorphous transition in zircon. J Mater Res 1994;9:688-98.
- [215] Weber WJ. Models and mechanisms of irradiation-induced amorphization in ceramics. Nucl Instrum Meth B 2000;166:98-106.
- [216] Zhang J, Lian J, Fuentes AF, Zhang F, Lang M, Lu F, et al. Enhanced radiation resistance of nanocrystalline pyrochlore Gd2(Ti0.65Zr0.35)207. Appl Phys Lett 2009;94:243110.
- [217] Ewing RC, Meldrum A, Wang LM, Weber WJ, Corrales LR. Radiation effects in zircon. Rev Mineral Geochem 2003;53:387–425.
- [218] Meldrum A, Boatner LA, White CW, Ewing RC. Ion irradiation effects in nonmetals: formation of nanocrystals and novel microstructures. Mater Res Innov 2000;3:190–204.
- [219] Meldrum A, Zinkle SJ, Boatner LA, Wu M, Mu R, Ueda A, et al. Radiation effects in zircon, hafnon, and thorite: Implications for Pu disposal. Microstruct Process Irradiated Mater 1999;540:395–400.
- [220] Wang SX, Wang LM, Ewing RC. Irradiation-induced amorphization: Effects of temperature, ion mass, cascade size, and dose rate. Phys Rev B 2001;63.
- [221] Elizabeth MGN, Fleischer L, Zaleski Mark A, Hertl William, Barry Carter J, Mayer James W. Microstructure of hardened and softened zirconia after xenon implantation. J Mater Res 1991;6:1905–12.
- [222] Zhang YW, Ishimaru M, Varga T, Oda T, Hardiman C, Xue HZ, et al. Nanoscale engineering of radiation tolerant silicon carbide. Phys Chem Chem Phys 2012;14:13429–36.
- [223] Jamison L, Zheng MJ, Shannon S, Allen T, Morgan D, Szlufarska I. Experimental and ab initio study of enhanced resistance to amorphization of nanocrystalline silicon carbide under electron irradiation. J Nucl Mater 2014;445:181–9.
- [224] Imada K, Ishimaru M, Xue HZ, Zhang YW, Shannon SC, Weber WJ. Amorphization resistance of nano-engineered SiC under heavy ion irradiation. J Nucl Mater 2016;478:310–4.
- [225] Huguet-Garcia J, Jankowiak A, Miro S, Gosset D, Serruys Y, Costantini JM. Study of the ion-irradiation behavior of advanced SiC fibers by Raman spectroscopy and transmission electron microscopy. J Am Ceram Soc 2015;98:675–82.
- [226] Jiang W, Wang H, Kim I, Zhang Y, Weber WJ. Amorphization of nanocrystalline 3C-SiC irradiated with Si+ ions. J Mater Res 2010;25:2341-8.

- [227] Intarasiri S, Yu LD, Singkarat S, Hallen A, Lu J, Ottosson M, et al. Effects of low-fluence swift iodine ion bombardment on the crystallization of ion-beam-synthesized silicon carbide. J Appl Phys 2007;101.
- [228] Jiang H, Wang X, Szlufarska I. The multiple roles of small-angle tilt grain boundaries in annihilating radiation damage in SiC. Sci Reports 2017;7.
- [229] Swaminathan N, Kamenski PJ, Morgan D, Szlufarska I. Effects of grain size and grain boundaries on defect production in nanocrystalline 3C-SiC. Acta Mater 2010;58:2843–53.
- [230] Jamison L, Sridharan K, Shannon S, Szlufarska I. Temperature and irradiation species dependence of radiation response of nanocrystalline silicon carbide. J Mater Res 2014:29:2871–80.
- [231] Uberuaga BP, Vernon LJ, Martinez E, Voter AF. The relationship between grain boundary structure, defect mobility, and grain boundary sink efficiency. Sci Reports 2015;5:9095.
- [232] Tschopp MA, Solanki KN, Gao F, Sun X, Khaleel MA, Horstemeyer MF. Probing grain boundary sink strength at the nanoscale: energetics and length scales of vacancy and interstitial absorption by grain boundaries in alpha-Fe. Phys Rev B 2012;85:064108.
- [233] Tschopp MA, Spearot DE, McDowell DL. Chapter 82 Influence of Grain Boundary Structure on Dislocation Nucleation in FCC Metals, vol. 14; 008. p. 43–139.
- [234] Bai XM, Uberuaga BP. The influence of grain boundaries on radiation-induced point defect production in materials: a review of atomistic studies. Jom 2013;65:360–73.
- [235] Li XY, Liu W, Xu YC, Liu CS, Fang QF, Pan BC, et al. An energetic and kinetic perspective of the grain-boundary role in healing radiation damage in tungsten. Nucl Fusion 2013;53:123014.
- [236] Han WZ, Demkowicz MJ, Fu EG, Wang YQ, Misra A. Effect of grain boundary character on sink efficiency. Acta Mater 2012;60:6341-51.
- [237] Barr CM, Vetterick GA, Unocic KA, Hattar K, Bai XM, Taheri ML. Anisotropic radiation-induced segregation in 316L austenitic stainless steel with grain boundary character. Acta Mater 2014:67:145–55.
- [238] Vetterick GA, Gruber J, Suri PK, Baldwin JK, Kirk MA, Baldo P, et al. Achieving radiation tolerance through non-equilibrium grain boundary structures. Sci Rep 2017;7:12275.
- [239] Zinkle SJ. Effect of H and He irradiation on cavity formation and blistering in ceramics. Nucl Instrum Meth B 2012;286:4-19.
- [240] Chen J. Jung P. Trinkaus H. Microstructural evolution of helium-implanted alpha-SiC. Phys Rev B 2000;61:12923-32.
- [241] Chen J, Jung P, Trinkaus H. Evolution of helium platelets and associated dislocation loops in alpha-SiC. Phys Rev Lett 1999;82:2709–12.
- [242] Tokitani M, Ohtawa Y, Yoshida N, Tokunaga K, Fujiwara T, Ashikawa N, et al. Micro/nano scale modification of plasma facing components in LHD and its impact on the metal dust generations. J Nucl Mater 2009;390–91:156–9.
- [243] Yoshida N, Iwakiri H, Tokunaga K, Baba T. Impact of low energy helium irradiation on plasma facing metals. J Nucl Mater 2005;337:946-50.
- [244] Yoshida N, Miyamoto M, Tokunaga K, Iwakiri H, Wakimoto H, Fujiwara T, et al. Microscopic damage of metals exposed to the helium discharges in TRIAM-1M tokamak and its impact on hydrogen recycling process. Nucl Fusion 2003;43:655–9.
- [245] Cui MH, Wang ZG, Pang LL, Shen TL, Yao CF, Li BS, et al. Temperature dependent defects evolution and hardening of tungsten induced by 200 keV Heions. Nucl Instrum Meth B 2013;307:507–11.
- [246] Perez D, Sandoval L, Blondel S, Wirth BD, Uberuaga BP, Voter AF. The mobility of small vacancy/helium complexes in tungsten and its impact on retention in fusion-relevant conditions. Sci Reports 2017;7.
- [247] Chen J, He ZY, Jung P. Microstructure of helium-implanted α-Al2O3 after annealing. Acta Mater 2006;54:1607–14.
- [248] Song P, Sun J, Wang Z, Cui M, Shen T, Li Y, et al. Irradiation resistance properties studies on helium ions irradiated MAX phase Ti3AlC2. Nucl Instrum Meth Phys Res Sect B: Beam Interact Mater Atoms 2014;326:332–6.
- [249] Trinkaus H, Singh BN. Helium accumulation in metals during irradiation where do we stand? | Nucl Mater 2003;323:229-42.
- [250] Ehrlich K. The role of precipitates for the development of irradiation-induced swelling and high-temperature embrittlement in an austenitic stainless steel of type X10 CrNiMoTiB 15 15. Z Metallkd 2003;94:485–91.
- [251] Dobmann G, Korshunov SN, Kroening M, Martynenko YV, Skorlupkin ID, Surkov AS. Helium and radiation defect accumulation in metals under stress. Vacuum 2008;82:856–66.
- [252] Tan XY, Luo LM, Chen HY, Zhu XY, Zan X, Luo GN, et al. Mechanical properties and microstructural change of W-Y2O3 alloy under helium irradiation. Sci Reports 2015:5.
- [253] Xu J, Wang CB, Zhang W, Ren CL, Gong HF, Huai P. Atomistic simulations of the interactions of helium with dislocations in nickel. Nucl Mater Energy 2016;7:12–9.
- [254] Martinez E, Uberuaga BP, Wirth BD. Atomistic modeling of helium segregation to grain boundaries in tungsten and its effect on de-cohesion. Nucl Fusion 2017:57.
- [255] Liontas R, Gu XW, Fu EG, Wang YQ, Li N, Mara N, et al. Effects of helium implantation on the tensile properties and microstructure of Ni73P27 metallic glass nanostructures. Nano Lett 2014;14:5176–83.
- [256] Ding MS, Du JP, Wan L, Ogata S, Tian L, Ma E, et al. Radiation-induced helium nanobubbles enhance ductility in submicron-sized single-crystalline copper. Nano Lett 2016;16:4118–24.
- [257] Gong HF, Wang CB, Zhang W, Huai P, Lu W, Zhu ZY. Atomistic simulation of the trapping capability of He- vacancy defects at Ni Sigma 3(1(1)overbar2)[110] grain boundary. Model Simul Mater Sci Eng 2016;24.
- [258] Gazda J, Chung HM, Loomis BA, Meshii M. Effects of heavy-ion irradiation on microstructure of V-4Cr-4Ti alloy at moderate temperatures. Microstruct Evol Irrad 1997;439:349–54.
- [259] Huang HF, Zhang W, De Los Reyes M, Zhou XL, Yang C, Xie R, et al. Mitigation of He embrittlement and swelling in nickel by dispersed SiC nanoparticles. Mater Des 2016;90:359–63.
- [260] Gao N, Victoria M, Chen J, Van Swygenhoven H. Helium-vacancy cluster in a single bcc iron crystal lattice. J Phys-Condens Mat 2011;23.
- [261] Zhang T, Vieh C, Wang K, Dai Y. Irradiation-induced evolution of mechanical properties and microstructure of Eurofer 97. J Nucl Mater 2014;450:48–53.
- [262] Zhang L, Fu CC, Hayward E, Lu GH. Properties of He clustering in alpha-Fe grain boundaries. J Nucl Mater 2015;459:247–58.
- [263] Zhang CH, Chen KQ, Wang YS, Sun JG, Shen DY. Formation of bubbles in helium implanted 316L stainless steel at temperatures between 25 and 550 °C. J Nucl Mater 1997;245:210–6.
- [264] Zhang CH, Chen KQ, Wang YS, Sun JG. Temperature dependence of bubble structure in 316L stainless steel irradiated with 2.5 MeV He ions. J Nucl Mater 1998;258:1623–7.
- [265] Zell V, Schroeder H, Trinkaus H. Helium bubble formation in nickel during hot implantation. J Nucl Mater 1994;212:358-63.
- [266] Yu JN, Zhao XJ, Zhang W, Yang W, Chu FM. Defect production and accumulation under hydrogen and helium ion irradiation. J Nucl Mater 1997;251:150–6.
- [267] Yamamoto T, Wu Y, Odette GR, Yabuuchi K, Kondo S, Kimura A. A dual ion irradiation study of helium-dpa interactions on cavity evolution in tempered martensitic steels and nanostructured ferritic alloys. J Nucl Mater 2014;449:190–9.
- [268] Yamamoto T, Odette GR, Miao P, Hoelzer DT, Bentley J, Hashimoto N, et al. The transport and fate of helium in nanostructured ferritic alloys at fusion relevant He/dpa ratios and dpa rates. J Nucl Mater 2007;367:399–410.
- [269] Yamamoto T, Odette GR, Miao P, Edwards DJ, Kurtz RJ. Helium effects on microstructural evolution in tempered martensitic steels: In situ helium implanter studies in HFIR. J Nucl Mater 2009;386–88:338–41.
- [270] Wang K, Dai Y, Spatig P. Microstructure and fracture behavior of F82H steel under different irradiation and tensile test conditions. J Nucl Mater 2016;468:246–54.
- [271] Wang J, Gao X, Gao N, Wang ZG, Cui MH, Wei KF, et al. Grain size effects on He bubbles distribution and evolution. J Nucl Mater 2015;457:182-5.
- [272] van Veen A, Konings RJM, Fedorov AV. Helium in inert matrix dispersion fuels. J Nucl Mater 2003;320:77-84.

- [273] Ullmaier H, Chen J, Low temperature tensile properties of steels containing high concentrations of helium, J Nucl Mater 2003;318:228–33.
- [274] Trinkaus H, Ullmaier H. High-Temperature Embrittlement of Metals Due to Helium Is the Lifetime Dominated by Cavity Growth or Crack-Growth. J Nucl Mater 1994:212:303–9
- [275] Trinkaus H. The effect of cascade induced gas resolution on bubble formation in metals. J Nucl Mater 2003;318:234-40.
- [276] Suzudo T, Tsuru T, Yamaguchi M, Kaburaki H. An atomistic modeling of He bubble stability at grain boundaries in alpha-Fe. J Nucl Mater 2013;442: S655-9.
- [277] Schroeder H, Dai Y. Helium concentration-dependence of embrittlement effects in Din 1.4970, 13-Percent Cw Austenitic Stainless-Steel at 873-K. J Nucl Mater 1992:191:781-5.
- [278] Ryazanov Al, Chugunov OK, Ivanov SM, Latushkin ST, Lindau R, Moslang A, et al. Tensile properties and microstructure of helium implanted EUROFER ODS. | Nucl Mater 2013;442:S153-7.
- [279] Peng L, Dai Y. Helium-induced hardening effect in ferritic/martensitic steels F82H and Optimax-A irradiated in a mixed spectrum of high energy protons and spallation neutrons. J Nucl Mater 2011;417:996–1000.
- [280] Oono N, Ukai S, Kondo S, Hashitomi O, Kimura A. Irradiation effects in oxide dispersion strengthened (ODS) Ni-base alloys for Gen IV nuclear reactors. | Nucl Mater 2015;465:835–9.
- [281] Nakamura Y, Kitajima S, Shinohara K, Ishimoto S, Shodai T, Torimaru T, et al. Low-temperature embrittlement of low-energy He implanted pure iron and iron-based alloys. J Nucl Mater 1991;179:749–52.
- [282] Miura T, Fujii K, Fukuya K. Micro-mechanical investigation for effects of helium on grain boundary fracture of austenitic stainless steel. J Nucl Mater 2015;457:279–90.
- [283] Magnusson P, Chen JC, Hoffelner W. High temperature creep of a helium-implanted titanium aluminide alloy. J Nucl Mater 2011;416:60-4.
- [284] Magnusson P, Chen J, Jung P, Sauvage T, Hoffelner W, Spatig P. Helium embrittlement of a lamellar titanium aluminide. J Nucl Mater 2013;434:252-8.
- [285] Kurtz RJ, Heinisch HL. The effects of grain boundary structure on binding of He in Fe. J Nucl Mater 2004;329:1199-203.
- [286] Jung P, Klein H, Henry J, Chen J. Effect of implanted deuterium on tensile properties of helium-doped RAFM EUROFER97. J Nucl Mater 2011;417:1013–7.
- [287] Jublot-Leclerc S, Lescoat ML, Fortuna F, Legras L, Li X, Gentils A. TEM study of the nucleation of bubbles induced by He implantation in 316L industrial austenitic stainless steel. J Nucl Mater 2015;466:646–52.
- [288] Imasaki K, Hasegawa A, Nogami S, Satou M. Helium effects on the tensile property of 316FR stainless steel at 650 and 750 degrees C. J Nucl Mater 2011;417:1030–3.
- [289] Gaganidze E, Petersen C, Aktaa J. Study of helium embrittlement in boron doped EUROFER97 steels. J Nucl Mater 2009;386-88:349-52.
- [290] Feng YX, Shang JX, Lu GH. Migration and nucleation of helium atoms at (110) twist grain boundaries in tungsten. J Nucl Mater 2017;487:200-9.
- [291] Edmondson PD, Parish CM, Zhang Y, Hallen A, Miller MK. Helium bubble distributions in a nanostructured ferritic alloy. J Nucl Mater 2013;434:210-6.
- [292] Dai Y, Henry J, Tong Z, Averty X, Malaplate J, Long B. Neutron/proton irradiation and He effects on the microstructure and mechanical properties of ferritic/martensitic steels T91 and EM10. J Nucl Mater 2011;415:306–10.
- [293] Chen J, Jung P, Rebac T, Duval F, Sauvage T, de Carlan Y, et al. Helium effects on creep properties of Fe-14CrWTi ODS steel at 650 degrees C. J Nucl Mater 2014;453:253–8.
- [294] Yao B, Edwards DJ, Kurtz RJ, Odette GR, Yamamoto T. Multislice simulation of transmission electron microscopy imaging of helium bubbles in Fe. J Electron Microsc 2012;61:393–400.
- [295] Zhang X, Ren CL, Han H, Wang CB, Huang HF, Yin YR, et al. First-principles prediction of interstitial carbon, nitrogen, and oxygen effects on the helium behavior in nickel. J Appl Phys 2017;122.
- [296] Liu PP, Zhan Q, Fu ZY, Wei YP, Wang YM, Wang FM, et al. Surface and internal microstructure damage of He-ion-irradiated CLAM steel studied by cross-sectional transmission electron microscopy. J Alloy Compd 2015;649:859–64.
- [297] Shi JY, Peng L, Ye MY, Gao F. Molecular dynamics study: effects of he bubble and Cr precipitate on tensile deformation of grain boundaries in alpha-Fe. IEEE T Plasma Sci 2017;45:289–93.
- [298] Chen JH, Guo LP, Luo FF, Li TC, Ren YY, Suo JP. Synergistic effects in reduced-activation martensitic steel under single and sequential helium/hydrogen ion irradiation. Fusion Sci Technol 2014;66:301–7.
- [299] Dai Y, Schroeder H. Creep-properties and microstructures of helium implanted Aisi 316l electron-beam weld and parent material. Fusion Eng Des 1995;30:261–73.
- [300] Chen J, Long Y. A first-principles study on the helium doped grain boundary in metal Al. Eur Phys J B 2012;85.
- [301] Hong MQ, Wang YQ, Ren F, Zhang HX, Fu DJ, Yang B, et al. Helium release and amorphization resistance in ion irradiated nanochannel films. Epl-Europhys Lett 2014:106.
- [302] Demkowicz MJ, Misra A, Caro A. The role of interface structure in controlling high helium concentrations. Curr Opin Solid St M 2012;16:101–8.
- [303] Terentyev D, He X. Effect of Cr precipitates and He bubbles on the strength of <110> tilt grain boundaries in BCC Fe: an atomistic study. Comp Mater Sci 2011:50:925–33.
- [304] Wang J, Gao X, Wang ZG, Wei KF, Yao CF, Cui MH, et al. TEM characterization of helium bubbles in T91 and MNHS steels implanted with 200 keV He ions at different temperatures. Chinese Phys Lett 2015;32.
- [305] Zhernenkov M, Gill S, Stanic V, DiMasi E, Kisslinger K, Baldwin JK, et al. Design of radiation resistant metallic multilayers for advanced nuclear systems. Appl Phys Lett 2014;104.
- [306] Liu XK, Liu Y, Qian DZ, Zheng Z. First-principles study of helium atom doped interstitial sites of Al. Acta Phys Sin-Ch Ed 2010;59:6450-6.
- [307] Tschopp MA, Gao F, Solanki KN. He-V cluster nucleation and growth in alpha-Fe grain boundaries. Acta Mater 2017;124:544-55.
- [308] Martinez E, Schwen D, Caro A. Helium segregation to screw and edge dislocations in alpha-iron and their yield strength. Acta Mater 2015;84:208–14.
- [309] Muntifering B, Dingreville R, Hattar K, Qu J. Electron beam effects during in-situ annealing of self-ion irradiated nanocrystalline nickel. In: MRS proceedings. Cambridge Univ Press; 2015. p. 13–8.
- [310] Detor AJ, Schuh CA. Grain boundary segregation, chemical ordering and stability of nanocrystalline alloys: Atomistic computer simulations in the Ni-W system. Acta Mater 2007;55:4221–32.
- [311] Chookajorn T, Murdoch HA, Schuh CA. Design of stable nanocrystalline alloys. Science 2012;337:951–4.
- [312] Kacher J, Elizaga P, House SD, Hattar K, Nowell M, Robertson IM. Thermal stability of Ni/NiO multilayers. Mater Sci Eng a-Struct 2013;568:49-60.
- [313] Gianola DS, Van Petegem S, Legros M, Brandstetter S, Van Swygenhoven H, Hemker KJ. Stress-assisted discontinuous grain growth and its effect on the deformation behavior of nanocrystalline aluminum thin films. Acta Mater 2006;54:2253–63.
- [314] Sagaradze VV, Litvinov AV, Shabashov VA, Vil'danova NF, Mukoseev AG, Kozlov KA. New method of mechanical alloying of ODS steels using iron oxides. Phys Met Metallogr+ 2006;101:566–76.
- [315] Dapeng Z, Yong L, Feng L, Yuren W, Liujie Z, Yuhai D. ODS ferritic steel engineered with bimodal grain size for high strength and ductility. Mater Lett 2011:65:1672–4.
- [316] Bachmaier A, Rathmayr GB, Bartosik M, Apel D, Zhang Z, Pippan R. New insights on the formation of supersaturated solid solutions in the Cu-Cr system deformed by high-pressure torsion. Acta Mater 2014;69:301–13.
- [317] Bryden KJ, Ying JY. Thermal stability and hydrogen absorption characteristics of palladium-yttrium nanoalloys. Acta Mater 1996;44:3847-54.
- [318] Darling KA, Tschopp MA, Guduru RK, Yin WH, Wei Q, Kecskes LJ. Microstructure and mechanical properties of bulk nanostructured Cu-Ta alloys consolidated by equal channel angular extrusion. Acta Mater 2014;76:168–85.
- [319] Dubois JB, Thilly L, Renault PO, Lecouturier F, Di Michiel M. Thermal stability of nanocomposite metals: In situ observation of anomalous residual stress relaxation during annealing under synchrotron radiation. Acta Mater 2010;58:6504–12.

- [320] Fan Z, Jian J, Liu Y, Chen Y, Song M, Jiao L, et al. In situ studies on superior thermal stability of bulk FeZr nanocomposites. Acta Mater 2015:101:125–35.
- [321] Millett PC, Selvam RP, Saxena A. Stabilizing nanocrystalline materials with dopants. Acta Mater 2007;55:2329-36.
- [322] Polyakov MN, Chookajorn T, Mecklenburg M, Schuh CA, Hodge AM. Sputtered Hf-Ti nanostructures: a segregation and high-temperature stability study. Acta Mater 2016:108:8–16.
- 13231 Saldana C. King AH. Chandrasekar S. Thermal stability and strength of deformation microstructures in pure copper. Acta Mater 2012;60:4107–16.
- [324] Schuh B, Mendez-Martin F, Volker B, George EP, Clemens H, Pippan R, et al. Mechanical properties, microstructure and thermal stability of a nanocrystalline CoCrFeMnNi high-entropy alloy after severe plastic deformation. Acta Mater 2015;96:258–68.
- [325] Zahid GH, Huang Y, Prangnell PB. Microstructure and texture evolution during annealing a cryogenic-SPD processed Al-alloy with a nanoscale lamellar HAGB grain structure. Acta Mater 2009;57:3509–21.
- [326] Zhang HW, Huang X, Pippan R, Hansen N. Thermal behavior of Ni (99.967% and 99.5% purity) deformed to an ultra-high strain by high pressure torsion. Acta Mater 2010;58:1698–707.
- [327] Zhang P, Zhang JY, Li J, Liu G, Wu K, Wang YQ, et al. Microstructural evolution, mechanical properties and deformation mechanisms of nanocrystalline Cu thin films alloyed with Zr. Acta Mater 2014;76:221–37.
- [328] Zhou F, Liao XZ, Zhu YT, Dallek S, Lavernia EJ. Microstructural evolution during recovery and recrystallization of a nanocrystalline Al-Mg alloy prepared by cryogenic ball milling. Acta Mater 2003;51:2777-91.
- [329] Botcharova E, Freudenberger J, Schutz L. High thermal stability of mechanically-alloyed nanocrystalline Cu-Nb alloys. Int J Mater Res 2006;97:1350-4.
- [330] Abad MD, Parker S, Kiener D, Primorac MM, Hosemann P. Microstructure and mechanical properties of CuxNb1-x alloys prepared by ball milling and high pressure torsion compacting. J Alloy Compd 2015;630:117–25.
- [331] Bhattacharya D, Rao TVC, Bhushan KG, Ali K, Debnath A, Singh S, et al. Thermal evolution of nanocrystalline co-sputtered Ni-Zr alloy films: Structural,
- magnetic and MD simulation studies. J Alloy Compd 2015;649:746–54.

 [332] Kotan H, Darling KA, Saber M, Koch CC, Scattergood RO. Effect of zirconium on grain growth and mechanical properties of a ball-milled nanocrystalline FeNi alloy. J Alloy Compd 2013;551:621–9.
- [333] Sadeghian Z, Lotfi B, Enayati MH, Beiss P. Microstructural and mechanical evaluation of Al-TiB2 nanostructured composite fabricated by mechanical alloying. J Alloy Compd 2011;509:7758–63.
- [334] Santhi K, Thirumal E, Karthick SN, Kim HJ, Narayanan V, Stephen A. Structural and magnetic investigations on metastable Ag-Fe nanophase alloy. J Alloy Compd 2013;557:172–8.
- [335] Zhao KY, Li CJ, Tao JM, Ng DHL, Zhu XK. The synthesis, microstructure, hardness and thermal properties of bulk nanocrystalline Al produced by in situ consolidation with low-energy ball milling. J Alloy Compd 2010;504:S306–10.
- [336] Chu JP, Hsieh YY, Lin CH, Mahalingam T. Thermal stability enhancement in nanostructured Cu films containing insoluble tungsten carbides for metallization. J Mater Res 2005;20:1379–84.
- [337] Donaldson OK, Wang WB, Hattar K, Trelewicz JR. Impurity stabilization of nanocrystalline grains in pulsed laser deposited tantalum. J Mater Res 2017;32:1351–60.
- [338] Natter H, Schmelzer M, Hempelmann R. Nanocrystalline nickel and nickel-copper alloys: synthesis, characterization, and thermal stability. J Mater Res 1998;13:1186–97.
- [339] Andrievski RA. Review of thermal stability of nanomaterials. J Mater Sci 2014;49:1449-60.
- [340] Kotan H, Darling KA, Saber M, Scattergood RO, Koch CC. Thermal stability and mechanical properties of nanocrystalline Fe-Ni-Zr alloys prepared by mechanical alloying. J Mater Sci 2013;48:8402–11.
- [341] Molinari A, Lonardelli I, Demetrio K, Menapace C. Effect of the particle size on the thermal stability of nanostructured aluminum powder: dislocation density and second-phase particles controlling the grain growth. J Mater Sci 2010;45:6739–46.
- [342] Rajgarhia RK, Saxena A, Spearot DE, Hartwig KT, More KL, Kenik EA, et al. Microstructural stability of copper with antimony dopants at grain boundaries: experiments and molecular dynamics simulations. J Mater Sci 2010;45:6707–18.
- [343] Shin DI, Gitzhofer F, Moreau C. Thermal property evolution of metal based thermal barrier coatings with heat treatments. J Mater Sci 2007;42:5915–23.
- [344] Wilde G, Rosner H. Stability aspects of bulk nanostructured metals and composites. | Mater Sci 2007;42:1772-81.
- [345] Zhou Y, Erb U, Aust KT, Palumbo G. Magnetic and interface microstructure contribution to bulk specific heat of nanocrystalline Ni-P alloy. J Mater Sci 2013:48:6141–9.
- [346] Zhu M, Wu ZF, Zeng MQ, Ouyang LZ, Gao Y. Bimodal growth of the nanophases in the dual-phase composites produced by mechanical alloying in immiscible Cu-Ag system. J Mater Sci 2008;43:3259–66.
- [347] Tawancy HM. Synthesis of bulk nanostructured DO22 superlattice of Ni-3(Mo, Nb) with high strength, high ductility, and high thermal stability. J Nanomater; 2012.
- [348] Wawer K, Lewandowska M, Kurzydlowski KJ. Precipitate Strengthening of Nanostructured Aluminium Alloy. J Nanosci Nanotechno 2012;12:8783-6.
- [349] Danielson T, Hin C. Structural and electronic effects of helium interstitials in Y2Ti2O7: a first-principles study. J Nucl Mater 2014;452:189–96.
- [350] Tai KP, Averback RS, Bellon P, Ashkenazy Y, Stumphy B. Temperature dependence of irradiation-induced creep in dilute nanostructured Cu-W alloys. J Nucl Mater 2012;422:8–13.
- [351] Roman I, Fratila C, Vasile E, Petre A, Soare ML. Electrochemical evaluation of the stability of ceramic nanostructured titanium oxide layers in Ringer solution. J Optoelectron Adv M 2010;12:1597–603.
- [352] Sarkar A, Murugan AV, Manthiram A. Synthesis and characterization of nanostructured Pd-Mo electrocatalysts for oxygen reduction reaction in fuel cells. J Phys Chem C 2008;112:12037–43.
- [353] Danielson T, Tea E, Hin C. First-principles investigation of helium in Y2O3. J Phys D Appl Phys 2016;49.
- [354] Samolyuk GD, Osetsky YN. Thermodynamic approach to the stability of multi-phase systems: application to the Y2O3-Fe system. J Phys-Condens Mater 2015;27.
- [355] Rajagopalan M, Darling K, Turnage S, Koju RK, Hornbuckle B, Mishin Y, et al. Microstructural evolution in a nanocrystalline Cu-Ta alloy: a combined in-situ TEM and atomistic study. Mater Des 2017;113:178–85.
- [356] Darling KA, Huskins EL, Schuster BE, Wei Q, Kecskes LJ. Mechanical properties of a high strength Cu-Ta composite at elevated temperature. Mater Sci Eng a-Struct 2015;638:322–8.
- [357] Hibbard GD, Radmilovic V, Aust KT, Erb U. Grain boundary migration during abnormal grain growth in nanocrystalline Ni. Mater Sci Eng a-Struct 2008;494:232–8.
- [358] Khodabakhshi F, Kazeminezhad M. The annealing phenomena and thermal stability of severely deformed steel sheet. Mater Sci Eng a-Struct 2011;528:5212–8.
- [359] Park KT, Shin DH. Annealing behavior of submicrometer grained ferrite in a low carbon steel fabricated by severe plastic deformation. Mater Sci Eng a-Struct 2002;334:79–86.
- [360] Sun YL, Xu SQ, Shan AD. Effects of annealing on microstructure and mechanical properties of nano-grained Ni-based alloy produced by severe cold rolling. Mater Sci Eng a-Struct 2015;641:181–8.
- [361] Tao JM, Chen GM, Jian WW, Wang J, Zhu YT, Zhu XK, et al. Anneal hardening of a nanostructured Cu-Al alloy processed by high-pressure torsion and rolling. Mater Sci Eng a-Struct 2015;628:207–15.
- [362] Asgharzadeh H, McQueen HJ. Grain growth and stabilisation of nanostructured aluminium at high temperatures: review. Mater Sci Tech-Lond 2015;31:1016–34.

- [363] Deng WJ, Li Q, Li BL, Xie ZC, He YT, Tang Y, et al. Thermal stability of ultrafine grained aluminium alloy prepared by large strain extrusion machining.

 Mater Sci Tech-Lond 2014:30:850–9.
- [364] Sun FS, Zuniga A, Rojas P, Lavernia EJ. Thermal stability and recrystallization of nanocrystalline Ti produced by cryogenic milling. Metall Mater Trans A 2006;37a:2069–78.
- [365] Xu WZ, Li LL, Saber M, Koch CC, Zhu YT, Scattergood RO. Microstructures and stabilization mechanisms of nanocrystalline iron-chromium alloys with hafnium addition. Metall Mater Trans A 2015;46a:4394–4404.
- [366] Hibbard G, Erb U, Aust KT, Klement U, Palumbo G. Thermal stability of nanostructured electrodeposits. Mater Sci Forum 2002;386–3:387–96.
- [367] Zhang HW, Lu K, Pippan R, Huang X, Hansen N. Strong and stable nanostructured Ni by light alloying. Riso Mater Sci 2012:399-406.
- [368] Lu K. Stabilizing nanostructures in metals using grain and twin boundary architectures. Nat Rev Mater 2016;1.
- 369 Huller M, Vlcek J, Dinkel M, Hoppel HW, Goken M. Hardening and thermal stability of nanocrystalline AlMg4.8 powder. Phil Mag 2008;88:1209–26.
- [370] Zhang W, Du K, Chen XQ, Sheng LY, Ye HQ. Thermally stable coherent domain boundaries in complex-structured Cr2Nb intermetallics. Phil Mag 2016;96:58–70.
- [371] Koch CC, Scattergood RO, VanLeeuwen BK, Darling KA. Thermodynamic stabilization of grain size in nanocrystalline metals. Recrystall Grain Growth Iv 2012;715–716:323-+.
- [372] Koch CC, Scattergood RO, Kotan H, Saber M. Thermal stability of nanocrystalline grain size in ternary Fe-base alloys. Recrystall Grain Growth V 2013;753:341–4.
- [373] Kolobov YR, Lipnitskii AG, Ivanov MB, Nelasov IV, Manokhin SS. Investigations of the thermal stability of the microstructure of titanium produced by intense plastic deformation. Russ Phys J+ 2012;54:918–36.
- [374] Dusoe KJ, Vijayan S, Bissell TR, Chen J, Morley JE, Valencia L, et al. Strong, ductile, and thermally stable Cu-based metal-intermetallic nanostructured composites. Sci Reports 2017:7.
- [375] Jiang L, Li JK, Cheng PM, Liu G, Wang RH, Chen BA, et al. Microalloying ultrafine grained Al alloys with enhanced ductility. Sci Reports 2014;4.
- [376] Zheng SJ, Carpenter JS, McCabe RJ, Beyerlein IJ, Mara NA. Engineering interface structures and thermal stabilities via SPD processing in bulk nanostructured metals. Sci Reports 2014;4.
- [377] Asgharzadeh H, Simchi A, Kim HS. High-temperature deformation and structural restoration of a nanostructured Al alloy. Scripta Mater 2012;66:911–4.
- [378] Shankar MR, Rao BC, Chandrasekar S, Compton WD, King AH. Thermally stable nanostructured materials from severe plastic deformation of precipitation-treatable Ni-based alloys. Scripta Mater 2008;58:675–8.
- [379] Wang YM, Jankowski AF, Hamza AV. Strength and thermal stability of nanocrystalline gold alloys. Scripta Mater 2007;57:301-4.
- [380] Zhang BB, Tao NR, Lu K. A high strength and high electrical conductivity bulk Cu-Ag alloy strengthened with nanotwins. Scripta Mater 2017;129:39–43.
- [381] Fecht HJ. Nanostructure formation and thermal stability of nanophase materials prepared by mechanical means. Z Metallkd 2003;94:1134-42.
- [382] K. Zhou, H. Li, J.B. Pang, Z. Wang, Effects of oxide distributed in grain boundaries on microstructure stability of nanocrystalline metals, in: Journal of Physics: Conference Series, IOP Publishing, 2013, pp. 012020.
- [383] Was GS. Ion-beam modification of metals compositional and microstructural changes. Progr Surf Sci 1989;32:211-332.
- [384] Beck L, Serruys Y, Miro S, Trocellier P, Bordas E, Leprêtre F, et al. Ion irradiation and radiation effect characterization at the JANNUS-Saclay triple beam facility. J Mater Res 2015;30:1183–94.
- [385] Taylor C, Muntifering B, Snow C, Hattar K, Senor D. Using in-situ TEM triple ion beam irradiations to study the effects of deuterium, helium, and radiation damage on TPBAR components. Microsc Microanal 2017;23:2216–7.
- [386] Chisholm C, Hattar K, Minor AM. In situ TEM concurrent and successive Au self-ion irradiation and He implantation. Mater Trans 2014;55:418-22.
- [387] Schuh CA. Replacing chrome coatings with safer metal alloys. Adv Manuf Technol 2009;30:1–3.
- [388] Valiev RZ, Langdon TG. Principles of equal-channel angular pressing as a processing tool for grain refinement. Prog Mater Sci 2006;51:881–981.
- [389] Valiev RZ, Islamgaliev RK, Alexandrov IV. Bulk nanostructured materials from severe plastic deformation. Prog Mater Sci 2000;45:103-89.
- [390] Zhu YT, Jiang H, Huang J, Lowe TC. A new route to bulk nanostructured metals. Metall Mater Trans A 2001;32:1559-62.
- [391] Valiev RZ, Estrin Y, Horita Z, Langdon TG, Zechetbauer MJ, Zhu YT. Producing bulk ultrafine-grained materials by severe plastic deformation. JOM 2006;58:33–9.
- [392] Estrin Y, Vinogradov A. Extreme grain refinement by severe plastic deformation: a wealth of challenging science. Acta Mater 2013;61:782-817.
- [393] Lowe TC, Valiev RZ. Investigations and applications of severe plastic deformation. Dordrecht; Boston: Kluwer Academic Publishers; 2000.
- [394] Mughrabi H, Höppel HW, Kautz M. Fatigue and microstructure of ultrafine-grained metals produced by severe plastic deformation. Scripta Mater 2004;51:807–12.
- [395] Zhu YT, Lowe TC, Langdon TG. Performance and applications of nanostructured materials produced by severe plastic deformation. Scripta Mater 2004;51:825–30.
- [396] Höchbauer T, Misra A, Hattar K, Hoagland R. Influence of interfaces on the storage of ion-implanted He in multilayered metallic composites. J Appl Phys 2005;98:123516.
- [397] Rao SI, Hazzledine PM. Atomistic simulations of dislocation-interface interactions in the Cu-Ni multilayer system. Phil Mag A 2000;80:2011–40.
- [398] Choudhury S, Morgan D, Uberuaga BP. Massive interfacial reconstruction at misfit dislocations in metal/oxide interfaces. Sci Reports 2014;4.
- [399] Koehler JS. Attempt to design a strong solid. Phys Rev B 1970;2:547-51.
- [400] Liu Y, Bufford D, Wang H, Sun C, Zhang X. Mechanical properties of highly textured Cu/Ni multilayers. Acta Mater 2011;59:1924–33.
- [401] Carpenter R, Liu C. Proceedings, second international conference on the strength of metals and alloys. Pacific Grove, California, ASM, vol. 2; 1970. p. 674
- [402] Brailsford A, Bullough R. The theory of sink strengths. Philos Trans Royal Soc Lond A: Math, Phys Eng Sci 1981;302:87–137.
- [403] Brailsford AD, Bullough R, Hayns MR. Point-defect sink strengths and void-swelling. | Nucl Mater 1976;60:246-56.
- [404] Bullough R, Hayns M, Woo C. The sink strength of dislocation loops and their growth in irradiated materials. | Nucl Mater 1979;84:93-100.
- [405] Rauht H, Wood M, Bullough R. Void sink strength including bulk recombination. Phil Mag A 1981;44:1255-76.
- [406] Doan N, Martin G. Elimination of irradiation point defects in crystalline solids: sink strengths. Phys Rev B 2003;67:134107.
- [407] Demkowicz M, Hoagland R, Uberuaga B, Misra A. Influence of interface sink strength on the reduction of radiation-induced defect concentrations and fluxes in materials with large interface area per unit volume. Phys Rev B 2011;84:104102.
- [408] Yu K, Sun C, Chen Y, Liu Y, Wang H, Kirk M, et al. Superior tolerance of Ag/Ni multilayers against Kr ion irradiation: an in situ study. Phil Mag 2013:93:3547–62.
- [409] Mao S, Dillon S, Averback RS. The influence of Cu-Nb interfaces on local vacancy concentrations in Cu. Scripta Mater 2013;69:21-4.
- [410] Chen Y, Li N, Bufford D, Li J, Hattar K, Wang H, et al. In situ study of heavy ion irradiation response of immiscible Cu/Fe multilayers. J Nucl Mater 2016:475:274–9.
- [411] Han W, Demkowicz MJ, Mara NA, Fu E, Sinha S, Rollett AD, et al. Design of radiation tolerant materials via interface engineering. Adv Mater 2013;25:6975–9.
- [412] Zinkle S. Microstructure of ion irradiated ceramic insulators. Nucl Instrum Meth Phys Res Sect B: Beam Interact Mater Atoms 1994;91:234-46.
- [413] Su Q, Cui B, Kirk MA, Nastasi M. Cascade effects on the irradiation stability of amorphous SiOC. Phil Mag Lett 2016;96:60-6.
- [414] Zhang X, Li N, Anderoglu O, Wang H, Swadener J, Höchbauer T, et al. Nanostructured Cu/Nb multilayers subjected to helium ion-irradiation. Nucl Instrum Meth Phys Res Sect B: Beam Interact Mater Atoms 2007;261:1129–32.
- [415] Beyerlein I, Demkowicz M, Misra A, Uberuaga B. Defect-interface interactions. Prog Mater Sci 2015;74:125–210.

- [416] Demkowicz M, Wang Y, Hoagland R, Anderoglu O. Mechanisms of He escape during implantation in CuNb multilayer composites. Nucl Instrum Meth Phys Res Sect B: Beam Interact Mater Atoms 2007:261:524–8.
- [417] Hattar K, Demkowicz M, Misra A, Robertson I, Hoagland R. Arrest of He bubble growth in Cu–Nb multilayer nanocomposites. Scripta Mater 2008:58:541–4.
- [418] Li N, Mara N, Wang Y, Nastasi M, Misra A. Compressive flow behavior of Cu thin films and Cu/Nb multilayers containing nanometer-scale helium bubbles. Scripta Mater 2011:64:974–7.
- [419] Zhernenkov M, Jablin MS, Misra A, Nastasi M, Wang Y, Demkowicz MJ, et al. Trapping of implanted He at Cu/Nb interfaces measured by neutron reflectometry. Appl Phys Lett 2011;98.
- [420] Li N, Nastasi M, Misra A. Defect structures and hardening mechanisms in high dose helium ion implanted Cu and Cu/Nb multilayer thin films. Int J Plast 2012;32:1–16.
- [421] Kashinath A, Wang P, Majewski J, Baldwin J, Wang Y, Demkowicz M. Detection of helium bubble formation at fcc-bcc interfaces using neutron reflectometry. J Appl Phys 2013;114:043505.
- [422] Han W, Mara N, Wang Y, Misra A, Demkowicz M. He implantation of bulk Cu–Nb nanocomposites fabricated by accumulated roll bonding. J Nucl Mater 2014;452:57–60.
- [423] Mao S, Özerinç S, King WP, Averback RS, Dillon SJ. Effect of irradiation damage on the shear strength of Cu–Nb interfaces. Scripta Mater 2014:90:29–32
- [424] Lach TG, Ekiz EH, Averback RS, Mara NA, Bellon P. Role of interfaces on the trapping of He in 2D and 3D Cu–Nb nanocomposites. J Nucl Mater 2015;466;36–42.
- [425] Li N, Demkowicz M, Mara N, Wang Y, Misra A. Hardening due to Interfacial He Bubbles in Nanolayered Composites. Mater Res Lett 2015;4:75-82.
- [426] Mao S, Shu S, Zhou J, Averback RS, Dillon SJ. Quantitative comparison of sink efficiency of Cu–Nb, Cu–V and Cu–Ni interfaces for point defects. Acta Mater 2015;82:328–35.
- [427] Bollmann W. O-Lattice calculation of an FCC-BCC interface. Phys Status Solidi (a) 1974;21:543-50.
- [428] Demkowicz MJ, Hoagland RG, Hirth JP. Interface structure and radiation damage resistance in Cu-Nb multilayer nanocomposites. Phys Rev Lett 2008;100:136102.
- [429] Demkowicz MI, Wang I, Hoagland RG, Interfaces between dissimilar crystalline solids. Dislocations in solids 2008:14:141–207.
- [430] Demkowicz M, Bhattacharyya D, Usov I, Wang Y, Nastasi M, Misra A. The effect of excess atomic volume on He bubble formation at fcc-bcc interfaces. Appl Phys Lett 2010;97:161903.
- [431] Kolluri K, Demkowicz MJ. Dislocation mechanism of interface point defect migration. Phys Rev B 2010;82:193404.
- [432] Kolluri K, Demkowicz MJ. Formation, migration, and clustering of delocalized vacancies and interstitials at a solid-state semicoherent interface. Phys Rev B 2012;85:205416.
- [433] Liu X-Y, Hoagland R, Demkowicz M, Nastasi M, Misra A. The influence of lattice misfit on the atomic structures and defect energetics of face centered cubic-body centered cubic interfaces. J Eng Mater Technol 2012;134:021012.
- [434] Liu X-Y, Überuaga BP, Demkowicz MJ, Germann TC, Misra A, Nastasi M. Mechanism for recombination of radiation-induced point defects at interphase boundaries. Phys Rev B 2012;85:012103.
- [435] Kashinath A, Misra A, Demkowicz M. Stable storage of helium in nanoscale platelets at semicoherent interfaces. Phys Rev Lett 2013;110:086101.
- [436] Kolluri K, Demkowicz MJ, Hoagland RG, Liu X-Y. Behavior of vacancies and interstitials at semicoherent interfaces. Jom 2013;65:374-81.
- [437] McPhie M, Capolungo L, Dunn A, Cherkaoui M. Interfacial trapping mechanism of He in Cu-Nb multilayer materials. J Nucl Mater 2013;437:222-8.
- [438] Zhang L, Demkowicz MJ. Morphological stability of Cu-Nb nanocomposites under high-energy collision cascades. Appl Phys Lett 2013;103:061604. [439] Vattré A, Abdolrahim N, Kolluri K, Demkowicz M. Computational design of patterned interfaces using reduced order models. Sci Reports 2014;4.
- [440] Yuryev D, Demkowicz M. Computational design of solid-state interfaces using O-lattice theory: an application to mitigating helium-induced damage.

 Appl Phys Lett 2014;105:221601.
- [441] Zhang L, Demkowicz M. Radiation-induced mixing between metals of low solid solubility. Acta Mater 2014;76:135–50.
- [442] Vattré A, Jourdan T, Ding H, Marinica M-C, Demkowicz M. Non-random walk diffusion enhances the sink strength of semicoherent interfaces. Nat Commun 2016:7.
- [443] Fu E, Carter J, Swadener G, Misra A, Shao L, Wang H, et al. Size dependent enhancement of helium ion irradiation tolerance in sputtered Cu/V nanolaminates. J Nucl Mater 2009;385:629–32.
- [444] Fu E, Wang H, Carter J, Shao L, Wang Y, Zhang X. Fluence-dependent radiation damage in helium (He) ion-irradiated Cu/V multilayers. Phil Mag 2013:93:883–98.
- [445] Li N, Carter J, Misra A, Shao L, Wang H, Zhang X. The influence of interfaces on the formation of bubbles in He-ion-irradiated Cu/Mo nanolayers. Phil Mag Lett 2011;91:18–28.
- [446] Zhang J, Zeng F, Wu K, Wang Y, Liang X, Liu G, et al. Size-dependent plastic deformation characteristics in He-irradiated nanostructured Cu/Mo multilayers: Competition between dislocation-boundary and dislocation-bubble interactions. Mater Sci Eng: A 2016;673:530–40.
- [447] Gao Y, Yang T, Xue J, Yan S, Zhou S, Wang Y, et al. Radiation tolerance of Cu/W multilayered nanocomposites. J Nucl Mater 2011;413:11-5.
- [448] Callisti M, Karlik M, Polcar T. Bubbles formation in helium ion irradiated Cu/W multilayer nanocomposites: effects on structure and mechanical properties. J Nucl Mater 2016;473:18–27.
- [449] González C, Iglesias R. Energetic analysis of He and monovacancies in Cu/W metallic interfaces. Mater Des 2016;91:171-9.
- [450] Sun C, Uberuaga BP, Yin L, Li J, Chen Y, Kirk MA, et al. Resilient ZnO nanowires in an irradiation environment: an in situ study. Acta Mater 2015;95:156–63.
- [451] Chen Y, Fu E, Yu K, Song M, Liu Y, Wang Y, et al. Enhanced radiation tolerance in immiscible Cu/Fe multilayers with coherent and incoherent layer interfaces. J Mater Res 2015;30:1300–9.
- [452] Wei Q, Li N, Mara N, Nastasi M, Misra A. Suppression of irradiation hardening in nanoscale V/Ag multilayers. Acta Mater 2011;59:6331-40.
- [453] Yu KY, Liu Y, Fu EG, Wang YQ, Myers MT, Wang H, et al. Comparisons of radiation damage in He ion and proton irradiated immiscible Ag/Ni nanolayers. J Nucl Mater 2013;440:310–8.
- [454] Chen F, Tang X, Yang Y, Huang H, Liu J, Li H, et al. Atomic simulations of Fe/Ni multilayer nanocomposites on the radiation damage resistance. J Nucl Mater 2016;468:164–70.
- [455] Chen F, Tang X, Yang Y, Huang H, Chen D. Investigation of structural stability and magnetic properties of Fe/Ni multilayers irradiated by 300keV Fe 10 +. J Nucl Mater 2014;452:31–6.
- [456] Shao S, Wang J, Misra A, Hoagland RG. Spiral patterns of dislocations at nodes in (111) semi-coherent FCC interfaces. Sci Reports 2013;3.
- [457] Reed D. A review of recent theoretical developments in the understanding of the migration of helium in metals and its interaction with lattice defects. Radiation Effects 1977;31:129–47.
- [458] Thomas G. Experimental studies of helium in metals. Radiation Effects 1983;78:37-51.
- [459] Lucas AA. Helium in metals. Physica B+C 1984;127:225-39.
- [460] Chen D, Li N, Yuryev D, Baldwin JK, Wang Y, Demkowicz MJ. Self-organization of helium precipitates into elongated channels within metal nanolayers. Sci Adv 2017;3.
- [461] Chen D, Li N, Yuryev D, Wen J, Baldwin K, Demkowicz MJ, et al. Imaging the in-plane distribution of helium precipitates at a Cu/V interface. Mater Res Lett 2017:1–8.
- [462] Demkowicz MJ, Anderoglu O, Zhang X, Misra A. The influence of ∑ 3 twin boundaries on the formation of radiation-induced defect clusters in nanotwinned Cu. J Mater Res 2011;26:1666–75.

- [463] Chen Y, Liu Y, Fu E, Sun C, Yu K, Song M, et al. Unusual size-dependent strengthening mechanisms in helium ion-irradiated immiscible coherent Cu/Co nanolayers. Acta Mater 2015:84:393–404.
- [464] Heinisch HL, Gao F, Kurtz RJ. The effects of interfaces on radiation damage production in layered metal composites. J Nucl Mater 2004;329:924-8.
- [465] Li N, Martin M, Anderoglu O, Misra A, Shao L, Wang H, et al. He ion irradiation damage in Al/Nb multilayers. J Appl Phys 2009;105:123522.
- [466] Milosavljević M, Stojanović N, Peruško D, Timotijević B, Toprek D, Kovač J, et al. Ion irradiation induced Al-Ti interaction in nano-scaled Al/Ti multilayers. Appl Surf Sci 2012;258:2043-6.
- [467] Peruško D, Petrović S, Stojanović M, Mitrić M, Čizmović M, Panjan M, et al. Formation of intermetallics by ion implantation of multilatered Al/Ti nano-structures. Nucl Instrum Meth Phys Res Sect B: Beam Interact Mater Atoms 2012;282:4–7.
- [468] Li N, Fu E, Wang H, Carter J, Shao L, Maloy S, et al. He ion irradiation damage in Fe/W nanolayer films. J Nucl Mater 2009;389:233-8.
- [469] Milosavljević M, Toprek D, Obradović M, Grce A, Peruško D, Dražič G, et al. Ion irradiation induced solid-state amorphous reaction in Ni/Ti multilayers. Appl Surf Sci 2013;268:516–23.
- [470] Liu B, Lai W, Zhang Q. Irradiation induced amorphization in metallic multilayers and calculation of glass-forming ability from atomistic potential in the binary metal systems. Mater Sci Eng: R: Reports 2000;29:1–48.
- [471] Yu KY, Fan Z, Chen Y, Song M, Liu Y, Wang H, et al. In situ observation of defect annihilation in Kr ion-irradiated bulk Fe/amorphous-Fe2Zr nanocomposite alloy. Mater Res Lett 2015;3:35–42.
- [472] Hobbs LW, Clinard FW, Zinkle SJ, Ewing RC. Radiation effects in ceramics. J Nucl Mater 1994;216:291–321.
- [473] Hong M, Ren F, Zhang H, Xiao X, Yang B, Tian C, et al. Enhanced radiation tolerance in nitride multilayered nanofilms with small period-thicknesses. Appl Phys Lett 2012;101:153117.
- [474] Hong M, Ren F, Wang Y, Zhang H, Xiao X, Fu D, et al. Size-dependent radiation tolerance and corrosion resistance in ion irradiated CrN/AlTiN nanofilms. Nucl Instrum Meth Phys Res Sect B: Beam Interact Mater Atoms 2015;342:137–43.
- [475] Jiao L, Chen A, Myers M, General M, Shao L, Zhang X, et al. Enhanced ion irradiation tolerance properties in TiN/MgO nanolayer films. J Nucl Mater 2013;434:217–22.
- [476] Kim I, Jiao L, Khatkhatay F, Martin M, Lee J, Shao L, et al. Size-dependent radiation tolerance in ion irradiated TiN/AlN nanolayer films. J Nucl Mater 2013;441:47–53.
- [477] Sickafus KE, Grimes RW, Valdez JA, Cleave A, Tang M, Ishimaru M, et al. Radiation-induced amorphization resistance and radiation tolerance in structurally related oxides. Nat Mater 2007;6:217–23.
- [478] Bi Z, Uberuaga B, Vernon L, Fu E, Wang Y, Li N, et al. Radiation damage in heteroepitaxial BaTiO3 thin films on SrTiO3 under Ne ion irradiation. J Appl Phys 2013;113:023513.
- [479] Dholabhai PP, Aguiar JA, Misra A, Uberuaga BP. Defect interactions with stepped CeO2/SrTiO3 interfaces: implications for radiation damage evolution and fast ion conduction. J Chem Phys 2014;140:194701.
- [480] Zinkle SJ, Skuratov VA, Hoelzer DT. On the conflicting roles of ionizing radiation in ceramics. Nucl Instrum Meth B 2002;191:758-66.
- [481] Milosavljević M, Peruško D, Milinović V, Stojanović Z, Zalar A, Kovač J, et al. Ion irradiation stability of multilayered AlN/TiN nanocomposites. J Phys D: Appl Phys 2010;43:065302.
- [482] Milosavljević M, Obradović M, Grce A, Peruško D, Pjević D, Kovač J, et al. High dose ion irradiation effects on immiscible AlN/TiN nano-scaled multilayers. Thin Solid Films 2013;544:562–6.
- [483] Milosavljević M, Grce A, Peruško D, Stojanović M, Kovač J, Dražič G, et al. A comparison of Ar ion implantation and swift heavy Xe ion irradiation effects on immiscible AlN/TiN multilayered nanostructures. Mater Chem Phys 2012;133:884–92.
- [484] Pedro Uberuaga B, Martinez E, Bi Z, Zhuo M, Jia Q, Nastasi M, et al. Defect distributions and transport in nanocomposites: a theoretical perspective.
- [485] Zhuo M, Fu E, Yan L, Wang Y, Zhang Y, Dickerson R, et al. Interface-enhanced defect absorption between epitaxial anatase TiO 2 film and single crystal SrTiO 3. Scripta Mater 2011;65:807–10.
- [486] Zhuo M, Uberuaga B, Yan L, Fu E, Dickerson R, Wang Y, et al. Radiation damage at the coherent anatase TiO2/SrTiO3 interface under Ne ion irradiation. I Nucl Mater 2012;429:177–84.
- [487] Kaspar TC, Bowden ME, Wang CM, Shutthanandan V, Overman NR, Van Ginhoven RM, et al. Epitaxial Fe/Y 2 O 3 interfaces as a model system for oxide-dispersion-strengthened ferritic alloys. J Nucl Mater 2015;457:352–61.
- [488] Chen Y, Jiao L, Sun C, Song M, Yu KY, Liu Y, et al. In situ studies of radiation induced crystallization in Fe/a-Y2O3 nanolayers. J Nucl Mater 2014;452:321-7.
- [489] Porter D, Garner F. Irradiation creep and embrittlement behavior of AISI 316 stainless steel at very high neutron fluences. J Nucl Mater 1988;159:114–21.
- [490] Murty K, Charit I. Structural materials for Gen-IV nuclear reactors: challenges and opportunities. J Nucl Mater 2008;383:189-95.
- [491] Zhang J, Liu Y, Chen J, Chen Y, Liu G, Zhang X, et al. Mechanical properties of crystalline Cu/Zr and crystal–amorphous Cu/Cu–Zr multilayers. Mater Sci Eng: A 2012:552:392–8.
- [492] Zhang J, Wang Y, Liang X, Zeng F, Liu G, Sun J. Size-dependent He-irradiated tolerance and plastic deformation of crystalline/amorphous Cu/Cu–Zr nanolaminates. Acta Mater 2015;92:140–51.
- [493] Uchic MD, Dimiduk DM, Florando JN, Nix WD. Sample dimensions influence strength and crystal plasticity. Science 2004;305:986-9.
- [494] Greer JR, Oliver WC, Nix WD. Size dependence of mechanical properties of gold at the micron scale in the absence of strain gradients. Acta Mater 2005;53:1821–30.
- [495] Uchic MD, Shade PA, Dimiduk DM. Plasticity of micrometer-scale single crystals in compression. Annu Rev Mater Res 2009;39:361–86.
- [496] Kiener D, Hosemann P, Maloy S, Minor A. In situ nano-compression testing of irradiated copper. Nat Mater 2011;10:608.
- [497] Kroupa F, Hirsch P. Elastic interaction between prismatic dislocation loops and straight dislocations. Discuss Faraday Soc 1964;38:49–55.
- [498] Friedel J. Dislocations. New York: Pergamon; 1964.
- [499] Zinkle SJ, Matsukawa Y. Observation and analysis of defect cluster production and interactions with dislocations. J Nucl Mater 2004;329:88–96.
- [500] Kocks U. The theory of an obstacle-controlled yield strength—report after an international workshop. Mater Sci Eng 1977;27:291-8.
- [501] Bacon DJ, Kocks UF, Scattergood RO. The effect of dislocation self-interaction on the orowan stress. Phil Mag 1973;28:1241-63.
- [502] Hashimoto N, Byun T, Farrell K, Zinkle S. Deformation microstructure of neutron-irradiated pure polycrystalline metals. J Nucl Mater 2004;329:947–52.
- [503] Wang J, Kang K, Zhang R, Zheng S, Beyerlein I, Mara N. Structure and property of interfaces in ARB Cu/Nb laminated composites. Jom 2012;64:1208–17.
- [504] Chen F, Tang X, Huang H, Liu J, Li H, Qiu Y, et al. Surface damage and mechanical properties degradation of Cr/W multilayer films irradiated by Xe 20+. Appl Surf Sci 2015;357:1225–30.
 [505] Callisti M, Lozano-Perez S, Polcar T. Structural and mechanical properties of γ-irradiated Zr/Nb multilayer nanocomposites. Mater Lett
- 2016;163:138–41.

 [506] Milosavljević M, Milinović V, Peruško D, Gree A, Stojanović M, Pjević D, et al. Stability of nano-scaled Ta/Ti multilayers upon argon ion irradiation.
- Nucl Instrum Meth Phys Res Sect B: Beam Interact Mater Atoms 2011;269:2090–7.
- [507] Setyawan W, Gerboth M, Yao B, Henager CH, Devaraj A, Vemuri VR, et al. Asymmetry of radiation damage properties in Al–Ti nanolayers. J Nucl Mater 2014;445:261–71.
- [508] Liang X, Zhang J, Wang Y, Wu S, Zeng F, Wu K, et al. Tuning the size-dependent He-irradiated tolerance and strengthening behavior of crystalline/ amorphous Cu/Ta nanostructured multilayers. Mater Sci Eng: A 2016;672:153–60.

- [509] Su Q, Price L, Shao L, Nastasi M. Dose dependence of radiation damage in nano-structured amorphous SiOC/crystalline Fe composite. Mater Res Lett 2016:4:48–54.
- [510] Su Q, Price L, Shao L, Nastasi M. Temperature-dependent helium ion-beam mixing in an amorphous SiOC/crystalline Fe composite. Metals 2016:6:261.
- [511] Lescoat ML, Ribis J, Chen Y, Marquis EA, Bordas E, Trocellier P, et al. Radiation-induced Ostwald ripening in oxide dispersion strengthened ferritic steels irradiated at high ion dose. Acta Mater 2014:78:328–40.
- [512] Anderoglu O, Zhou M, Zhang J, Wang Y, Maloy S, Baldwin J, et al. He+ ion irradiation response of Fe-TiO 2 multilayers. | Nucl Mater 2013;435:96-101.
- [513] Xu Y, Yadav SK, Aguiar JA, Anderoglu O, Baldwin JK, Wang Y, et al. Irradiation-induced formation of a spinel phase at the FeCr/MgO interface. Acta Mater 2015;93:87–94.
- [514] Li N, Yadav S, Xu Y, Aguiar J, Baldwin J, Wang Y, et al. Cr incorporated phase transformation in Y203 under ion irradiation. Sci Reports 2017;7.
- [515] Bufford D, Liu Y, Wang J, Wang H, Zhang X. In situ nanoindentation study on plasticity and work hardening in aluminium with incoherent twin boundaries. Nat Commun 2014:5.
- [516] Njoroge E, Theron C, Malherbe J, van der Berg N, Hlatshwayo T, Skuratov V. Surface and interface modification of Zr/SiC interface by swift heavy ion irradiation. Nucl Instrum Meth Phys Res Sect B: Beam Interact Mater Atoms 2015;354:249–54.
- [517] Bugnet M, Cabioc'h T, Mauchamp V, Guérin P, Marteau M, Jaouen M. Stability of the nitrogen-deficient Ti2AlN x MAX phase in Ar2+-irradiated (Ti, Al) N/Ti2AlN x multilayers. J Mater Sci 2010;45:5547–52.
- [518] Lu L, Shen Y, Chen X, Qian L, Lu K. Ultrahigh strength and high electrical conductivity in copper. Science 2004;304:422-6.
- [519] Zhang X, Misra A, Wang H, Nastasi M, Embury JD, Mitchell TE, et al. Nanoscale-twinning-induced strengthening in austenitic stainless steel thin films. Appl Phys Lett 2004;84:1096.
- [520] Anderoglu O, Misra A, Wang H, Ronning F, Hundley MF, Zhang X. Epitaxial nanotwinned Cu films with high strength and high conductivity. Appl Phys Lett 2008;93:083108.
- [521] Zhang X, Wang H, Chen XH, Lu L, Lu K, Hoagland RG, et al. High-strength sputter-deposited Cu foils with preferred orientation of nanoscale growth twins. Appl Phys Lett 2006;88:173116.
- [522] Xue S, Fan Z, Chen Y, Li J, Wang H, Zhang X. The formation mechanisms of growth twins in polycrystalline Al with high stacking fault energy. Acta Mater 2015;101:62–70.
- [523] Zhao X, Xiao B, Fletcher AJ, Thomas KM, Bradshaw D, Rosseinsky MJ. Hysteretic adsorption and desorption of hydrogen by nanoporous metal-organic frameworks. Science 2004;306:1012–5.
- [524] Lu L, You ZS, Lu K, Work hardening of polycrystalline Cu with nanoscale twins. Scripta Mater 2012;66:837-42.
- [525] Anderoglu O, Misra A, Wang J, Hoagland RG, Hirth JP, Zhang X. Plastic flow stability of nanotwinned Cu foils. Int J Plast 2010;26:875-86.
- [526] Bufford D, Wang H, Zhang X. High strength, epitaxial nanotwinned Ag films. Acta Mater 2011;59:93-101.
- [527] Ott RT, Geng J, Besser MF, Kramer MJ, Wang YM, Park ES, et al. Optimization of strength and ductility in nanotwinned ultra-fine grained Ag: twin density and grain orientations. Acta Mater 2015;96:378–89.
- [528] Wu ZX, Zhang YW, Srolovitz DJ. Dislocation-twin interaction mechanisms for ultrahigh strength and ductility in nanotwinned metals. Acta Mater 2009;57:4508–18.
- [529] Zhu LL, Ruan HH, Li XY, Dao M, Gao HJ, Lu J. Modeling grain size dependent optimal twin spacing for achieving ultimate high strength and related high ductility in nanotwinned metals. Acta Mater 2011;59:5544–57.
- [530] Furnish TA, Hodge AM. On the mechanical performance and deformation of nanotwinned Ag. Appl Mater 2014;2.
- [531] Li J, Zhang JY, Liu G, Sun J. New insight into the stable grain size of nanotwinned Ni in steady-state creep: effect of the ratio of effective-to-internal stress. Int J Plast 2016;85:172–89.
- [532] Cao AJ, Wei YG. Molecular dynamics simulation of plastic deformation of nanotwinned copper. J Appl Phys 2007;102.
- [533] Sinha T, Kulkarni Y. Alternating brittle and ductile response of coherent twin boundaries in nanotwinned metals. J Appl Phys 2014;116.
- [534] Makin MJ, Whapham AD, Minter FJ. Dislocation loops and hardening in neutron irradiated copper. Phil Mag 1961;6:465.
- [535] Norris D. The growth of voids in nickel in a high-voltage electron microscope. Phil Mag 1971;23:135–52.
- [536] Jahn RJ, King AH. Vacancy deposition during diffusion-induced grain-boundary migration. Philos Mag A 1986;54:L3-7.
- [537] King A, Smith D. Stress-induced absorption and emission of point defects by grain boundaries. Metal Sci 1980;14:57-63.
- [538] Segall RL. Coherent annealing twin boundaries as vacancy sinks. Acta Metall 1964;12:117.
- [539] Gao J, Liu ZJ, Wan FR. Limited effect of twin boundaries on radiation damage. Acta Metall Sin-Engl 2016;29:72-8.
- [540] Xiao XZ, Song DK, Chu HJ, Xue JM, Duan HL. Mechanical behaviors of irradiated FCC polycrystals with nanotwins. Int J Plast 2015;74:110–26.
- [541] Niewczas M, Hoagland R. Molecular dynamic studies of the interaction of $a/6\langle 112\rangle$ Shockley dislocations with stacking fault tetrahedra in copper. Part II: Intersection of stacking fault tetrahedra by moving twin boundaries. Phil Mag 2009;89:727–46.
- [542] Wang J, Huang HC. Novel deformation mechanism of twinned nanowires. Appl Phys Lett 2006;88:203112.
- [543] Jin ZH, Gumbsch P, Albe K, Ma E, Lu K, Gleiter H, et al. Interactions between non-screw lattice dislocations and coherent twin boundaries in face-centered cubic metals. Acta Mater 2008;56:1126–35.
- [544] Zhu T, Li J, Samanta A, Kim HG, Suresh S. Interfacial plasticity governs strain rate sensitivity and ductility in nanostructured metals. Proc Natl Acad Sci USA 2007;104:3031–6.
- [545] Wang J, Anderoglu O, Hirth J, Misra A, Zhang X. Dislocation structures of S3 112 twin boundaries in face centered cubic metals. Appl Phys Lett 2009;95:021908.
- [546] Hodge AM, Furnish TA, Shute CJ, Liao Y, Huang X, Hong CS, et al. Twin stability in highly nanotwinned Cu under compression, torsion and tension. Scripta Mater 2012;66:872–7.
- [547] Wang YM, Sansoz F, LaGrange T, Ott RT, Marian J, Barbee Jr TW, et al. Defective twin boundaries in nanotwinned metals. Nat Mater 2013;12:697–702.
- [548] Li N, Wang J, Misra A, Zhang X, Huang JY, Hirth JP. Twinning dislocation multiplication at a coherent twin boundary. Acta Mater 2011;59:5989–96.
- [549] Chen DK, Kulkarni Y. Elucidating the kinetics of twin boundaries from thermal fluctuations. Mrs Commun 2013;3:241-4.
- [550] Chen DK, Kulkarni Y. Entropic interaction between fluctuating twin boundaries. J Mech Phys Solids 2015;84:59-71.
- [551] Jiao SY, Kulkarni Y. Molecular dynamics study of creep mechanisms in nanotwinned metals. Comp Mater Sci 2015;110:254–60.
- [552] Tucker GJ, Foiles SM. Quantifying the influence of twin boundaries on the deformation of nanocrystalline copper using atomistic simulations. Int J Plast 2015;65:191–205.
- [553] Zhang SB, Wang Y. Molecular dynamics simulation of tension-compression asymmetry in plasticity of fivefold twinned Ag nanopillars. Phys Lett A 2015;379:603–6.
- [554] Zhao X, Lu C, Tieu AK, Pei LQ, Zhang L, Su LH, et al. Deformation mechanisms in nanotwinned copper by molecular dynamics simulation. Mater Sci Eng a-Struct 2017;687:343–51.
- [555] Zhou XL, Li XY, Chen CQ. Atomistic mechanisms of fatigue in nanotwinned metals. Acta Mater 2015;99:77-86.
- [556] Zhu LL, Wen CS, Gao CY, Guo X, Lu J. A study of dynamic plasticity in austenite stainless steels with a gradient distribution of nanoscale twins. Scripta Mater 2017;133:49–53.
- [557] Wang J, Misra A, Hirth JP. Shear response of Sigma 3(112) twin boundaries in face-centered-cubic metals. Phys Rev B 2011;83:064106.
- [558] Chen Y, Wang H, Kirk MA, Li M, Wang J, Zhang X. Radiation induced detwinning in nanotwinned Cu. Scripta Mater 2017;130:37-41.
- [559] Embury J, Nicholson R. The nucleation of precipitates: the system Al-Zn-Mg. Acta Metall 1965;13:403–17.
- [560] Burke J, Stuckey D. Dislocation loop-free zones around grain boundaries in quenched aluminium and aluminium alloys. Phil Mag 1975;31:1063–80.
- [561] Chen Y, Zhang X, Wang J. Radiation enhanced absorption of frank loops by nanovoids in Cu. Jom 2016;68:235-41.

- [562] Li J, Yu KY, Chen Y, Song M, Wang H, Kirk MA, et al. In situ study of defect migration kinetics and self-healing of twin boundaries in heavy ion irradiated nanotwinned metals. Nano Lett 2015;15:2922–7.
- [563] Bahmanpour H, Youssef KM, Horky J, Setman D, Atwater MA, Zehetbauer MJ, et al. Deformation twins and related softening behavior in nanocrystalline Cu-30% Zn alloy. Acta Mater 2012;60:3340–9.
- [564] Choi IC, Kim YJ, Wang YM, Ramamurty U, Jang JI. Nanoindentation behavior of nanotwinned Cu: influence of indenter angle on hardness, strain rate sensitivity and activation volume. Acta Mater 2013;61:7313–23.
- [565] Jerusalem A, Dao M, Suresh S, Radovitzky R. Three-dimensional model of strength and ductility of polycrystalline copper containing nanoscale twins.
- [566] Kulkarni Y, Asaro RJ, Are some nanotwinned fcc metals optimal for strength, ductility and grain stability? Acta Mater 2009;57:4835-44.
- [567] Pan QS, Lu L. Strain-controlled cyclic stability and properties of Cu with highly oriented nanoscale twins. Acta Mater 2014;81:248-57.
- [568] Yoo BG, Boles ST, Liu Y, Zhang X, Schwaiger R, Eberl C, et al. Quantitative damage and detwinning analysis of nanotwinned copper foil under cyclic loading. Acta Mater 2014;81:184–93.
- [569] You ZS, Lu L, Lu K. Tensile behavior of columnar grained Cu with preferentially oriented nanoscale twins. Acta Mater 2011;59:6927–37.
- [570] Zeng Z, Li XY, Lu L, Zhu T. Fracture in a thin film of nanotwinned copper. Acta Mater 2015;98:313-7.
- [571] Liu Y, Jian J, Chen Y, Wang H, Zhang X. Plasticity and ultra-low stress induced twin boundary migration in nanotwinned Cu by in situ nanoindentation studies. Appl Phys Lett 2014;104.
- [572] Zhu LL, Guo X, Ruan HH, Lu J. Prediction of mechanical properties in bimodal nanotwinned metals with a composite structure. Compos Sci Technol 2016;123:222–31.
- [573] Deng C, Sansoz F. A new form of pseudo-elasticity in small-scale nanotwinned gold. Extreme Mech Lett 2016;8:201-7.
- [574] Zhang S, Zhou JQ, Wang L, Wang Y. The effect of the angle between loading axis and twin boundary on the mechanical behaviors of nanotwinned materials. Mater Des 2013;45:292–9.
- [575] Li J, Zhang JY, Jiang L, Zhang P, Wu K, Liu G, et al. Twinning/detwinning-mediated grain growth and mechanical properties of free-standing nanotwinned Ni foils: grain size and strain rate effects. Mater Sci Eng a-Struct 2015;628:62–74.
- [576] Borovikov V, Mendelev MI, King AH, LeSar R. Effect of stacking fault energy on mechanism of plastic deformation in nanotwinned FCC metals. Modell Simul Mater Sci Eng 2015;23.
- [577] Wang J, Zhang XH. Twinning effects on strength and plasticity of metallic materials. Mrs Bull 2016;41:274-85.
- [578] Mieszala M, Guillonneau G, Hasegawa M, Raghavan R, Wheeler JM, Mischler S, et al. Orientation-dependent mechanical behaviour of electrodeposited copper with nanoscale twins. Nanoscale 2016;8:15999–6004.
- [579] Lu N, Du K, Lu L, Ye HQ. Transition of dislocation nucleation induced by local stress concentration in nanotwinned copper. Nat Commun 2015;6.
- [580] Li J, Zhang JY, Zhang P, Wu K, Liu G, Sun J. Grain size effects on microstructural stability and creep behaviour of nanotwinned Ni free-standing foils at room temperature. Phil Mag 2016;96:3016–40.
- [581] Ovid'ko IA, Sheinerman AG. Plastic deformation through De-twinning mediated by incoherent twin boundaries in nanotwinned metallic alloys. Rev Adv Mater Sci 2016;47:1–8.
- [582] Sim GD, Krogstad JA, Reddy KM, Xie KY, Valentino GM, Weihs TP, et al. Nanotwinned metal MEMS films with unprecedented strength and stability. Sci Adv 2017;3.
- [583] Shaw LL, Ortiz AL, Villegas JC. Hall-Petch relationship in a nanotwinned nickel alloy. Scripta Mater 2008;58:951-4.
- [584] Zhang X, Misra A. Superior thermal stability of coherent twin boundaries in nanotwinned metals. Scripta Mater 2012;66:860-5.
- [585] Beyerlein IJ, Zhang XH, Misra A. Growth twins and deformation twins in metals. Annu Rev Mater Res 2014;44:329-63.
- [586] Li N, Wang J, Huang JY, Misra A, Zhang X. Influence of slip transmission on the migration of incoherent twin boundaries in epitaxial nanotwinned Cu. Scripta Mater 2011:64:149–52.
- [587] Wang J, Anderoglu O, Hirth JP, Misra A, Zhang X. Dislocation structures of Sigma 3 112 twin boundaries in face centered cubic metals. Appl Phys Lett 2009;95.
- [588] Zhang X, Misra A, Wang H, Lima AL, Hundley MF, Hoagland RG. Effects of deposition parameters on residual stresses, hardness and electrical resistivity of nanoscale twinned 330 stainless steel thin films. J Appl Phys 2005;97.
- [589] Zhu YT, Liao XZ, Wu XL. Deformation twinning in nanocrystalline materials. Prog Mater Sci 2012;57:1-62.
- [590] Zhu YT, Wu XL, Liao XZ, Narayan J, Kecskes LJ, Mathaudhu SN. Dislocation-twin interactions in nanocrystalline fcc metals. Acta Mater 2011;59:812–21.
- [591] Jiao S, Kulkarni Y. Radiation tolerance of nanotwinned metals an atomistic perspective. Comp Mater Sci 2018;142:290–6.
- [592] Li N, Wang J, Wang YQ, Serruys Y, Nastasi M, Misra A. Incoherent twin boundary migration induced by ion irradiation in Cu. J Appl Phys 2013;113:023508.
- [593] Yu KY, Bufford D, Khatkhatay F, Wang H, Kirk MA, Zhang X. In situ studies of irradiation-induced twin boundary migration in nanotwinned Ag. Scripta Mater 2013;69:385–8.
- [594] Fan C, Li J, Fan Z, Wang H, Zhang X. In situ studies on the irradiation-induced twin boundary-defect interactions in Cu. Metall Mater Trans A 2017;48:5172–80.
- [595] Xu L, Xu D, Tu KN, Cai Y, Wang N, Dixit P, et al. Structure and migration of (112) step on (111) twin boundaries in nanocrystalline copper. J Appl Phys 2008;104:113717.
- [596] Singh BN, Horsewell A, Toft P, Edwards DJ. Temperature and dose dependencies of microstructure and hardness of neutron-irradiated ofhi copper. J Nucl Mater 1995;224:131–40.
- [597] Kiritani M. Story of stacking fault tetrahedra. Mater Chem Phys 1997;50:133–8.
- [598] Zinkle S, Seitzman L, Wolfer W. I. Energy calculations for pure metals. Phil Mag A 1987;55:111–25.
- [599] Was GS. Fundamentals of radiation materials science: metals and alloys. Springer Science & Business Media; 2007.
- [600] Saintoyant L, Lee HJ, Wirth BD. Molecular dynamics study of the interactions between dislocation and imperfect stacking fault tetrahedron in Cu. J Nucl Mater 2007;361:206–17.
- [601] Lee HJ, Wirth BD. Molecular dynamics simulation of the interaction between a mixed dislocation and a stacking fault tetrahedron. Phil Mag 2009;89:821–41.
- [602] Marian J, Martinez E, Lee HJ, Wirth BD. Micro/meso-scale computational study of dislocation-stacking-fault tetrahedron interactions in copper. J Mater Res 2009;24:3628–35.
- [603] Rodney D. Molecular dynamics simulation of screw dislocations interacting with interstitial frank loops in a model FCC crystal. Acta Mater 2004;52:607–14.
- [604] Chen Y, Li J, Yu KY, Wang H, Kirk MA, Li M, et al. In situ studies on radiation tolerance of nanotwinned Cu. Acta Mater 2016;111:148-56.
- [605] Sørensen MR, Mishin Y, Voter AF. Diffusion mechanisms in Cu grain boundaries. Phys Rev B 2000;62:3658.
- [606] Li J, Chen Y, Wang H, Zhang X. In situ studies on twin-thickness-dependent distribution of defect clusters in heavy ion-irradiated nanotwinned Ag. Metall Mater Trans A 2017;48:1466–73.
- [607] Fan YCC, Li Jin, Ding Jie, Wang H, Zhang X. Defect evolution in heavy ion irradiated nanotwinned Cu with nanovoids. J Nucl Mater 2017;496:293-300.
- [608] Joo SH, Choi SJ, Oh I, Kwak J, Liu Z, Terasaki O, et al. Ordered nanoporous arrays of carbon supporting high dispersions of platinum nanoparticles. Nature 2001:412:169–72.
- [609] Davis ME. Ordered porous materials for emerging applications. Nature 2002;417:813-21.
- [610] Scott BJ, Wirnsberger G, Stucky GD. Mesoporous and mesostructured materials for optical applications. Chem Mater 2001;13:3140-50.

- [611] Shang Z, Li Jin, Fan C, Chen Y, Li Q, Wang H, et al. In situ study on surface roughening in radiation-resistant Ag nanowires. Nanotechnology 2018:29:215708.
- [612] Vogel R, Hoyer P, Weller H. Quantum-sized Pbs, Cds, Ag2s, Sb2s3, and Bi2s3 particles as sensitizers for various nanoporous wide-bandgap semiconductors. J Phys Chem-Us 1994;98:3183–8.
- [613] Lang X, Hirata A, Fujita T, Chen M. Nanoporous metal/oxide hybrid electrodes for electrochemical supercapacitors. Nat Nanotechnol 2011;6:232-6.
- [614] Morris RE, Wheatley PS. Gas storage in nanoporous materials. Angew Chem Int Ed Engl 2008;47:4966-81.
- [615] Zheng H, Liu Y, Cao F, Wu S, Jia S, Cao A, et al. Electron beam-assisted healing of nanopores in magnesium alloys. Sci Rep 2013;3.
- [616] Fujita T, Guan P, McKenna K, Lang X, Hirata A, Zhang L, et al. Atomic origins of the high catalytic activity of nanoporous gold. Nat Mater 2012;11:775–80.
- [617] Biener J, Hodge AM, Hayes JR, Volkert CA, Zepeda-Ruiz LA, Hamza AV, et al. Size effects on the mechanical behavior of nanoporous Au. Nano Lett 2006:6:2379–82.
- [618] Asthana A, Momeni K, Prasad A, Yap YK, Yassar RS. In situ observation of size-scale effects on the mechanical properties of ZnO nanowires. Nanotechnology 2011;22:265712.
- [619] Sun C, Bufford D, Chen Y, Kirk MA, Wang YQ, Li M, et al. In situ study of defect migration kinetics in nanoporous Ag with enhanced radiation tolerance. Sci Rep 2014;4:3737.
- [620] Li Jin, Fan C, Li Q, Wang H, Zhang X. In situ studies on irradiation resistance of nanoporous Au through temperature-jump tests. Acta Mater 2018;143:30–42.
- [621] Zhu XF, Williams JS, Conway MJ, Ridgway MC, Fortuna F, Ruault MO, et al. Direct observation of irradiation-induced nanocavity shrinkage in Si. Appl Phys Lett 2001;79:3416.
- [622] Xu W, Zhang Y, Cheng G, Jian W, Millett PC, Koch CC, et al. In-situ atomic-scale observation of irradiation-induced void formation. Nat Commun 2013:4:2288.
- [623] Bringa EM, Monk JD, Caro A, Misra A, Zepeda-Ruiz L, Duchaineau M, et al. Are nanoporous materials radiation resistant? Nano Lett 2012;12:3351-5.
- [624] Li Jin, Chen Y, Wang Jie, Zhang X. In situ study on enhanced heavy ion irradiation tolerance of porous Mg. Scripta Mater 2018;144:13-7.
- [625] Zhang CG, Li YG, Zhou WH, Hu L, Zeng Z. Anti-radiation mechanisms in nanoporous gold studied via molecular dynamics simulations. J Nucl Mater 2015;466:328–33.
- [626] Misra A, Demkowicz MJ, Zhang X, Hoagland RG. The radiation damage tolerance of ultra-high strength nanolayered composites. Jom 2007;59:62-5.
- [627] Liu WQ, Chen PH, Qiu RZ, Khan M, Liu J, Hou MD, et al. A molecular dynamics simulation study of irradiation induced defects in gold nanowire. Nucl Instrum Meth B 2017;405:22–30.
- [628] Jarvi TT, Nordlund K. Sputtering of freestanding metal nanocrystals. Nucl Instrum Meth B 2012;272:66-9.
- [629] Bufford DC, Hattar K. Physical response of gold nanoparticles to single self-ion bombardment. J Mater Res 2014;29:2387–97.
- [630] Birtcher RC, Donnelly SE. Plastic flow induced by single ion impacts on gold. Phys Rev Lett 1996;77:4374-7.
- [631] Ghaly M, Averback RS. Effect of viscous flow on ion damage near solid surfaces. Phys Rev Lett 1994;72:364-7.
- [632] Kissel R, Urbassek HM. Sputtering from spherical Au clusters by energetic atom bombardment. Nucl Instrum Meth B 2001;180:293-8.
- [633] Berthelot A, Hemon S, Gourbilleau F, Dufour C, Dooryhee E, Paumier E. Nanometric size effects on irradiation of tin oxide powder. Nucl Instrum Meth B 1998:146:437–42.
- [634] Bufford D, Pratt SH, Boyle TJ, Hattar K. In situ TEM ion irradiation and implantation effects on Au nanoparticle morphologies. Chem Commun (Camb) 2014;50:7593–6.
- [635] Greaves G, Hinks JA, Busby P, Mellors NJ, Ilinov A, Kuronen A, et al. Enhanced sputtering yields from single-ion impacts on gold nanorods. Phys Rev Lett 2013;111:065504.
- [636] Ilinov A, Kuronen A, Nordlund K, Greaves G, Hinks J, Busby P, et al. Sputtering yields exceeding 1000 by 80keV Xe irradiation of Au nanorods. Nucl Instrum Meth Phys Res Sect B: Beam Interact Mater Atoms 2014;341:17–21.
- [637] Baranov I, Kirillov S, Novikov A, Obnorskii V, Toulemonde M, Wien K, et al. Desorption of gold nanoclusters (2–150nm) by 1GeV Pb ions. Nucl Instrum Meth Phys Res Sect B: Beam Interact Mater Atoms 2005:230:495–501.
- [638] Jarvi TT, Kuronen A, Nordlund K, Albe K. Damage production in nanoparticles under light ion irradiation. Phys Rev B 2009;80.
- [639] Kissel R, Urbassek HM. Sputtering of a Au surface covered with large spherical clusters. Int J Mass Spectrom 2001;208:29–35.
- [640] Uglov VV, Remnev GE, Kvasov NT, Safronov IV, Shymanski VI. Radiation stability of iron nanoparticles irradiated with accelerated iron ions. Nucl Instrum Meth B 2015;354:259–63.
- [641] Dmitrieva O, Rellinghaus B, Kastner J, Liedke MO, Fassbender J. Ion beam induced destabilization of icosahedral structures in gas phase prepared FePt nanoparticles. J Appl Phys 2005;97.
- [642] Wiedwald U, Klimmer A, Kern B, Han L, Boyen H-G, Ziemann P, et al. Lowering of the L10 ordering temperature of FePt nanoparticles by He+ ion irradiation. Appl Phys Lett 2007;90:62508.
- [643] Jarvi TT, Kuronen A, Nordlund K, Albe K. Structural modification of a multiply twinned nanoparticle by ion irradiation: a molecular dynamics study. J Appl Phys 2007;102:124304.
- [644] Jarvi TT, Pohl D, Albe K, Rellinghaus B, Schultz L, Fassbender J, et al. From multiply twinned to fcc nanoparticles via irradiation-induced transient amorphization. Epl-Europhys Lett 2009;85:26001.
- [645] Ledentsov NN, Ustinov VM, Shchukin VA, Kop'ev PS, Alferov ZI, Bimberg D. Quantum dot heterostructures: fabrication, properties, lasers (Review) Semiconductors+ 1998:32:343-65.
- [646] Mishra YK, Singh F, Avasthi DK, Pivin JC, Malinovska D, Pippel E. Synthesis of elongated Au nanoparticles in silica matrix by ion irradiation. Appl Phys Lett 2007;91:063103.
- [647] Meldrum A, Haglund RF, Boatner LA, White CW. Nanocomposite materials formed by ion implantation. Adv Mater 2001;13:1431.
- [648] Allen TR, Gan J, Cole JI, Miller MK, Busby JT, Shutthanandan S, et al. Radiation response of a 9 chromium oxide dispersion strengthened steel to heavy ion irradiation. J Nucl Mater 2008;375:26–37.
- [649] Bailey NA, Stergar E, Toloczko M, Hosemann P. Atom probe tomography analysis of high dose MA957 at selected irradiation temperatures. J Nucl Mater 2015;459:225–34.
- [650] Baker BW, Brewer LN. Joining of oxide dispersion strengthened steels for advanced reactors. Jom 2014;66:2442-57.
- [651] Bhattacharyya D, Dickerson P, Odette GR, Maloy SA, Misra A, Nastasi MA. On the structure and chemistry of complex oxide nanofeatures in nanostructured ferritic alloy U14YWT. Phil Mag 2012;92:2089–107.
- [652] Brimbal D, Beck L, Troeber O, Gaganidze E, Trocellier P, Aktaa J, et al. Microstructural characterization of Eurofer-97 and Eurofer-ODS steels before and after multi-beam ion irradiations at JANNUS Saclay facility. J Nucl Mater 2015;465:236-44.
- [653] Chen TY, Gigax JG, Price L, Chen D, Ukai S, Aydogan E, et al. Temperature dependent dispersoid stability in ion-irradiated ferritic-martensitic dual-phase oxide-dispersion-strengthened alloy: coherent interfaces vs. incoherent interfaces. Acta Mater 2016;116:29–42.
- [654] Dou P, Kimura A, Kasada R, Okuda T, Inoue M, Ukai S, et al. TEM and HRTEM study of oxide particles in an Al-alloyed high-Cr oxide dispersion strengthened steel with Zr addition. J Nucl Mater 2014;444:441–53.
- [655] He JC, Wan FR, Sridharan K, Allen TR, Certain A, Wu YQ. Response of 9Cr-ODS steel to proton irradiation at 400 degrees C. J Nucl Mater 2014;452:87-94.
- [656] Heintze C, Bergner F, Hernandez-Mayoral M, Kogler R, Muller G, Ulbricht A. Irradiation hardening of Fe-9Cr-based alloys and ODS Eurofer: Effect of helium implantation and iron-ion irradiation at 300 degrees C including sequence effects. J Nucl Mater 2016;470:258–67.
- [657] Hosemann P, Stergar E, Peng L, Dai Y, Maloy SA, Pouchon MA, et al. Macro and microscale mechanical testing and local electrode atom probe measurements of STIP irradiated F82H, Fe-8Cr ODS and Fe-8Cr-2W ODS. J Nucl Mater 2011;417:274–8.

- [658] Hsiung L, Fluss M, Tumey S, Kuntz J, El-Dasher B, Wall M, et al. HRTEM study of oxide nanoparticles in K3-ODS ferritic steel developed for radiation tolerance. J Nucl Mater 2011;409:72–9.
- [659] Huang ZJ, Harris A, Maloy SA, Hosemann P. Nanoindentation creep study on an ion beam irradiated oxide dispersion strengthened alloy. J Nucl Mater 2014;451:162–7.
- [660] Jung JA, Kim SH, Shin SH, Bang IC, Kim JH. Feasibility study of fuel cladding performance for application in ultra-long cycle fast reactor. J Nucl Mater 2013:440:596–605.
- [661] Kim S, Ohtsuka S, Kaito T, Yamashita S, Inoue M, Asayama T, et al. Formation of nano-size oxide particles and delta-ferrite at elevated temperature in 9Cr-ODS steel. J Nucl Mater 2011:417:209–12.
- [662] Klimenkov M, Moslang A, Lindau R. EELS analysis of complex precipitates in PM 2000 steel. Eur Phys J-Appl Phys 2000;42(2008):293–303.
- [663] Krajnikov AV, Morito F, Danylenko MI. Embrittlement of molybdenum-rhenium welds under low and high temperature neutron irradiation. J Nucl Mater 2014;444:404–15.
- [664] Liu S, Odette GR, Segre CU. Evidence for core-shell nanoclusters in oxygen dispersion strengthened steels measured using X-ray absorption spectroscopy. J Nucl Mater 2014;445:50–6.
- [665] London AJ, Lozano-Perez S, Moody MP, Amirthapandian S, Panigrahi BK, Sundar CS, et al. Quantification of oxide particle composition in model oxide dispersion strengthened steel alloys. Ultramicroscopy 2015;159(Pt 2):360–7.
- [666] Lu CY, Lu Z, Xie R, Liu CM, Wang LM. Microstructure of HIPed and SPSed 9Cr-ODS steel and its effect on helium bubble formation. J Nucl Mater 2016:474:65–75.
- [667] Mathon MH, Perrot M, Poirier L, Ratti M, Herve N, de Carlanc Y. Development of new ferritic alloys reinforced by nano titanium nitrides. J Nucl Mater 2015;456:449–54.
- [668] Mazumder B, Parish CM, Bei H, Miller MK. The role of processing route on the microstructure of 14YWT nanostructured ferritic alloy. J Nucl Mater 2015;465;204–11.
- [669] Miao P, Odette GR, Yamamoto T, Alinger M, Klingensmith D. Thermal stability of nano-structured ferritic alloy. | Nucl Mater 2008;377:59-64.
- [670] Mo K, Yun D, Miao Y, Liu X, Pellin M, Almer J, et al. Investigation of high-energy ion-irradiated MA957 using synchrotron radiation under in-situ tension. Materials 2016;9.
- [671] Nakajima K, Shibayama T, Kayano H. Development of Ods vanadium alloy and irradiation effects on its properties. J Atom Energ Soc Jpn 1995;37:338–45.
- [672] Robertson C, Panigrahi BK, Balaji S, Kataria S, Serruys Y, Mathon MH, et al. Particle stability in model ODS steel irradiated up to 100 dpa at 600 degrees C: TEM and nano-indentation investigation. J Nucl Mater 2012;426:240–6.
- [673] Rogozhkin SV, Aleev AA, Zaluzhnyi AG, Iskanderov NA, Nikitin AA, Vladimirov P, et al. Atom probe tomography of nanoscaled features of oxide-dispersion-strengthened ODS Eurofer steel in the initial state and after neutron irradiation. Phys Met Metallogr+ 2012;113:98–105.
- [674] Roldan M, Fernandez P, Vila R, Gomez-Herrero A, Sanchez FJ. The effect of triple ion beam irradiation on cavity formation on pure EFDA iron. J Nucl Mater 2016;479:100–11.
- [675] Rowcliffe AF, Mansur LK, Hoelzer DT, Nanstad RK. Perspectives on radiation effects in nickel-base alloys for applications in advanced reactors. J Nucl Mater 2009;392:341–52.
- Mater 2009;392:341–52.
 [676] Toloczko MB, Garner FA, Voyevodin VN, Bryk VV, Borodin OV, Mel'nychenko VV, et al. Ion-induced swelling of ODS ferritic alloy MA957 tubing to 500
- dpa. J Nucl Mater 2014;453:323–33.
 [677] Veternikova JS, Slugen V, Sojak S, Skarba M, Korhonen E, Stancek S, et al. Application of slow positron beam for study of commercial oxide-dispersion-strengthened steels. J Nucl Mater 2014;450:99–103.
- [678] Xu WZ, Li LL, Saber M, Koch CC, Zhu YT, Scattergood RO. Nano ZrO2 particles in nanocrystalline Fe-14Cr-1.5Zr alloy powders. J Nucl Mater 2014:452:434-9.
- [679] Zhang HQ, Zhang CH, Yang YT, Meng YC, Jang J, Kimura A. Irradiation hardening of ODS ferritic steels under helium implantation and heavy-ion irradiation. | Nucl Mater 2014;455:349-53.
- [680] Zhong SY, Ribis J, Lochet N, de Carlan Y, Klosek V, Mathon MH. Influence of nano-particle coherency degree on the coarsening resistivity of the nano-oxide particles of Fe-14Cr-1W ODS alloys. J Nucl Mater 2014;455:618–23.
- [681] Lazauskas T, Kenny SD, Smith R, Nagra G, Dholakia M, Valsakumar MC. Simulating radiation damage in a bcc Fe system with embedded yttria nanoparticles. J Nucl Mater 2013;437:317–25.
- [682] Ramjauny Y, Rizza G, Perruchas S, Gacoin T, Botha R. Controlling the size distribution of embedded Au nanoparticles using ion irradiation. J Appl Phys 2010:107.
- [683] Rizza G, Cheverry H, Gacoin T, Lamasson A, Henry S. Ion beam irradiation of embedded nanoparticles: toward an in situ control of size and spatial distribution. J Appl Phys 2007;101:014321.
- [684] Sprouster DJ, Giulian R, Araujo LL, Kluth P, Johannessen B, Cookson DJ, et al. Swift heavy-ion irradiation-induced shape and structural transformation in cobalt nanoparticles. J Appl Phys 2011;109:113504.
- [685] Oliver A, Reyes-Esqueda JA, Cheang-Wong JC, Roman-Velazquez CE, Crespo-Sosa A, Rodriguez-Fernandez L, et al. Controlled anisotropic deformation of Ag nanoparticles by Si ion irradiation. Phys Rev B 2006;74:245425.
- [686] Giulian R, Kluth P, Araujo LL, Sprouster DJ, Byrne AP, Cookson DJ, et al. Shape transformation of Pt nanoparticles induced by swift heavy-ion irradiation. Phys Rev B 2008;78:125413.
- [687] Amekura H, Johannessen B, Sprouster DJ, Ridgway MC. Amorphization of Cu nanoparticles: effects on surface plasmon resonance. Appl Phys Lett 2011;99:043102.
- [688] Amekura H, Okubo N, Ishikawa N, Tsuya D, Mitsuishi K, Nakayama Y, et al. Swift heavy ion irradiation of ZnO nanoparticles embedded in silica: radiation-induced deoxidation and shape elongation. Appl Phys Lett 2013;103:203106.
- [689] Song M, Mitsuishi K, Yasuda H, Furuya K. Dynamic process of nano-structured inert gas precipitates introduced with ion implantation in aluminium. J Electron Microsc 2002;51:S211–4.
- [690] Jiang W, Weber WJ, Young JS, Boatner LA. Irradiation-induced formation of nanoparticles in cadmium niobate pyrochlore. Appl Phys Lett 2002;80:670–2.
- [691] Tiwari VK, Kulriya PK, Avasthi DK, Maiti P. Radiation-resistant behavior of poly (vinylidene fluoride)/layered silicate nanocomposites. ACS Appl Mater Interfaces 2008;1:311–8.
- [692] Thomas J, Myara M, Troussellier L, Burov E, Pastouret A, Boivin D, et al. Radiation-resistant erbium-doped-nanoparticles optical fiber for space applications. Opt Express 2012;20:2435–44.
- [693] Ridgway MC, Kluth P, Giulian R, Sprouster DJ, Araujo LL, Schnohr CS, et al. Changes in metal nanoparticle shape and size induced by swift heavy-ion irradiation. Nucl Instrum Meth B 2009;267:931–5.
- [694] Nelson RS, Hudson JA, Mazey DJ. The stability of precipitates in an irradiation environment. J Nucl Mater 1972;44:318-30.
- [695] Wells PB, Yamamoto T, Miller B, Milot T, Cole J, Wu Y, et al. Evolution of manganese-nickel-silicon-dominated phases in highly irradiated reactor pressure vessel steels. Acta Mater 2014;80:205–19.
- [696] Yablinsky CA, Tippey KE, Vaynman S, Anderoglu O, Fine ME, Chung YW, et al. Concepts for the development of nanoscale stable precipitation-strengthened steels manufactured by conventional methods. Jom 2014;66:2467–75.
- [697] Alinger MJ, Odette GR, Hoelzer DT. The development and stability of Y-Ti-O nanoclusters in mechanically alloyed Fe-Cr based ferritic alloys. J Nucl Mater 2004;329:382–6.
- [698] Liu PP, Yu R, Zhu YM, Zhao MZ, Bai JW, Wan FR, et al. Deuterium ion irradiation induced precipitation in Fe-Cr alloy: characterization and effects on irradiation behavior. J Nucl Mater 2015;459:81–9.

- [699] Kaneko K, Kato T, Kitayama M, Tomokiyo Y. Precipitation of MgO-nAl(2)O(3) in Mg-doped alpha-Al2O3 under electron irradiation. J Am Ceram Soc 2003:86:161–8.
- [700] Zheng C, Auger MA, Moody MP, Kaoumi D. Radiation induced segregation and precipitation behavior in self-ion irradiated Ferritic/Martensitic HT9 steel. J Nucl Mater 2017;491:162–76.
- [701] Getto E, Vancoevering G, Was GS. The co-evolution of microstructure features in self-ion irradiated HT9 at very high damage levels. J Nucl Mater 2017:484:193–208.
- [702] Zhang X, Shu SP, Bellon P, Averback RS. Precipitate stability in Cu-Ag-W system under high-temperature irradiation. Acta Mater 2015;97:348–56.
- [703] Zhao MZ, Liu PP, Bai JW, Zhu YM, Wan FR, Ohnuki S, et al. In-situ observation of the effect of the precipitate/matrix interface on the evolution of dislocation structures in CLAM steel during irradiation. Fusion Eng Des 2014;89:2759–65.
- [704] Martin G, Sabathier C, Carlot G, Desgardin P, Raepsaet C, Sauvage T, et al. Irradiation damage effects on helium migration in sintered uranium dioxide. Nucl Instrum Meth B 2012:273:122–6.
- [705] Ahmedabadi P, Kain V, Gupta M, Samajdar I, Sharma SC, Bhagwat P, et al. The role of niobium carbide in radiation induced segregation behaviour of type 347 austenitic stainless steel. J Nucl Mater 2011;415:123–31.
- [706] Stoller RE. The impact of mobile point defect clusters in a kinetic model of pressure vessel embrittlement. Am Soc Test Mater 1999;1325:14–29.
- [707] Lee EH, Mansur LK. Relationships between phase-stability and void swelling in Fe-Cr-Ni alloys during irradiation. Metall Trans A 1992;23:1977-86.
- [708] Sipahigil A, Evans RE, Sukachev DD, Burek MJ, Borregaard J, Bhaskar MK, et al. An integrated diamond nanophotonics platform for quantum-optical networks. Science 2016;354:847–50.
- [709] Freestone I, Meeks N, Sax M, Higgitt C. The Lycurgus Cup A Roman nanotechnology. Gold Bull 2007;40:270-7.